# UNIVERSITY OF SOUTHAMPTON

FACULTY OF NATURAL AND ENVIRONMENTAL SCIENCES

Chemistry

# Synthesis and Evaluation of New Molecular Precursors for the Chemical Vapour Deposition of Electronic Materials

by

**Samantha Louise Hawken**

Thesis for the degree of Doctor of Philosophy

April 2018

UNIVERSITY OF SOUTHAMPTON

# ABSTRACT

FACULTY OF NATURAL AND ENVIRONMENTAL SCIENCES

Chemistry

Thesis for the degree of Doctor of Philosophy

## Synthesis and Evaluation of New Molecular Precursors for the Chemical Vapour Deposition of Electronic Materials

Samantha Louise Hawken

$MCl_3$ (M = Sb, Bi) react with $E^nBu_2$ (E = Se, Te) to form $[MCl_3(E^nBu_2)_3]$, which are effective single source precursors for the low pressure chemical vapour deposition (LPCVD) of metal chalcogenide, $M_2E_3$, thin films. The precursors are extensively dissociated in solution. Flash evaporation of the precursor led to polycrystalline (by XRD), stoichiometric (EDX) $M_2E_3$ films, and their electrical properties have been established by Hall and van de Pauw measurements. It is possible to selectively deposit the p-type $Sb_2Te_3$ onto TiN over $SiO_2$ using $[SbCl_3(Te^nBu_2)_3]$, Combining $[SbCl_3(Te^nBu_2)_3]$ and $[BiCl_3(Te^nBu_2)_3]$ in various ratios allows the deposition of the ternary phase, $(Sb_xBi_{1-x})_2Te_3$, where x varies mainly with deposition temperature.

The synthesis of the germanium tellurolate compound, $[Ge(Te^nBu)_4]$, has been developed by reacting $GeCl_4$ with $^nBuTeLi$ and optimised by the alternative reaction of activated Ge with $^nBu_2Te_2$. It has been demonstrated that using $[Ge(Te^nBu)_4]$ leads to the deposition of thin stoichiometric and polycrystalline GeTe films by LPCVD at 723 K at 0.02 mmHg. Deposition conditions were varied to reduce the co-deposition of crystalline tellurium in these films. These films were characterised by XRD, Raman spectroscopy, SEM and EDX analysis.

The distorted octahedral coordination complexes $[SnCl_4\{^nBuS(CH_2)_3S^nBu\}]$ and $[SnCl_4(S^nBu_2)_2]$ are effective precursors for the deposition of $SnS_2$ at 559 and 645 K respectively, and 0.02 mm Hg whilst $SnSe_2$ can be deposited via LPCVD between 598 K and 743 K and 0.02 mm Hg using the selenoether analogue, $[SnCl_4(Se^nBu_2)_2]$. By optimising the conditions, it is also possible to produce polycrystalline SnS and SnSe thin films, as determined by XRD, Raman spectroscopy and EDX analysis, using the

dichalcogenoether precursors, $[SnCl_4\{^nBuS(CH_2)_3S^nBu\}]$ and $[SnCl_4\{^nBuSe(CH_2)_3Se^nBu\}]$ at higher temperature (831 K and 861 K, respectively). The electrical properties of these films were also measured by Hall and van de Pauw measurements.

$[SnCl_4\{^nBuSe(CH_2)_3Se^nBu\}]$ has also been used to grow $SnSe_2$ nanowires (~100 nm) using a liquid injection CVD and vapour liquid solid (VLS) method and a silicon substrate with Au nanoparticles or a 3 nm Au film. The density and morphology of the nanowires can be controlled by the carrier gas flow rate and concentration of precursor. The nanowires produced were stoichiometric by EDX. Preliminary experiments using this method have also produced $M_2Se_3$ (M = Bi, Sb) nanowires from $[BiCl_3(Se^nBu_2)_3]$ and $[SbCl_3(Se^nBu_2)_3]$, respectively, though further optimisation is required. Nanowires were also characterised by SEM, TEM, XRD and Raman spectroscopy.

Films of $TiSe_2$ can be deposited via LPCVD from $[TiCl_4\{^nBuSe(CH_2)_nSe^nBu\}]$ (n = 2, 3) between 723 and 873 K. XRD analysis of the films grown from ~ 5 mg of precursor showed a high degree of preferred orientation of the c axis perpendicular to the substrate. A series of hybrid amine-selenoether and telluroether ligands were prepared in an effort to tether the soft donor to the Ti(IV) ion more securely. However, this approach did not prove successful and was not pursued further.

# Table of Contents

## Chapter 6: Precursors for the Deposition of Titanium Chalcogenides 209

# List of Tables

# List of Schemes

# List of Equations

# List of Figures

# DECLARATION OF AUTHORSHIP

I, SAMANTHA LOUISE HAWKEN, declare that this thesis and the work presented in it are my own and has been generated by me as the result of my own original research.

Synthesis and Evaluation of Novel Single Source Precursors for the Chemical Vapour Deposition of Electronic Materials

I confirm that:

1. This work was done wholly or mainly while in candidature for a research degree at this University;
2. Where any part of this thesis has previously been submitted for a degree or any other qualification at this University or any other institution, this has been clearly stated;
3. Where I have consulted the published work of others, this is always clearly attributed;
4. Where I have quoted from the work of others, the source is always given. With the exception of such quotations, this thesis is entirely my own work;
5. I have acknowledged all main sources of help;
6. Where the thesis is based on work done by myself jointly with others, I have made clear exactly what was done by others and what I have contributed myself;
7. Parts of this work have been published as:

    - Tin(IV) chalcogenoether complexes as single source precursors for the chemical vapour deposition of $SnE_2$ and SnE (E = S, Se) thin films - Chitra Gurnani, Samantha L. Hawken, Andrew L. Hector, Ruomeng Huang, Marek Jura, William Levason, James Perkins, Gillian Reid and Gavin B. G. Stenning, *Dalton Transactions*, **2018**, 14, 2628 - 2637.
    - Tunable Ternary $Bi_2(Se_{1-x}Te_x)_3$ and $(Bi_{1-y}Sb_y)_2Te_3$ Thin Films via Low Pressure Chemical Vapor Deposition - Sophie L. Benjamin, C. H. (Kees) de Groot, Chitra Gurnani, Samantha L. Hawken, Andrew L. Hector, Ruomeng Huang, Marek Jura, William Levason, Eleanor Reid, Gillian Reid,

Stephen P. Richards, Gavin B. G. Stenning, *Submitted to Journal of Materials Chemistry C.*

Signed:………………………………………………………………………………………………

Date: …………………………………………………………………………………………………

# Acknowledgements

I would like to acknowledge Prof. Gill Reid, Prof Andrew Hector, Dr. Chitra Gurnani, and the research group for their support and advice throughout the duration of my PhD. I would like to thank Prof. William Levason for multinuclear NMR spectroscopy.

I would like to thank Dr. Ruomeng Huang from ECS at the University of Southampton for producing the PVD $SiO_2$ and patterned $SiO_2$/TiN substrates, Raman spectroscopy, electrical measurements and cross-sectional SEM.

I would also like to thank Dr. Marek Jura and Dr. Gavin Stenning as well as EPSRC and STFC for funding and for use of the materials characterisation laboratory.

I would like to acknowledge Ellie Reid and James Perkins, who contributed to preliminary work as undergraduate project students under my supervision. Ellie worked with $[BiCl_3(Se^nBu_2)]$ and $[SbCl_3(Se^nBu_2)_2]$ whilst James worked with $[SnCl_4\{^nBuE(CH_2)_3E^nBu\}]$ (E = S, Se).

I would finally like to acknowledge University College Cork for access to their facilities, Prof. Justin Holmes for accommodating me within his research group, Dr. Subhajit Biswas and Fionan Davitt for collaborative work on the nanowire systems. Whilst I synthesised the precursors and travelled to UCC to demonstrate the handling of the precursors and to carry out initial deposition experiments, Subhajit and Fionan carried out several later deposition experiments in my absence.

# Definitions and Abbreviations

AACVD – Aerosol Assisted Chemical Vapour Deposition

AFM – Atomic Force Microscopy

ALD – Atomic Layer Deposition

APCVD – Atmospheric Pressure Chemical Vapour Deposition

AuNP – Gold Nanoparticle

Bu – Butyl

CDW – Charge Density Wave

CVD – Chemical Vapour Deposition

DSP – Dual Source Precursor

EDX – Energy Dispersive X-Ray

Et – Ethyl

FID – Frequency Induction Decay

FT – Fourier Transform

GIXRD – Grazing Incidence X-Ray Diffraction

GST – Germanium Antimony Telluride

HOMO – Highest Occupied Molecular Orbital

IPXRD – In Plane X-Ray Diffraction

IR – Infra-Red

J – Coupling constant

LPCVD – Low Pressure Chemical Vapour Deposition

LUMO – Lowest Unoccupied Molecular Orbital

MBE – Molecular Beam Epitaxy

MDC – Metal Dichalcogenide

Chapter 1

Me – Methyl

NMR – Nuclear Magnetic Resonance

Ppm – Parts per million

PVD – Physical Vapour Deposition

PXRD – Powder X-Ray Diffraction

SCCM – Standard Cubic Centimetres per Minute

SEM – Scanning Electron Microscopy

SSP – Single Source Precursor

TEM – Transmission Electron Microscopy

TGA – Thermogravimetric Analysis

THF – Tetrahydrofuran

TM – Transition Metal

TMDC – Transition Metal Dichalcogenide

VLS – Vapour Liquid Solid

XRD – X-Ray Diffraction

1D – One Dimensional

2D – Two Dimensional

# Chapter 1: Introduction

The main scope of this work is to design and develop a range of single source precursors for the low pressure chemical vapour deposition of metal chalcogenide thin films and nanowires. The conditions for deposition will be optimised and the materials characterised by a range of techniques. The introduction that follows lays out the importance of metal chalcogenides with discussion surrounding their properties and applications, as well as the techniques used to deposit and characterise them.

## 1.1 2D Metal Chalcogenide Materials (ME, $ME_2$, $M_2E_3$) Why Study Metal Chalcogenides?

Metal chalcogenides are narrow band gap semiconductors. Semiconductors are of global importance and are found in a large number of everyday electronic applications from phones and computers to air conditioning units and ATMs.

Metal dichalcogenides (MDCs) and transition metal dichalcogenides (TMDCs), $ME_2$ (E= S, Se or Te), often form layered structures similar to $CdI_2$.[1] Many of these materials are becoming widely acknowledged as significant functional materials. Development of these materials and their properties is closely linked with investigations into the electronic properties of graphene. However, whilst functionalisation of graphene is required for chemical activity, metal dichalcogenides are often semiconductors with a wide range of chemistry available to them.[1,2] The size of the band gap is correlated to the number of layers in the material in a range of metal dichalcogenides.[3] Hence, tuning of the band gap via control of dimensionality is possible. Furthermore, superconductivity[4,5,6] and charge density waves[5,7,8] are exhibited by some TMDCs, such as $TiSe_2$[6,8] and $TaS_2$.[4] Group 14 dichalcogenides such as $SnSe_2$, often form similar structures to Group 4 dichalcogenides such as $TiSe_2$.[9]

The development of a practical methodology for the synthesis of continuous, high purity, ultra-thin (<20 nm thick) transition metal diselenide and ditelluride films would constitute a major advance in this field. A number of exfoliation techniques (liquid, intercalation assisted and mechanical) exist and have been successfully utilised in the synthesis of two dimensional TMDCs.[10] However, the films produced are on the micrometre scale, and large scale films are not accessible by these routes. The potential for an attractive alternative lies in chemical vapour deposition (CVD). This is a method which has been applied to graphene synthesis on a large scale[11] but the modification and application of this technique to the synthesis of MDCs, which pose greater chemical versatility, than graphene, due to their variable band gaps and magnetic properties, whilst challenging, would be a breakthrough. Although CVD has been frequently used for the deposition of MDCs, it has not been utilised for the deposition of few layer MDCs.

Due to their diverse range of properties, a wide range of applications are available to thin films of these materials. $WSe_2$ and $WTe_2$, for example, have been found to be strong candidates for potential use in spintronic applications, in which electron spin transport is exploited rather than electron transport in traditional electronics.[12] This is thought to suffer less electronic fluctuation and has a lower power consumption.[12] $MoS_2$ has been used as an electrocatalyst for hydrogen evolution[13] and in lithium ion battery electrodes.[14] A more in depth discussion on the properties and applications of these materials can be found in Sections 1.1.3 and 1.1.4.

### 1.1.1 Structure and Bonding

Typically, Group 4-7 TMDCs crystallise into layered structures similar to graphite. The layers are held together by weak van der Waals forces. The commonest three structural polytypes are 2H, 3R and 1T. 2H consists of metal atoms arranged hexagonally between two layers of chalcogen atoms which are bonded with trigonal prismatic coordination. There are two layers per repeat unit. 3R exhibits rhombohedral symmetry and three layers per repeat unit. Again, trigonal prismatic coordination between metal and chalcogen atoms is present. 1T consists of only one layer per repeat unit and tetragonal symmetry is displayed. There is octahedral coordination between metal and chalcogen atoms.[1,2] These structures are illustrated in Figure 1-1 below.

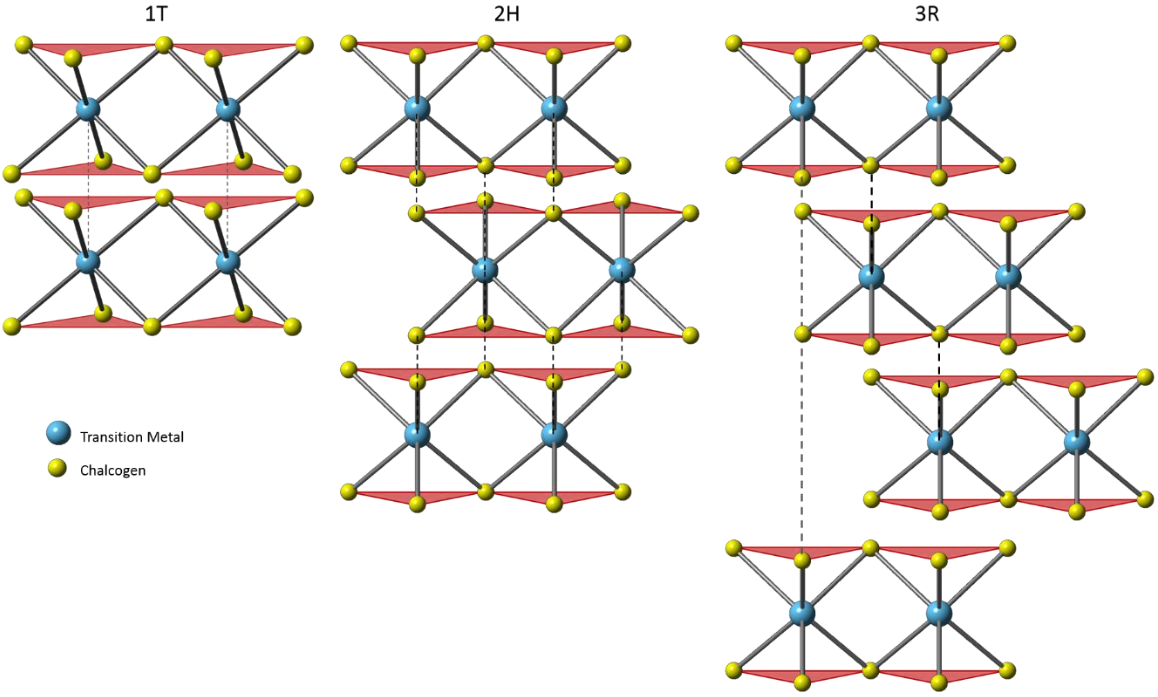

Figure 1-1: A diagram showing the structural polytypes of transition metal dichalcogenides.

For monolayer TMDCs, only two structural polytypes are possible: octahedral ($O_h$) coordination or trigonal prismatic ($D_{3h}$) coordination.[1,2]

For both trigonal prismatic and octahedral geometries, the d orbitals (non-bonding) are positioned between the bonding (σ) and antibonding (σ*) orbitals. The d orbitals of transition metals in octahedral coordination split into two groups: $d_{x^2-y^2}$ and $d_{z^2}$ ($e_g$), and $d_{xy}$,$d_{xz}$ and $d_{yz}$ ($t_{2g}$). Trigonal prismatic TMDCs, on the other hand, split into three groups: $d_{z^2}$ ($a^1$), $d_{xy}$ and $d_{x^2-y^2}$ (e), and $d_{xz}$ and $d_{yz}$ (e'). This is shown in Figure 1-2Figure 1-2: Electronic structure of TMDCs of both octahedral and trigonal prismatic geometries with two different electron counts. below. TMDCs involving Groups 4, 7 and 10 elements typically form octahedral structures, whereas those from groups 5 and 6 form trigonal prismatic structures.[1,2]

Group 14 metal dichalcogenides, such as $SnSe_2$[15] and $SnS_2$,[16] form similar structures to Group 4 TMDCs whilst SnS[17] and SnSe[18] crystallise in an orthorhombic crystal system.

Group 15 metal chalcogenides are typically found in the form $M_2E_3$. $Bi_2Se_3$, $Bi_2Te_3$ and $Sb_2Te_3$, and are part of the tetradymite ($Bi_2Te_2S$) group, as they have essentially the same crystal structure: trigonal, space group: R(-3)m.[19] $Sb_2Se_3$ on the other hand, exists in an orthorhombic phase.[20]

Electrons fill the d orbitals from the lowest energetic state. Group 5 TMDCs have one d electron and therefore the lowest band, above the $\sigma$ orbital, is half filled with the $d_{z^2}$ orbital containing one electron (Figure 1-2). Partially filled bands give rise to metallic character. Consequently, TMDCs based on Group 5 metals such as niobium or tantalum, are metallic. Group 6 TMDCs, on the other hand, have a fully occupied band as the $d_{z^2}$ orbital contains two electrons. Fully occupied orbitals give rise to semiconducting behaviour as in the case of molybdenum or tungsten diselenide. Empty d orbitals, in the case of Group 4 TMDCs (i.e. $TiSe_2$), also results in semiconducting behaviour.[1,2]

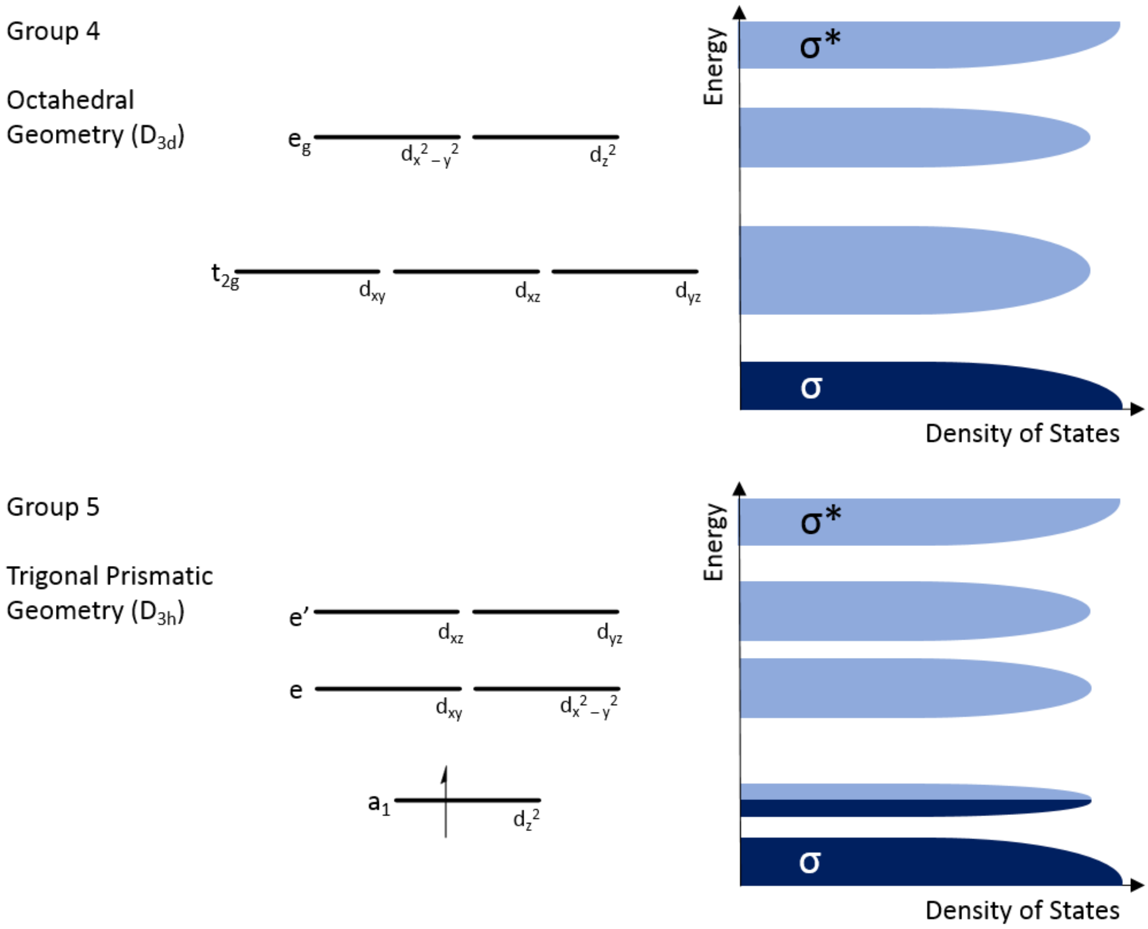

Figure 1-2: Electronic structure of TMDCs of both octahedral and trigonal prismatic geometries with two different electron counts.

Semiconductors contain a modest band gap: this is the minimum difference in energy between the valence band, the highest occupied molecular orbital (HOMO) and the conduction band, the lowest unoccupied molecular orbital (LUMO). Thus, the band gap of a Group 4 TMDC semiconductor is the energy difference between the σ orbital and the $t_{2g}$ band.

Materials exhibiting semiconducting behaviour have either a direct or an indirect band gap. The former is where the maximum energy of the valence band and the minimum energy of the conduction band occur at the same crystal orbital momentum (K-space). An indirect band gap is where the maximum energy of the valence band and the minimum energy of the conduction band occur at a different crystal orbital momentum. This is shown in Figure 1-3 below. The crystal orbital momentum is analogous to real momentum; however, it only takes value in the reciprocal lattice space (the Brillouin zone).

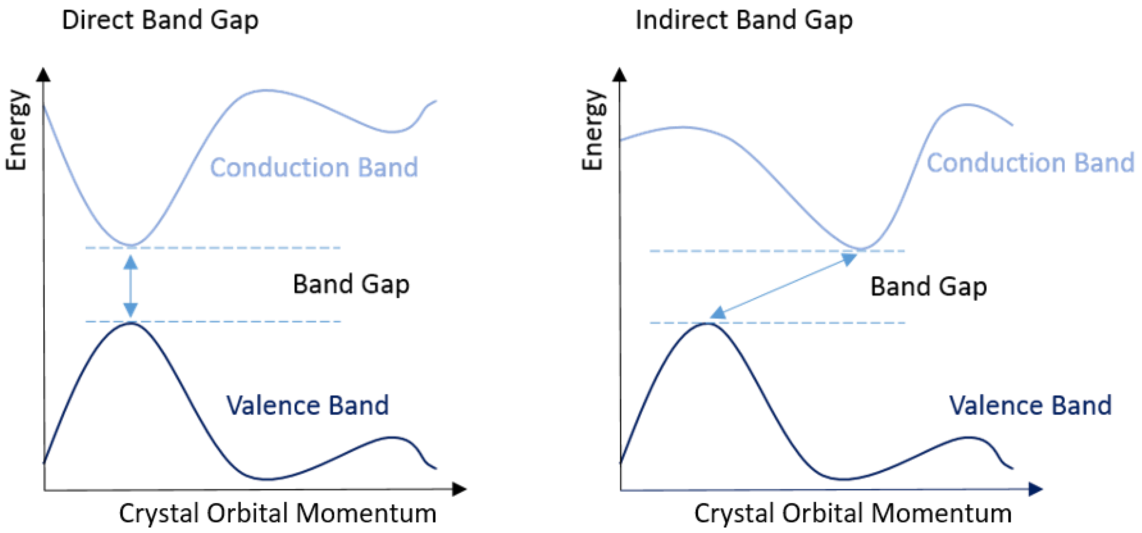

Figure 1-3: The differences between a direct (left) and an indirect band gap (right).

### 1.1.2 Properties

Some of the most important properties of MDCs and TMDCs are:

#### a) Mechanical Properties

Like graphene, 2D sheets of metal chalcogenides are exceptionally thin, strong (in the plane) and flexible. Materials such as $MoS_2$ and $WS_2$ have shown good elasticity properties. [21] These mechanical properties mean these materials will be durable and suitable for use in a range of applications such as field effect transistors (FETs) and as solid-state lubricants. [21]

### b) Tuneable Band Gap

Silicon, commonly used in the electronics industry,[22] has a band gap of 1.1 eV; a number comparable to that of many (transition) metal (di)chalcogenide films.[2] However, there are a number of factors affecting the electronic structure of a (transition) metal (di)chalcogenide. For example: despite the d electron count and the coordination of the transition metal being the major factors in the resulting electronic structure of (transition) metal (di)chalcogenides,[1] a small trend of reduction in band gap with increase in atomic number of chalcogen, due to the broadening of the d bands, is also observed.[1,23] For instance, this is seen in the case of 2H molybdenum dichalcogenides with the band gap decreasing from 1.3 eV in 2H-$MoS_2$ to 1.0 eV in 2H-$MoTe_2$.[23] Similarly, in the case of the Group 15 metal chalcogenides a decrease in band gap is seen for $Bi_2Te_3$ (0.16 eV)[19] compared to $Bi_2Se_3$ (0.24 eV)[24] and from $Sb_2Te_3$ (0.28 eV)[19] compared to $Sb_2Se_3$ (1.1 eV).[25] It can also be seen here that the band gap decreases down the group.

Furthermore, a trend is also seen between the number of layers in a metal chalcogenide structure and its band structure: as the number of layers in a material is reduced from bulk to monolayer, its band gap makes the transition from indirect in the bulk to direct in the monolayer.[1,2,5,10,26] A number of studies into the electronic structure of the molybdenum dichalcogenides have shown that this is accompanied by an increase in band gap energy, [27] and the appearance of strong photoluminescence.[26] These investigations put forward that this trend displayed is a result of quantum confinement. [10,26] Quantum confinement is a change in electronic and optical properties when then radius of the particle is smaller than that of the Bohr radius.

### c) Charge Density Wave

Due to 'intrinsic instabilities' of the electronic structure, the crystal lattices of some metal chalcogenides can undergo periodic distortions, otherwise known as charge density waves (CDWs).[5,7,8] These instabilities are typical of these layered dichalcogenide materials of low dimensions,[8] and the Jahn-Teller effect is believed to be the primary cause of this phenomenon.[5] Titanium diselenide was one of the first materials for which a CDW state was discovered. Now, however, there are many analogous layered $ME_2$ materials in which a CDW phase is known to exist.[8]

### d) Magnetism

An intrinsic property of all matter, diamagnetism can be described as the motion of electrons, orbiting atoms, changing as a result to being subjected to an external magnetic field creating an opposing field. A diamagnetic material's molar susceptibility is negative. It is also very small and consequently only detected in materials that do not display other types of magnetism. Paramagnetism arises due to orbital and/or spin angular momenta interactions between unpaired electrons and the applied external magnetic field. It is a phenomenon where a magnetic dipole aligns with the magnetic field; its molar susceptibility is positive.[28]

There are three types of magnetism in magnetically ordered solids: ferromagnetism, antiferromagnetism and ferrimagnetism. These are illustrated below in Figure 1-4. In ferromagnetic materials, the dipoles align parallel to one another to give a bulk magnetic moment. Antiferromagnetic materials, on the other hand, have an antiparallel arrangement of dipoles so the overall magnetization is zero. In ferrimagnetic materials, there is an antiferromagnetic arrangement of dipoles present but there is a bulk magnetic moment as the dipoles which are aligned in different directions are of different magnitudes. Ferromagnetic materials and antiferromagnetic materials become paramagnetic above the Curie and the Néel temperature respectively.[28]

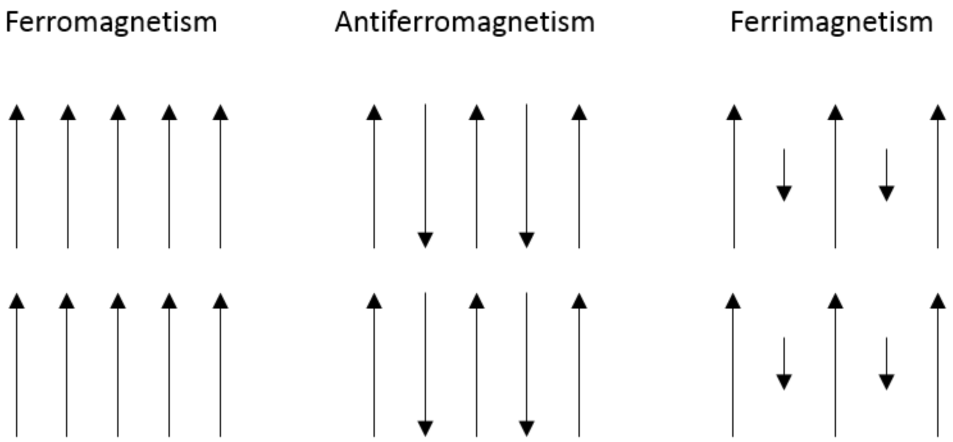

Figure 1-4: Diagram showing magnetic moments align in differenct types of magnetism.

Considering Figure 1-4, we can see that Group 5 TMDCs have one unpaired d electron per metal ion. This gives rise to magnetic properties in these materials ($VE_2$, $NbE_2$ and

$TaE_2$). Studies into tantalum dichalcogenides have shown that the magnetic properties of these materials arise principally as a result of the tantalum atom and the chalcogens contribute little to the overall magnetic moment.[29] Furthermore, they have shown that strain also affects the magnetic behaviour of a material with monolayers of $TaS_2$ and $TaSe_2$ being paramagnetic below 6% strain, but ferromagnetic at 6% strain and above.[29]

#### e) Superconductivity

Superconductivity is the absence of electronic resistance and was first discovered at temperatures near absolute zero.[30] Materials exhibiting CDWs can also be superconducting and at low temperatures, and they are thought to be competing electronic states. However, some investigations have shown evidence to support the theory that superconductivity and CDWs can coexist in Cu doped $TiSe_2$.[8] Unlike the CDW state, superconductivity is an effect resulting from the structure as a whole.[30] Interestingly, when an external magnetic field is applied, magnetism is not induced in a material in a superconducting state; all superconductors are perfect diamagnets.[28,30]

2D superconductors can have very different superconducting properties when compared with their bulk counterparts. Furthermore, there is the potential to induce superconductivity in an otherwise non-superconducting material. For instance, superconductivity can be induced in a neighbouring film by a superconducting film, the film will then exhibit the Meissner effect.[30]

#### f) Conductivity

High electrical conductivity is very important for a number of applications. These include thermoelectric devices where a high conductivity is needed for a current to flow and phase change materials where highly contrasting electrical (or optical) properties between crystalline and amorphous states are key.

### 1.1.3 Applications of (T)MDCs

$MoS_2$ is one of the most widely studied of the transition metal dichalcogenide materials, in terms of properties and potential applications. However, its similarity in structure and properties to other materials in the same class means these investigations also give an insight into future applications for many of these similar materials.[1,2,31]

Photoluminescence is exhibited by monolayer $MoS_2$. There is also the potential for valley polarization to be both generated and detected in these monolayers. These properties offer these materials as prospects for spintronic devices.[31] Investigations into spin-orbit splitting of some metal chalcogenides find that $WTe_2$ and $WSe_2$ offer large spin-orbit splitting of 500 meV and 428 meV respectively, meaning these materials have the potential to be applied to optoelectronic and spintronic devices.[12] Thin films of $MoS_2$ have also been used as an active co-catalyst in a photocatalysis system for the hydrogen evolution reaction. The activity of the monolayer of $MoS_2$ compared to its bulk counterpart is due to the increased number of edge sites. It has been determined that the sulfur atoms being under coordinated at the edge sites catalyses the process by facilitating water dissociation.[13,32,33]

Energy storage is another viable application for metal chalcogenides. A possible use for metal chalcogenides is for the creation of flexible solid-state supercapacitors. Tin diselenide, a Group 14 metal chalcogenide, has intriguing electronic properties and nanodisks have shown a high specific capacitance of 168 $Fg^{-1}$ and thus, this class of materials is an exciting prospect for these types of systems.[34] Another application of significant interest in the electronics industry is transistors; the large direct band gap of monolayers of metal chalcogenides is important for this application. Field-effect transistors fabricated from layered 2D structures have been reported by Roy *et al.* (2014).[35] These use sheets of graphene, h-BN, $MoS_2$, $SiO_2$ and Si and have been shown to have an electron mobility of $33cm^2/V.s$ and an ON/OFF current ratio of more than $10^6$.[35] This is an extremely active area of research and there are other examples in the literature describing the use of 2D $WSe_2$ and $MoS_2$, produced by exfoliation, for these types of application.[36–39] This gives hope for the use of other metal chalcogenides in this field.

Electrode materials are a vital part of lithium ion batteries in order to ensure a good performance. Graphite anodes are common, but the addition of 2D $MoS_2$, $WS_2$ or $SnS_2$ to form a composite material leads to enhanced performance mainly due to the capability to operate at a higher capacity.[40]

The high surface area to volume ratio of these 2D materials means that metal chalcogenide sheets should be highly sensitive to changes in the surrounding environment. Adsorption or intercalation of molecules or charge transfer with neighbouring molecules theoretically results in a change in the electronic properties of the materials. Measuring these electronic changes is the basis of sensors derived from TMDCs. It has been suggested that combined with a transistor, the current/voltage output could be used to do this.[21] Alternatively, photoluminescence or Raman techniques could be used to measure this change.[2] Monolayer $MoS_2$ has been combined within a transistor to create a sensor which detects humidity as water molecules adsorb to the surface and alter the electronic response of the system.[41] Furthermore, there have been studies into single layer $MoS_2$ for use as a hydrogen sensor and even more interestingly, for use in hydrogen storage. The adsorption of the $H_2$ causes a decrease in band gap which is easily measured. Additionally, due to the large energy barrier $H_2$ is unable to cross the $MoS_2$ barrier. However, the application of strain to the monolayer reduces this energy barrier resulting in the creation of a valve.[42]

## Thermoelectric Materials

Thermoelectric devices convert thermal energy (temperature gradient) into electrical energy, thus providing a sustainable energy source. This phenomenon, known as the Seebeck effect (or thermoelectric effect), was first discovered in 1821.[43,44] Charged species flow from hot to cold so by applying a temperature gradient and connecting alternate p and n type semiconductors in series a current can flow. This is shown in Figure 1-5.

The reverse, and equally important aspect of the thermoelectric effect is the Peltier effect. This is where a current flowing through a junction of two different materials will result in the absorption or radiation of heat depending on the direction of the current.[45] This is useful for applications requiring heating or cooling. For example, dehumidifiers may use the Peltier effect to remove water from the air by cooling.[46]

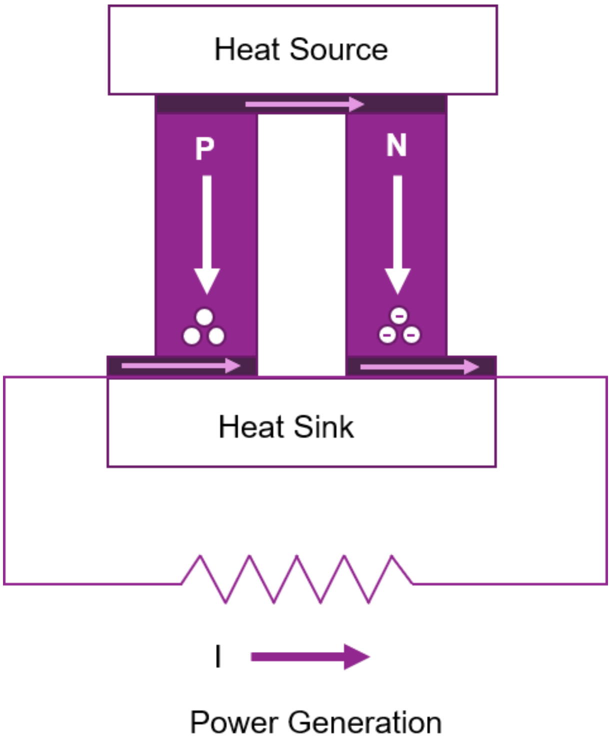

Figure 1-5: Power generation via the thermoelectric effect.

Good thermoelectric materials are required to have a high electrical conductivity and low thermal conductivity. This low thermal conductivity ensures that the temperature gradient is not compromised. The effectiveness of a thermoelectric material also depends on its Seebeck coefficient (thermopower). This is defined as 'the thermoelectric voltage generated per unit temperature difference'.[45]

The ubiquitous form of thermoelectric efficiency of a material is the dimensionless figure of merit, *ZT*. Z was developed by Altenkirch in 1911 as a way of measuring thermoelectric efficiency.[47] α is the Seebeck coefficient, σ is the electrical conductivity, T is the absolute temperature and K is the thermal conductivity.

$$ZT = \frac{\alpha^2 \sigma T}{K}$$

Equation 1-1: Dimensionless figure of merit, *ZT*

Thermoelectric devices have been used as an energy source in space, for example, to power the Mars rover. In this case, decaying Pu-238 was used as the heat source and PbTe and PbSnTe as the n and p semiconductors.[48] However, currently commercial use of thermoelectric devices is limited due to their low efficiencies.[45] Owing to the requirement for high electrical conductivity and low thermal conductivity, an intrinsic conflict is present due to the Wiedermann-Franz Law. Therefore, more research is required to improve the efficiency of this green energy resource.

Materials that have good thermoelectric properties, for near room temperature applications, include Group 15 chalcogenides such as $Sb_2Te_3$, $Bi_2Te_3$ and $Bi_2Se_3$ which have shown conductivities of around 1695,[49–52] 8620[49,53–56] and 549[57] $Scm^{-1}$ respectively. Whilst *ZT* values of 0.41[58] and 2.6[59] have been reported for Group 14 monochalcogenides, SnS and SnSe at 848 and 923 K respectively.

### Phase Change Materials

Phase change materials are interesting due to the stark difference in their optical or electrical properties between their crystalline and amorphous states, combined with extremely fast switching times.[60–62] Typically, the crystalline phase is highly reflective and conductive whilst the amorphous phase has low conductivity and poor reflectivity. The concept of utilising these properties for data storage can be traced back to S. R. Ovshinsky in the 1960's.[63]

The method by which information can be stored and erased in a phase change material is shown in Figure 1-6. A short high intensity laser pulse, applied locally to a crystalline phase change material will result in the melting of that region. Supercooling the liquid state quenches it, into an amorphous state. Due to the differences in optical/electrical properties between the crystalline and amorphous states, these amorphous regions are easily detectable by low intensity lasers and the information is stored.[60]

This information can be erased using an intermediate powered laser to melt the amorphous state to above the crystalline temperature. At this temperature atoms relax into the more energetically favourable ordered crystalline state.[60] Alternatively, the material can be switched between phases by application of a voltage,[64] making them suitable for electronic memory devices such as e readers.[65]

The most researched materials for phase change applications lie along the $Sb_2Te_3$-GeTe line, and the most common of these is $Ge_2Sb_2Te_5$ (GST-225). These materials typically have been shown to have switching times of 30-50 ns and a crystallisation temperature of ~150 °C.[66–68] The binary GeTe has also shown promise with switching times demonstrated to be as low as 1 ns[69] and a high crystallisation temperature of ~184 °C.[66,68]

However, more recently superlattices (alternating layers) of $Sb_2Te_3$ and GeTe have shown improved performance with switching times of 10 ns and write/erase lifetimes of $10^7$.[70,71] These superlattices have also shown reduced energy consumption.[71] These characteristic are key for commercial phase change material devices.

Another promising phase change memory material is $SnSe_2$ which has a switching time of just 20 ns and a high resistivity contrast of $10^5$.[72,73] This is comparable to the renowned GST-225.

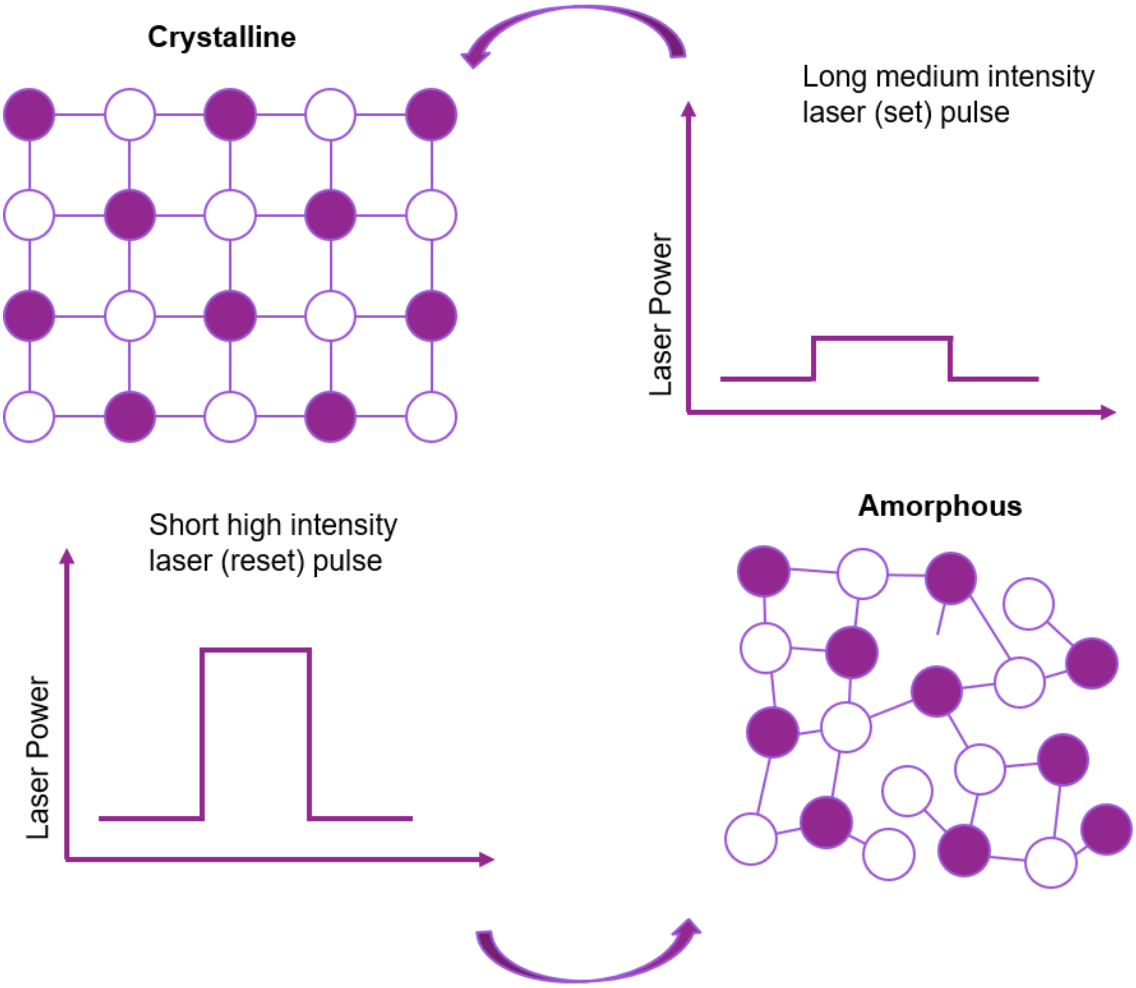

Figure 1-6: Mechanism of rewritable data storage using phase change materials.

## 1.2 Metal Chalcogenide Thin Film and Nanowire Growth Methods

Thin films have been prepared via exfoliation methods, however, these films are only produced on the micrometre scale.[10] This technique has most commonly been applied to metal disulfides. Thin film deposition techniques pose a number of advantages. For example, chemical vapour deposition (CVD), discussed in more detail below, can be applied to large surfaces and also for selenide and telluride materials[9,56,74,75] which are much less suited to exfoliation conditions than their sulfide analogues due to a lower stability in air. Other techniques such as electrodeposition,[76] spin coating,[77] molecular beam epitaxy (MBE), [78] atomic layer deposition (ALD)[79] and physical vapour deposition (PVD)[80] are also commonly used.

### 1.2.1 Molecular Beam Epitaxy

Molecular beam epitaxy (MBE) is a technique which involves mounting an extremely thin substrate wafer on a heated block. This substrate has been engineered to have an ‘atomically clean surface’. Source ovens are used to evaporate the atomic/ molecular precursors and a beam of this material is incident onto the substrate. The chamber in which it takes place is under an ultra-high vacuum to ensure that the film remains pure throughout its growth. The system also includes an electron gun which is used to produce a diffraction pattern in order to monitor the process. Although this method is useful as the composition of the film can be carefully controlled and altered to create boundaries, it is relatively slow compared to CVD, which is also more readily applied in cases of mass production and large area coverage.[81] For example, MBE has been used to deposit GeTe at 220-270 °C onto Si (111).[78]

### 1.2.2 Chemical Vapour Deposition

Chemical vapour deposition (CVD) involves the chemical reactions of precursor molecules to deposit a thin crystalline film upon a substrate. Initially, the precursor molecules, as a solid or oil, are heated to high temperature so that they evaporate. They then undergo mass transport to the reactor containing the substrate. (Here, gas phase molecules may react to create reactive intermediates (the ligand may dissociate from the metal in coordination compounds). The precursor then travels as a vapour to the surface of the substrate. The reactants are adsorbed onto the hot surface and undergo surface reactions. Diffusion across the substrate occurs, followed by nucleation and film growth. The leftover fragments desorb, and along with the other by products undergo mass transport away from the reaction zone.[82] This is illustrated in Figure 1-7 below.

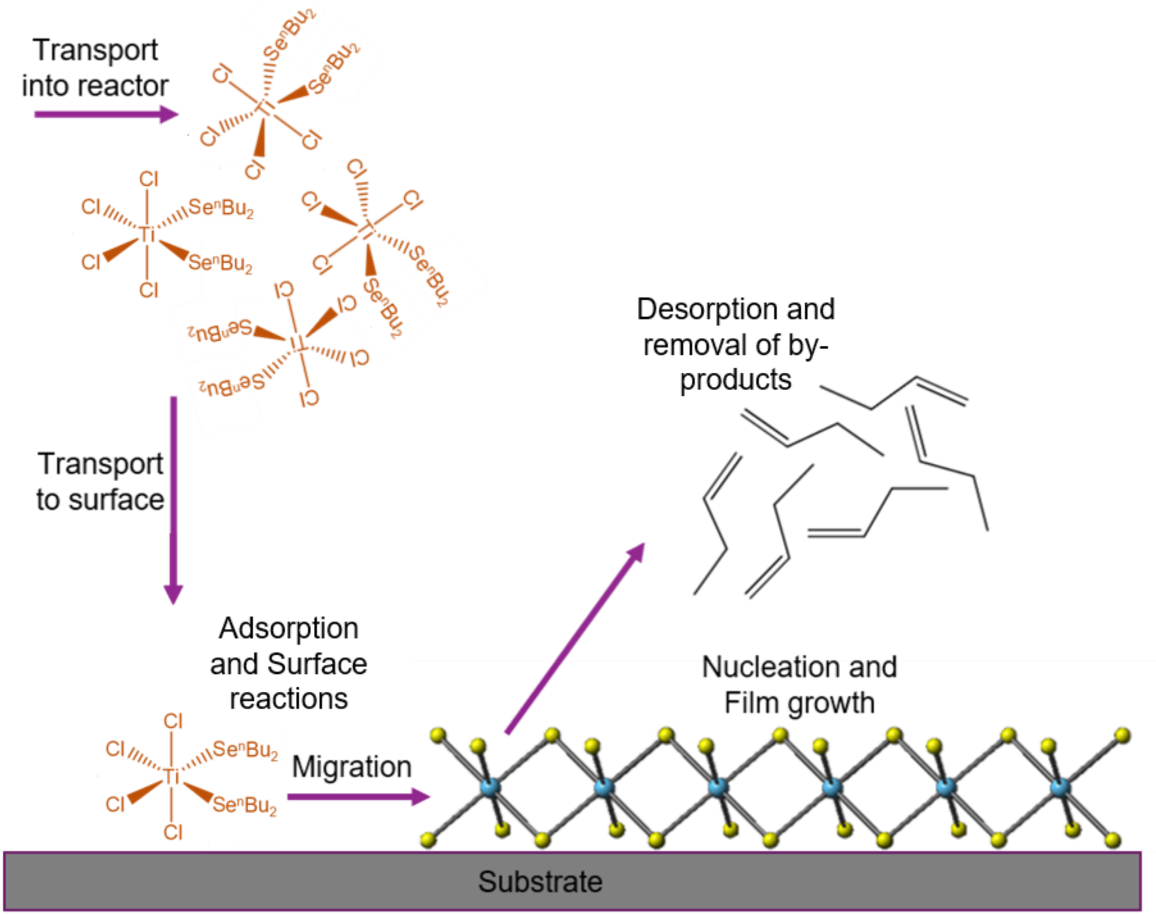

Figure 1-7: Illustration showing the process of chemical vapour deposition of [TiCl$_4$(Se$^n$Bu$_2$)$_2$][74] and possible by-products.

There needs to be careful thought in the design of precursor molecules. A single source or a dual source approach may be employed. A single source precursor (SSP) involves the use of one type of molecular compound, often an organometallic or coordination compound which contains at least one M-E bond and usually the correct ratio of metal and chalcogen. A dual source precursor (DSP) approach, on the other hand, involves the use of two distinct molecular species, one metal containing and one chalcogen containing in the case of (T)MDCs.

To achieve good deposition, precursors must be suitably volatile. This enables good growth rates to be achieved at modest temperatures.[82] Volatility is easily achievable for DSPs as they are often of low molecular weight. SSPs, however, have higher molecular weights and consequently volatility can be harder to achieve.

Precursors should also be stable enough so that they do not begin to pyrolyse during evaporation and the temperature range between evaporation and decomposition should be large enough to ensure that the precursor vapour is transported into the reaction zone, before decomposition, so that the film is deposited on the substrate.[83]

Precursors need to be of high purity and a clean low energy decomposition pathway is vital to ensure impurity free films. For SSPs, this means that the inclusion of methyl groups is usually a flawed design as it can lead to carbon contamination. For tellurium analogues, however, the use of methyl groups may be permissible due to the extremely weak Te-C bond. Butyl groups often have a β-hydride elimination pathway (as seen in Figure 1-8) available and hence are often incorporated into SSPs. However, a longer carbon chain length means added molecular weight and therefore lower volatility. Hence, there needs to be a trade-off.

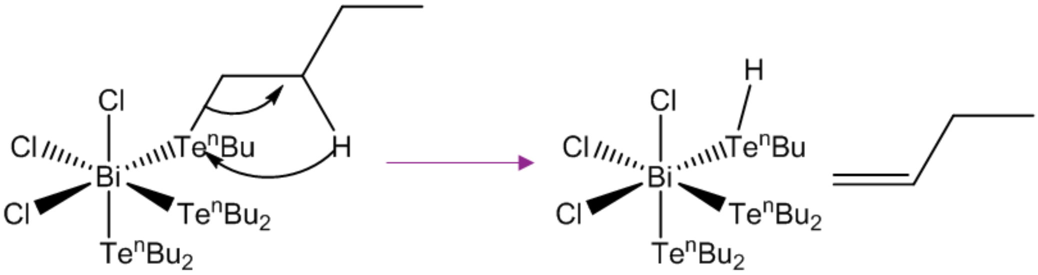

Figure 1-8: An illustration of a β-hydride elimination mechanism.

In an ideal world, these precursors would all be non-hazardous, stable in ambient conditions and manufactured at low cost to achieve high yield. DSPs habitually involve the use of metal chlorides, metal alkyls or metal amides, selenols, tellurols and thiols.[84] Metal alkyls are pyrophoric and challenging to handle whist the toxicity of selenols and tellurols is also an issue. Whilst SSPs are not typically pyrophoric, complexes containing selenium or tellurium are readily oxidised or hydrolysed in air and consequently need to be stored under inert conditions. Furthermore, in industry DSPs are typically used due to the lower cost and more facile synthesis. However, in some experiments a large excess of chalcogen source is required suggesting that single source approach may be more efficient. A discussion about CVD precursors can be found in Section 1.3.1.

There are a number of different variants of CVD including low pressure chemical vapour deposition (LPCVD), atmospheric pressure chemical vapour deposition (APCVD), aerosol assisted chemical vapour deposition (AACVD) and plasma enhanced chemical vapour deposition (PECVD). A typical set up for an LPCVD experiment as used in this work is depicted in Figure 1-9.

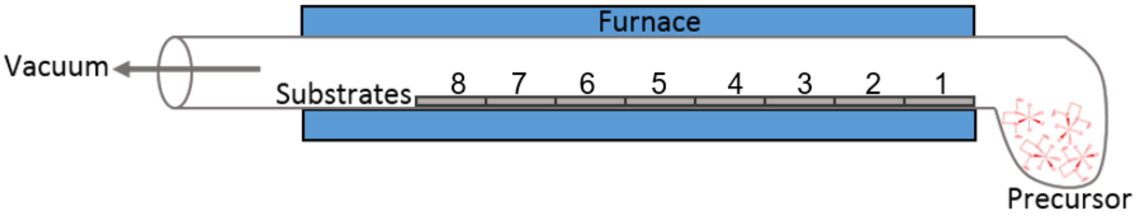

Figure 1-9: Diagram depicting set up for a typical hot wall LPCVD experiment used in this work.

LPCVD involves placing the reaction chamber under a vacuum. This means that once the precursor has evaporated it is easily pulled into the heated zone where it reacts at the hot substrate surface. Furthermore, eliminated volatile by-products are easily removed. APCVD on the other hand is executed at atmospheric pressure and requires more volatile reagents. AACVD is a technique that can be used if a precursor has limited volatility, however, it requires the precursor to be soluble in a suitable solvent such as hexane or toluene. Once dissolved in a suitable solvent, it is transported into the system as an aerosol. PECVD employs the use of electrical energy as in addition to thermal energy in a traditional CVD.

### 1.2.3 Vapour Liquid Solid Growth

This is one catalytic growth method to produce one dimensional materials via chemical vapour deposition. This was first described for the growth of Si nanowires by R. S. Wagner and W. C. Ellis in 1964.[85] The mechanism of vapour liquid solid (VLS) growth involves a ‘seed’ (typically gold) forming an alloy droplet in the liquid state. This needs to have a low freezing point. This droplet absorbs the material being deposited until saturation, at which point that material is precipitated, resulting in the growth of a nanowire. As only a very small proportion of the ‘seed’ (Au) is precipitated, the liquid droplet becomes detached from substrate and instead sits at the tip of the nanowire.[85] $Sb_2E_3$ (E = S, Se) nanowires have been grown via this techniques using $Sb(NMe_2)_3$ with $H_2S$ or $Et_2Se_2$ as the precursors and a deposition temperature of 623 K.[86] Ge nanowires have been deposited from $GeI_4$,[87] whilst $Sb_2Te_3$ and $GeTe/Sb_2Te_3$ have been deposited via VLS using GeTe, Te and Sb powders at 703 and 753 K. [88]

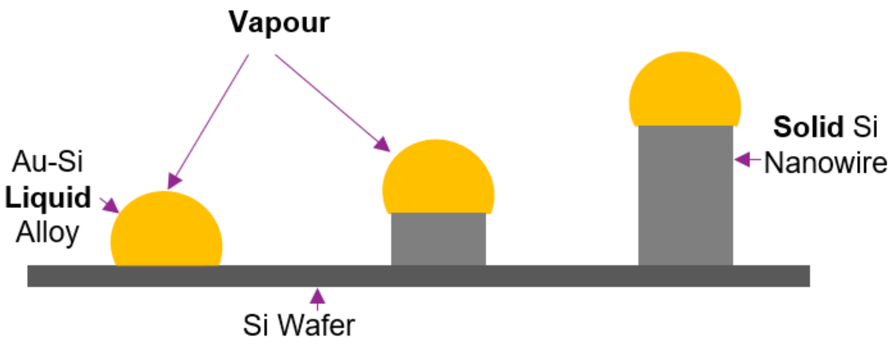

Figure 1-10: An illustration of the Vapour Liquid Solid growth method as described by Wagner et al (1964).[85]

The VLS mechanism directs growth in one direction. Speed of saturation of the liquid alloy depends on rate of precursor injection, temperature and pressure. It has also been shown that doping the gold nanoparticles with another metal such as silver changes the supersaturation equilibrium.[87]

### 1.2.4 Liquid Injection Chemical Vapour Deposition

This is a chemical vapour deposition method where the precursor is dissolved in a solvent and injected into the CVD rig. For this to be feasible, the precursor must be soluble in a suitable solvent, however, this means that volatility of the precursor is not an issue. An advantage of this method is that the rate of injection of the precursor can be easily controlled by use of a syringe pump. GeTe films have been deposited using this method, $[Ge(NMe_2)_4]$ in toluene as the metal source and $Te^iPr_3$ in toluene as the chalcogen source were injected into the reaction chamber set to 290-295 °C.[89]

### 1.2.5 Substrate Types

There are a number of different materials that can be used as a substrate for CVD growth of thin films. This includes, but is not limited to, fused (amorphous) $SiO_2$, PVD (crystalline) $SiO_2$, TiN, etched TiN, Si, mica and Au. Each substrate has its own advantages and disadvantages depending on application. Mica is cheap and available whereas Au and TiN are highly conducting. The use of Si is compatible with electronic devices. Substrates incorporating gold can be catalytic.

Although not common, under a narrow range or precursors and CVD conditions, it has been shown that some materials have an affinity for one substrate, TiN, over another, $SiO_2$ or etched TiN.[9,74] Recent work investigating this phenomenon has shown that TiN is more hydrophobic than $SiO_2$ and has a higher conductivity and it was suggested that these properties are key. Furthermore, the lower the resistivity of the material deposited the more likely the material can be deposited selectively onto one substrate over another.[90] This means that by using a patterned substrate, you can deposit material only where you want it, which would be useful for nanodevices for applications such as thermoelectric devices.

### 1.2.6 Physical Vapour Deposition

Physical vapour deposition (PVD) is similar to CVD but in this case, there are no chemical reactions that occur. A material is evaporated and transported to the surface of a substrate, where it is condensed and adsorbed onto the surface. Commonly, thermal evaporation or a sputtering technique is used. Sputtering uses physical rather than thermal vaporisation of the precursor.[91] Furthermore, it does require an ultra-high vacuum which is expensive. $Bi_2Se_3$ thin films have been grown by this method using a $Bi_2Se_3$ powder and depositing onto Au-mica or Au-Si substrates at 200-400 °C.[80]

### 1.2.7 Atomic Layer Deposition

Atomic layer deposition (ALD) is a specific variant of CVD. It involves two sets of precursors which are applied sequentially. Each precursor pulse must result in saturating surface reactions, this ensures that the growth of the film is self-limiting and results in easy control over the thickness of the film. The system is purged with an inert gas or evacuated in between precursor pulses. This is to avoid reactions occurring in the gas phase instead of at the surface of the substrate/film. ALD can be used to cover large surface areas with dense films with a high degree of control. However, the deposition rate is much slower than that of CVD and furthermore, there is a limited number of materials that this process can be applied to because there are a limited number of reactions that can be used to build up the film layer by layer.[92] For example, ALD has been used for the deposition of GeTe using the following reactions. $HGeCl_3$ can be cleaved into $GeCl_2$ and HCl. $GeCl_2$ reacts with $((CH_3)_3Si)_2Te$ to deposit GeTe and produce a removable by-product, $(CH_3)_3SiCl$.[93]

## 1.3 Precursors for Chemical Vapour Deposition

There is the potential to develop a diverse range of precursors for the metal (di)chalcogenides. The advantages and disadvantages of single source precursors and dual source precursors have been discussed previously.

### 1.3.1 Precursors for Metal Chalcogen Containing Thin Films

Previous dual source CVD based approaches to the deposition of transition metal dichalcogenides have typically included $MCl_x$ as the metal source and a thiol, thiolate or dialkyl diselenide as the chalcogen source. Adopting an AACVD approach, $M(NMe_2)_x$ with RSH or $^tBu_2Se$ have been used.[94–98] In the case of Group 15 metal chalcogenides, trialkyl stibines $SbR_3$, (R = Me, Et) have been used along with dialkyl chalcogenides, $TeR_2$ (R = Et, $^iPr$).[99–101] $Sb_2Te_3$ has also been deposited between 400 and 500 °C using $Sb^iPr_3$ and $Et_2Te_2$.[102] Amongst Group 14 chalcogenides, GeTe has been deposited from $Ge(NMe_2)_4$ and $Te(^iPr)_2$ using a LICVD method.[103] SnE and $SnE_2$ (E = S, Se) has been deposited from $SnCl_4$ with $H_2S$ or $Et_2Se$. [104–106]

A common single source approach for the deposition of metal sulfide films has been to use thiolates or thiocarbamates. The tin thiolate precursor, $[(PhS)_4Sn]$, has been used in AACVD to deposit $SnS_2$ and SnS with a 10 % $H_2S$ carrier gas at temperatures below and above 500 °C respectively.[107] A similar method has also been used for $[Sn(SCH_2CH_2S)]$.[108] The organotin dithiocarbamates, $[RSn\{S_2CN(Me)(^nBu)\}_3]$ ( R= Me, $^nBu$), have been used to deposit SnS at over 500 °C in the presence of 1 % $H_2S$ via APCVD.[109] However, the tin dithiocarbamate precursors, $[Sn(S_2CNRR^1)_2]$ (R = Et, $R^1$ = $^nBu$; R = Me, $R^1$ = $^nBu$; R = $R^1$ = Et) deposited SnS via AACVD with no additional sulfur source. There was minor contamination with $SnO_2$.[110]

For the deposition of $Sb_2Se_3$, thiolates, $[Sb(SR)_3]$ (R = $^tBu$, $CH_2CF_3$) at 300 and 450 °C under LPCVD conditions have been used,[111] and the dithiocarbamates, $[Sb(S_2CNMeR)_3]$ (R = $^nBu$, Hex, Bz) led to deposition at under 300 °C in AACVD.[112]

Other organometallic precursors for the CVD of metal chalcogenide thin films include precursors of the form $[RM(ER^1)_2]$ and $[R_2M(ER^1)]$. It has been demonstrated that $[Et_2BiTeEt]$ is a suitable single source precursor for the LPCVD of $Bi_2Te_3$ films at 230 °C.[113] Meanwhile $[MeSb(E^nBu)_2]$ (E = Se, Te) has been used to deposit $Sb_2Te_3$ and $Sb_2Se_3$ at 500 °C via LPCVD.[50] Interestingly, a different synthesis was used in each case, the first used a simple exchange reaction whereas the latter used a more challenging synthesis involving ${}^{n}$BuLi and ultra-low temperature. Both schemes are depicted in Figure 1-11.

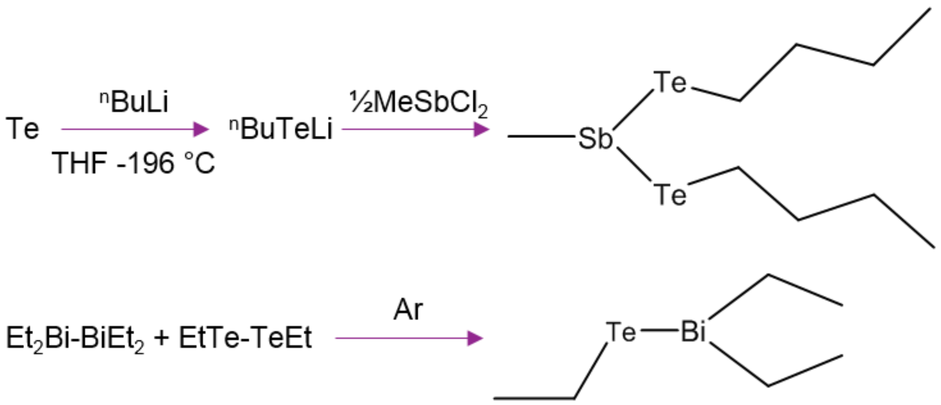

Figure 1-11: Schemes for synthesis of [$MeSb(Te^{n}Bu)_2$][50] (top) and [$Et_2BiTeEt$][113] (bottom).

The remit of this work focusses on coordination complexes. Previous approaches to single source precursors for the chemical vapour deposition of metal chalcogenide thin films involving neutral metal chloride chalcogenoether complexes have included compounds of the form: [$MCl_3(L)$], [$MCl_3(L)_3$], [$MCl_5(L)$], [$MCl_4(L)_2$] and [$MCl_4(L\text{-}L)$] as defined below.

$Ga_2E_3$ (E = Se, Te) has been deposited from [$GaCl_3(E^{n}Bu_2)$] via LPCVD[114] whilst [$NbCl_5(E^{n}Bu_2)$] has been used to deposit $NbE_2$ thin films.[115] Both Group 4 and 14 dichalcogenoether thin films have been deposited via [$MCl_4(L)_2$] and [$MCl_4(L\text{-}L)$] precursors including [$TiCl_4(ER_2)$] (E = Se R = Et, ${}^{n}$Bu; E = S, R = Me),[74,116,117] [$TiCl_4\{o\text{-}C_6H_4(CH_2EMe)_2\}$] (E = S, Se), [$SnCl_4(SeEt_2)$][118] and [$SnCl_4[{}^{n}BuSe(CH_2)_nSe^{n}Bu\}$] (n = 2,3).[9]

$Bi_2Te_3$ has been deposited from [$BiCl_3(Te^{n}Bu_2)_3$].[56] In the case of germanium chalcogenides, there are no examples of germanium chloride chalcogenoether complexes as single source precursors in the literature. This is due to the extremely weak Lewis acidity of the metal chloride resulting in little to no interaction between it and the chalcogenoether.[119,120] The types of precursor discussed here are discussed in more detail at the start of each chapter.

### 1.3.2 Metal Chalcogenoether Bonding

The majority of this work focusses on main group chloride chalcogenoether complexes. The main group elements often exhibit hypervalency. This is when the number of valence electrons exceeds the octet rule. A common model to explain the bonding in these hypervalent complexes is the 3 centre 4 electron bonding model. Take $[MCl_6]^{2-}$ for example. it can be thought of as three linear Cl-M-Cl units with the bonding model depicted below.[121]

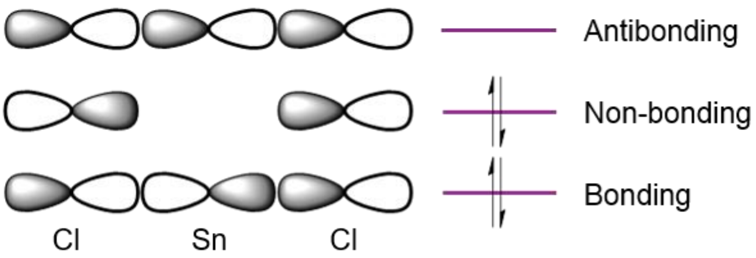

Figure 1-12: An illustration of the 3 centre 4 electron bonding model.

In terms of metal chloride chalcogenoether complexes such as $[MCl_4(ER_2)_2]$, this model can be adapted to include E-M-Cl asymmetric 3c-4e bonds. This is typically with a primary M-Cl bond and a secondary M-E bond.[121] In a number tin chloride with macrocyclic thioether ligands including $[(SnCl_4)_2([18]aneS_6)]$, Sn-S bond lengths have been demonstrated to be 0.2 - 0.3 Å longer than Sn-Cl bonds via X-ray crystallography.[122] Furthermore, in solution metal chloride chalcogenoether complexes are broadly dissociated in solution.[121]

For $[MCl_3(ER_2)_3]$ (M = Bi, Sb) species however, the Bi and Sb have a lone pair and in the case of Sb, it can be stereochemically active (normally deemed to be $ns^2$). This makes the 3c-4e model more difficult to apply. Here the donor acceptor bonding model can be used to rationalise the bonding through considering the Lewis acidity of the metal chloride and Lewis basicity of the chalcogenoether. Typically both the Lewis acidity of the Group 15 chlorides and the Lewis basicity of the chalcogenoethers decreases down the Group.[121] The heavier the chalcogen, the weaker the bond to the main group metal. In contrast to this, there is increased sigma donation down Group 16 chalcogenoethers towards low valent transition metal centres.[121]

In the donor acceptor model, the M-Cl bonding orbital is polarized towards the highly electronegative halide and the antibonding orbital polarised towards the metal. The chalcogenoether donor forms a bond via sigma donation from one of its lone pairs into this antibonding orbital.

There is the opportunity for the chalcogenoether to act as a π acceptor due to the empty E-C antibonding orbital. Furthermore, due to its lone pair, polymeric complexes could be formed.[121]

Descending Group 16, the chalcogenoethers become more reactive with a larger tendency to decompose. This is due to the weak Te-C bond which means that the ligands undergo easy dealkylation and are also thermally and photolytically sensitive, as well as readily oxidising in air. [123,124]

| Chalcogen | S | Se | Te |
|---|---|---|---|
| Pauling Electronegativity | 2.6 | 2.6 | 2.1 |
| E-H Bond Energy/ kJmol$^{-1}$ | 366 | 276 | 238 |
| E-C Bond Energy/ kJmol$^{-1}$ | 272 | 234 | 200 |
| E-E Bond Energy/ kJmol$^{-1}$ | 266 | 192 | 149 |

Table 1-1: Showing electronegativities and bond energies for the chalcogens.[125]

### 1.3.3 Chalcogenoether Ligand Synthesis

Thioethers can be synthesised by the reaction of an alkyl halide with aqueous sodium sulfide.[126] The bidentate thioether, $^nBuS(CH_2)_3S^nBu$ has a more complex synthesis. It can be synthesised by dissolving the thiol, $HS(CH_2)_3SH$ in ethanol and dissolving elemental sodium and refluxing. Next, $^nBuBr$ is added and the solution refluxed again to form a white solid. Saturated NaCl and $NaHCO_3$ solutions are added and the solution filtered. The product can then be extracted from the filtrate using diethyl ether and dried *en* vacuo.[127]

Monodentate selenoethers and telluroethers can be synthesised by reaction of the elemental chalcogen with RLi in THF at -196 ° followed by the addition of RCl at room temperature. It is extracted with a suitable solvent and dried *en* vacuo. Bidentate ligands,

$RE(CH_2)_nER$ can be produced in a similar way but the ratio is modified and 1,3 dichloropropane or 1,2-dichloro ethane is added rather than RCl.[128,129]

In the case of RTeLi and 1,2-dichloroethane, the bidentate chalcogenoether is not formed. Due to the weak Te-C bond, ethene is eliminated and instead you have an easy route to $R_2Te_2$ via the clean decomposition of $RTe(CH_2)_2TeR$.[129]

## 1.4 Characterisation Techniques

### 1.4.1 Precursor Characterisation Techniques

Below are listed some of the main characterisation techniques used in this work to identify the coordination complexes and ligands synthesised.

**Infra-Red Spectroscopy (IR)**

Infra-Red spectroscopy falls under the category of vibrational spectroscopy. It is a relatively readily accessible technique which can be used in the study of gas, liquid and solid samples. Liquids can be run as neat thin films between CsI plates, whereas solids can be run as Nujol mulls between the plates or as powders in ATR mode for air stable materials. The choice of sampling method is dependent on the sensitivity of the material being studied. IR spectroscopy divulges information about the types of bond present in a molecule.

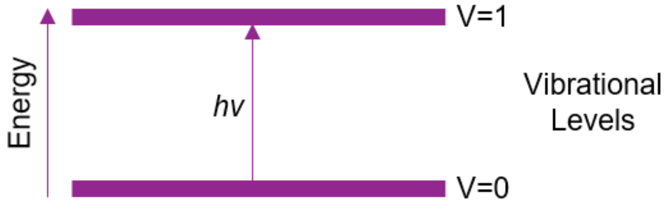

Figure 1-13: Showing energy levels involved in IR spectroscopy.

When electromagnetic radiation of equivalent frequency to an oscillating molecular dipole interacts with that dipole, the radiation is absorbed and the dipole is raised in energy to the next vibrational level.[130] This is shown in Figure 1-13 above. The frequency at which a vibration occurs is normally reported in terms of wavenumber ($cm^{-1}$). A typical range for techniques using CsI plates is from 200-4000 $cm^{-1}$.

Different types of vibrational mode for a simple triatom are shown in Figure 1-14 overleaf.

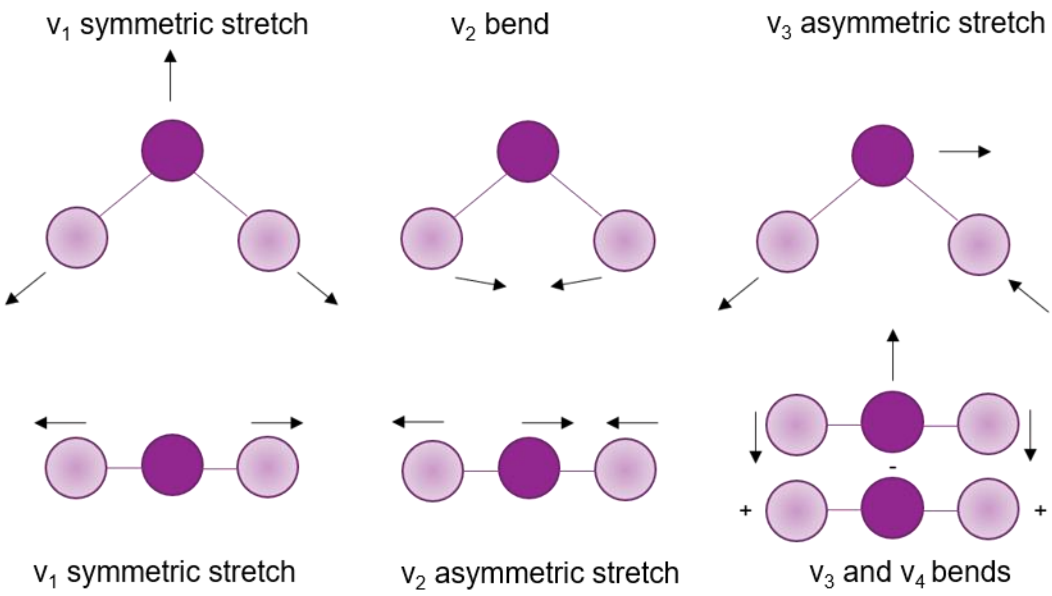

Figure 1-14: Vibrational modes of a bent triatomic and linear triatomic.

The frequency is proportional to the reduced mass $\mu = (M_1 + M_2)/(M_1 \times M_2)$ and consequently atoms bonded to hydrogen atoms have a reduced mass of approximately one whereas heavier elements would have a much smaller reduced mass. Consequently, whilst O-H and C-H feature at 3600 $cm^{-1}$ and 3000 $cm^{-1}$ respectively, M-Cl stretches feature at a much lower wavenumber, in the fingerprint region (1500 – 500 $cm^{-1}$). Ti-Cl stretches in $[TiCl_4(Se^nBu_2)_2]$ feature at ~ 395 $cm^{-1}$,[74] Sn-Cl stretches at 311 $cm^{-1}$ in $[SnCl_4\{^nBuSe(CH_2)_3Se^nBu\}]$,[9] A Bi-Cl stretch at 248 $cm^{-1}$ in $[BiCl_3(Te^nBu_2)_3]$[56] and Sb-Cl stretches at 254 $cm^{-1}$ and 235 $cm^{-1}$ in $[SbCl_3\{MeS(CH_2)_3SMe\}]$.[131]

It is a requirement that there is a change in dipole in order to probe a molecule by IR spectroscopy.[130] Group theory can be used to determine the number of expected M-Cl IR bands in a spectrum if the correct symmetry of the molecule is known.

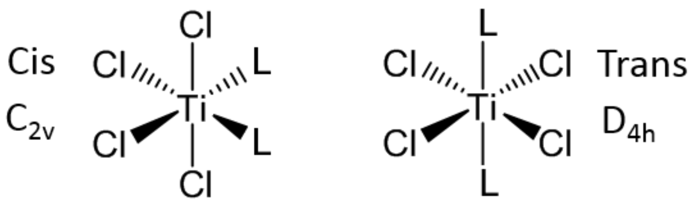

Figure 1-15: Showing the cis and trans structures of octahedral titanium (IV) complexes.

[$TiCl_4L_2$] complexes can exist as either *cis* or *trans* isomers as illustrated above (Figure 1-15). *Cis* isomers exhibit $C_{2v}$ symmetry whereas *trans* isomers exhibit $D_{4h}$ symmetry. Character tables, unique for each point group, can then be used to predict the number of IR or Raman stretches that would be present in a spectrum. For each symmetry operation, the number of bonds unchanged is multiplied by the number prefixing each symmetry operation. This is applied to each number in the character table to produce a product table (Table 1-2).

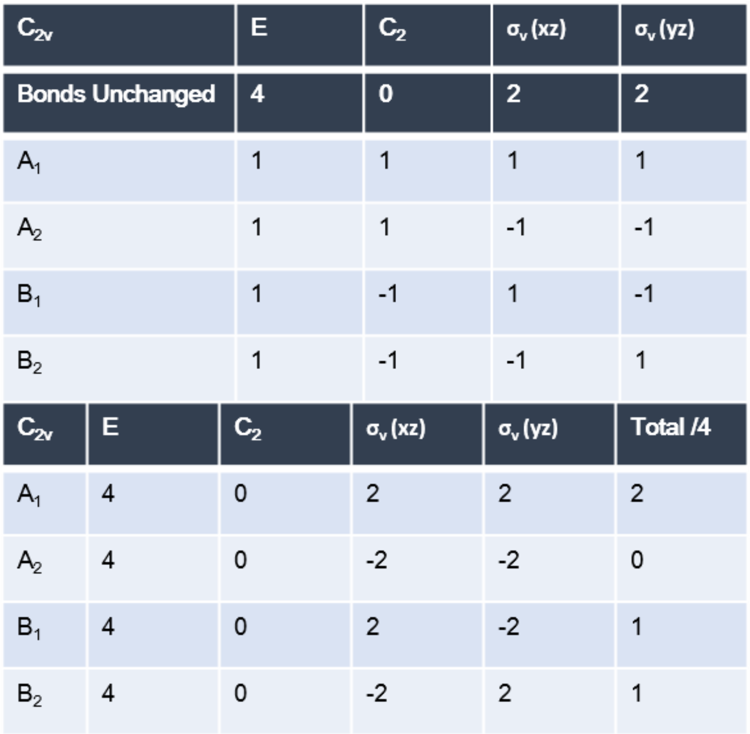

| $C_{2v}$ | E | $C_2$ | $\sigma_v$ (xz) | $\sigma_v$ (yz) |
|---|---|---|---|---|
| **Bonds Unchanged** | **4** | **0** | **2** | **2** |
| $A_1$ | 1 | 1 | 1 | 1 |
| $A_2$ | 1 | 1 | -1 | -1 |
| $B_1$ | 1 | -1 | 1 | -1 |
| $B_2$ | 1 | -1 | -1 | 1 |

| $C_{2v}$ | E | $C_2$ | $\sigma_v$ (xz) | $\sigma_v$ (yz) | Total /4 |
|---|---|---|---|---|---|
| $A_1$ | 4 | 0 | 2 | 2 | 2 |
| $A_2$ | 4 | 0 | -2 | -2 | 0 |
| $B_1$ | 4 | 0 | 2 | -2 | 1 |
| $B_2$ | 4 | 0 | -2 | 2 | 1 |

Table 1-2: Character table for $C_{2v}$ symmetry and table of irreducible representations for Ti-Cl stretches of *cis* isomer.

For the *cis* isomer, this leads to $2A_1 + B_1 + B_2$. These are all IR active stretches and consequently group theory predicts four Ti-Cl stretches in the IR spectrum.

The *trans* isomer, on the other hand, (character and irreducible representations illustrated in Table 1-3) results in $A_{1g} + B_{1g} + E_u$ stretches. However, only the $E_u$ stretch is IR active and hence group theory predicts one Ti-Cl stretch in the IR spectrum for this isomer.

| $D_{4h}$ | E | $2C_4$ | $C_2$ | $2C'_2$ | $2C''_2$ | i | $2S_4$ | $\sigma_h$ | $2\sigma_v$ | $2\sigma_d$ |
|---|---|---|---|---|---|---|---|---|---|---|
| **Bonds Unchanged** | **4** | **0** | **0** | **2** | **0** | **0** | **0** | **4** | **2** | **0** |
| $A_{1g}$ | 1 | 1 | 1 | 1 | 1 | 1 | 1 | 1 | 1 | 1 |
| $A_{2g}$ | 1 | 1 | 1 | -1 | -1 | 1 | 1 | 1 | -1 | -1 |
| $B_{1g}$ | 1 | -1 | 1 | 1 | -1 | 1 | -1 | 1 | 1 | -1 |
| $B_{2g}$ | 1 | -1 | 1 | -1 | 1 | 1 | -1 | 1 | -1 | 1 |
| $E_g$ | 2 | 0 | -2 | 0 | 0 | 2 | 0 | -2 | 0 | 0 |
| $A_{1u}$ | 1 | 1 | 1 | 1 | 1 | -1 | -1 | -1 | -1 | -1 |
| $A_{2u}$ | 1 | 1 | 1 | -1 | -1 | -1 | -1 | -1 | 1 | 1 |
| $B_{1u}$ | 1 | -1 | 1 | 1 | -1 | -1 | 1 | -1 | -1 | 1 |
| $B_{2u}$ | 1 | -1 | 1 | -1 | 1 | -1 | 1 | -1 | 1 | -1 |
| $E_u$ | 2 | 0 | -2 | 0 | 0 | -2 | 0 | 2 | 0 | 0 |

| $D_{4h}$ | E | $2C_4$ | $C_2$ | $2C'_2$ | $2C''_2$ | i | $2S_4$ | $\Sigma_h$ | $2\sigma_v$ | $2\sigma_d$ | Total /16 |
|---|---|---|---|---|---|---|---|---|---|---|---|
| $A_{1g}$ | 4 | 0 | 0 | 4 | 0 | 0 | 0 | 4 | 4 | 0 | 1 |
| $A_{2g}$ | 4 | 0 | 0 | -4 | 0 | 0 | 0 | 4 | -4 | 0 | 0 |
| $B_{1g}$ | 4 | 0 | 0 | 4 | 0 | 0 | 0 | 4 | 4 | 0 | 1 |
| $B_{2g}$ | 4 | 0 | 0 | -4 | 0 | 0 | 0 | 4 | -4 | 0 | 0 |
| $E_g$ | 8 | 0 | 0 | 0 | 0 | 0 | 0 | -8 | 0 | 0 | 0 |
| $A_{1u}$ | 4 | 0 | 0 | 4 | 0 | 0 | 0 | -4 | -4 | 0 | 0 |
| $A_{2u}$ | 4 | 0 | 0 | -4 | 0 | 0 | 0 | -4 | 4 | 0 | 0 |
| $B_{1u}$ | 4 | 0 | 0 | 4 | 0 | 0 | 0 | -4 | -4 | 0 | 0 |
| $B_{2u}$ | 4 | 0 | 0 | -4 | 0 | 0 | 0 | -4 | 4 | 0 | 0 |
| $E_u$ | 8 | 0 | 0 | 0 | 0 | 0 | 0 | 8 | 0 | 0 | 1 |

Table 1-3: Character table for $D_{4h}$ symmetry and table of irreducible representations for Ti-Cl stretches of *trans* isomer.

### Nuclear Magnetic Resonance (NMR) Spectroscopy

Nuclear magnetic resonance (NMR) spectroscopy is a useful and widely applicable technique for characterising molecules. It often allows determination of a molecule's constitution and structure. However, typically it is required that the molecule is soluble. If a molecule is not soluble, solid state NMR spectroscopy techniques can be used. NMR spectroscopy is dependent on an intrinsic property of the nucleus, its spin. For a molecule to be studied by NMR, it must contain an element that has a naturally occurring isotope with a nucleus of spin quantum number (*I*) of n/2 where n is an odd integer. The properties of relative nuclei are summarised in Table 1-5 below.

| Isotope | Spin | Natural Abundance (%) | Magnetogyric ratio ($10^7$ rad$T^{-1}s^{-1}$) | NMR Frequency (MHz) | Relative Receptivity |
|---|---|---|---|---|---|
| $^1H$ | ½ | 99.98 | 26.7510 | 100.00 | 1.00 |
| $^{13}C$ | ½ | 1.11 | 6.7263 | 25.14 | $1.76 \times 10^{-4}$ |
| $^{77}Se$ | ½ | 7.60 | 5.1008 | 19.07 | $5.26 \times 10^{-4}$ |
| $^{119}Sn$ | ½ | 8.60 | -9.9707 | 32.27 | $4.44 \times 10^{-3}$ |
| $^{125}Te$ | ½ | 7.00 | -8.4525 | 31.60 | $2.21 \times 10^{-3}$ |

Table 1-4: Magnetic properties of specific nuclei for NMR spectroscopy[132] relevant to this work.

If an isotope has a high natural abundance, its relative receptivity will also be high and an NMR signal easier to obtain. The magnetogyric ratio also has an effect on receptivity. The magnetogyric ratio is a constant and a property of each nuclei, large values represent those with large separation between energy levels and hence sensitivity for detection is higher.[130] It is the proportionality constant between the magnetic moment **μ** and the spin angular momentum ***I***.[133]

$$\mu = \gamma I$$

Equation 1-2: Equation showing proportionality between the magnetic moment and spin angular momentum.

The quadrupole moment is a non-symmetric (elipsoidal) charge distribution of the nucleus and results in extensive shortening of the $T_2$ relaxation time (relaxation of spin states back to the normal distribution in the magnetic field). This causes broadening of the lines in an NMR spectrum and makes it difficult to decipher or not observable at all.[130]

In this work precursors for Ti, Sb, Bi and Ge chalcogenides will be synthesised. However, despite all these elements having nuclei of non-zero nuclear spins, they all have moderate quadrupolar moments. This means that in low symmetry environments, the relaxation times will be extremely short. With a very short relaxation time, the actual time spent in the excited state is very small and due to the Heisenberg principle, the line widths will extremely broad due to the uncertainty of the chemical shift, rendering them unsuitable for characterisation. Table 1-5 tabulates the magnetic properties of relevant nuclei very rarely used as a characterisation tool.

| Isotope | Spin | Natural Abundance (%) | Magnetogyric ratio ($10^7$ radT$^{-1}$s$^{-1}$) | NMR Frequency (MHz) | Quadrupole Moment ($10^{-28}$ m$^2$) |
|---|---|---|---|---|---|
| $^{33}$S | 3/2 | 0.76 | 2.0517 | 7.67 | $-6.4 \times 10^{-2}$ |
| $^{47}$Ti* | 5/2 | 7.28 | 1.5079 | 5.64 | -0.30 |
| $^{73}$Ge | 9/2 | 7.80 | 0.9332 | 3.49 | -0.2 |
| $^{121}$Sb* | 5/2 | 57.21 | 6.4435 | 23.93 | -0.36 |
| $^{209}$Bi | 7/2 | 100.00 | 4.3750 | 16.07 | -0.52 |

Table 1-5: Magnetic properties of specific nuclei for NMR spectroscopy.[132,134] * there are other stable quadrupolar isotopes.

In an NMR experiment, the molecule, in deuterated solvent, is subjected to a pulse of radiofrequency radiation. This excites the nuclei and causes them to precess in phase, each at unique frequencies. This precession decays over time, this is known as the free induction decay (FID). The FID or each nuclei is detected and measured in the time domain and a Fourier transform (FT) is used to convert it into the frequency domain to produce the signals typically seen in an NMR spectrum.[133,135]

The NMR frequency of a nucleus depends on its magnetogyric ratio **γ**, the strength of the magnetic field **B** and its local environment. Consequently, protons resonate at roughly 400 MHz if a 9.4 T field is used.[133] However, protons do not all resonate at the same frequency because of the electronic effect of each nucleus. For example, proximity to a highly electronegative atom, will de-shield the nucleus causing an increase in chemical shift.

$$\nu = \frac{\gamma B}{2\pi}$$

Equation 1-3: Equation to determine the frequency of a nucleus.

### CHN Microanalysis

This is a technique where the compound is combusted entirely in an oxidising atmosphere. Combustion products (e.g. $CO_2$, $H_2O$, $N_2$) are separated on a gas chromatography (GC) column providing quantification on the C, H and N present. Each is detected and each signal is proportional in intensity to the quantity of each constituent atom.[136] This allows determination of the composition of a compound which gives an insight into whether assignments in other characterisation techniques are correct. Typically, only a couple of mg is required and due to this small sample size, there may be a small degree of error (~+/- 0.5 %). This characterisation was outsourced to MEDAC Ltd.

### Single Crystal X-Ray Diffraction

A useful technique in determining a complex's structure is single crystal X-ray diffraction. However, in this work, due to the incorporation of $^{n}$Bu groups to improve the stability of the precursors and to incorporate a β-elimination pathway, the precursors tend to be oils or liquids and do not crystallise. One challenge, in this technique, when the sample is solid, is the requirement that a single crystal (at least several tens of µm in size) of the molecule be grown, and this can be very difficult in some circumstances and often careful recrystallisation is required.

A single crystal is an array of highly ordered molecules. In this technique, monochromatic X-rays are directed towards a sample and undergo Thomson scattering to produce a diffraction pattern. Thomson scattering involves the oscillation of electrons in the field and the re radiation of X-rays at the incident frequency.[137] The heavier the atom the larger the diffraction of the X-ray. Due to the highly ordered system there is a high degree of symmetry. The diffraction pattern can be converted into an electron density map which can be used to confirm a proposed structure. Typically, the data needs to go through a number of refinement cycles before a clear picture is obtained of which elements constitute the structure.[138] When the data is recorded, the detector only records the amplitude of the electromagnetic wave, the vital phase data is lost which means a complex method, such as the Patterson method, is required to retrieve this information.

Single crystal X-ray diffraction gives an insight into the coordination of the ligands, the geometry of the molecule, the atom types and positions, as well as bond lengths and angles. This allows determination of how strong or weak an interaction is between a ligand and metal centre.

### 1.4.2 Thin Film and Nanowire Characterisation

Below are listed some of the main characterisation techniques used in this work to identify the thin films and nanowires synthesised.

#### X-Ray Diffraction

This is a non-destructive technique, used to probe the structure of thin films of material. The X-rays are directed onto the sample's surface where they are scattered by crystallites to create a diffraction pattern. As with the single crystal X-ray diffraction, the mass of the atom and its position in the unit cell affect the diffraction of the X-ray. An X-ray detector is used to measure the position of the diffracted X-rays. The diffraction pattern constitutes a number of reflections (diffraction maxima), each at an angle (2ϴ) corresponding to different spacing of parallel atomic planes (d).[136] The angle where constructive interference arises between waves of wavelength λ can be calculated from the Bragg equation (Equation 1-4) and the phase of the crystallites determined- each reflection plane corresponding to an angle (2ϴ) in the diffraction pattern. In order for constructive interference to occur (Figure 1-16) the distance ab + bc must be equal to an integer value of the wavelength (nλ). As ab = bc = dSinϴ, ab + bc = nλ = 2dSinϴ.

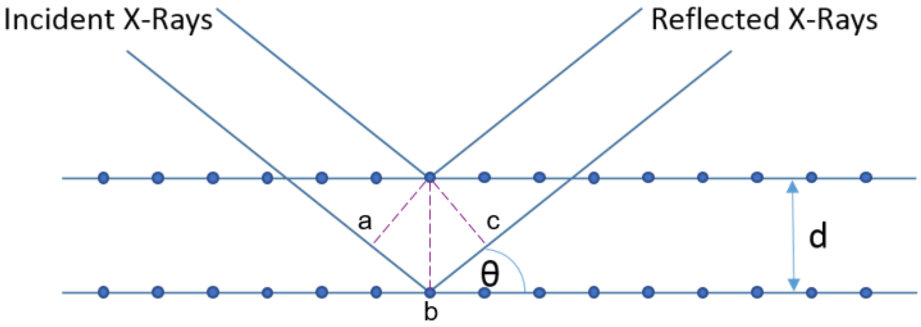

Figure 1-16: An illustration of the reflection of an X-ray satisfying Bragg's Law. ϴ = angle of reflection and d = spacing between atomic planes.

$$n\lambda = 2d_{hkl}sin\theta$$

Equation 1-4: The Bragg Equation where λ is the wavelength of the incident X-ray, d is the spacing between atomic planes, ϴ is the angle of reflection and n is an integer.

Each solid has a unique diffraction pattern and consequently, once a diffraction pattern is collected it can be matched to a database,[139] which allows determination of the crystal structure and composition. In this work, lattice parameters were also calculated by further optimisation of the fit using PDXL.[140] It is also possible to calculate crystallite size, using the Scherrer equation.

$$t = \frac{0.9\lambda}{\sqrt{B_M^2 - B_S^2}\ cos\theta}$$

Equation 1-5: Scherrer equation where t is the crystallite size, λ the X-ray wavelength, ϴ the Bragg angle, BM and BS are the width of the diffraction peaks at half height in radians. BS is a highly crystalline standard which is used to eliminate the effect of instrument broadening.

This technique is typically known as powder XRD (PXRD) and a typical sample would include a large number of randomly orientated crystallites (0.1-10 µm in diameter). This is sufficient to obtain a suitable diffraction pattern should the sample size be moderate.[141] Typically, the XRD reflections are measured in an out of plane mode. The incident angle is changed by theta and the detector by two theta and detects the value of the diffraction at each. This is a symmetric scan (2ϴ/ϴ) (Figure 1-17) and typically X rays penetrate tens of µm in the sample and measures planes parallel to the surface.[142] This means that for samples that are less than 1 µm thick, such as thin films, the diffraction patterns are extremely weak and consequently this method was not often utilised in this work.

For the analysis of thin films, a scan is normally executed using a constant small angle (1 ° or less for this work) slightly above that of the angle of total reflection and measures planes at an incline to the surface. This means that the beam of electrons will not penetrate far into the sample resulting in a larger signal ratio of film: substrate. This is called grazing incidence XRD (GI XRD). It is an out of plane asymmetric reflection measurement (2ϴ) and the detector scans over the range of two theta.[142]

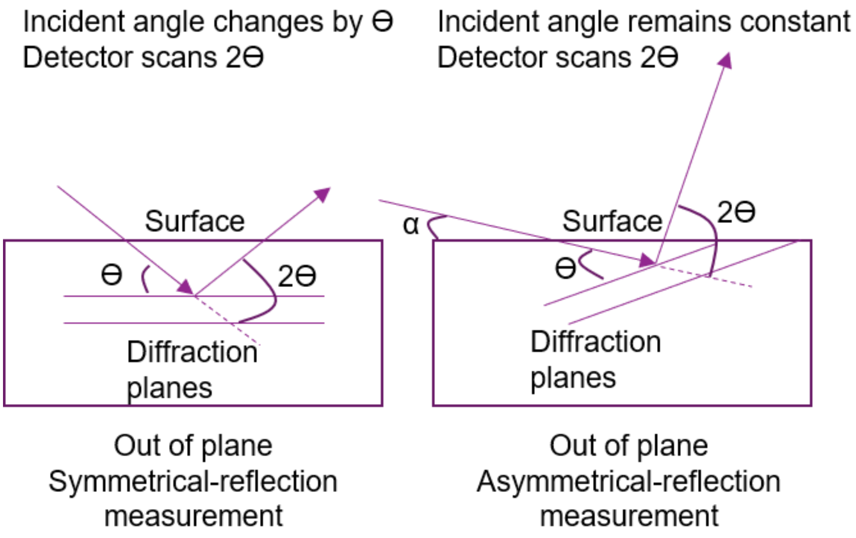

Figure 1-17: Illustration of symmetric and asymmetric out of plane reflection measurements.

In some cases, the crystallites can be highly orientated. This can result in one reflection dominating the spectrum and little detail of other reflections meaning that the pattern cannot be reliably matched to one in the literature. In plane techniques ($2ϴ_X/ϕ$) measure reflections from planes that are perpendicular to the surface. The beam of X-rays is directed in the plane of the sample so that the beam travels inside the sample for the longest possible period.[143] This increases the strength of the diffraction pattern and allows the observation of reflections that are not visible using the asymmetric out of plane grazing incidence technique.

The orientation of the crystallites can affect the overall properties of a semiconducting thin film. The degree of orientation can be measured using a pole figure measurement. 2ϴ is fixed (often the dominating diffraction maxima/ reflection) and the intensity of the diffraction of X-Rays is collected whilst varying *α* and *β*. *α* is the tilt angle between the surface and surface normal. Β is the rotation angle (ϕ).[144]

For thin film measurements, 90 ° is defined as the centre of the pole figure and this is where the lattice vector is perpendicular to the surface.[144] For metal chalcogenides with a hexagonal crystal structure, such as $TiSe_2$, $SnSe_2$, $Sb_2Te_3$, $Bi_2Se_3$ and $Bi_2Te_3$, the hexagonal platelets will lie parallel to the surface at $\alpha = 90$ °.

**Scanning Electron Microscopy (SEM)**

Scanning electron microscopy (SEM) is a microscopy technique that allows you to magnify and image the surface of a sample. In SEM, a beam of primary electrons is directed towards a sample. Some electrons are backscattered, and some interact to produce photons or another electron (secondary electron) which is reemitted. These are detected, the process repeated over the whole sample area you are imaging, and the signals are combined to produce an image of the surface. Topography and composition of the surface affects the interactions between the electrons and the surface and hence a magnified image can be built up.[145]

The technique is executed in a vacuum to ensure that the interactions observed are a result of the specimen alone. Furthermore, the shorter the wavelength of incident beam of electrons, the smaller the feature that can be observed. Consequently, SEM has an advantage over optical spectroscopy as the wavelengths of the incident electron beam are $10^{-12}$ m and $5 \times 10^{-7}$ m respectively.[145]

For thin films, this method allows you to image the surface and it can be determined if the films are continuous or not. The thicknesses of thin films can be measured via cross sectional SEM. Furthermore, this technique allows for the observation of how successful selective deposition experiments have been.

### Transmission Electron Microscopy (TEM)

In transmission electron microscopy (TEM), a beam of primary electrons is directed towards a sample, as with SEM. However, in this case, it is the electrons which are transmitted through the sample that are analysed. The degree of scattering of the electrons is positively correlated with the mass of the element which it passes through with regions of low scattering appearing brighter. This results in an image being built up. As the electrons travel through the sample in this method, a sample thickness of less than 100 nm is required. Consequently, the technique is invasive as it requires the deposited material to be removed from the substrate (often by sonication and placed on a TEM grid). TEM has the advantage of being able to reveal sub micrometre details, even below a 1 nm resolution is possible.[146] Furthermore, the atoms diffract the electrons to produce a diffraction pattern from which crystallographic information about the sample can be gleaned.

### Energy Dispersive X-ray Spectroscopy (EDX)

This is most commonly found as an attachment to the SEM. When an electron moves from one shell to another at lower energy, a characteristic X-ray for that element is emitted. However, in order for this to happen a beam of electrons is used to first excite the specimen. Each characteristic X-ray is named after the shell the electron has jumped to as each shell is given a letter starting from K for the innermost shell. The name is also dependant on where the electron was excited to. For example, dropping down just one shell into the K shell would result in a K-α emission. Dropping down two shells into K however would result in a K-β emission. These emissions are detected, and this enables determination of what elements are present in sample. The data can also be quantified to determine the ratio of  elements present.[147] The main advantage over other techniques such as X-ray photoelectron spectroscopy (XPS), is the penetration depth of the technique. In XPS, less than 10 nm of the surface is analysed[148] which can result in large errors due to surface contamination, such as dust. Electron penetration via EDX, on the other hand, is on the micrometre scale[147] and therefore samples the bulk rather than the surface. However, the consequence of this for this work is that electrons will penetrate into the substrate for thin films, and large errors, typically 5 %,[149] will be incurred specifically for thin film sample sizes of less than 1 $\mu m^3$.

### Atomic Force Microscopy (AFM)

Unlike SEM, atomic force microscopy (AFM) can be performed at atmospheric pressure. The sample requires no pre-treatment, doesn’t need to be conductive and is placed below the tip and the tip lowered so that it is in close proximity to the surface. It can be moved laterally to allow analysis of a specific site on the surface. It involves measurement of the variation in force between the surface and the sharp tip (connected to a cantilever) that is scanned over the sample at very close distances, (<10 nm). This allows the instrument to build up an image of the topography of the surface. Normal mode involves a feedback loop that moves the tip to keep the force constant throughout. Alternatively, the instrument can be used in tapping mode. This involves moving the tip up and down over the surface and measuring the force between the tip and surface.[150] The resolution of the features is dependent upon the size of the tip. As well as mapping the topography of the surface, the roughness of a sample can be measured.

### Raman Spectroscopy

In terms of quantum theory, Raman scattering involves the simultaneous absorption of a photon and excitation of the molecule; and the emission of the scattered photon and the relaxation of the molecule. As the two processes are simultaneous, the excited state is a virtual one. This also means that Raman scattering can occur when using a wavelength in a region where no electronic transitions are possible.[151]

As shown in Figure 1-18, Rayleigh scattering involves the elastic scattering of a photon whereas Raman scattering (Stokes and Anti-stokes) involves the inelastic scattering of a photon. This is a shift in energy of the photon as it interacts with a molecule. The Raman shift is the energy lost by a photon and consequently Stokes scattering results in a positive Raman shift and Anti-stokes, a negative Raman shift.

In classical terms, Raman scattering is described as the consequence of an induced dipole.[152] This dipole can be induced by an electromagnetic wave and the strength of the induced dipole is proportional to the polarizability of the molecule and the electric field strength.[153]

Raman spectroscopy is a non-invasive technique and each Raman active material has a unique fingerprint.

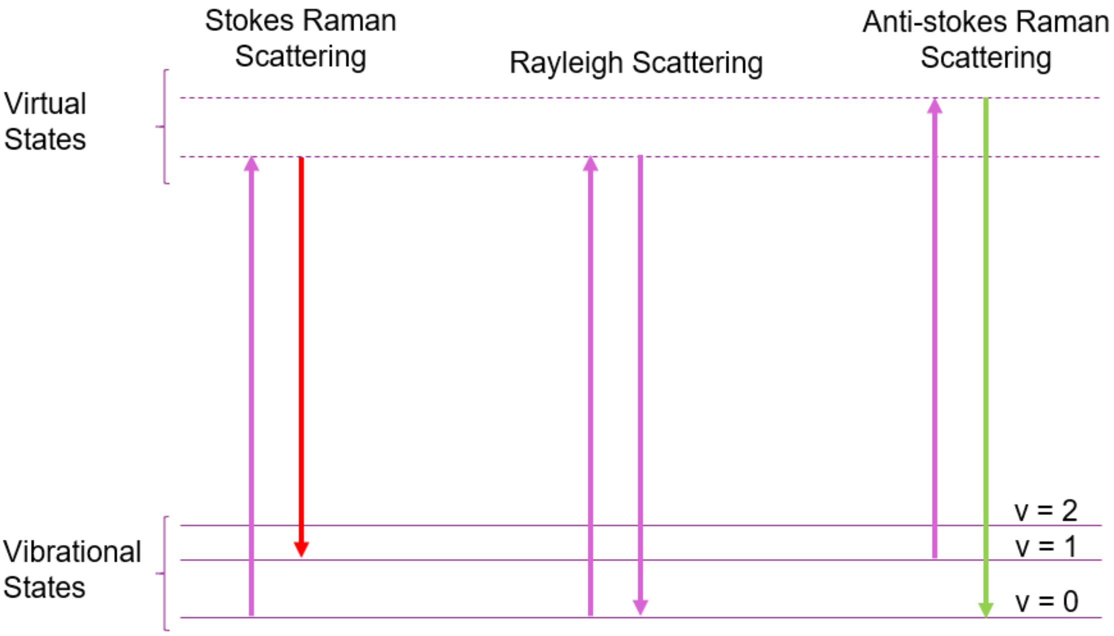

Figure 1-18: Simplified Jablonski diagram showing the differences between Raman (Stokes and Anti-stokes) and Rayleigh scattering. Each pair of arrows represent two simultaneous processes.

### Electrical Measurements

The sheet resistance of a thin film may be measured using the Hall and van der Pauw method. This involves applying a current using a four-point probe method. The four probes are placed linearly and equally spaced and a current induced through the outer two probes. The voltage is measured between the two inner probes. Measuring the thickness of the films, by cross sectional SEM, allows for calculation of the resistivity.[154,155]

Application of a magnetic field perpendicular to the flow of electrons results in charges particles experiencing a Lorentz force ($F_L$). This is proportional to both the magnetic field strength (B) and the travelling velocity (v), (q) is particle charge.

$$F_L = \mathrm{q\nu B}$$

Equation 1-6: Formula for Lorentz force

The Lorentz force can also be expressed in terms of current (I), magnetic field strength (B), carrier density ($\eta_m$) and area (A). The following equation can be used to calculated carrier density as all other quantities are known.

$$F_L = \frac{IB}{\eta_m A}$$

Equation 1-7: Formula for Lorentz force

Once both the resistivity and carrier density have been calculated, the carrier mobility ($\mu_m$) can also be calculated.

$$\rho = \frac{1}{q\eta_m \mu_m}$$

Equation 1-8: Formula for resistivity

A low carrier density and a high carrier mobility are an indication of high semiconductor purity.

Electrical measurements were performed by Dr. Ruomeng Huang at ECS, University of Southampton.

## 1.5 Aims and Objective

The aims of these works are to design and develop a range of novel single source precursors for the chemical vapour deposition of mainly binary metal chalcogenide (sulfide, selenide, telluride) thin films and nanowires, and investigation of their morphology, structure, composition and electrical properties.

The focus of this project is to improve the CVD conditions for the growth of high quality, oriented crystalline ME, $ME_2$ and $M_2E_3$ thin films and nanowires and to determine their compositional, structural and electrical properties. The prospect of being able to deposit a dense array of individual oriented nanocrystals of materials such as $Sb_2Te_3$ or GeTe is exciting as it will lead to the possibility of a number of interesting applications. As well as main group chalcogenides, early transition metal chalcogenides will also be investigated.

Precursors to be explored are mainly complexes such as metal halide selenoether and telluroether complexes, $[MCl_4(L)_2]$, $[MCl_4(L\text{-}L)]$ or $[MCl_3(L)_3]$. Alternatively, selenolate/tellurolate complexes, $[M(ER)_4]$, may be used. In the case of the early transition metal chalcogenides, such as $TiSe_2$, a 'hybrid' ligand approach will be employed combining a hard nitrogen donor alongside the soft chalcogen in order to increase the stability of the complex.

Characterisation of the new complexes (single source CVD reagents) will be via spectroscopic analysis ($^{1}H$, $^{13}C\{^{1}H\}$, $^{77}Se$, $^{125}Te$ NMR and IR spectroscopy) and in some cases single crystal X-ray structure analysis. TGA analysis may also be utilised in order to guide the CVD conditions.

Deposition will primarily focus on a low-pressure CVD approach, this requires the precursor to be sufficiently volatile. Of course, the conditions will need to be optimised. Furthermore, the testing of the developed precursors in additional CVD rigs such as for liquid injection CVD where the precursors need to be sufficiently soluble in a suitable solvent may show the versatility of the precursor for other solvent based techniques such as aerosol assisted CVD.

In terms of materials characterisation, the materials will be characterised by SEM, coupled with EDX, XRD, Raman spectroscopy and electrical measurements.

## 1.6 References

1 M. Chhowalla, H. S. Shin, G. Eda, L.-J. Li, K. P. Loh and H. Zhang, *Nat. Chem.*, 2013, **5**, 263–275.

2 Q. H. Wang, K. Kalantar-Zadeh, A. Kis, J. N. Coleman and M. S. Strano, *Nat. Nanotechnol.*, 2012, **7**, 699–712.

3 A. Kuc, N. Zibouche and T. Heine, *Phys. Rev. B*, 2011, **83**, 5213–5214.

4 B. Sipos, A. F. Kusmartseva, A. Akrap, H. Berger, L. Forró and E. Tutis, *Nat. Mater.*, 2008, **7**, 960–965.

5 A. H. Castro Neto, *Phys. Rev. Lett.*, 2001, **86**, 4382–4385.

6 J. Rasch, T. Stemmler, B. Müller, L. Dudy and R. Manzke, *Phys. Rev. Lett.*, 2008, **101**, 76021–76024.

7 J. A. Wilson, F. J. Di Salvo and S. Mahajan, *Adv. Phys.*, 2010, **50**, 1171–1248.

8 E. Morosan, H. W. Zandbergen, B. S. Dennis, J. W. G. Bos, Y. Onose, T. Klimczuk, A. P. Ramirez, N. P. Ong and R. J. Cava, *Nat. Phys.*, 2006, **2**, 544–550.

9 C. H. de Groot, C. Gurnani, A. L. Hector, R. Huang, M. Jura, W. Levason and G. Reid, *Chem. Mater.*, 2012, **24**, 4442–4449.

10 K. F. Mak, C. Lee, J. Hone, J. Shan and T. F. Heinz, *Phys. Rev. Lett.*, 2010, **105**, 68051–68054.

11 K. S. Novoselov, V. I. Fal′ko, L. Colombo, P. R. Gellert, M. G. Schwab and K. Kim, *Nature*, 2012, **490**, 192–200.

12 N. Zibouche, A. Kuc, J. Musfeldt and T. Heine, *Ann. Phys.*, 2014, **526**, 395–401.

13 Q. Xiang, J. Yu and M. Jaroniec, *J. Am. Chem. Soc.*, 2012, **134**, 6575–6578.

14 C. Feng, J. Ma, H. Li, R. Zeng, Z. Guo and H. Liu, *Mater. Res. Bull.*, 2009, **44**, 1811–1815.

15 G. Busch, C. Froehlich and F. Hullinger, *Helv. Phys. Acta*, 1961, **34**, 359–368.

16 R. M. Hazen and L. W. Finger, *Am. Mineral.*, 1978, **63**, 293–296.

17 W. Hofmann, *Zeitschrift. Krist.*, 1935, **92**, 161–173.

18 K. Adouby, C. Perez-Vicente and J. C. Jumas, *Zeitschrift. Krist.*, 1998, **213**, 343–349.

19 O. Madelung, *Semiconductors: Data Handbook vol 14*, Springer Berlin Heidelberg, Berlin Heidelberg, 2004.

20 G. Ghosh, *J. Phase Equilibria*, 1993, **14**, 753–763.

21 V. Sorkin, H. Pan, H. Shi, S. Y. Quek and Y. W. Zhang, *Crit. Rev. Solid State Mater. Sci.*, 2014, **39**, 319–367.

22 A. Anopchenko, D. Cavalcoli, A. Cavallini, C. Cavalotti, B. Ceccaroli, G. Coletti, R. S. Hocklett, V. Kveder, D. Macdonald, L. Pavesi, S. Pizzini and L. Polenta, *Advanced Silicon Materials for Photovoltaic Applications*, John Wiley & Sons, Ltd, Chichester, 2012.

23 J. A. Wilson and A. D. Yoffe, *Adv. Phys.*, 1969, **18**, 193–335.

24 S. K. Mishra, S. Satpathy and O. Tepsen, *J. Phys. Condens. Matter*, 1997, **9**, 461–470.

25 S. Messina, M. T. S. Nair and P. K. Nair, *J. Electrochem. Soc.*, 2009, **156**, H327–H332.

26 A. Splendiani, L. Sun, Y. Zhang, T. Li, J. Kim, C. Y. Chim, G. Galli and F. Wang, *Nano Lett.*, 2010, **10**, 1271–1275.

27 K. . Kam and B. A. Parkinson, *J. Phys. Chem.*, 1982, **86**, 463–467.

28 F. E. Mabbs and D. J. Machin, *Magnetism and Transition Metal Complexes*, Dover Publications, Inc, Mineola, New York, 2008.

29 P. Manchanda, V. Sharma, H. Yu, D. J. Sellmyer and R. Skomski, *Appl. Phys. Lett.*, 2015, **107**, 24021–24025.

30 V. Z. Kresin and S. A. Wolf, *Fundamentals of superconductivity*, Plenum, New York, NY, USA, 1990.

31 H. Zeng, J. Dai, W. Yao, D. Xiao and X. Cui, *Nat. Nanotechnol.*, 2012, **7**, 490–493.

32 S. Min and G. Lu, *J. Phys. Chem. C*, 2012, **116**, 25415−25424.

33 T. F. Jaramillo, K. P. Jørgensen, J. Bonde, J. H. Nielsen, S. Horch and I. Chorkendorff, *Science.*, 2007, **317**, 100–103.

34 C. Zhang, H. Yin, M. Han, Z. Dai, H. Pang, Y. Zheng, Y. Q. Lan, J. Bao and J. Zhu, *ACS Nano*, 2014, **8**, 3761–3770.

35 T. Roy, M. Tosun, J. S. Kang, A. B. Sachid, S. B. Desai, M. Hettick, C. C. Hu and A. Javey, *ACS Nano*, 2014, **8**, 6259–6264.

36 J. Yoon, W. Park, G. Bae, Y. Kim and H. S. Jang, *Small*, 2013, **9**, 3295–3300.

37 R. Cheng, D. Li, H. Zhou, C. Wang, A. Yin, S. Jiang, Y. Liu, Y. Chen, Y. Huang and X. Duan, *Nano Lett.*, 2014, **14**, 5590–5597.

38 H. Fang, C. Battaglia, C. Carraro, S. Nemsak, B. Ozdol and J. Seuk, *Proc. Natl. Acad. Sci. U.S.A*, 2014, **111**, 6198–6202.

39 B. W. H. Baugher, H. O. H. Churchill, Y. Yang and P. Jarillo-Herrero, *Nat. Nanotechnol.*, 2014, **9**, 262–267.

40 D. Chen, W. Chen, L. Ma, G. Ji, K. Chang and J. Y. Lee, *Mater. Today*, 2014, **17**, 184–193.

41 D. J. Late, B. Liu, H. S. S. R. Matte, V. P. Dravid and C. N. R. Rao, *ACS Nano*, 2012, **6**, 5635–5641.

42 E. W. Keong Koh, C. H. Chiu, Y. K. Lim, Y. W. Zhang and H. Pan, *Int. J. Hydrogen Energy*, 2012, **37**, 14323–14328.

43 T. J. Seebeck, *Ann. Phys.*, 1826, **82**, 133–160.

44 J. R. Sootsman, D. Y. Chung and M. G. Kanatzidis, *Angew. Chem. Int. Ed.*, 2009, **48**, 8616–8639.

45 M. Hamid Elsheikh, D. A. Shnawah, M. F. M. Sabri, S. B. M. Said, M. Haji Hassan, M. B. Ali Bashir and M. Mohamad, *Renew. Sustain. Energy Rev.*, 2014, **30**, 337–355.

46 J. G. Vián, D. Astrain and M. Domínguez, *Appl. Therm. Eng.*, 2002, **22**, 407–422.

47 E. Altenkirch, *Phys. Zeitschrift*, 1911, **12**, 920–924.

48 T. C. Holgate, R. Bennett, T. Hammel, T. Caillat, S. Keyser and B. Sievers, *J. Electron. Mater.*, 2015, **44**, 1814–1821.

49 N. Peranio, M. Winkler, Z. Aabdin, J. König, H. Böttner and O. Eibl, *Phys. Status Solidi*, 2012, **209**, 289–293.

50 S. L. Benjamin, C. H. de Groot, A. L. Hector, R. Huang, E. Koukharenko, W. Levason and G. Reid, *J. Mater. Chem. C*, 2015, **3**, 423–430.

51 S. Zastrow, J. Gooth, T. Boehnert, S. Heiderich, W. Toellner, S. Heimann, S. Schulz and K. Nielsch, *Semicond. Sci. Technol.*, 2013, **28**, 350101–350106.

52 P. Fan, Z. H. Zheng, G. X. Liang, D. P. Zhang and X. M. Cai, *J. Alloys Compd.*, 2010, **505**, 278–280.

53 H. You, S. Hyub Baek, K.-C. Kim, O.-J. Kwon, J.-S. Kim and C. Park, *J. Cryst. Growth*, 2012, **346**, 17–21.

54 X. Wang, H. He, N. Wang and L. Miao, *Appl. Surf. Sci.*, 2013, **276**, 539–542.

55 M. M. Rashid, K. H. Cho and G.-S. Chung, *Appl. Surf. Sci.*, 2013, **279**, 23–30.

56 S. L. Benjamin, C. H. de Groot, C. Gurnani, A. L. Hector, R. Huang, E. Koukharenko, W. Levason and G. Reid, *J. Mater. Chem. A*, 2014, **2**, 4865–4869.

57 A. Al Bayaz, A. Giani, A. Foucaran, F. Pascal-Delannoy and A. Boyer, *Thin Solid Films*, 2003, **441**, 1–5.

58 C. Wang, Y. Chen, J. Jiang, R. Zhang, Y. Niu, T. Zhou, J. Xia, H. Tian, J. Hu and P. Yang, *RSC Adv.*, 2017, **7**, 16795–16800.

59 L.-D. Zhao, S.-H. Lo, Y. Zhang, H. Sun, G. Tan, C. Uher, C. Wolverton, V. P. Dravid and M. G. Kanatzidis, *Nature*, 2014, **508**, 373–377.

60 M. Wuttig and N. Yamada, *Nat. Mater.*, 2007, **6**, 824–832.

61 D. Lencer, M. Salinga, B. Grabowski, T. Hickel, J. Neugebauer and M. Wuttig, *Nat. Mater.*, 2008, **7**, 972–977.

62 A. V Kolobov, P. Fons, A. I. Frenkel, A. L. Ankudinov, J. Tominaga and T. Uruga, *Nat. Mater.*, 2004, **3**, 703–708.

63 S. . Ovshinsky, *Phys. Rev. Lett.*, 1968, **21**, 1450–1453.

64 H. Tanaka, T. Nishihara, T. Ohtsuka, K. Morimoto, N. Yamada and K. Morita, *Jpn. J. Appl. Phys.*, 2002, **41**, L1443–L1445.

65 D. Ielmini and A. L. Lacaita, *Mater. Today*, 2011, **14**, 600–607.

66 J. Arciniega, E. Prokhorov, F. Beltran and G. Trapaga, in *Crystallization - Science and Technology*, ed. M. R. B. Andreeta, InTech, Vienna, 2012, pp. 433–460.

67 N. Yamada, E. Ohno, K. Nishiuchi, N. Akahira and M. Takao, *J. Appl. Phys.*, 1991, **69**, 2849–2856.

68 M. H. R. Lankhorst, *J. Non. Cryst. Solids*, 2002, **297**, 210–219.

69 G. Bruns, P. Merkelbach, C. Schlockermann, M. Salinga, M. Wuttig, T. D. Happ, J. B. Philipp and M. Kund, *Appl. Phys. Lett.*, 2009, **95**, 0431081–0431083.

70 T. C. Chong, L. P. Shi, R. Zhao, P. K. Tan, J. M. Li, H. K. Lee, X. S. Miao, A. Y. Du and C. H. Tung, *Appl. Phys. Lett.*, 2006, **88**, 3–6.

71 S. Cecchi, E. Zallo, J. Momand, R. Wang, B. J. Kooi, M. A. Verheijen and R. Calarco, *APL Mater.*, 2017, **5**, 0261071–0261076.

72 K.-M. Chung, D. Wamwangi, M. Woda, M. Wuttig and W. Bensch, *J. Appl. Phys.*, 2008, **103**, 0835231–0835237.

73 R. Y. Wang, M. A. Caldwell, R. G. D. Jeyasingh, S. Aloni, R. M. Shelby, H. S. P. Wong and D. J. Milliron, *J. Appl. Phys.*, 2011, **109**, 1135061–1135066.

74 S. L. Benjamin, C. H. de Groot, C. Gurnani, A. L. Hector, R. Huang, K. Ignatyev, W. Levason, S. J. Pearce, F. Thomas and G. Reid, *Chem. Mater.*, 2013, **25**, 4719–4724.

75 K. George, C. H. De Groot, C. Gurnani, A. L. Hector, R. Huang, M. Jura, W. Levason and G. Reid, *Phys. Procedia*, 2013, **46**, 142–148.

76 A. S. Baranski and W. R. Fawcett, *J. Electrochem. Soc.*, 1980, **127**, 766–767.

77 S. H. Chaki, H. J. Joshi, J. P. Tailor and M. P. Deshpande, *Mater. Res. Express*, 2017, **4**, 0764021–0764028.

78 A. Giussani, K. Perumal, M. Hanke, P. Rodenbach, H. Riechert and R. Calarco, *Phys. Status Solidi Basic Res.*, 2012, **249**, 1939–1944.

79 T. Gwon, T. Eom, S. Yoo, H. K. Lee, D. Y. Cho, M. S. Kim, I. Buchanan, M. Xiao, S. Ivanov and C. S. Hwang, *Chem. Mater.*, 2016, **28**, 7158–7166.

80 L. Gao, H. Li, W. Ren, G. Wang, H. Li, E. Ashalley, Z. Zhong, H. Ji, Z. Zhou, J. Wu and X. Niu, *Vaccum*, 2017, **140**, 58–62.

81 J. R. Arthur, *Surf. Sci.*, 2002, 159–217.

82 A. C. Jones and M. L. Hitchman, *Chemical Vapour Deposition: Precursors, Processes and Applications*, Royal Society of Chemistry, Cambridge, First Edn., 2009.

83 A. C. Jones and M. L. Hitchman, *Chem. Vap. Depos. Precursors, Process. Appl.*, 2009, 1–36.

84 C. J. Carmalt, T. D. Manning, I. P. Parkin, E. S. Peters and A. L. Hector, *Thin Solid Films*, 2004, **469–470**, 495–499.

85 R. S Wagner, W. C. Ellis, *Appl. Phys. Lett.*, 1964, **4**, 89–90.

86 R. Bin Yang, J. Bachmann, E. Pippel, A. Berger, J. Woltersdorf, U. Gösele and K. Nielsch, *Adv. Mater.*, 2009, **21**, 3170–3174.

87 S. Biswas, C. O. Regan, M. A. Morris and J. D. Holmes, *Mater. Views*, 2014, **11**, 103–111.

88 J. S. Lee, S. Brittman, D. Yu and H. Park, *J. Am. Chem. Soc.*, 2008, **130**, 46252–6258.

89 A. Abrutis, V. Plausinaitiene, M. Skapas, C. Wiemer, W. Gawelda, J. Siegel and S. Rushworth, *J. Cryst. Growth*, 2009, **311**, 362–367.

90 R. Huang, S. L. Benjamin, C. Gurnani, A. L. Hector, W. Levason, G. Reid and C. H. De Groot, *Sci. Rep.*, 2016, **6**, 1–16.

91 D. M. Mattox, *Handbook of Physical Vapour Deposition (PVD) Processing*, Elsevier, Burligton, MA, USA, Second Edn., 2010.

92 M. Ritala and J. Niinisto, *Chemical Vapour Deposition: Precursors, Processes and Applications*, Royal Society of Chemistry, Cambridge, First Edn., 2009.

93 T. Gwon, T. Eom, S. Yoo, H.-K. Lee, D.-Y. Cho, M.-S. Kim, I. Buchanan, M. Xiao, S. Ivanov and C. S. Hwang, *Chem. Mater.*, 2016, **28**, 7158–7166.

94 N. D. Boscher, C. J. Carmalt and I. P. Parkin, *Chem. Vap. Depos.*, 2006, **12**, 54–58.

95 N. D. Boscher, C. S. Blackman, C. J. Carmalt, I. P. Parkin and A. G. Prieto, *Appl. Surf. Sci.*, 2007, **253**, 6041.

96 N. D. Boscher, C. J. Carmalt and I. P. Parkin, *Eur. J. Inorg. Chem.*, 2006, **12**, 55.

97 C. J. Carmalt, I. P. Parkin and E. S. Peters, *Polyhedron*, 2003, **22**, 1263–1269.

98 E. S. Peters, C. J. Carmalt, I. P. Parkin and D. A. Tocher, *Eur. J. Inorg. Chem.*, 2005, **2005**, 4179–4185.

99 J.-H. Kim, S.-D. Kwon, D.-Y. Jeong, B.-K. Ju, S.-J. Yoon and J.-S. Kim, *25th Int. Conf. Thermoelectr.*, 2006, 411–413.

100 J. H. Kim, Y. C. Jung, S. H. Suh and J. S. Kim, *J. Nanosci. Nanotechnol.*, 2006, **6**, 3325–3328.

101 A. Giani, A. Boulouz, F. P. Delannoy, A. Foucaran, A. Boyer, B. Aboulfarah and A. Mzerd, *J. Mater. Sci. Lett.*, 1999, **18**, 541–543.

102 G. Bendt, S. Zastrow, K. Nielsch, P. S. Mandal, J. Sánchez-Barriga, O. Rader and S. Schulz, *J. Mater. Chem. A*, 2014, **2**, 8215–8222.

103 O. Salicio, C. Wiemer, M. Fanciulli, W. Gawelda, J. Siegel, C. N. Afonso, V. Plausinaitiene and A. Abrutis, *J. Appl. Phys.*, 2009, **105**, 0335201–0335206.

104 L. S. Price, I. P. Parkin, T. G. Hibbert and K. C. Molloy, *Chem. Vap. Depos.*, 1998, **4**, 222–225.

105 L. S. Price, I. P. Parkin, A. M. E. Hardy, R. J. H. Clark, T. G. Hibbert and K. C. Molloy, *Chem. Mater.*, 1999, **11**, 1792–1799.

106 N. D. Boscher, C. J. Carmalt, R. G. Palgrave and I. P. Parkin, *Thin Solid Films*, 2008, **516**, 4750–4757.

107 G. Barone, T. G. Hibbert, M. F. Mahon, K. C. Molloy, L. S. Price, I. P. Parkin, A. M. E. Hardy and M. N. Field, *J. Mater. Chem.*, 2001, **11**, 464–468.

108 I. P. Parkin, L. S. Price, T. G. Hibbert and K. C. Molloy, *J. Mater. Chem.*, 2001, **11**, 1486–1490.

109 A. T. Kana, T. G. Hibbert, M. F. Mahon, K. C. Molloy, I. P. Parkin and L. S. Price, *Polyhedron*, 2001, **20**, 2989–2995.

110 P. Kevin, D. J. Lewis, J. Raftery, M. Azad Malik and P. O’Brien, *J. Cryst. Growth*, 2015, **415**, 93–99.

111 J. Rodriguez-Castro, P. Dale, M. F. Mahon, K. C. Molloy and L. M. Peter, *Chem. Mater.*, 2007, **19**, 3219–3226.

112 J. Rodriguez-Castro, M. F. Mahon and K. C. Molloy, *Chem. Vap. Depos.*, 2006, **12**, 601–607.

113 G. Bendt, S. Gassa, F. Rieger, C. Jooss and S. Schulz, *J. Cryst. Growth*, 2018, **490**, 77–83.

114 K. George, C. H. de Groot, C. Gurnani, A. L. Hector, R. Huang, M. Jura, W. Levason and G. Reid, *Chem. Mater.*, 2013, **25**, 1829–1836.

115 S. L. Benjamin, Y.-P. Chang, C. Gurnani, A. L. Hector, M. Huggon, W. Levason and G. Reid, *Dalton Trans.*, 2014, **43**, 16640–16648.

116 P. J. McKarns, T. S. Lewkebandara, G. P. A. Yap, L. M. Liable-Sands, A. L. Rheingold and C. H. Winter, *Inorg. Chem.*, 1998, **37**, 418–424.

117 T. Su. Lewkebandara, P. J. Mckarns, B. S. Haggerty, G. P. A. Yap, A. L. Rheingold and C. H. Winter, *Polyhedron*, 1998, **5387**, 1–9.

118 S. D. Reid, A. L. Hector, W. Levason, G. Reid, B. J. Waller and M. Webster, *Dalton Trans.*, 2007, **4**, 4769–4777.

119 M. F. Davis, W. Levason, G. Reid, M. Webster and W. Zhang, *Dalton Trans.*, 2008, **4334**, 533–538.

120 W. Levason, G. Reid and W. Zhang, *Coord. Chem. Rev.*, 2011, **255**, 1319–1341.

121 W. Levason, G. Reid and W. Zhang, *Dalton Trans.*, 2011, **40**, 8491–8506.

122 W. Levason and G. Reid, *J. Chem. Soc. Dalton Trans.*, 2001, 2953–2960.

123 W. Levason, N. J. Hill and G. Reid, *J. Chem. Soc. Dalton Trans.*, 2002, **6**, 4316–4317.

124 T. Chivers and R. S. Laitinen, *Chem. Soc. Rev.*, 2015, **44**, 1725–1739.

125 C. E. Housecroft and A. G. Sharpe, *Inorganic Chemistry*, Pearson Education Ltd., Essex, 2005.

126 D. T. McAllan, T. V. Cullum, R. A. Dean and F. A. Fidler, *J. Am. Chem. Soc.*, 1951, **73**, 3627–3632.

127 C. Gurnani, S. L. Hawken, A. L. Hector, R. Huang, M. Jura, W. Levason, J. Perkins, G. Reid and G. B. G. Stenning, *Dalt. Trans.*, 2018, **4**, 2628–2637.

128 D. J. Gulliver, E. G. Hope, W. Levason, S. G. Murray, D. M. Potter, S. Sn, G. L. Marshall, R. A. East and L. Se, *J. Chem. Soc. Perkin Trans. 2*, 1984, **0**, 429–434.

129 E. G. Hope, T. Kemmltt and W. Levason, *Organometallics*, 1987, **6**, 206–207.

130 D. W. H. Rankin, N. W. Mitzel and C. A. Morrison, *Structural Methods in Molecular Inorganic Chemistry*, John Wiley & Sons, Ltd, Chichester, First Edn., 2013.

131 A. J. Barton, N. J. Hill, W. Levason and G. Reid, *J. Chem. Soc. Dalt. Trans.*, 2001, 1621–1627.

132 R. K. Harris, *Chem. Soc. Rev.*, 1976, **5**, 1–22.

133 P. J. Hore, *Nuclear Magnetic Resonance*, Oxford University Press Inc., New York, 1995.

134 R. K. Harris, E. D. Becker, S. M. Cabral de Menezes, R. Goodfellow and P. Granger, *Magn. Reson. Chem.*, 2002, **40**, 489–505.

135 J. A. Iggo, *NMR Spectroscopy in Inorganic Chemistry*, Oxford University Press Inc., New York, 1999.

136 M. Weller, T. Overton, J. Rourke and F. Armstrong, *Inorganic Chemistry*, Oxford University Press, Oxford, Sixth Edn., 2014.

137 C. Giacovazzo, H. L. Monaco, D. Viterbo, F. Scordari, G. Gilli, G. Zanotti and M. Catti, *Fundamentals of Crystallography*, Oxford University Press, New York, 1992.

138 W. Clegg, *Crystal Structure Analysis: Principles and Practice*, Oxford University Press, Oxford, Second Edn., 2009.

139 ICSD: Inorganic Crystal Structure Database (ICSD), Fachinformationszentrum Karlsruhe (FIZ), accessed via the EPSRC funded National Chemical Database Service hosted by the Royal Society of Chemistry.

140 Rigaku, *Rigaku J.*, 2010, **26**, 23–27.

141 D. Shriver, P. Atkins, T. Overton, J. Rourke, M. Weller and F. Armstrong, *Shriver & Atkins Inorganic Chemistry*, Oxford University Press, Oxford, Fourth., 2006.

142 T. Mitsunaga, *Rigaku J.*, 2009, **25**, 7–12.

143 S. Kobayashi, *Rigaku J.*, 2010, **26**, 3–11.

144 K. Nagao and E. Kagami, *Rigaku J.*, 2011, **27**, 6–14.

145 D. J. Stokes, *Principles and Practice of Variable Pressure/ Environmental Scanning Electron Microscopy (VP-ESEM)*, John Wiley & Sons, Ltd, Chichester, 2008.

146 R. Brydson, *Aberration-Corrected Analytical Electron Microscopy*, John Wiley & Sons, Ltd, 2011.

147 J. C. Russ, *Fundamentals of Energy Dispersive X-Ray Analysis*, Butterworths & Co Ltd, London, 1984.

148 D. K. Schroder, *Semiconductor Material and Device Characterisation*, Wiley, New York, USA, Second Edn., 1998.

149 D. E. Newbury and N. W. M. Ritchie, *Scanning*, 2013, **35**, 141–168.

150 G. Binnig, C. Gerber, E. Stoll, T. R. Albrecht and C. F. Quate, *Europhys. Lett.*, 1987, **3**, 1281–1286.

151 E. C. Le Ru and P. G. Etchegoin, *Principles of surface-enhanced Raman spectroscopy and related plasmonic effects.*, Elsevier Science, Oxford, 1st Edition., 2009.

152 W. J. Moore, *Physical Chemistry.,* Longmans Green & Co Ltd, 5th Editio., 1972.

153 J. Ferraro, K. Nakamoto and C. Brown, *Introductory Raman spectroscopy*, San Diego, 2003.

154 L. J. van der Pauw, *Philips Tech. Rev.*, 1958, **20**, 220–224.

155 L. J. van der Pauw, *Philips Res. Reports*, 1958, **13**, 1–9.

# Chapter 2: Precursors for the Deposition of Bismuth and Antimony Chalcogenides

## 2.1 Introduction

Antimony and bismuth chalcogenides, $M_2E_3$ (M = Sb, Bi) (E = Se, Te) are layered semiconducting materials with narrow bandgaps (Table 2-1).

| Material | Bandgap/ eV |
|---|---|
| $Sb_2Se_3$[1] | 1.1 |
| $Sb_2Te_3$[2] | 0.28 |
| $Bi_2Se_3$[3] | 0.24 |
| $Bi_2Te_3$[2] | 0.16 |

Table 2-1: Bandgaps for $M_2E_3$ (M = Sb, Bi) (E = Se, Te).

$Bi_2Se_3$, $Bi_2Te_3$ and $Sb_2Te_3$ are part of the tetradymite ($Bi_2Te_2S$) group as they have essentially the same crystal structure: trigonal and space group: R(-3)m.[2] They have many interesting properties such as high electrical conductivity which makes them ideal candidates for thermoelectric materials for near room temperature applications. Thermoelectric materials need to have high electrical conductivity but be thermally insulating and are usually defined by figure of merit, *ZT*. This is discussed in more detail in Chapter 1, Section 1.1.3. Electrical conductivity (σ) for $Bi_2Se_3$ thin films has been reported as 101- 549 $Scm^{-1}$,[4] thin films of $Bi_2Te_3$ has shown conductivities of 312 – 8620 $Scm^{-1}$ from a range of deposition methods.[5–9] $Sb_2Te_3$ thin films have shown conductivities of 104 – 1695 $Scm^{-1}$.[8,10–12] It has been shown that by controlling the dimensionality of the film, *ZT* can be increased.[13] Thermoelectric materials are discussed in more detail in Chapter 1.

$Sb_2Se_3$ on the other hand, exists in an orthorhombic phase[14] and with its comparatively larger band gap (1.1 eV),[1] it has intrinsically low electrical conductivity in the region of $10^{-6}$ to $10^{-7}$ $Scm^{-1}$.[15] Consequently it is not suitable as a thermoelectric material. However, it does have a high absorption coefficient (> $10^5$ $cm^{-1}$)[16] and a dielectric constant of 29-18 within a 2 KHz to 2 MHz frequency range.[17] Such properties make it an ideal candidate for use in photovoltaics.[18,19]

Other applications of these thin films include the use of $Sb_2Te_3$ in quantum computing as it is a topological insulator.[20] $Bi_2Se_3$, also a topological insulator (materials that are insulating in their interior but conducting on their surface), is a candidate for field effect transistors.[21]

Furthermore, $Sb_2Te_3$, $Sb_2Se_3$ and $Bi_2Te_3$ have all been used in optical recording systems.[22]

Antimony and bismuth chalcogenide layered materials can be synthesised by a variety of different methods. $Bi_2Se_3$ has been deposited by reactive evaporation,[23] a solvothermal method using $BiCl_3$, Se and NaI,[24] and successive ionic layer absorption and reaction method using $[Bi(NO_3)_3.5H_2O]$ and $Na_2SeSO_3$.[25] $Bi_2Te_3$ films have been deposited by methods such as molecular beam epitaxy,[8] co-sputtering[6] and an electrodeposition method using $[Bi(NO_3)_3.5H_2O]$ and $TeO_2$.[7] $Sb_2Te_3$ films have been deposited by molecular beam epitaxy,[8] atomic layer deposition using $SbCl_3$ and $(Et_3Si)_2Te$,[11] and by low temperature ion beam sputtering.[12] Films of $Sb_2Se_3$ have been deposited by thermal evaporation using $Sb_2Se_3$ powder,[19] chemical bath deposition from $2[Sb^{3+}(citrate)]$ and $3Se^{2-}$[26] or $[Sb_2(C_4O_6H_2)_2]^{2-}$ and $Na_2SeSO_3$.[27] and electrodeposition from $K(SbO)C_4H_4O_6.0.5H_2O$ and $H_2SeO_3$ in the presence of $NH_4Cl$[28] or $Sb^{3+}$ and $SeO_2$.[29]

A number of CVD approaches have previously been employed to deposit thin films. $Bi_2Se_3$ has been deposited using trimethyl bismuth, diethyl selenium with a $H_2$ carrier gas[4] or using $Bi[(EPR_2)_2N]_3$ (E = Se; R = Ph, $^iPr$) under low pressure or using an aerosol assisted technique.[30,31] $Bi_2Te_3$ has been deposited using atmospheric pressure CVD using trimethyl bismuth and diisopropyl telluride.[5] Trialkyl stibines $SbR_3$ (R = Me, Et) have also been used along with $TeR_2$ (R = Et, $^iPr$) to deposit $Sb_2Te_3$ via CVD.[32–34]

$[Sb\{(TeP^iPr_2)_2N\}_3]$[35] and $[Sb\{SeC_5H_3(Me\text{-}3)N\}_3]$[36] have been used under AACVD conditions to deposit $Sb_2Te_3$ and $Sb_2Se_3$, whilst $[MeSb(E^nBu_2)_2]$ (E = Se, Te) has led to the deposition of both $Sb_2Se_3$ and $Sb_2Te_3$ under LPCVD conditions.[10] In previous work in our group $[BiCl_3(Te^nBu_2)_3]$ has been used under LPCVD conditions to deposit $Bi_2Te_3$.[9]

CVD is an inexpensive and scalable technique. With the use of single source precursors, substrate selective deposition can also be achieved, which is important in the development of complex nanostructured devices. For example, it has been demonstrated that both $Bi_2Te_3$[9] and $Sb_2Te_3$[37] can be deposited selectively onto TiN wells, without deposition onto the surrounding $SiO_2$, as shown in Figure 2-1. It is not just a phenomenon of single source precursors however, selective deposition via ALD has also been reported.[38]

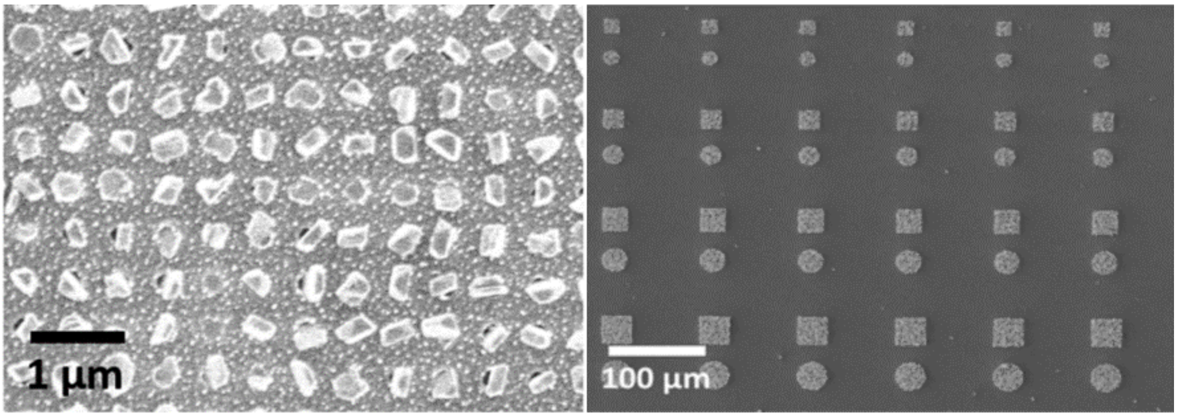

Figure 2-1: Showing arrays of $Sb_2Te_3$ single crystals deposited onto a nanopatterned substrate (left)[37] and $Bi_2Te_3$ (right)[9] grown by CVD onto a patterned $SiO_2$/TiN substrate. (Reproduced from references 9 and 37 with permission form the RSC).

The high conductivity and hydrophobicity of the TiN are thought to be significant factors.[37] The hydrophobicity of both the butyl groups in the precursor and the TiN substrate is thought to facilitate adsorption of the precursor.[37] Furthermore, it has been demonstrated that substrates with a high conductivity have an increased growth rate compared to insulating substrates[39] and it is thought that this electron donation may improve precursor decomposition and hence enable nucleation. A lower resistivity of the material being deposited is shown to increase the likelihood of a selective deposition being achievable and this links well with the electron donation mechanism.[37]

$[BiCl_3(Te^nBu_2)_3]$ has been synthesised from the Lewis acid, $BiCl_3$ and chalcogenoether ligand, $Te^nBu_2$ as shown in Scheme 2-1.[9]

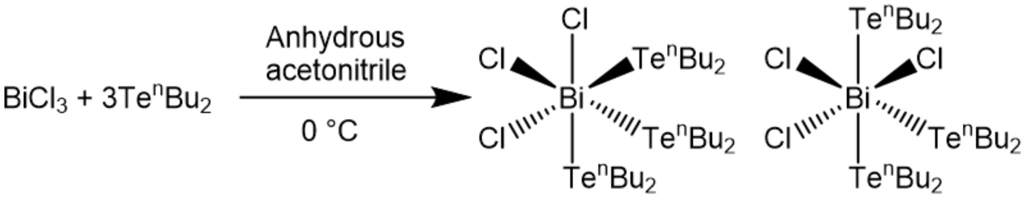

Scheme 2-1: The synthesis of $[BiCl_3(Te^nBu_2)_3]$ to produce the fac or mer isomer.[9]

$BiCl_3$ is a modest Lewis acid and accepts electrons from the telluroether ligand (Lewis base). Replacing bismuth with antimony results in a weaker Lewis acid and consequently a weaker interaction between the metal chloride acceptor and the ligand. Both Sb(III) and Bi(III) have a lone pair, which if active, would distort the complexes.[40]

Although $Bi_2Te_3$ and $Sb_2Te_3$ have been shown to display promising thermoelectric properties, superlattices of $Bi_2Te_3$ and $Sb_2Te_3$ have shown some of the highest ZT values claimed.[41] Previous work at the University of Southampton has demonstrated the deposition of a $Bi_2(Te_xSe_{1-x})_3$ n-type ternary phase from $[BiCl_3(Te^nBu_2)_3]$ and $[BiCl_3(Se^nBu_2)_3]$, whilst there are reports of $SbBiTe_3$ being synthesized by a high pressure synthesis route resulting in a p-type material with enhanced thermoelectric properties.[42] $(Sb_xBi_{1-x})_2Te_3$ has also been synthesised via a solvothermal method and it was demonstrated that bismuth-rich phases were n-type whereas antimony-rich phases were p-type with electrical properties differing with composition.[43]

This chapter aims to show the synthesis of precursors analogous to $[BiCl_3(Te^nBu_2)_3]$ using antimony and bismuth chlorides with selenoether and telluroether ligands and to show the deposition of $M_2E_3$ (M = Sb, Bi; E = Se, Te) and characterisation of the resulting films. Additional aims include using $[BiCl_3(Te^nBu_2)_3]$ with $[SbCl_3(Te^nBu_2)_3]$ to deposit a ‘p-type’ ternary phase, $(Sb_xBi_{1-x})_2Te_3$.

## 2.2 Results and Discussion

### 2.2.1 Synthesis and Characterisation of [MCl$_3$(E$^n$Bu)$_3$] (E = Se, Te)

The distorted octahedral Bi(III) chloride complex with neutral telluroether ligands, [BiCl$_3$(Te$^n$Bu$_2$)$_3$], has been reported to give rise to $Bi_2Te_3$ films under LPCVD conditions. Furthermore, the position and orientation of the crystals can be controlled on the nanoscale.[9] Completing this family of precursors, [BiCl$_3$(Se$^n$Bu$_2$)$_3$], [SbCl$_3$(Se$^n$Bu$_2$)$_3$] and [SbCl$_3$(Te$^n$Bu$_2$)$_3$] have been synthesized by the direct 1:3 reaction of MCl$_3$ with E$^n$Bu$_2$ in dry MeCN. These are illustrated in Scheme 2-2 below.

Bi(III) and Sb(III) six coordinate complexes are expected to form in distorted octahedral geometries. However, each has a lone pair and if stereochemically active,[44] a distorted pentagonal bypyramidal geometry with a vacant site is expected.

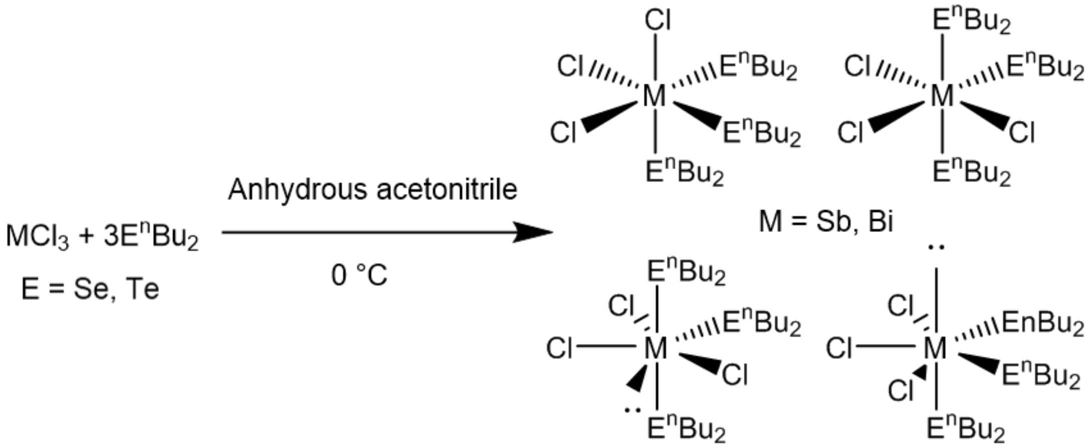

Scheme 2-2: Typical reactions of BiCl$_3$ and SbCl$_3$ with Se$^n$Bu$_2$ and Te$^n$Bu$_2$ ligands and showing possible isomers.

The six-coordinate Bi(III) chloride complexes with neutral selenoether or telluroether ligands, [BiCl$_3$(Se$^n$Bu$_2$)$_3$] and [BiCl$_3$(Te$^n$Bu$_2$)$_3$], were synthesised in good yields as viscous yellow and red oils, respectively, by the reaction of BiCl$_3$ with Se$^n$Bu$_2$ or Te$^n$Bu$_2$ in $CH_3CN$ at room temperature. The change in colour from colourless to yellow or red upon addition of the ligand indicated the rapid association with the metal centre. Samples were manipulated in an $N_2$ purged glove box and were stored at -4 °C. [BiCl$_3$(Se$^n$Bu$_2$)$_3$] was stable at this temperature for at least a year, whereas $[BiCl_3(Te^nBu_2)_3]$ was only stable for 1-2 months.

The six-coordinate Sb(III) analogues were synthesised in good yields as yellow and red liquids, respectively, by the reaction of $SbCl_3$ with $Se^nBu_2$ or $Te^nBu_2$ in $CH_3CN$ or neat at room temperature. These complexes were paler in colour than their Bi analogues. Samples were manipulated in an $N_2$ purged glove box and were stored at -4 °C. $[SbCl_3(Se^nBu_2)_3]$ was stable for months at this temperature whereas the telluroether analogue was stable for only a few days after synthesis.

Characterisation of new precursors by IR spectroscopy, $^1H$, $^{13}C\{^1H\}$, $^{77}Se\{^1H\}$ and $^{125}Te\{^1H\}$ NMR spectroscopy and microanalysis show the data to be in good agreement with the proposed structures and composition, and consistent with a distorted octahedral coordination environment.

IR spectroscopy results in broad bands for the observed Bi-Cl and Sb-Cl stretches. The band at 271 $cm^{-1}$ for $[BiCl_3(Se^nBu_2)_3]$ compares favourably with 248 $cm^{-1}$ reported for the heavier $[BiCl_3(Te^nBu_2)_3]$.[9] These bands, and those at 306 and 294 $cm^{-1}$ for $[SbCl_3(Se^nBu_2)_3]$.and $[SbCl_3(Te^nBu_2)_3]$, respectively, are consistent with literature values of 230 to 280 $cm^{-1}$ for Bi-Cl stretches[44] and 230 to 280 $cm^{-1}$ for Sb-Cl stretches.[45]

The proton NMR spectra, data displayed in Table 2-2, show that the resonances produced from $[SbCl_3(Se^nBu_2)_3]$ and $[SbCl_3(Te^nBu_2)_3]$ are shifted very little from the free ligand with the protons closest to the coordinating chalcogen only shifting to 2.59 from 2.57 ppm and 2.72 from 2.62 ppm for the selenoether and telluroether complexes, respectively. This suggests that the ligands are extensively dissociated in solution. In comparison, the resonances in the spectra of the analogous bismuth chloride complexes show a much greater change in chemical shift. In $[BiCl_3(Se^nBu_2)_3]$ the α-protons show a shift to 3.11 from 2.57 ppm and in $[BiCl_3(Te^nBu_2)_3]$, a shift from 2.62 to 3.24 ppm is observed.

| | δ($CH_3$)/ ppm | δ($CH_2$)/ ppm | δ($CH_2$)/ ppm | δ($CH_2E$)/ ppm |
|---|---|---|---|---|
| $Se^nBu_2$ | 0.93 | 1.41 | 1.65 | 2.57 |
| $[BiCl_3(Se^nBu_2)_3]$ | 0.94 | 1.45 | 1.73 | 3.11 |
| $[SbCl_3(Se^nBu_2)_3]$ | 0.93 | 1.42 | 1.66 | 2.59 |
| $Te^nBu_2$ | 0.90 | 1.37 | 1.71 | 2.62 |
| $[BiCl_3(Te^nBu_2)_3]$ | 0.96 | 1.46 | 1.81 | 3.24 |
| $[SbCl_3(Te^nBu_2)_3]$ | 0.92 | 1.41 | 1.71 | 2.72 |

Table 2-2: $^1$H NMR spectroscopic data for Bi(III) and Sb(III) chloride complexes with selenoether and telluroether ligands and the associated ligands in $CDCl_3$ at room temperature.

The $^{13}C\{^1H\}$ NMR spectra, data portrayed in Table 2-3 below, show a similar trend, with very little change in chemical shift for the Sb(III) halide complexes with chalcogenoether ligands. The resonance for the α-carbons of $[SbCl_3(Te^nBu_2)_3]$ is just 4.28 ppm compared to 2.24 ppm for $Te^nBu_2$, whereas the resonance for the α-carbons of $[BiCl_3(Te^nBu_2)_3]$ is 11.9 ppm, significantly shifted from that of the free ligand. The selenoether complexes show the same trend, but it is not as enhanced.

| | δ($CH_3$)/ ppm | δ($CH_2$)/ ppm | δ($CH_2$)/ ppm | δ($CH_2E$)/ ppm |
|---|---|---|---|---|
| $Se^nBu_2$ | 13.6 | 23.1 | 32.8 | 23.6 |
| $[BiCl_3(Se^nBu_2)_3]$ | 13.6 | 22.9 | 32.4 | 28.4 |
| $[SbCl_3(Se^nBu_2)_3]$ | 13.6 | 23.1 | 32.6 | 24.4 |
| $Te^nBu_2$ | 13.3 | 25.0 | 34.3 | 2.24 |
| $[BiCl_3(Te^nBu_2)_3]$ | 13.5 | 25.1 | 33.6 | 11.9 |
| $[SbCl_3(Te^nBu_2)_3]$ | 13.5 | 25.8 | 34.9 | 4.28 |

Table 2-3: $^{13}C\{^1H\}$ NMR spectroscopic data for Bi(III) and Sb(III) halide complexes with selenoether and telluroether ligands and the associated ligands in $CDCl_3$ at room temperature.

$^{77}Se\{^1H\}$ and $^{125}Te\{^1H\}$ NMR spectra were acquired, as appropriate, for each of the complexes. Data for these are displayed in Table 2-4. Again, the Sb(III) complexes with the chalcogenoether ligands are similar to the 'free ligand'. This may be explained by the relative Lewis acidities of $BiCl_3$ and $SbCl_3$. The latter is the weaker Lewis acid and hence less readily accepts electrons from the donating ligands, consequently the ligands may be more extensively dissociated in solution.

| | δ($^{77}$Se)/ ppm | δ($^{125}$Te)/ ppm |
|---|---|---|
| $Se^nBu_2$ | 167 | |
| $[BiCl_3(Se^nBu_2)_3]$ | 196 | |
| $[SbCl_3(Se^nBu_2)_3]$ | 168 | |
| $Te^nBu_2$ | | 248 |
| $[BiCl_3(Te^nBu_2)_3]$ | | 262 |
| $[SbCl_3(Te^nBu_2)_3]$ | | 237 |

Table 2-4: $^{77}Se\{^1H\}$ and $^{125}Te\{^1H\}$ NMR spectroscopic data for Bi(III) and Sb(III) halide complexes with selenoether and telluroether ligands and the associated ligands in $CH_2Cl_2/CD_2Cl_2$ at room temperature.

Typically, microanalyses were consistent with the proposed structure and composition, however, it was noticed that the ligand was easily removed under low pressure and this led to complexes with less than the desired 3:1 stoichiometry of chalcogen to metal. Consequently, care was required to prevent this when solvent was being removed during synthesis by removing the solvent slowly under a weak vacuum and releasing the vacuum once all solvent had been removed. However, initial LPCVD experiments were undertaken with $[BiCl_3(Se^nBu_2)]$ and $[SbCl_3(Se^nBu_2)_2]$ with the aim of depositing $M_2Se_3$ (M = Sb, Bi) films despite not having the 1:3 ratio of metal to chalcogen.

## 2.2.2 Deposition of $Bi_2Se_3$ Thin Films

Initial experiments involved LPCVD of bismuth selenide using 30 mg of $[BiCl_3(Se^nBu_2)]$. It is important to note that here deposition experiments were carried out using a precursor with only a 1:1 ratio of chalcogen to metal. Depositions were completed using furnace temperatures of 798, 823 and 848 K at 0.1 mm Hg, leading to complete evaporation of the precursor and the deposition of silvery, highly reflective films or dull grey films onto fused $SiO_2$ substrates. Deposition occurred only on the substrate closest to the precursor.

The films were imaged by scanning electron microscopy (SEM). SEM images revealed that at 823 K a flat film had been deposited with crystallites lying flat to the surface as displayed in Figure 2-2. The images show that a very regular triangular crystallite morphology and orientation has been achieved. It is worth mentioning that the area of the film that was imaged was a very thin region and was rougher than the bulk of the film. This was because it was difficult to focus the SEM on the very smooth reflective region of the film. By eye, it could be seen that the material deposited was very reflective, likely as a result of the orientation of the crystallites.

The films deposited at 798 and 848 K appear to be far less consistent. Each film is non-continuous with a sparse coverage of crystallites on the substrate. Furthermore, the orientation of the crystallites is more random, and the morphology of the crystallites very inconsistent.

EDX analysis was also performed on the films to determine the elemental composition. An EDX spectrum for the film deposited at 823 K is shown in Figure 2-2. Quantification of this spectrum led to a ratio of Bi: Se of 48:52. This is closer to the 1:1 ratio of Bi:Se present in the precursor rather than the stoichiometry of the desired $Bi_2Se_3$. This could most likely be improved by using the precursor with higher selenoether incorporation, e.g. $[BiCl_3(Se^nBu_2)_3]$.

The films deposited at 798 and 848 K, analysed by EDX, have a Bi:Se ratio of 43:57, closer to the desired stoichiometry of $Bi_2Se_3$. This difference in stoichiometry suggests that the temperature used for the deposition influences the stoichiometry of the resulting film.

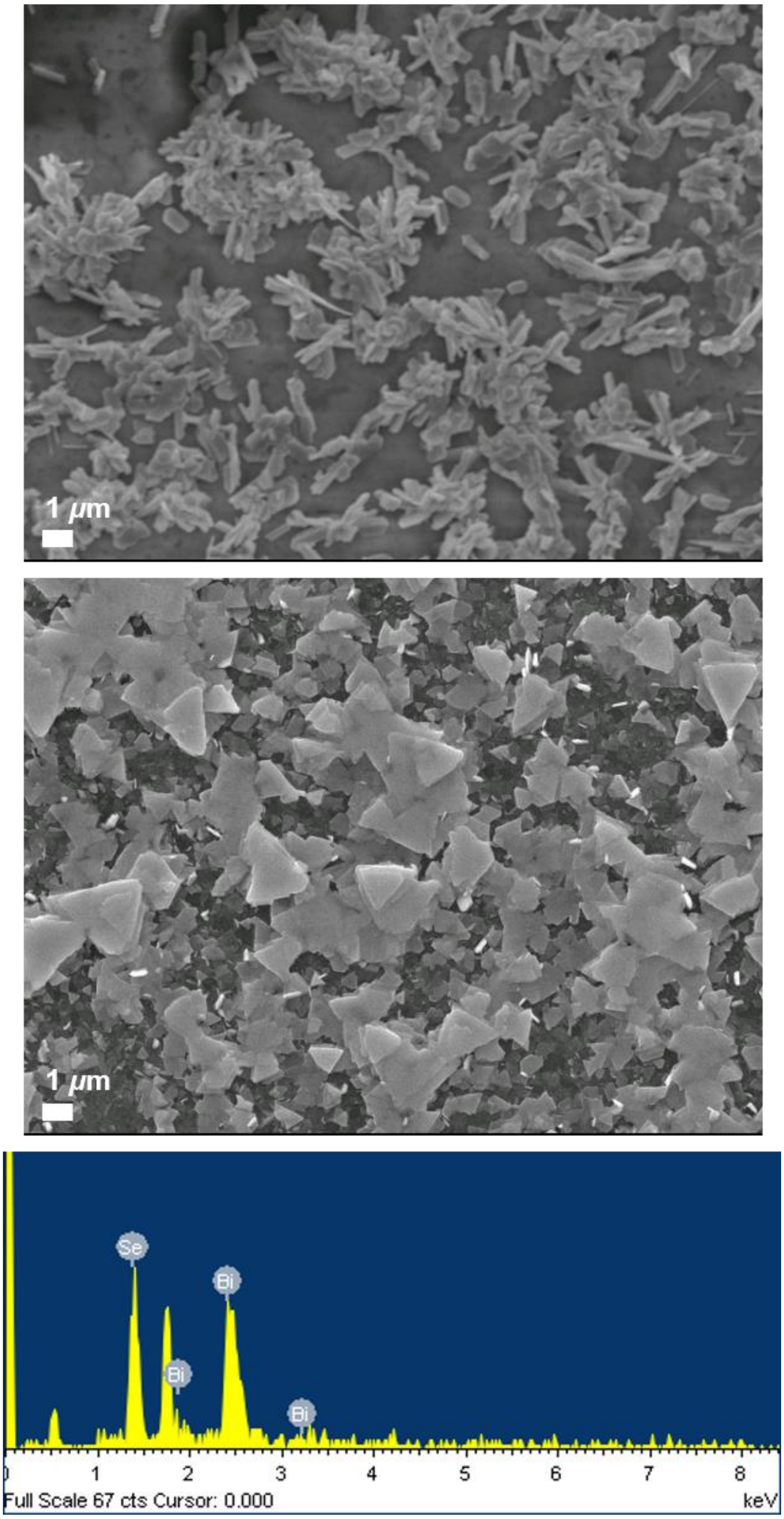

Figure 2-2 SEM images of thin films of $Bi_2Se_3$ deposited from [$BiCl_3$($^nBu_2Se$)] at 798 K (top) and 823 K (middle) at 0.1 mm Hg onto a fused $SiO_2$ substrate. EDX spectrum (bottom) of the film deposited at 823 K.

Grazing incidence X-ray diffraction measurements were performed on the films to identify the crystallographic phases present. XRD patterns are shown in Figure 2-3 (B, C, D). The data show that all films were crystalline $Bi_2Se_3$ with the space group $R\bar{3}mh$, the small amorphous peak is due to the fused $SiO_2$ substrate. The film grown at 823 K shows a high degree of orientation with an enhancement of the (0 0 6) peak. Consequently, an in plane XRD pattern was also acquired for this film in order to observe the other planes and to obtain reliable lattice parameters. This pattern is also shown in Figure 2-3 (A). The enhancement of the (0 0 6) peak is consistent with the c-axis being perpendicular to the substrate and the faces of the crystallites parallel (lying flat) to the substrate.

The films grown at 798 and 823 K showed pure $Bi_2Se_3$, whereas the film deposited at the higher temperature of 848 K(D) shows a slight impurity which is marked with an asterisk. This can be attributed to a more selenium deficient phase, $Bi_{0.755}Se_{0.745}$ (BiSe).[46]

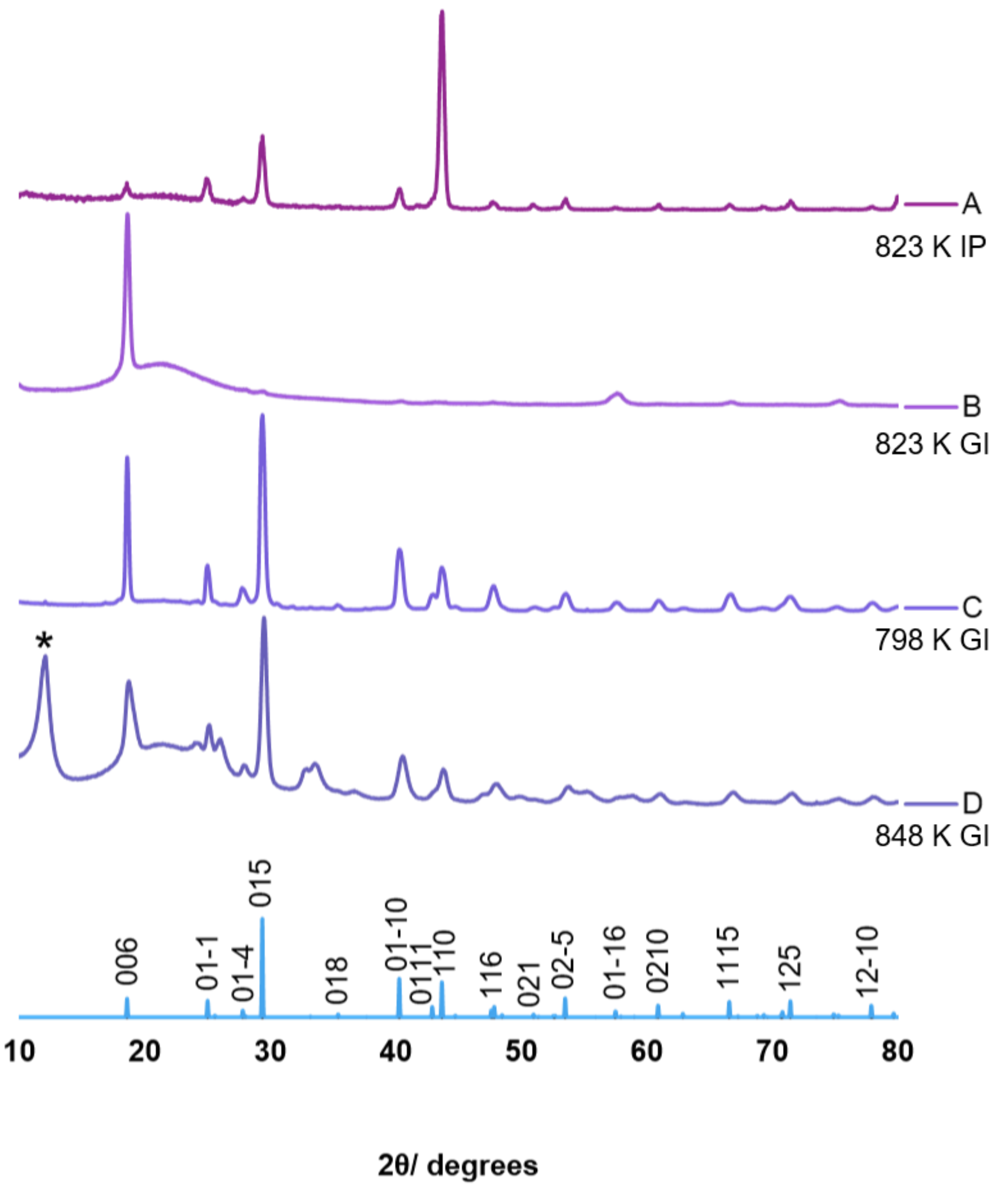

Figure 2-3: In plane (A) and grazing incidence (B) XRD patterns of $Bi_2Se_3$ deposited at 823 K and grazing incidence XRD patterns of $Bi_2Se_3$ films deposited at 798 K (C) and 848 K (D) from $[BiCl_3(Se^nBu_2)]$ and a bulk pattern for $Bi_2Se_3$.[47] The star represents the major reflection of BiSe present in D.

Lattice parameters of, a = 4.143(6) Å and c = 28.61(7) Å and a = 4.145(2) Å and c = 28.63(3) Å, for the films deposited at 798 K and 823 K, respectively, match well with the values reported in the literature of 4.143 and 28.638.[47] These were calculated by optimisation of the fit in PDXL2.

Pole figure measurements were also acquired for the key reflections in the film grown at 823 K in order to further investigate the preferred orientation observed. These are displayed in Figure 2-4. For the (0 0 6) reflection, a sharp maximum can be observed at α = 90 °. This means that the tilt angle of the normal of the plane does not diverge far from 90 ° which suggests that the c-axis of the crystallites is orientated perpendicular to the substrate and the a and b-axis of the crystallites lie parallel. This results in a very smooth, and consequently highly reflective, thin film. The narrow peak width at α = 90 ° and small spot size in the pole figure projections demonstrate the strong alignment and high degree of orientation of the crystallites. For the (0 1 -1) reflection there is a ring at ~α = -7 ° (calculated values for α in this case are 90.0 ° for (0 0 6) and 7.1 ° for (0 1 -1) (tan α = *a*cos30/*c*)). This is uneven due to the measurement on a small sample size. It is, however, consistent with the c-axis being at 90 ° to the substrate.

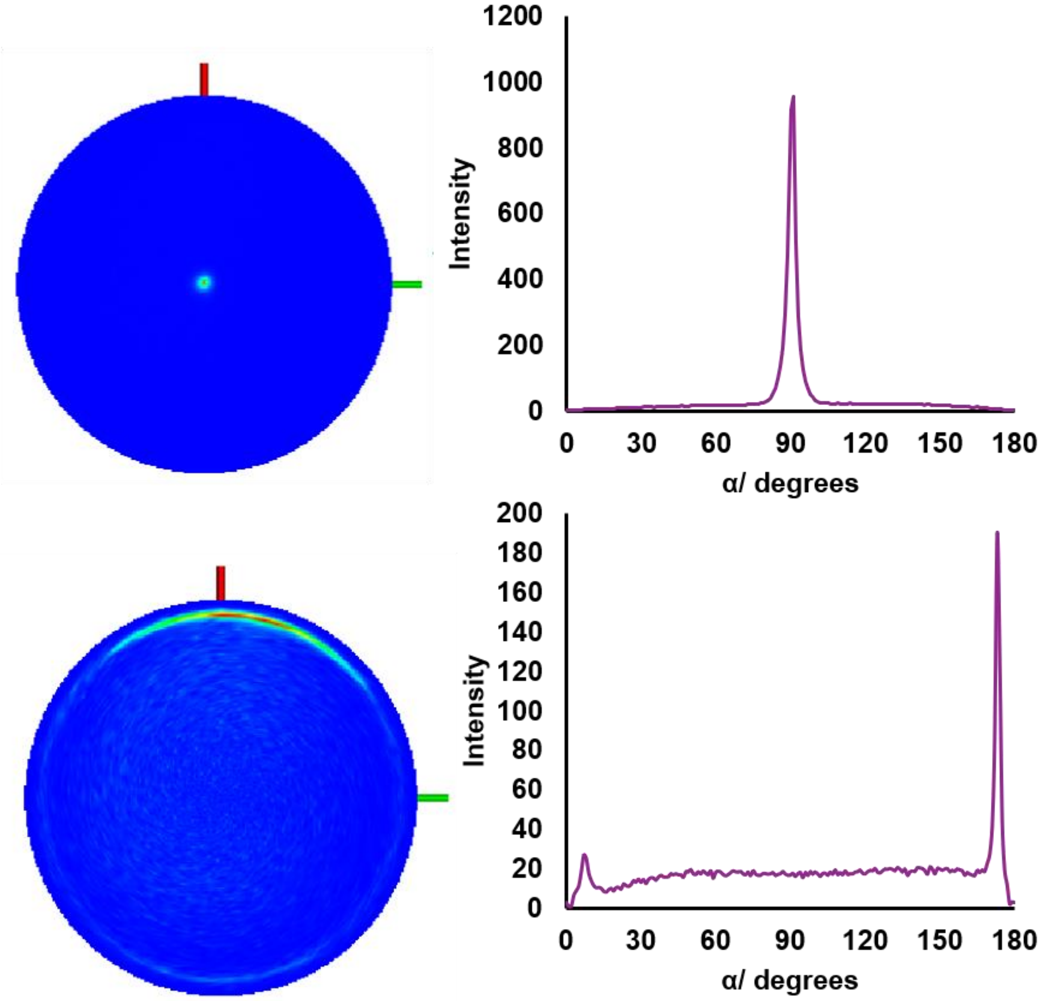

Figure 2-4: 3D pole figure projections with α integrals of the $Bi_2Se_3$ thin film deposited at 823 K, showing the (0 0 6) plane (top) and (0 1 -1) plane (bottom) where α is the tilt angle from the sample surface normal direction Note: the cut lines for the (0 1 -1) plane are uneven due to a small sample area taken.

Later depositions onto fused $SiO_2$ used 50 mg [$BiCl_3(Se^nBu_2)_3$] with a furnace temperature of 823 K and pressure of 0.1 mm Hg. Using a precursor with a 1:3 ratio of metal to chalcogen should ensure that in $M_2E_3$ films, there is not a chalcogen deficiency. Films deposited were typically dull silver/ grey in appearance and lacking the high reflectivity seen in the previous example. Grazing incidence XRD (Figure 2-5) revealed that the material deposited was $Bi_2Se_3$ with space group $R\bar{3}mh$. No strong orientation of the crystallites was inferred by the diffraction pattern. Lattice parameters of a = 4.092(14) Å and c = 28.59 (11) Å match well with the bulk.[47] These were calculated by optimisation of the fit in PDXL2.

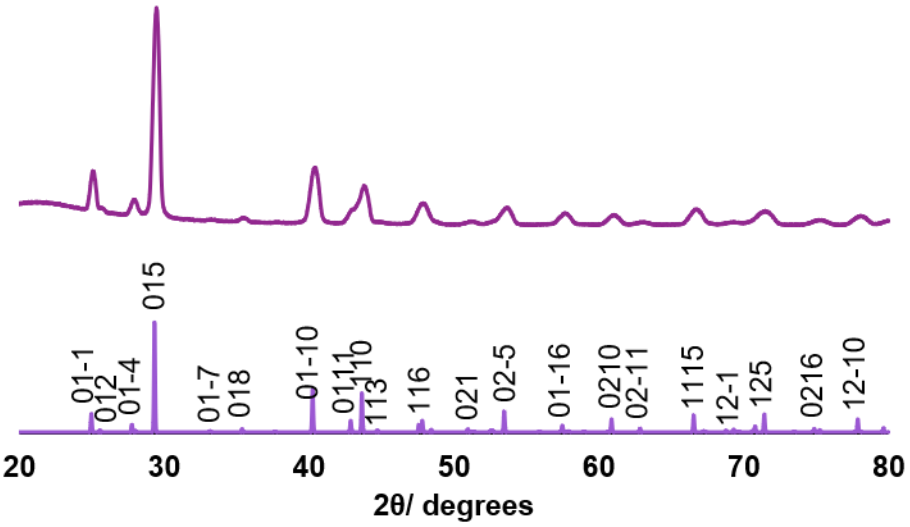

Figure 2-5: Grazing incidence XRD pattern for $Bi_2Se_3$ deposited from [$BiCl_3(Se^nBu_2)_3$] at 823 K onto fused $SiO_2$ and an indexed bulk pattern of $Bi_2Se_3$.[47]

SEM analysis revealed the random orientation of hexagonal crystallites (Figure 2-6). The film also appears to be rougher and not completely continuous. Which is in contrast to the very smooth film grown at the same temperature of 823 K from [$BiCl_3(Se^nBu_2)$]. The elemental composition was probed by EDX analysis, a spectrum is shown in Figure 2-6. Quantification of this EDX spectrum shows a ratio of bismuth to selenium of 42:58 % which is within experimental error of the desired 40:60 stoichiometry of a $M_2E_3$ film. Given the thinness of the deposited material, the error in the EDX will be larger than that for a bulk material due to a large substrate to film ratio. This shows the improvement of using [$BiCl_3(Se^nBu_2)_3$] over [$BiCl_3(Se^nBu_2)$] which previously resulted in a selenium deficient film. No residual chloride was apparent from the EDX spectrum (2.6 keV).

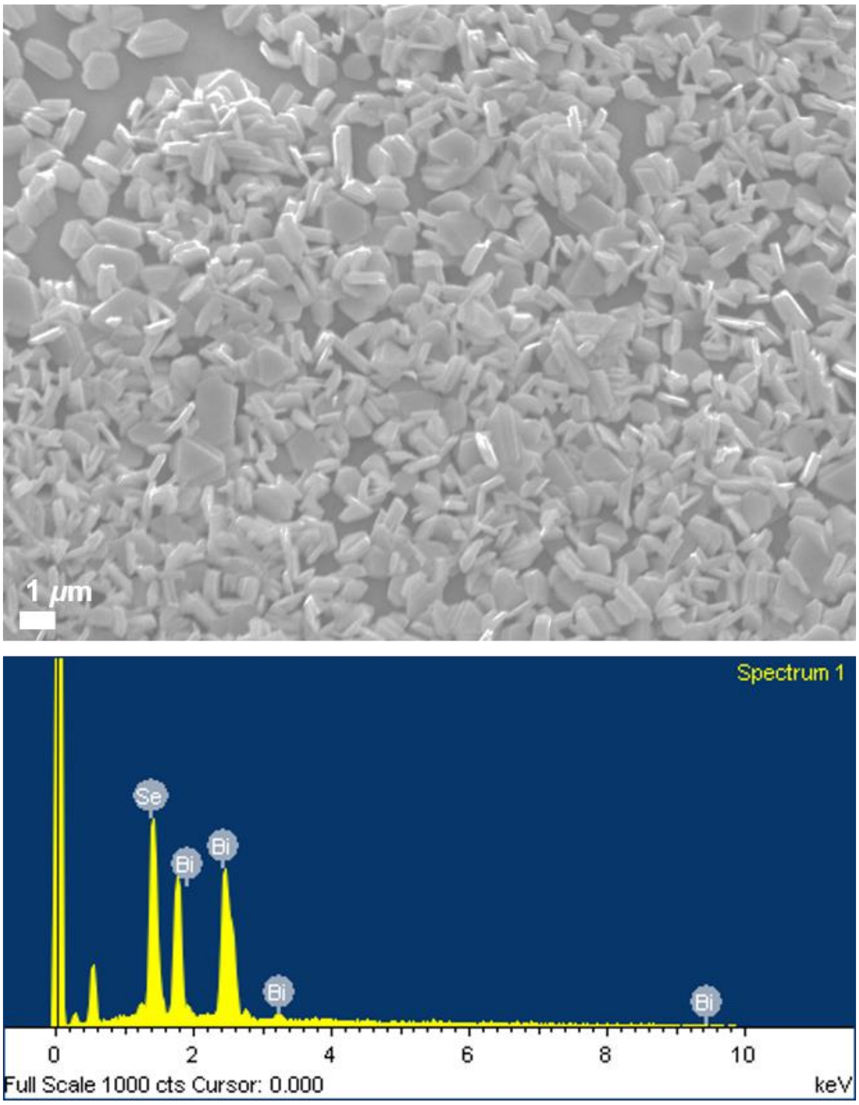

Figure 2-6: SEM image (top) and EDX spectrum (bottom) of $Bi_2Se_3$ thin film deposited from $[BiCl_3(Se^nBu_2)_3]$ at 823 K onto fused $SiO_2$. The peaks at 0.5 and 1.7 keV are due to the O and Si from the substrate.

Raman analysis shows two intense peaks at 130 and 172 $cm^{-1}$. These can be assigned as the $E^2_g$ (in plane) and the $A^2_{1g}$ (out of plane) vibrational modes respectively and are consistent with values reported in the literature.[48]

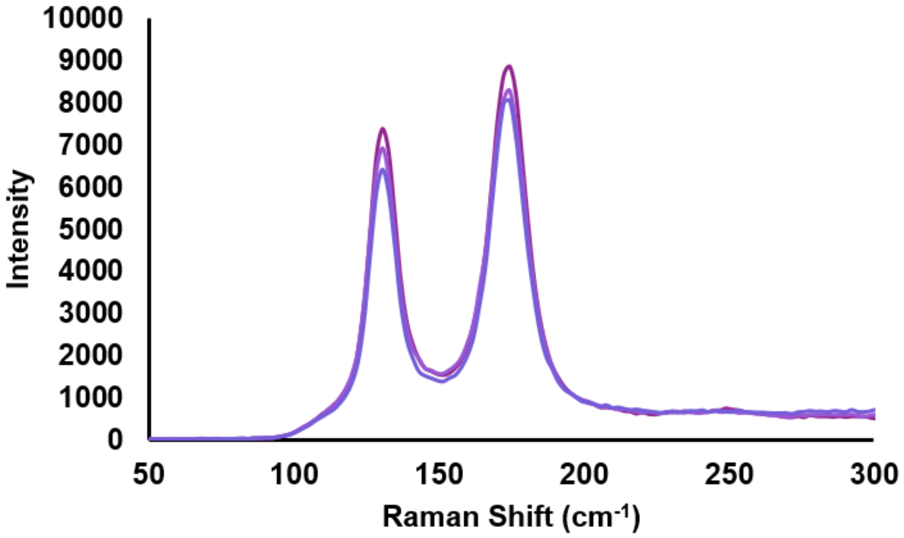

Figure 2-7: Raman spectra recorded from different regions of a $Bi_2Se_3$ film deposited from [$BiCl_3(Se^nBu_2)_3$] at 823 K onto fused $SiO_2$.

.

### 2.2.3 Deposition of $Sb_2Se_3$ Thin Films

Initial experiments involved LPCVD of $Sb_2Se_3$ using 30 mg of [$SbCl_3(Se^nBu_2)_2$]. It is important to note that here deposition experiments were carried out using a precursor with only a 1:2 ratio of metal to chalcogen, however this ratio is still selenium rich in comparison to the desired 1:1.5 ratio in a $M_2E_3$ film. Depositions were completed using furnace temperatures of 798, 823 and 848 K at 0.1 mm Hg. Subsequent depositions were completed using [$SbCl_3(Se^nBu_2)_3$] at 823 K. These experiments led to complete evaporation of the precursor and the deposition of silvery grey dull films onto fused (amorphous) $SiO_2$ substrates. Films were not well adhered to the substrate. Deposition occurred only on the substrate closest to the precursor in all experiments.

The films were imaged by SEM (Figure 2-8). This revealed a random orientation of nanorod like crystallites. At the lower temperature of 798 K, the crystallites appear to be more needle like in appearance. The deposition onto PVD (crystalline) $SiO_2$ shows the crystallites to be less uniform in shape than those deposited onto fused $SiO_2$.

Quantitative EDX analysis showed that all films had a stoichiometry very close to that of the 40:60 Sb:Se with the films deposited onto fused $SiO_2$ from [$SbCl_3(Se^nBu_2)_2$] at 798 K and 823 K having an Sb:Se ratio of 40:60 and 42:58 respectively and the film deposited onto PVD $SiO_2$ from [$SbCl_3(Se^nBu_2)_2$] at 823 K 41:59. This shows that the difference in precursor had little effect, as both were selenium rich and selenium is relatively volatile and so is easily removed under low pressure resulting in the desired stoichiometry in each case. A typical EDX spectrum is shown in Figure 2-9. Large peaks from the $SiO_2$ substrate can be seen (0.5 (O) and 1.7 (Si) keV) which shows that the films are very thin and therefore a large degree of error (typically 5 % for a film)[49] on the quantitative values.

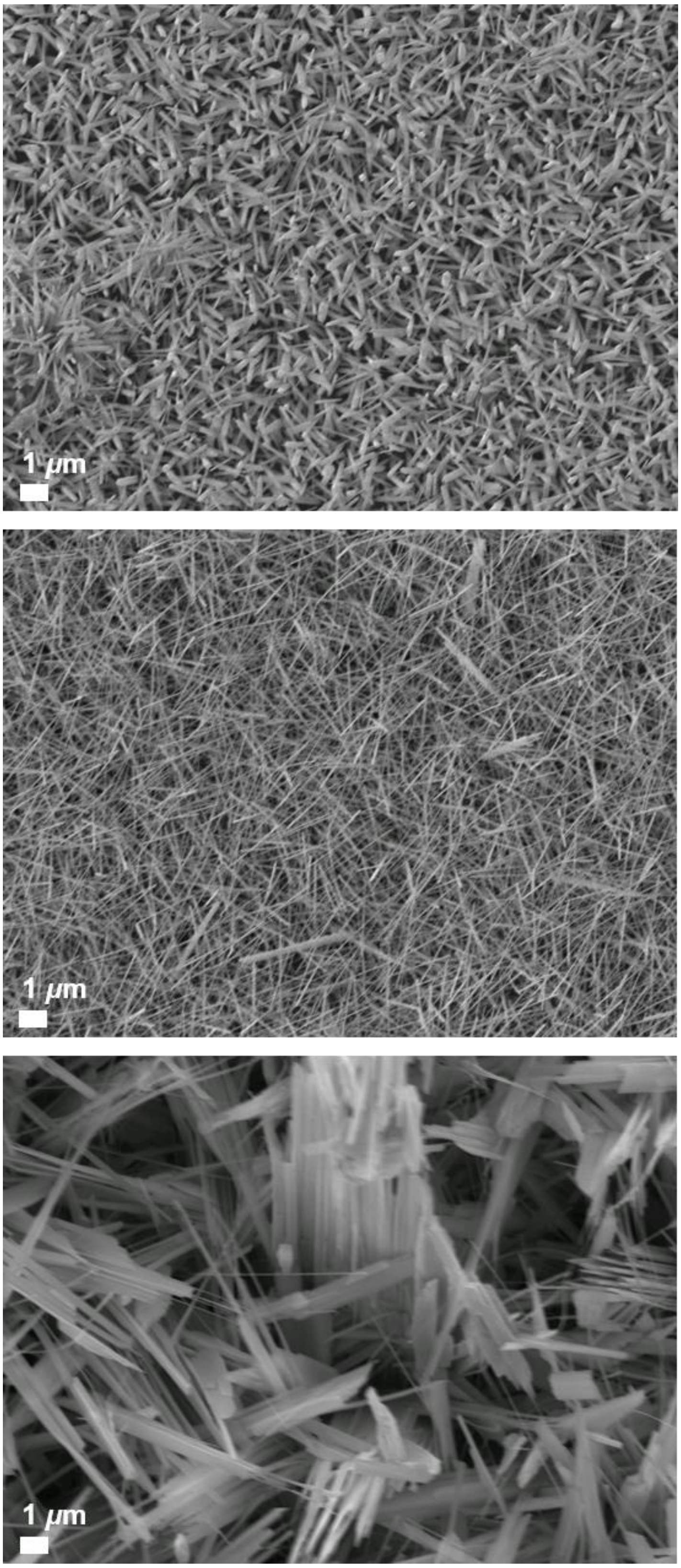

Figure 2-8: SEM images of an $Sb_2Se_3$ film deposited from $[SbCl_3(Se^nBu_2)_x]$ at 823 K onto fused $SiO_2$ (top, x= 2) and at 798 K onto fused $SiO_2$ (middle, x=2) and at 823 K onto PVD (crystalline) $SiO_2$ (bottom, x = 3).

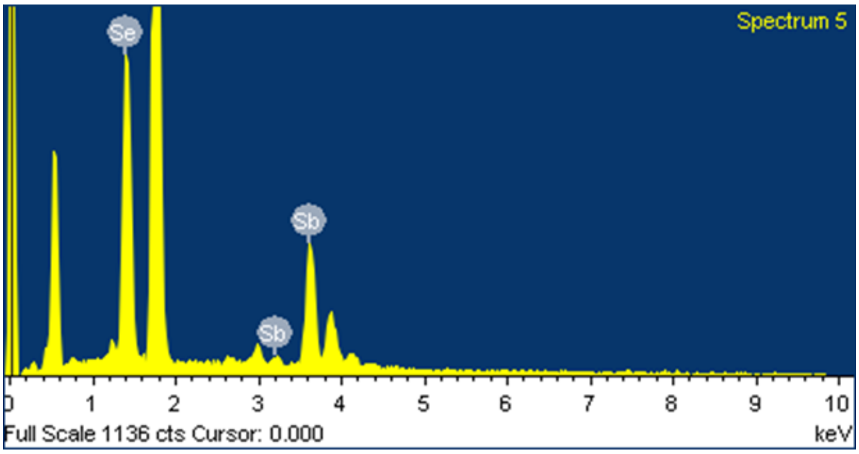

Figure 2-9: An EDX spectrum of an $Sb_2Se_3$ film deposited at 823 K from $[SbCl_3(Se^nBu_2)_3]$ onto PVD $SiO_2$. Peaks at 0.5 and 1.7 keV are from the O and Si in the substrate.

Cross sectional SEM showed that the $Sb_2Se_3$ film deposited from $[SbCl_3(Se^nBu_2)_3]$ at 823 K was quite thick, measuring approximately 20 µm in places as shown in Figure 2-10 below.

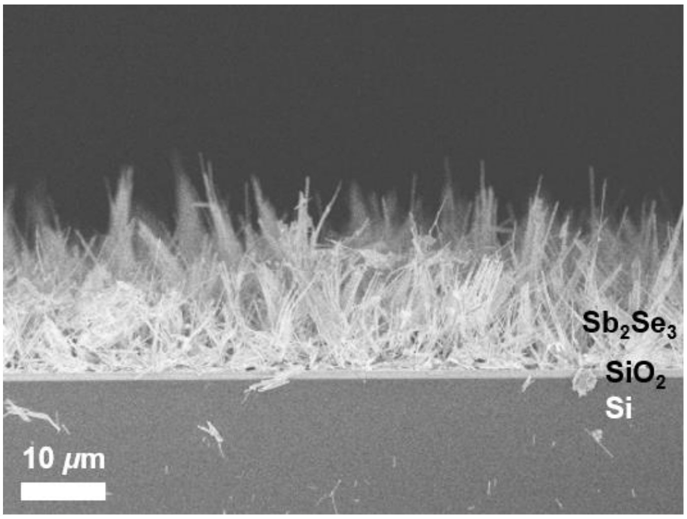

Figure 2-10: Cross sectional SEM image of $Sb_2Se_3$ film deposited from $[SbCl_3(Se^nBu_2)_3]$ at 823 K onto PVD $SiO_2$.

Grazing incidence XRD (Figure 2-11) showed all the films to match well to the literature pattern for Pbmn $Sb_2Se_3$.[50] A small impurity is present at ~ 30 ° (X) in the film deposited onto PVD $SiO_2$. Depositions attempted at higher temperatures led to an increase in this peak. This is because selenium is volatile enough to be lost under low pressure at higher temperatures. Looking back to the EDX data, both films deposited at 823 K are fractionally selenium deficient and consequently it can be said that the lower temperature of 798 K is best suited to the deposition of $Sb_2Se_3$.

The lattice parameters, displayed in Table 2-5, are all consistent with those of bulk $Sb_2Se_3$ (a = 11.62(1) Å, b = 11.77(1) Å and c = 3.962(7))[50] and $Sb_2Se_3$ deposited via LPCVD from $MeSb(Se^nBu_2)_2$ onto fused $SiO_2$ (a = 11.610(7) Å, b = 11.756(7) Å and c = 3.969(2) Å)[10] but those that match most closely are from the film deposited from $[SbCl_3(Se^nBu_2)_2]$ at 798 K onto fused $SiO_2$. This again, suggests that these conditions are most suited to the deposition of $Sb_2Se_3$ using this precursor type. These lattice parameters were calculated by optimisation of the fit in PDXL2.

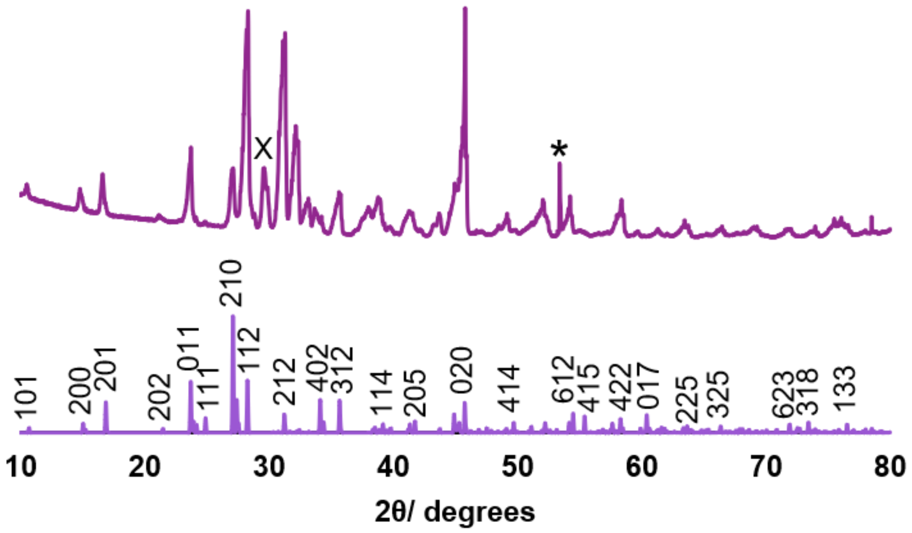

Figure 2-11: GIXRD pattern of an $Sb_2Se_3$ film deposited from $[SbCl_3(Se^nBu_2)_3]$ at 823 K onto PVD $SiO_2$ with an indexed bulk pattern for $Sb_2Se_3$.[50] The reflection marked with an asterisk is due to the Si in the substrate, X marks an unknown impurity.

| Deposition | a/ Å | b/ Å | c/ Å |
|---|---|---|---|
| PVD $SiO_2$, 823 K | 11.81(3) | 11.73(6) | 3.958(8) |
| Fused $SiO_2$, 823 K | 11.80(4) | 11.58(4) | 3.986(12) |
| Fused $SiO_2$, 798 K | 11.64(2) | 11.81(3) | 3.989(12) |

Table 2-5: Refined lattice parameters for the as-deposited $Sb_2Se_3$.

Raman spectra were acquired on the same thin film samples. In all cases, the spectra appeared a little noisy which was attributed to the thinness of the films. Peaks were present at 125, 150 and 190 cm$^{-1}$ which represent the $E^2_g$, $A^2_{2u}$ and $A^1_g$ modes respectively. The $E^2_g$ mode relates to the Se-Se bonds, the $A^2_{2u}$ to the vibration of Sb-Sb bonds and the $A^1_g$ mode represents Sb–Se stretching mode of the $SbSe_{3/2}$-pyramids.[10,51–53] Typical Raman spectra of these films are shown in Figure 2-12 below. The shoulder present at ~215 cm$^{-1}$ can be attributed to a second order Raman mode, a combination of two $E^2_g$ modes.[52]

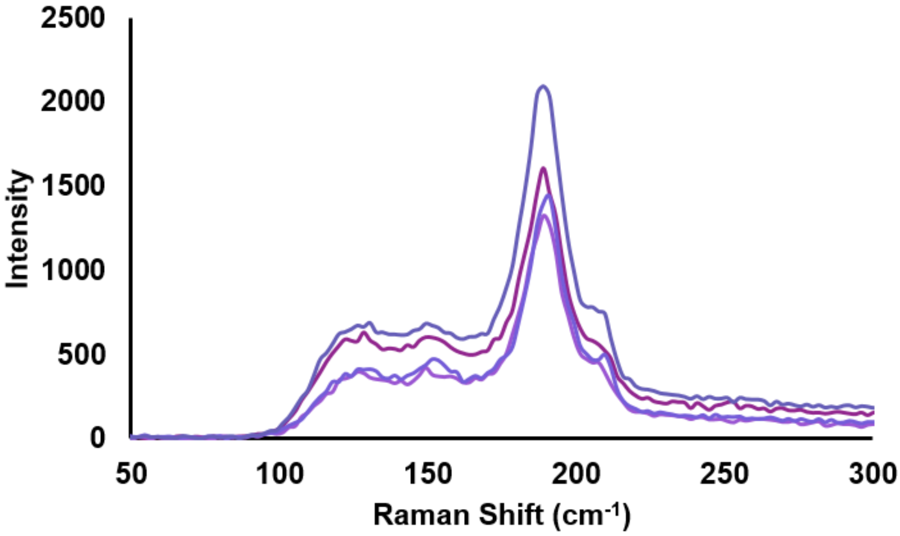

Figure 2-12: Raman spectra recorded from different regions of an $Sb_2Se_3$ film deposited at 823 K from $[SbCl_3(^nBu_2Se)_3]$ onto PVD $SiO_2$

### 2.2.4 Depositions of $Sb_2Te_3$ Thin Films

Initial LPCVD experiments took place using 30-50 mg of $[SbCl_3(Te^nBu_2)_3]$ at 723 K and 773 K onto PVD $SiO_2$ with the precursor positioned about 2 cm from the hot zone and gradually moved closer until evaporation was observed. In all cases this resulted in the deposition of $Sb_2Te_3$ and crystalline tellurium. It appeared that under the low pressure and high temperature the ligand was being distilled from the precursor across the CVD tube and hence depositing crystalline tellurium. In the case of the selenoether analogues discussed previously, this would not be an issue as selenium itself is volatile and hence easily removed under low pressure.

Adaptation of the method led to the tube being repositioned such that the precursor was moved quickly to the edge of the hot zone once the target temperature had been reached. This allowed for ‘flash evaporation’ of the precursor and prevented ligand being distilled from the precursor, allowing films to be produced without co-deposition of crystalline tellurium. It is worth noting, however, that $Sb_2Te_3$ was clean on the first substrate, but on subsequent substrates further into the furnace, some crystalline tellurium was also detected. This is likely to be a result of the nature of the precursor. There is a 1:3 ratio of antimony to tellurium in the precursor, but only a 1:1.5 ratio is desired in the resulting film. Consequently, the precursor is tellurium-rich, and this excess tellurium is not volatile enough to be removed under low pressure at these temperatures. At 723 K the tiny crystallites of $Sb_2Te_3$ deposited are very scattered and no continuous film is produced. Increasing the temperature to 773 K to increase nucleation led to much better coverage and continuous films of $Sb_2Te_3$ being produced.

Analysis of these films by SEM (Figure 2-13) showed regular hexagonal crystallites. In the case of the films contaminated with tellurium, large rods of crystalline tellurium can be seen amongst the hexagons of $Sb_2Te_3$. The film produced at 723 K shows the crystallites to be just ~100 nm in diameter. In comparison, those grown at 773 K are much larger at ~1 µm across. This film was also shown to be continuous and the crystallites regular in size and shape. In comparison to the $Sb_2Te_3$ deposited from $MeSb(Te^nBu_2)_2$,[10] the film deposited here was rather more randomly orientated with some crystallites flat and some perpendicular This shows that perhaps the precursor derived from $SbCl_3$ has less control over orientation of the crystallites than the tellurolate-based precursor.

The elemental composition of the continuous film of $Sb_2Te_3$ produced was probed by EDX spectroscopy. The spectrum is displayed in Figure 2-14. Quantification of this spectrum revealed an Sb:Te ratio of 38:62 so the film is tellurium rich despite there being no evidence for crystalline tellurium being present. However, there is some degree of error, normally ± 5 %.[49] Features from the substrate are present in the EDX spectrum meaning the film is thin. Furthermore, the peaks from antimony and tellurium overlap. The spectrum shows no residual chloride, but a small carbon peak was visible, most likely due to surface contamination.

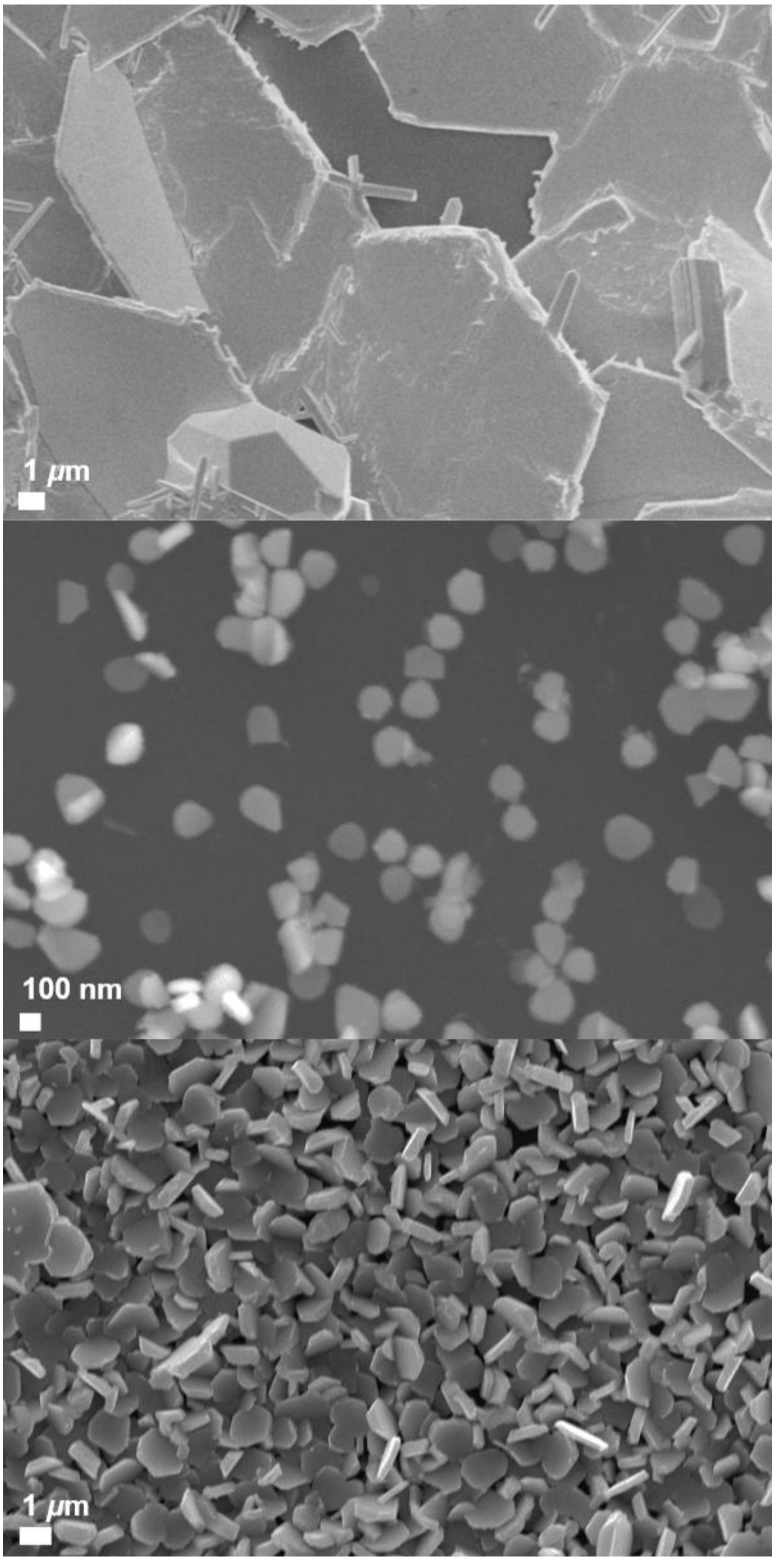

Figure 2-13: SEM images of $Sb_2Te_3$ films deposited from $[SbCl_3(Te^nBu_2)_3]$ at 723 K (top and middle) and at 773 K (bottom) onto PVD $SiO_2$. In the latter images, the precursor has been evaporated quickly to avoid Te contamination.

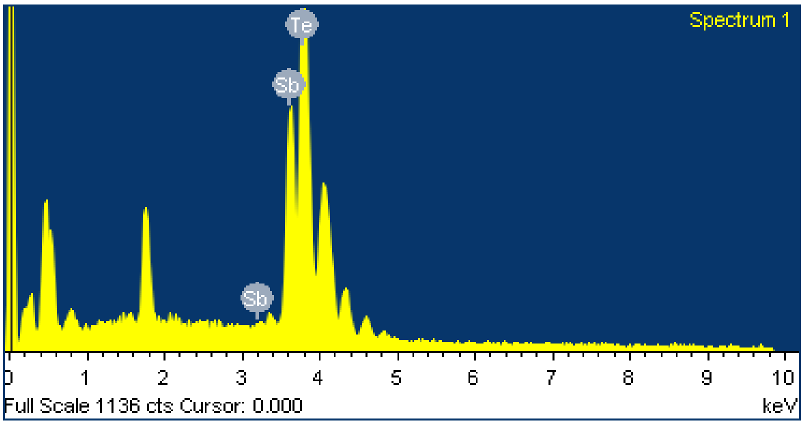

Figure 2-14: An EDX spectrum of $Sb_2Te_3$ deposited form [$SbCl_3(Te^nBu_2)_3$] at 773 K onto PVD $SiO_2$. Quantification of the spectrum leads to a Sb:Te ratio of 38:62 being obtained. The peaks at 0.5 and 1.7 keV are due to O and Si in the substrate. The peaks at 4.2

Cross sectional SEM shows that the film deposited is less than 1 µm thick, as shown in Figure 2-15 below.

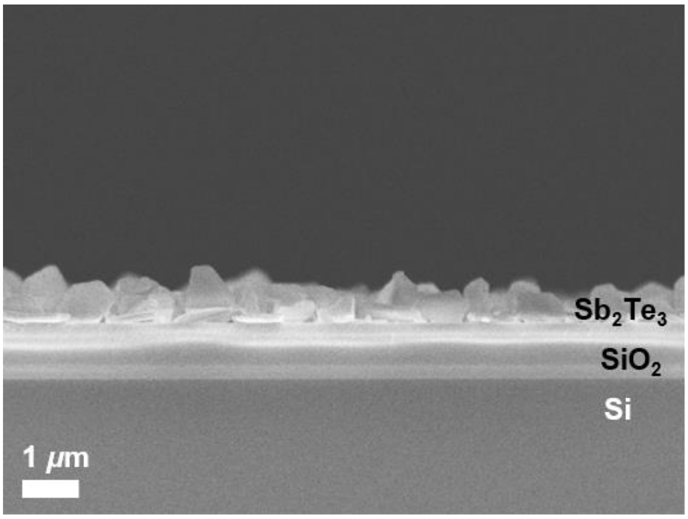

Figure 2-15: Cross sectional SEM image of an $Sb_2Te_3$ film deposited from [$SbCl_3(Te^nBu_2)_3$] at 773 K onto PVD $SiO_2$.

Grazing incidence XRD is consistent with an R-3mh $Sb_2Te_3$ film with no evidence of crystalline tellurium. Refined lattice parameters of a = 4.254(3) Å and c = 30.36(2) Å are close to the values reported for $Sb_2Te_3$ deposited by LPCVD from $MeSb(Te^nBu_2)_2$ onto PVD $SiO_2$ (a = 4.2492(3) Å and c = 30.374(2) Å)[10] and those for bulk $Sb_2Te_3$ (a = 4.264(1) Å and c = 30.458(7) Å).[54] These were calculated by optimisation of the fit in PDXL2. The XRD pattern, shown in Figure 2-16 below has the key reflections indexed. It shows no sign of preferred orientation.

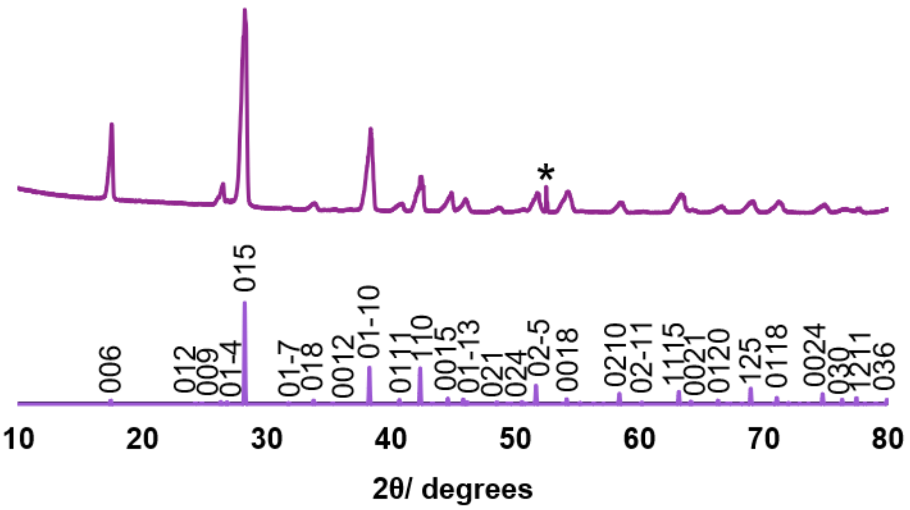

Figure 2-16: Grazing incidence XRD pattern for a $Sb_2Te_3$ film deposited from $[SbCl_3(Te^nBu_2)_3]$ at 773 K onto PVD $SiO_2$ with an indexed bulk pattern.[54] The reflection marked with an asterisk is due to the Si in the substrate.

The Raman spectrum (Figure 2-17) of the film shows peaks at 120, 140 and 165 $cm^{-1}$. This is consistent with films deposited from $MeSb(Te^nBu_2)_2$ via LPCVD.[10] The peak at 120 $cm^{-1}$ is attributed to the $E_{2g}$ vibrational mode, 140 $cm^{-1}$ to the $A_{2u}$ vibrational mode and 165 $cm^{-1}$ to the $A_{1g}$ vibrational mode.[55] This confirms that the film is $Sb_2Te_3$.

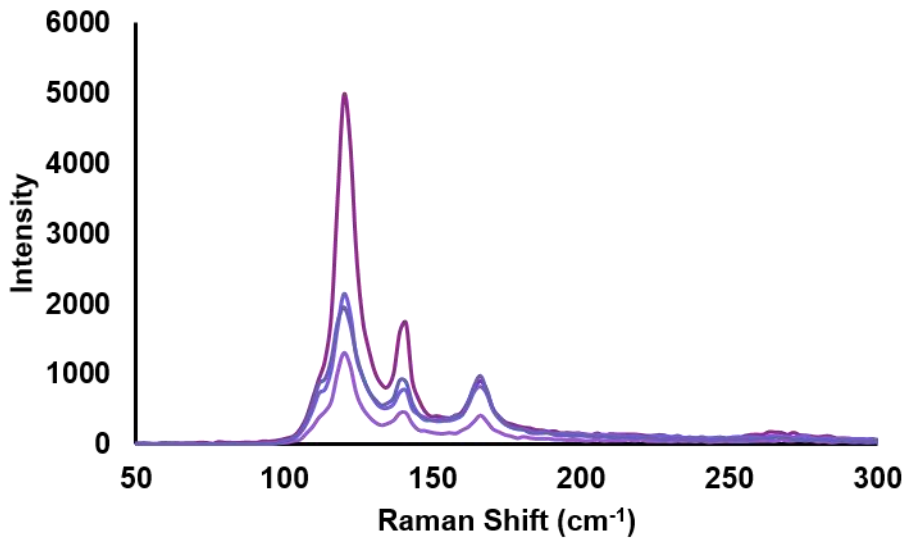

Figure 2-17:Raman spectra of different regions of an $Sb_2Te_3$ film deposited at 773 K from [$SbCl_3(Te^nBu_2)_3$] onto PVD $SiO_2$

### 2.2.5 Selective Deposition of $Bi_2Se_3$ and $Sb_2Te_3$ onto TiN/$SiO_2$

Previously, it was demonstrated that materials such as $SnSe_2$,[56] can be selectively deposited onto PVD TiN over PVD $SiO_2$. This is attributed to the high hydrophobicity and conductivity of the TiN. It is also thought that the lower the resistivity of the material being deposited the more likely that the material can be selectively deposited.[37] This phenomenon has also been demonstrated in the chemical vapour deposition of $Bi_2Te_3$ from [$BiCl_3(Te^nBu_2)_3$],[9] $TiSe_2$ from [$TiCl_4(Se^nBu_2)_2$],[57] and $Sb_2Te_3$ from [$MeSb(Te^nBu_2)_2$].[10,37] In all cases the resistivity of the deposited material was very low ($Bi_2Te_3$: $(5.6 \pm 0.1) \times 10^{-4}$ Ωcm, $TiSe_2$: $(3.4 \pm 0.1) \times 10^{-3}$ Ωcm, and $Sb_2Te_3$: $(9.9 \pm 0.8) \times 10^{-4}$ Ωcm).[37] It is useful to be able to deposit selectively in the fabrication of semiconductor devices and this is a feature of single source precursor LPCVD which gives it an advantage over other deposition techniques (except electrodeposition).

The precursor systems used here are similar to that of the [$BiCl_3(Te^nBu_2)_3$] mentioned above. $Sb_2Te_3$ has been selectively deposited from [$MeSb(Te^nBu_2)_2$] previously.[10,37] This work involved the use of lithographically patterned substrates as shown in Figure 2-18. Consequently, the selective deposition of $Sb_2Te_3$ has been attempted using [$SbCl_3(Te^nBu_2)_3$]. Initial depositions used ~5 mg of precursor, patterned $SiO_2$/ TiN substrates and a temperature of 723 K and 0.02 mm Hg. The substrates were $SiO_2$

surfaces with photolithographically etched TiN wells. Experiments led to complete evaporation of the precursor and uneven deposition across the substrates.

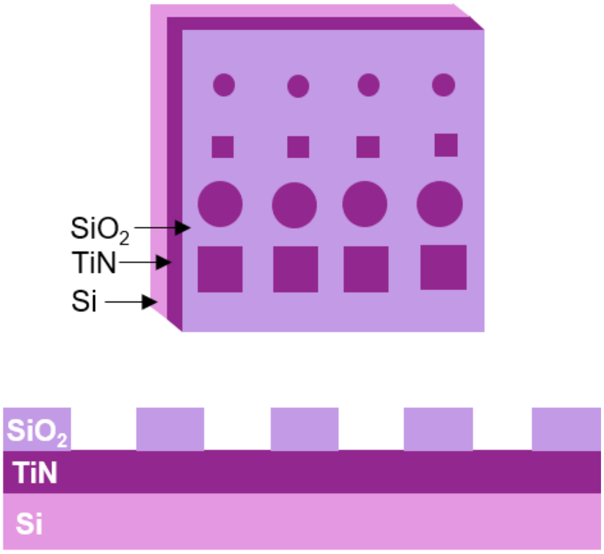

Figure 2-18: Illustrations of a lithographically patterned TiN/$SiO_2$ substrate. On a typical patterned substrate TiN wells ranged from 10 µm to 100 µm.

SEM images of the thinner region of the film revealed that $Sb_2Te_3$ was selectively deposited into the 10 µm diameter TiN wells. This can be seen in Figure 2-19. It shows a high degree of selectivity can be obtained with very few crystallites deposited outside of the TiN wells. Quantitative EDX analysis revealed both Sb and Te to be present with a ratio of 41:59. The features from the substrate dominate the spectrum, due to the small quantity of deposited $Sb_2Te_3$. Errors in EDX for a thin film are typically ± 5 %,[49] and for these small areas it is likely to be much higher.

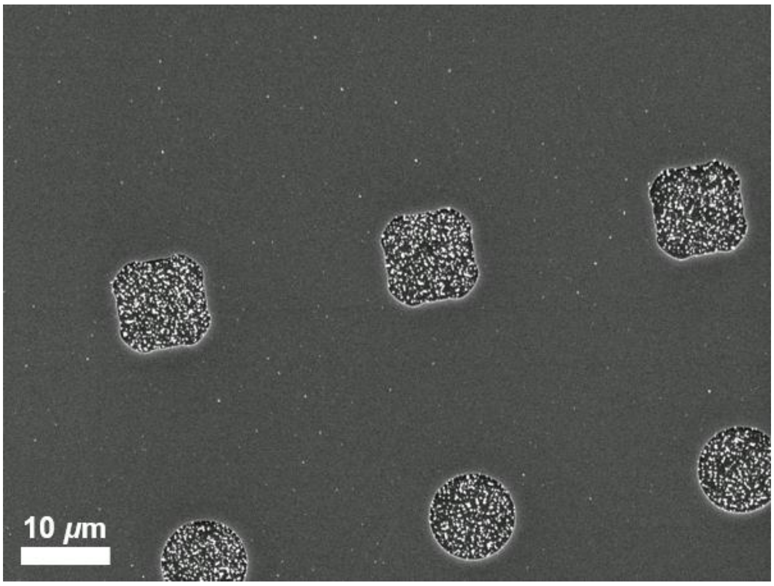

Figure 2-19: SEM image of $Sb_2Te_3$ deposited from $[SbCl_3(^nBu_2Te)_3]$ into 10 μm TiN holes.

Grazing incidence XRD (Figure 2-20) shows that $R\bar{3}mh$ $Sb_2Te_3$ has been deposited and no crystalline tellurium is present. As with the EDX spectrum, the XRD pattern is dominated by reflections from the TiN substrate due to the small amount of material that has been deposited.

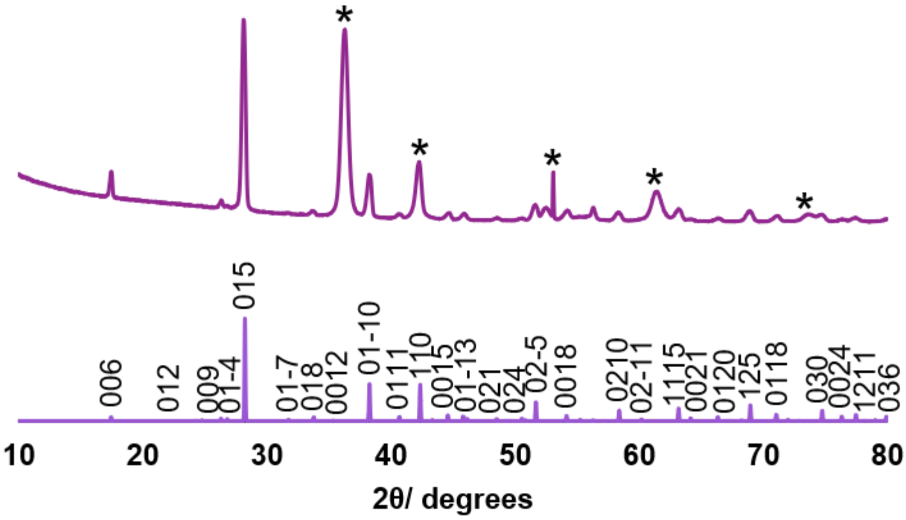

Figure 2-20: XRD pattern for $Sb_2Te_3$ deposited into TiN holes and an indexed bulk pattern of $Sb_2Te_3$.[54] The substrate peaks are indicated with an asterisk, the sharp peak at ~52° is due to the Si in the substrate and the rest due to TiN.

Selective depositions were also attempted with [$BiCl_3(Se^nBu_2)_3$] using the same deposition conditions as with [$SbCl_3(Te^nBu_2)_3$] analogue. This was less successful than for the $Sb_2Te_3$ and the SEM showed that few crystallites were deposited in the TiN wells. Where there was more coverage of the TiN, there were also more $Bi_2Se_3$ crystallites deposited on the PVD $SiO_2$. $Bi_2Se_3$ shows a low resistivity of $1.82 – 9.85 \times 10^{-3}$ $\Omega cm^4$ which suggests that further optimisation of the deposition conditions is required.

EDX analysis was not acquired due to the extremely low quantity of material deposited which would have led to unreliable data. Grazing incidence XRD was dominated by peaks from the substrate. A number of the peaks from $Bi_2Se_3$ could be identified and indexed, interestingly, the (0 2 7) reflection is much intensified in comparison with that of the bulk suggesting a high degree of orientation.

### 2.2.6 Ternary Depositions using [$SbCl_3(Te^nBu_2)_3$]/[$BiCl_3(Te^nBu)_3$]

Previous work within the group at the University of Southampton, has shown that by varying the quantity of [$BiCl_3(Te^nBu_2)_3$] and [$BiCl_3(Se^nBu_2)_3$] used in an experiment a range of compositions of ternary $Bi_2(Te_xSe_{1-x})_3$ could be deposited. Electrical measurements showed that these materials were n-type semiconductors. A thermoelectric device requires both n and p-type elements to function. The ability to tune the properties of each component through controlling the composition of the material deposited would allow the creation of a fully optimised device.

It was therefore proposed that using the chemically compatible [$BiCl_3(Te^nBu_2)_3$] and [$SbCl_3(Te^nBu_2)_3$] precursors together should allow for the deposition of the ternary phase, $(Sb_xBi_{1-x})_2Te_3$, in an analogous way to that described above. To ascertain the compatibility of the two precursors, a range of ratios were analysed by $^{125}Te$ NMR spectroscopy (Figure 2-21). The two precursors were dissolved in $CH_2Cl_2$ and $CD_2Cl_2$ added. In all cases, just one Te resonance is present. This shows that the ligands are labile and freely exchanging between the two metal centres. A gradual change in chemical shift was observed, with increasing Bi content, from 237 ppm for pure [$SbCl_3(Te^nBu_2)_3$] to 262 ppm for pure [$BiCl_3(Te^nBu_2)_3$].

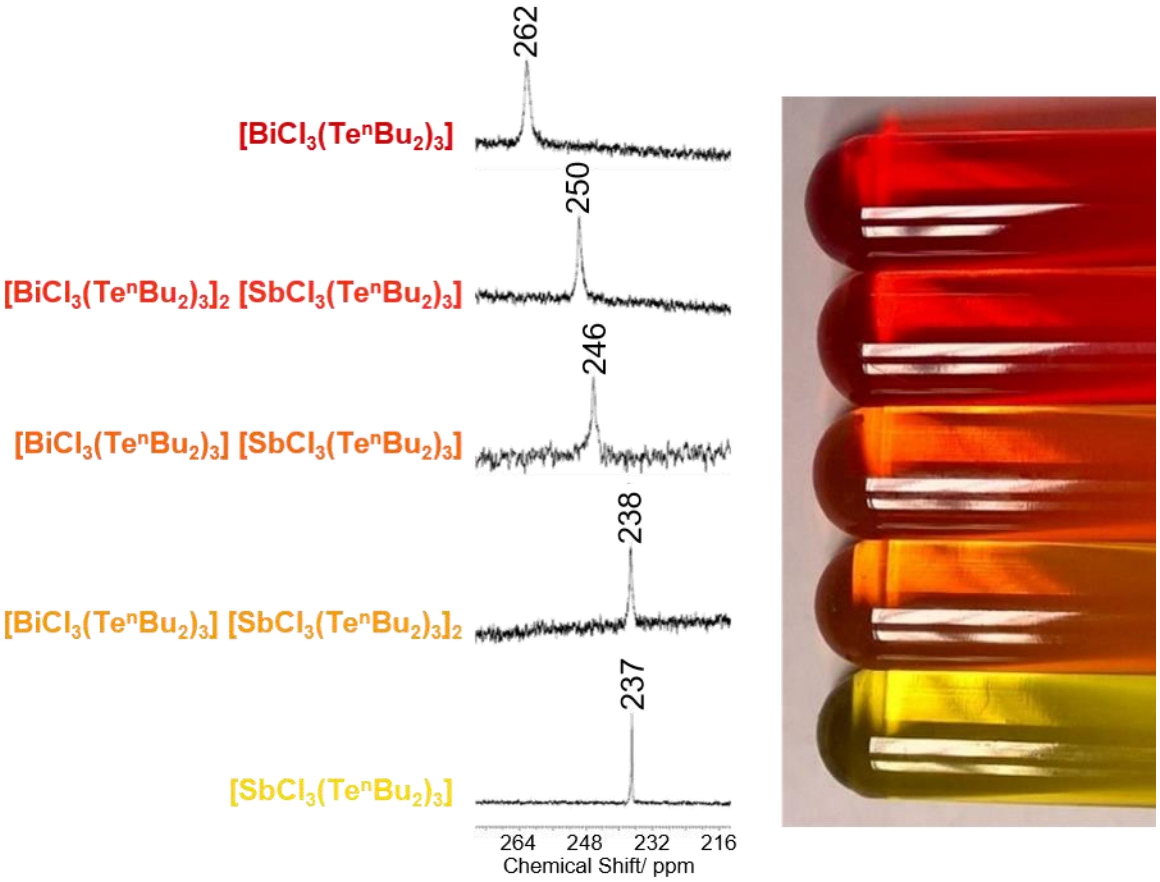

| $[MCl_3(Te^nBu_2)_3]$ Bi:Sb molar ratio | $^{125}Te\{^1H\}$ NMR/ ppm |
|---|---|
| 1:0 | 262 |
| 2:1 | 250 |
| 1:1 | 246 |
| 1:2 | 238 |
| 0:1 | 237 |

Figure 2-21: Showing the NMR spectra and data and an image of the solutions containing different ratios of $[BiCl_3(Te^nBu_2)_3]$ and $[SbCl_3(Te^nBu_2)_3]$ in $CH_2Cl_2$.

Initial experiments used the same precursor ratios as the NMR experiment, i.e ~60-70 mg of the combined precursors, at 723 K and 0.02 mm Hg and onto PVD $SiO_2$ substrates. As for the deposition of $Sb_2Te_3$ from this precursor, a ‘flash evaporation’ method was employed. This led to a grey/ silver deposition on all six substrates. XRD analysis of the substrates placed in the cooler zone of the furnace (closest to the precursor) revealed that only $Bi_2Te_3$ had been deposited irrespective of the precursor ratio used. Further analysis on the substrates placed in the hottest region of the furnace revealed that for the 1:1 ratio of precursors, there was some evidence of a ternary phase being produced. Figure 2-22 shows the shift in the (0 1 5) reflection as well as the difference in morphology compared to the regular hexagonal crystallites of $Bi_2Te_3$ or $Sb_2Te_3$. Consequently, subsequent experiments were performed at 773 K and 0.02 mm Hg with a precursor ratio of 1:1.

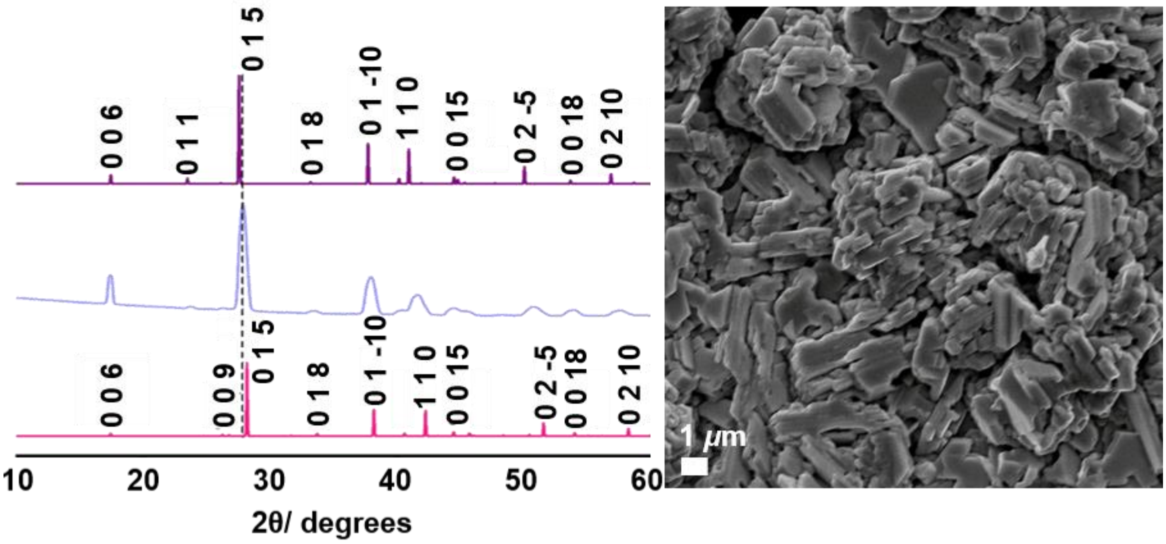

Figure 2-22: GI XRD (left) of a ternary $(Sb_xBi_{1-x})_2Te_3$ phase deposited from 1:1 $[SbCl_3(Te^nBu_2)_3]$ and $[BiCl_3(Te^nBu_2)_3]$ at 773 K and 0.02 mm Hg onto PVD $SiO_2$ (middle) $Bi_2Te_3$ (top[58]) and $Sb_2Te_3$ (bottom).[54] SEM image (right) of the ternary $(Sb_xBi_{1-x})_2Te_3$ phase.

Typical LPCVD experiments using 60 mg of a ratio of 1:1 $[BiCl_3(Te^nBu_2)_3]$ and $[SbCl_3(Te^nBu_2)_3]$ with the furnace set to 773 K onto PVD $SiO_2$ substrates led to silver/ grey films. Analysis by XRD, EDX, SEM and Raman spectroscopy revealed that there was a varying composition across the substrates with increasing Sb content corresponding to higher deposition temperatures. With the set-up employed, there is a temperature gradient across the furnace, which is largest at the edges of the furnace. Temperature profiling of the furnace revealed that when set to 773 K, the temperature spanned from 542 K at the edge to 769 K in the centre. The following analysis focusses on a single substrate (20 mm in length) with ~ 75 % coverage, that was placed in a region such that deposition occurred where the temperature spanned 745 to 755 K as depicted in Figure 2-23 below. The composition switches from Bi-rich at the cooler end to Sb-rich at the hotter end.

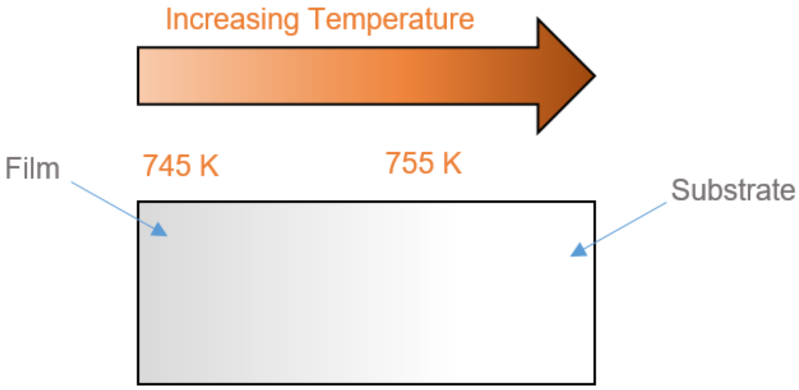

Figure 2-23: The actual temperatures at which ternary $(Sb_xBi_{1-x})_2Te_3$ was deposited on a substrate from a 1:1 ratio of $[SbCl_3(Te^nBu_2)_3]$: $[BiCl_3(Te^nBu_2)_3]$ onto PVD $SiO_2$. Characterisation was done at intervals along the substrate.

SEM and EDX analysis was used to map across the sample at regular intervals, these intervals were closer together where a bigger rate of change of composition was observed. Grazing incidence XRD data were also recorded at three positions across the length of the substrate.

SEM images (Figure 2-24) show that at ~747 K the morphology was irregular unlike the hexagonal morphology observed for either of the individual binary materials. Moving across the substrate to the more Sb-rich region, individual plate-like crystallites can be observed.

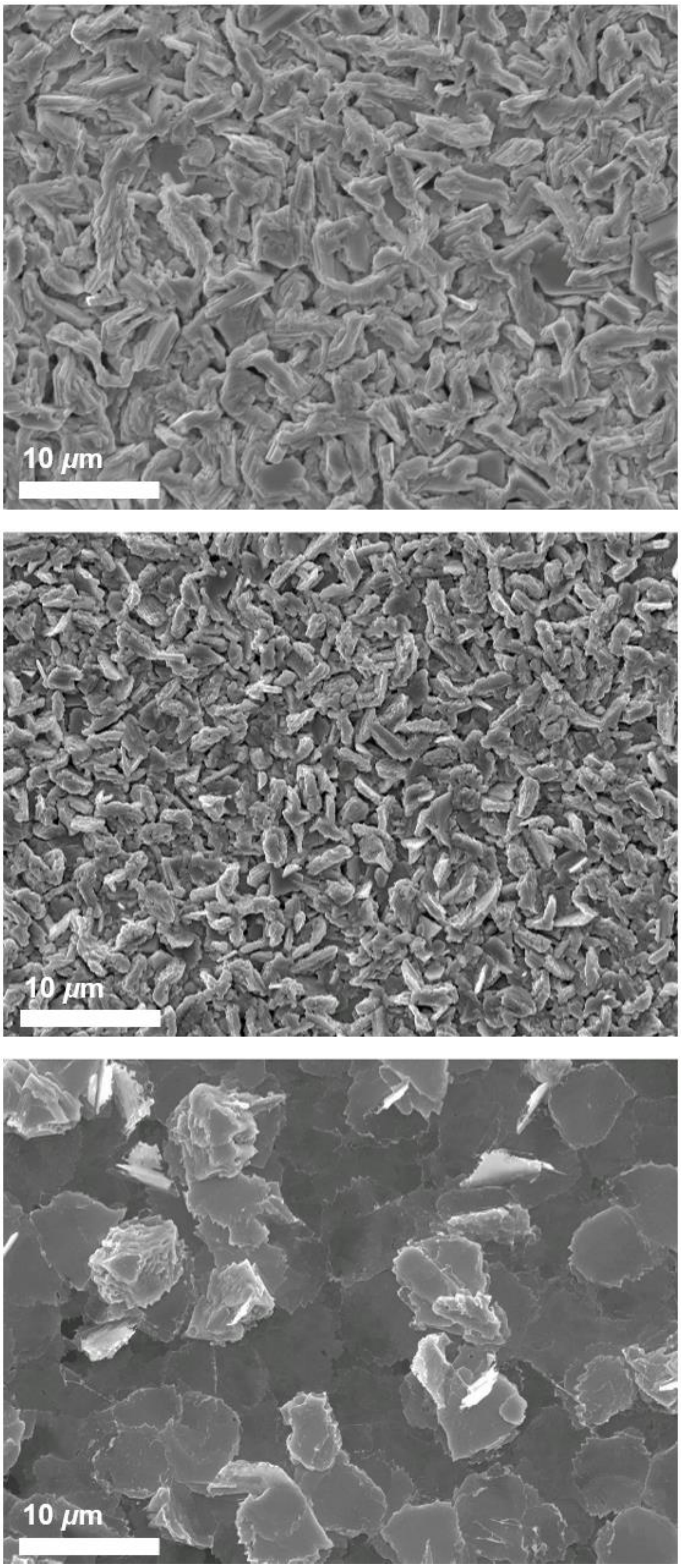

Figure 2-24: SEM images of three sections of the film deposited from a 1:1 ratio of $[SbCl_3(Te^nBu_2)_3]$ and $[BiCl_3(Te^nBu_2)_3]$ at 773 K onto PVD $SiO_2$. $(Bi_{0.66}Sb_{0.34})_2Te_s$ deposited at ~ 747 K (top), $(Bi_{0.60}Sb_{0.40})_2Te_3$ deposited at ~ 751 K (middle), $(Bi_{0.16}Sb_{0.84})_2Te_3$ deposited at ~755 K (bottom).

Grazing incidence XRD analysis (Figure 2-25) shows that the reflections gradually shift from a lower 2ϴ value for $Bi_2Te_3$ to a higher 2ϴ value with increasing Sb content, consistent with the literature.[43] Furthermore, there is no evidence of any crystalline tellurium present in the as deposited thin films.

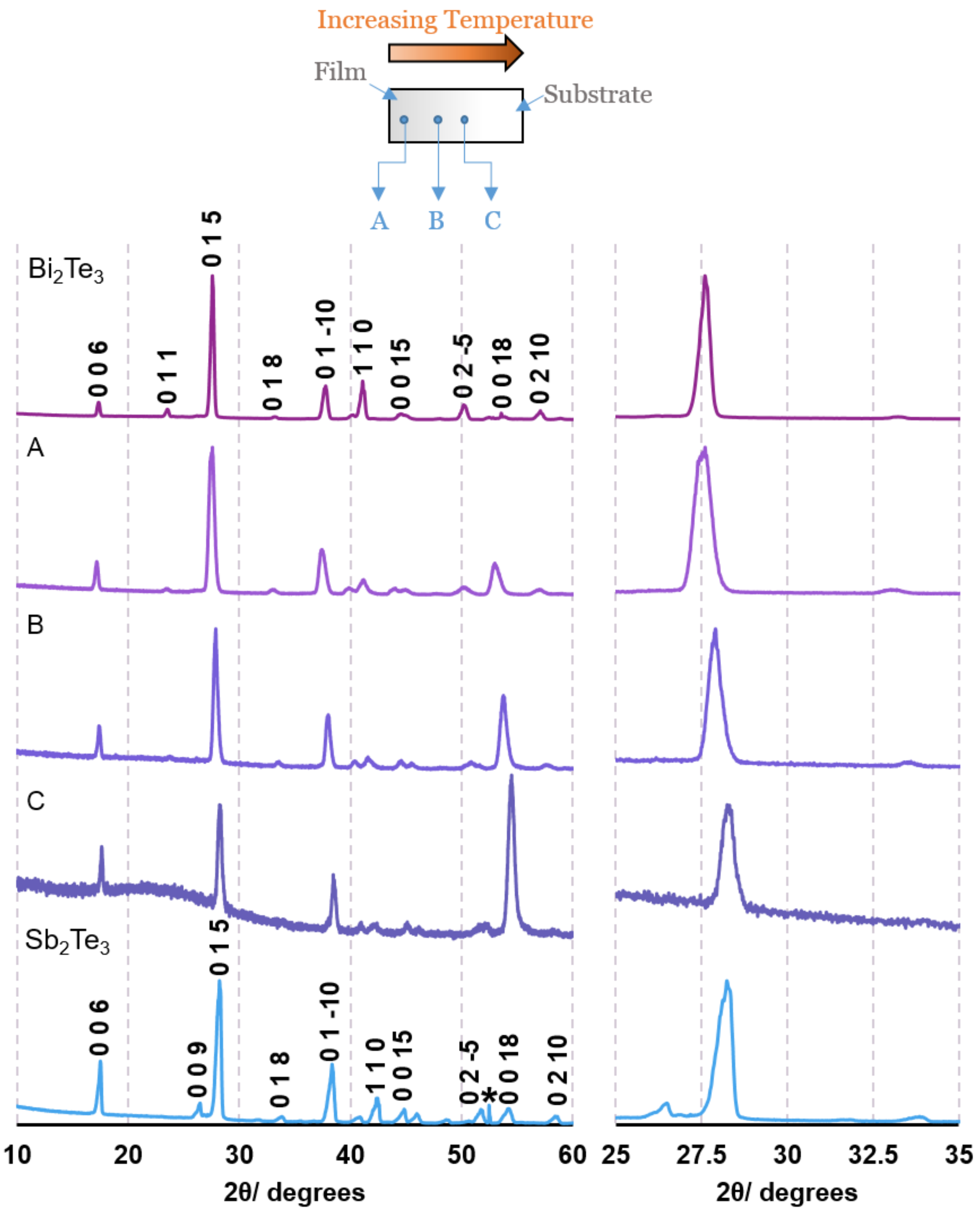

Figure 2-25: Grazing incidence XRD patterns from three ternary phases deposited from a 1:1 ratio of [$SbCl_3(Te^nBu_2)_3$] and [$BiCl_3(Te^nBu_2)_3$] and the binary phases ($Sb_2Te_3$ and $Bi_2Te_3$) deposited from the appropriate individual single source precursors at 773 K onto PVD $SiO_2$. A: $(Bi_{0.66}Sb_{0.34})_2Te_s$ deposited at ~ 747 K, B: $(Bi_{0.60}Sb_{0.40})_2Te_3$ deposited at ~ 751 K, C: $(Bi_{0.16}Sb_{0.84})_2Te_3$ deposited at ~755 K.

Figure 2-26, shows the change in both lattice parameter a and the position of (0 1 5) reflection with antimony content. It is important to note, however, that there will be a degree of error as to the exact location of the XRD measurement as the sample was positioned by eye, rather than computer, in the XRD diffractometer. A 2 mm slit sized was used. Lattice parameters a and c decrease with increasing antimony content whilst the 2Ɵ value of the (0 1 5) reflection increases. This is less pronounced than that seen in the $Bi_2(Te_xSe_{1-x})_3$ but still consistent with Vegard behaviour.

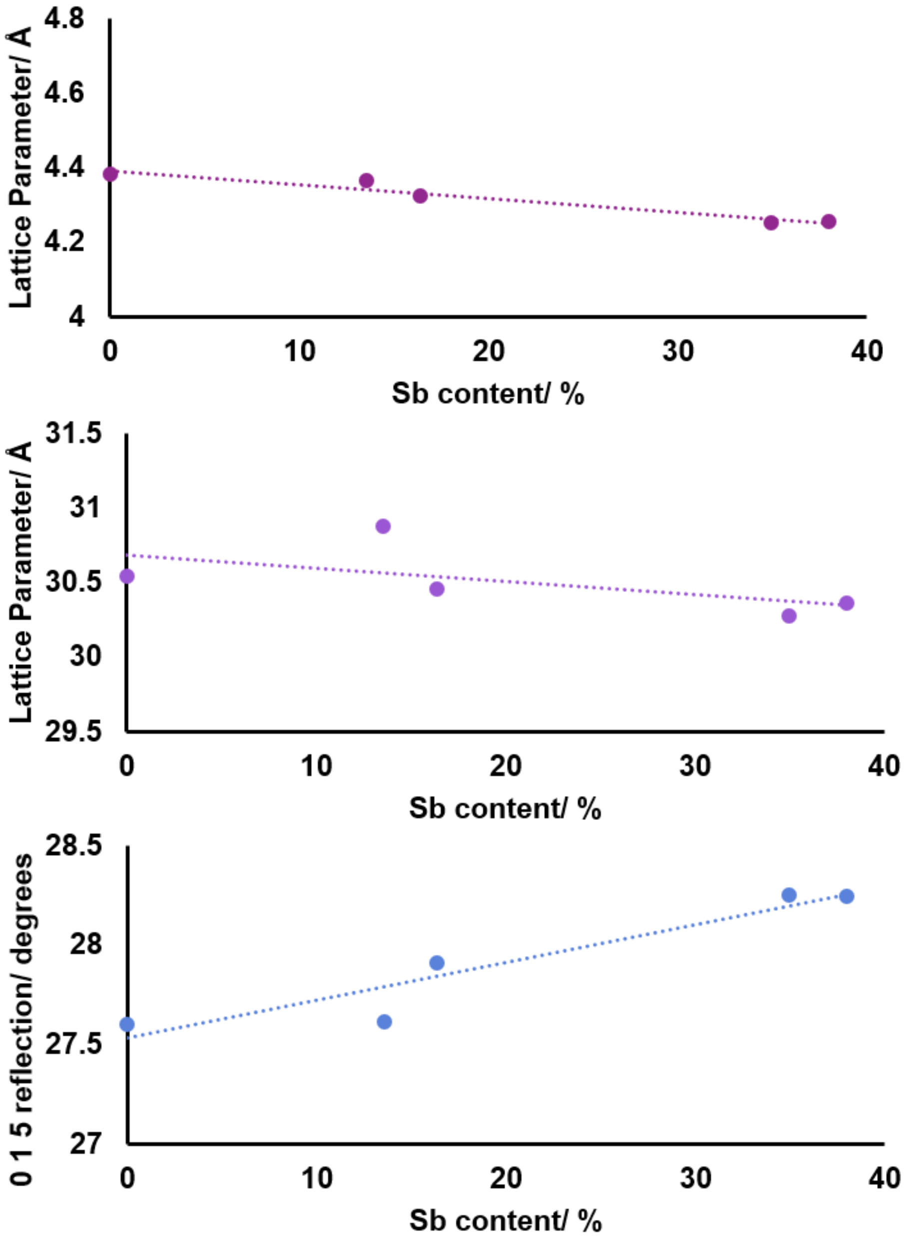

Figure 2-26: The change in lattice parameter a (top), c (middle) and the position of the 0 1 5 reflection (bottom) with increasing antimony content in $(Sb_xBi_{1-x})_2Te_3$, the film deposited from a 1:1 ratio of $[SbCl_3(Te^nBu_2)_3]$ and $[BiCl_3(Te^nBu_2)_3]$ at 773 K onto PVD $SiO_2$.

The sample was also analysed by Raman spectroscopy ( Figure 2-27). This shows the shift in peaks from $Bi_2Te_3$ to $Sb_2Te_3$. The $E_{2g}$ vibrational mode shifts from 110 to 120 $cm^{-1}$, the $A_{2u}$ mode shifts from 125 to 140 $cm^{-1}$ and the $A_{1g}$ mode shifts from 140 to 170 $cm^{-1}$ showing the change in composition of the solid solution of the ternary phase. This is consistent with Raman spectra of $(Sb_xBi_{1-x})_2Te_3$ deposited by solvothermal synthesis.[43]

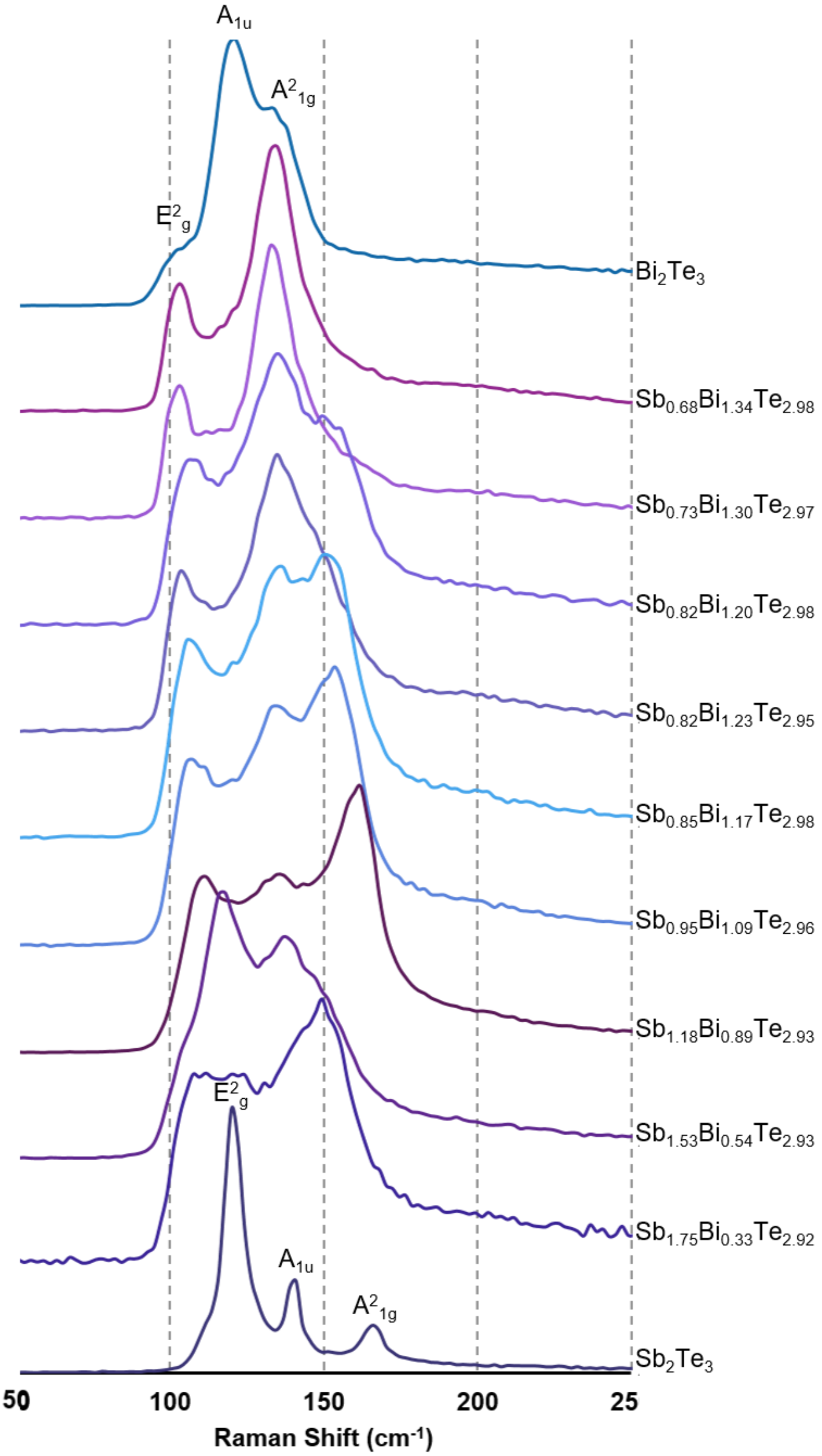

Figure 2-27: Raman spectra observed at increments along a film (left to right with respect to Figure 2-23) (top to bottom) deposited from a 1:1 ratio of $[SbCl_3(Te^nBu_2)_3]$ and $[BiCl_3(Te^nBu_2)_3]$ at 773 K onto PVD $SiO_2$.The shift in peaks shows the change in composition of the solid state solution of $(Sb_xBi_{1-x})_2Te_3$. X is the antimony content in $(Sb_xBi_{1-x})_2Te_3$.

Figure 2-28 shows the change in Sb content with temperature as calculated from EDX analysis. Measurements were taken from cooler to hotter with respect to Figure 2-23. It is easy to observe the Bi % decreasing in Figure 2-28. It was apparent from the EDX spectra that the film becomes thinner in the hotter region with the appearance of more dominating features from the substrate. This was also apparent from the cross-sectional SEM (Figure 2-29). The overlap of the Sb/Te signal will also lead to some error.

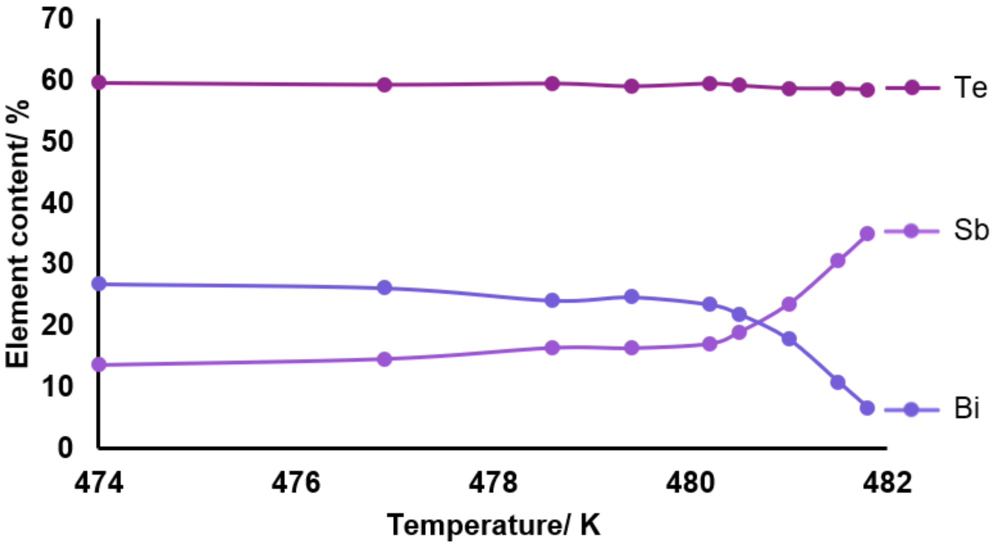

Figure 2-28: Change in elemental composition with temperature, (left to right with respect toFigure 2-23) across the film deposited from a 1:1 ratio of [$SbCl_3(Te^nBu_2)_3$] and [$BiCl_3(Te^nBu_2)_3$] at a furnace temperature of 773 K onto PVD $SiO_2$.

It is apparent that the antimony rich phases are deposited within a very small temperature range (480 – 482 K). However, this may not be a direct effect of the temperature itself. It is clear that $Bi_2Te_3$ is more easily deposited at lower temperatures than $Sb_2Te_3$ and consequently the bismuth content in the vapour phase of the precursor is heavily depleted in the early stages of the hot zone which means there is less of the bismuth precursor in the vapour that reaches the substrates at higher temperatures.

Depositions using 2:1 or 1:2 ratios of [$BiCl_3(Te^nBu_2)_3$] and [$SbCl_3(Te^nBu_2)_3$] were not successful in depositing a ternary phase of $(Sb_xBi_{1-x})_2Te_3$ and in most cases only $Bi_2Te_3$ was observed. This is most interesting for the case where there is twice as much antimony content as bismuth in the 'scrambled' precursor. This has been attributed to the weak Lewis acidity of $SbCl_3$. The ligands undergo rapid exchange at room temperature and higher. In the NMR discussion, of $[SbCl_3(Te^nBu_2)_3]$, earlier it was noted that the coordination between the Te and Sb centre is weak. This means that the combination and ‘scrambling’ of the two precursors leads to a stronger interaction as the ligands are labile and exchange between both metal centres. This leads to the 1:1 mixture of the precursors being more stable and easier to handle than the pure $[SbCl_3(Te^nBu_2)_3]$.

While a gradient of compositions is produced from this experimental set-up, these results show that by combining and ‘scrambling’ the two binary precursors, it is possible to produce a ternary $(Sb_xBi_{1-x})_2Te_3$ phase. It is likely that optimisation of the CVD parameters would allow the deposition of specific ternary $(Sb_xBi_{1-x})_2Te_3$ phases.

Cross sectional SEM shows a small variation in thickness across the film. Figure 2-29 shows two areas of thicknesses ~2.3 and 1.7 Å respectively.

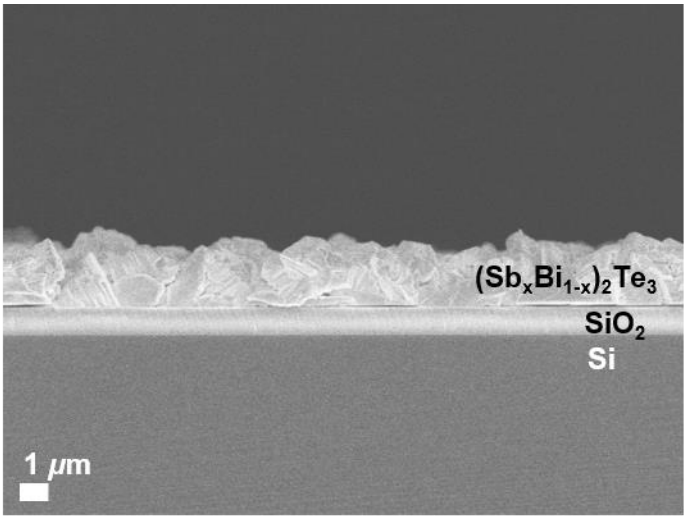

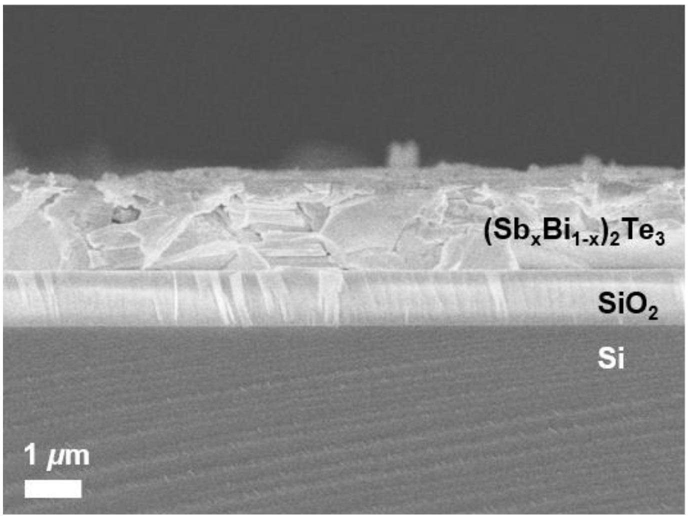

Figure 2-29: Cross sectional SEM images of two regions of an $(Sb_xBi_{1-x})_2Te_3$ film deposited from a 1:1 ratio of $[SbCl_3(Te^nBu_2)_3]$ and $[BiCl_3(Te^nBu_2)_3]$ at a furnace temperature of 773 K onto PVD $SiO_2$.

### 2.2.7 Electrical Measurements

The electrical properties of these different compositions were investigated by Hall measurements performed at room temperature. As each ternary film had a compositional variation, electrical measurements are not very reliable and hence this data has been omitted. However, bismuth rich phases were determined to be n-type semiconductors and then switch to a p-type semiconductor comes with increasing antimony content with the switch at roughly x=1. This is consistent with $(Sb_xBi_{1-x})_2Te_3$ films deposited by solvothermal methods.[43] $Sb_2Te_3$ is a p-type semiconductor and $Sb_2Se_3$ is an n-type semiconductor. Electrical measurements are shown below in Table 2-6.

$Sb_2Se_3$ was found to have a very high resistivity (4.4 x $10^4$ Ωcm), this is comparable to that for films deposited by LPCVD from [MeSb($Se^nBu_2$)$_2$] (8.8 x $10^5$ Ωcm)[10] and by rapid thermal evaporation ( ~ $10^6$ Ωcm).[17] This high resistivity and low conductivity is consistent with the relatively large band gap of 1.1 eV in $Sb_2Se_3$.[1]

$Sb_2Te_3$ was observed to have a very low resistivity (1.26 x $10^{-3}$ Ωcm) of comparable magnitude to that of $Sb_2Te_3$ deposited by LPCVD from [MeSb($Te^nBu_2$)$_2$] (9.9 x $10^{-4}$ Ωcm),[10] by MBE (5.9 x $10^{-4}$ Ωcm),[8] by ALD (9.6 x $10^{-3}$ Ωcm),[11] by solvothermal synthesis (6.7 x $10^{-4}$ Ωcm)[43] and stoichiometric $Sb_2Te_3$ deposited by ion beam sputtering (9.09 x $10^{-3}$ Ωcm).[12]

| Composition | Type | Resistivity/ Ωcm | Mobility μ/ $cm^2V^{-1}S^{-1}$ | Carrier Concentration N / $cm^{-3}$ |
|---|---|---|---|---|
| $Sb_2Se_3$ | n | 8.4(2) x $10^4$ | 22.7 ± 1.5 | 6(5) x $10^{12}$ |
| $Sb_2Te_3$ | p | 1.26(1) x $10^{-3}$ | 78.7 ± 1.3 | 6.3(1) x $10^{19}$ |
| $Bi_2Te_3$[9] | n | 5.65(2) x $10^{-4}$ | 56.6 | 1.95 x $10^{20}$ |

Table 2-6: Electrical measurements from selected films.

It is worth mentioning that despite the resistivity values of the varying compositions being typically higher than that of their binary counterparts, all are lower than the resistivity of $SnSe_2$ (2.1 x $10^{-1}$ Ωcm)[56] and many comparable to $TiSe_2$ (3.4 x $10^{-3}$ Ωcm)[57] deposited by LPCVD methods. It has been demonstrated with both these systems that selective depositions are achievable,[56,57] and consequently, selective depositions should be achievable in the case of ternary $(Sb_xBi_{1-x})_2Te_3$ compositions.

## 2.3 Conclusions and Further Work

In conclusion, the results of this chapter demonstrated the synthesis of three new molecular precursors similar to $[BiCl_3(Te^nBu_2)_3]$, completing the set of the precursors $[MCl_3(E^nBu_2)_3]$ (M = Sb, Bi; E = Se, Te). These precursors have been characterised by: $^1H$, $^{13}C\{^1H\}$, $^{77}Se\{^1H\}$ and $^{125}Te\{^1H\}$ NMR spectroscopy as appropriate, IR spectroscopy and microanalysis. The telluroether complexes are less stable and decompose much more rapidly upon storing compared to the selenoether complexes.

It has been demonstrated that all of these complexes function as single source CVD precursors to give thin $M_2E_3$ films. However, it is apparent that the same control perhaps cannot be afforded as that through the use of $MeSb(E^nBu_2)_2$ (E = Se, Te).[10] The precursors $[SbCl_3(E^nBu_2)_3]$ (E = Se, Te) do however, have the benefit of a simpler synthesis route than the selenolate and tellurolate compounds.

The capability to selectively deposit $Sb_2Te_3$ using $[SbCl_3(Te^nBu_2)_3]$ has been demonstrated.

It has been shown that by combining $[BiCl_3(Te^nBu_2)_3]$ and $[SbCl_3(Te^nBu_2)_3]$, the deposition of ternary $(Sb_xBi_{1-x})_2Te_3$ phases can be demonstrated. A gradient in compositions was observed across the substrate due to the indirect effect of temperature. However, by using a more sophisticated CVD set-up, and through careful optimisation of conditions, it should be possible to deposit a single $(Sb_xBi_{1-x})_2Te_3$ phase of a desired composition.

Films have been characterised by SEM, EDX, XRD and Raman spectroscopy and ascertained to be $M_2E_3$ and free from Cl.

The ability to selectively deposit a desired ternary phase would be very promising for the design and fabrication of thermoelectric thin film devices.

## 2.4 Experimental

### 2.4.1 Synthesis and Characterisation of [$MCl_3(E^nBu_2)_3$] (M = Sb, Bi) (E = Se, Te)

All reactions were conducted using Schlenk, vacuum line and glove box techniques under a dry nitrogen atmosphere. The reagents were stored and manipulated using a glove box. MeCN was dried by distillation over a $CaH_2$. $^nBu_2Se$,[59] and $^nBu_2Te$[60] were prepared according to the literature methods. $SbCl_3$ and $BiCl_3$ were obtained from Sigma-Aldrich. $^nBu_2Te$ was made by other members of the research group.

**$Te^nBu_2$:**

Freshly ground tellurium (5.06 g, 40.0 mmol) was suspended in anhydrous THF (100 mL) and frozen in liquid nitrogen. $^nBuLi$ solution (25.35 mL, 1.6 M) was added slowly and the solution allowed to warm to room temperature to afford a pale-yellow solution. 1-chlorobutane (4.20 mL, 40.0 mmol) was added and the solution stirred for 1 hour at which point it turned red. The solution was then gently refluxed for 1 hour. The solvent was removed in *vacuo* and the contents washed with degassed brine, $NaHCO_3$ and water. The organic phase was separated and dried over $MgSO_4$ for 15 hours before filtering off the drying agent. The solvent was removed in *vacuo* to afford a yellow-orange oil (5.26 g, 54.4%).

**[$BiCl_3(Se^nBu_2)_3$]:**

Freshly sublimed $BiCl_3$ (0.315 g, 1.0 mmol) was dissolved in anhydrous MeCN (10 mL) and the solution cooled to 0 °C. A solution of $Se^nBu_2$ (0.580 g, 3.0 mmol) in MeCN (10 mL) was slowly added, giving a pale-yellow solution which was allowed to warm to room temperature and then stirred for 1 h. The volatile components were removed, and the viscous yellow oil was dried *in vacuo*. $^1H$ NMR ($CDCl_3$): $\delta$ = 0.94 (*t*, [3H], $CH_3$), 1.45 (*m*, [2H], $CH_2$), 1.72 (*q*, [2H], $CH_2$), 3.04 (*t*, [2H], $CH_2Se$); $^{13}C\{^1H\}$ NMR ($CDCl_3$): $\delta$ = 14.0, 23.6, 28.4, 33.1; $^{77}Se\{^1H\}$ NMR ($CH_2Cl_2/CDCl_3$): $\delta$ = 196. IR (thin film/$cm^{-1}$): $v$ = 267 br(Bi−Cl).

Typically, the precursor was stable when stored under $N_2$ in the freezer for several months.

In the case of [$BiCl_3(Se^nBu_2)$], the same method was employed but upon completion the precursor was left under low pressure for longer on removal of the solvent.

**[$SbCl_3(Se^nBu_2)_3$]:**

Freshly sublimed $SbCl_3$ (0.228 g, 1.0 mmol) was dissolved in anhydrous MeCN (10 mL) and the solution cooled to 0 °C. A solution of $Se^nBu_2$ (0.580 g, 3.0 mmol) in MeCN (10 mL) was slowly added, giving a pale-yellow solution which was allowed to warm to room temperature and then stirred for 1 h. The volatile components were removed and the pale-yellow oil was dried *in vacuo*. $^1$H NMR ($CDCl_3$): $\delta$ = 0.91 (*t*, [3H], $CH_3$), 1.39 (*m*, [2H], $CH_2$), 1.63 (*q*, [2H], $CH_2$), 2.54 (*t*, [2H], $CH_2Se$); $^{13}C\{^1H\}$ NMR ($CDCl_3$): $\delta$ = 13.9, 23.6, 24.4, 33.3; $^{77}Se\{^1H\}$ NMR ($CH_2Cl_2$): $\delta$ = 168. IR (thin film/cm$^{-1}$): $v$ = 306 br (Sb−Cl). Anal. calcd for $C_{24}H_{54}SbCl_3Se_3$: C 35.69, H 6.74; found: C 34.54, H 7.25%.

Typically, the precursor was stored under $N_2$ in the freezer and was stable for several months.

In the case of [$SbCl_3(Se^nBu_2)_2$], the precursor was left under vacuum for longer.

**[$SbCl_3(Te^nBu_2)_3$]:**

A solution of $Te^nBu_2$ (0.725 g, 3.0 mmol) in anhydrous $CH_3CN$ (~10 mL) was added slowly to a solution of freshly sublimed $SbCl_3$ (0.228 g, 1.0 mmol) in $CH_3CN$ (~10 mL) at 0 °C under $N_2$. The solution immediately changed colour to orange which darkened to red over a few minutes. The solution was allowed to warm at room temperature and then stirred for 1 hour. The volatile components were removed *in vacuo*, leaving a red coloured oil which was dried *in vacuo*. $^1$H NMR ($CDCl_3$): $\delta$ = 0.92 (t, [3H], $CH_3$), 1.41 (m, [2H], $CH_2$), 1.71(q, [2H], $CH_2$), 2.72 (t, [2H], $CH_2Te$); $^{13}C\{^1H\}$ NMR: $\delta$ = 4.28, 13.5, 25.8, 34.9; $^{125}Te\{^1H\}$ NMR: $\delta$ = 237. IR (thin film/ cm$^{-1}$): $v$ = 248 br (Sb–Cl). Anal. calcd for $C_{24}H_{54}SbCl_3Te_3$ : C 30.23, H 5.71; found: C 29.89, H 5.75%

The precursor was stored in the freezer but tended to decompose after ~1 week. The precursor was therefore normally made fresh and used immediately for CVD experiments.

**[$BiCl_3(Te^nBu_2)_3$]:**

Synthesised using the same method as above, in accordance with the literature method.[9]

### 2.4.2 LPCVD

In a typical experiment, 30-60 mg of the reagent and six substrates (~1 × 7 × 20 mm) were loaded into a closed-end silica tube in a glove box. The substrates were positioned adjacently through the heated zone. The tube was put in the furnace with the precursor positioned (ca. 3 cm) away from the edge of the heated zone. The tube was evacuated to 0.1 mmHg, and the furnace was set to the desired temperature. Once the desired temperature had been reached, the tube position was adjusted such that the precursor was moved quickly to the edge of the hot zone (ca. 0 cm away from edge of the heated zone). At this point the sample position was maintained until the entire precursor had evaporated, leaving behind no residue. Evaporation of the precursor was often quick at this position. The tube was then cooled to room temperature and transferred to the glove box where the substrates were removed and stored for further characterisation. LPCVD using $[MCl_3(E^nBu_2)_3]$ (M = Sb, Bi), (E = Se, Te) was executed using 30-50 mg of reagent at temperatures between of 723 and 798 K and resulted in deposition of grey/ silver films mainly concentrated on substrate 1 of 6. LPCVD using $[BiCl_3(Te^nBu_2)_3]$: $[SbCl_3(Te^nBu_2)_3]$ typically used 60 mg at 723 and 773 K and deposition occurred on 4-6 substrates.

### 2.4.3 Substrates and Pre-treatment

**$SiO_2$ substrate:**

See Appendix 1

**Patterned $SiO_2$/TiN substrate:**

PVD TiN films with thickness of 100 nm were deposited on a p-type Si (100) wafer by the medium frequency magnetron sputtering method (Leybold HELIOS Pro) at room temperature. The films were deposited from a Ti (99.99% purity) target with a direct current (DC) power of 3000 W in a $N_2$/Ar atmosphere. The $N_2$ and Ar flow rates were maintained at 30 and 35 SCCM respectively. A high drive speed of 180 rpm was applied to enhance the film uniformity. The deposition rate was found to be 0.161 nm $s^{-1}$.

PVD $SiO_2$ was deposited as described in Appendix 1.

The patterned samples were fabricated via a photolithographic process followed by a reactive-ion etching of $SiO_2$ to reveal TiN. For photolithography, a positive resist, S1813 was chosen. The spin speed was set to be 5000 rpm for 30 seconds which gives a resist thickness of 1000 nm. This is followed by a soft bake at 110 °C for 90 seconds to dry the resist. In the exposure process, an exposure time of 5.5 seconds was chosen. The resist patterning took place in the following development step where the wafer was immersed in a container filled with the required developer, MF 319. The exposed area was corroded by the developer and the exact replica of the photomask was formed in the resist. The developing time was around 35 to 40 seconds. The wafer was then soaked in and rinsed with DI water. Etching of $SiO_2$ was performed by a RIE80+ with $CHF_3$ and Ar, with gas rates of 16 sccm and 34 sccm, respectively for both photolithography and E-beam lithography patterned samples. The RIE power was set to 200 W and the etching rate was found to be 0.47 nm·$s^{-1}$.

Substrates were provided by Dr. Ruomeng Huang.

### 2.4.4 Thin Film Characterisation

See Appendix 1

## 2.5 References

1 S. Messina, M. T. S. Nair and P. K. Nair, *J. Electrochem. Soc.*, 2009, **156**, H327–H332.

2 O. Madelung, *Semiconductors: Data Handbook vol 14*, Springer Berlin Heidelberg, Berlin Heidelberg, 2004.

3 S. K. Mishra, S. Satpathy and O. Tepsen, *J. Phys. Condens. Matter*, 1997, **9**, 461–470.

4 A. Al Bayaz, A. Giani, A. Foucaran, F. Pascal-Delannoy and A. Boyer, *Thin Solid Films*, 2003, **441**, 1–5.

5 H. You, S. Hyub Baek, K.-C. Kim, O.-J. Kwon, J.-S. Kim and C. Park, *J. Cryst. Growth*, 2012, **346**, 17–21.

6 X. Wang, H. He, N. Wang and L. Miao, *Appl. Surf. Sci.*, 2013, **276**, 539–542.

7 M. M. Rashid, K. H. Cho and G.-S. Chung, *Appl. Surf. Sci.*, 2013, **279**, 23–30.

8 N. Peranio, M. Winkler, Z. Aabdin, J. König, H. Böttner and O. Eibl, *Phys. Status Solidi*, 2012, **209**, 289–293.

9 S. L. Benjamin, C. H. de Groot, C. Gurnani, A. L. Hector, R. Huang, E. Koukharenko, W. Levason and G. Reid, *J. Mater. Chem. A*, 2014, **2**, 4865–4869.

10 S. L. Benjamin, C. H. de Groot, A. L. Hector, R. Huang, E. Koukharenko, W. Levason and G. Reid, *J. Mater. Chem. C*, 2015, **3**, 423–430.

11 S. Zastrow, J. Gooth, T. Boehnert, S. Heiderich, W. Toellner, S. Heimann, S. Schulz and K. Nielsch, *Semicond. Sci. Technol.*, 2013, **28**, 350101–350106.

12 P. Fan, Z. H. Zheng, G. X. Liang, D. P. Zhang and X. M. Cai, *J. Alloys Compd.*, 2010, **505**, 278–280.

13 C. J. Vineis, A. Shakouri, A. Majumdar and M. G. Kanatzidis, *Adv. Funct. Mater.*, 2010, **22**, 3970–3980.

14 G. Ghosh, *J. Phase Equilibria*, 1993, **14**, 753–763.

15 L. . Gilbert, B. Van Pelt and C. Wood, *J. Phys. Chem. Solids*, 1974, **35**, 1629–1632.

16 Y. Zhou, M. Leng, Z. Xia, J. Zhong, H. Song, X. Liu, B. Yang, J. Zhang, J. Chen, K. Zhou, J. Han, Y. Cheng and J. Tang, *Adv. Energy Mater.*, 2014, **4**, 13018461–13018468.

17 C. Chen, D. C. Bobela, Y. Yang, S. Lu, K. Zeng, C. Ge, B. Yang, L. Gao, Y. Zhao, M. C. Beard and J. Tang, *Front. Optoelectron.*, 2017, **10**, 18–30.

18 Y. C. Choi, T. N. Mandal, W. S. Yang, Y. H. Lee, S. H. Im, J. H. Noh and S. Il Seok, *Angew. Chem. Int. Ed.*, 2014, **53**, 1329–1333.

19 X. Liu, J. Chen, M. Luo, M. Leng, Z. Xia, Y. Zhou, S. Qin, D. J. Xue, L. Lv, H. Huang, D. Niu and J. Tang, *ACS Appl. Mater. Interfaces*, 2014, **6**, 10687–10695.

20 H. Zhang, C.-X. Liu, X.-L. Qui, X. Dai, Z. Fang and S. Zhang, *Nat. Phys.*, 2009, **5**, 438–442.

21 V. Gunasekaran, G. H. Park, M. Suemitsu and H. Fukidome, *Mater. Sci. Semicond. Process.*, 2017, **68**, 128–132.

22 K. Watanabe, N. Sato and S. Miyaoka, *J. Appl. Phys.*, 1983, **54**, 1256–1260.

23 K. J. John, B. Pradeep and E. Mathai, *Solid State Commun.*, 1993, **85**, 879–881.

24 W. Wang, Y. Geng, Y. Qian, Y. Xie and X. Liu, *Mater. Res. Bull.*, 1999, **34**, 131–134.

25 B. R. Sankapal, R. S. Mane and C. D. Lokhande, *Mater. Chem. Phys.*, 2000, **63**, 230–234.

26 H. Maghraoui-Meherzi, T. Nasr and M. Dachraoui, *Mater. Sci. Semicond. Process.*, 2013, **16**, 179–184.

27 Y. Rodriguez-Lazcano, Y. Pena, M. T. S. Nair and P. K. Nair, *Thin Solid Films*, 2005, **493**, 77–82.

28 Y. Lai, Z. Chen, C. Han, L. Jiang, F. Liu, J. Li and Y. Liu, *Appl. Surf. Sci.*, 2012, **261**, 510–514.

29 X. Shi, X. Zhang, Y. Tian, C. Shen, C. Wang and H.-J. Gao, *Appl. Surf. Sci.*, 2012, **258**, 2169–2173.

30 J. Waters, D. Crouch, J. Raftery and P. O'Brien, *Chem. Mater.*, 2004, **16**, 3289–3298.

31 J. Waters, D. Crouch, P. O. Brien and J. Park, *J. Mater. Sci. Mater. Electron.*, 2003, **14**, 599–602.

32 J.-H. Kim, S.-D. Kwon, D.-Y. Jeong, B.-K. Ju, S.-J. Yoon and J.-S. Kim, *25th Int. Conf. Thermoelectr.*, 2006, 411–413.

33 A. Giani, A. Boulouz, F. P. Delannoy, A. Foucaran, A. Boyer, B. Aboulfarah and A. Mzerd, *J. Mater. Sci. Lett.*, 1999, **18**, 541–543.

34 J. H. Kim, Y. C. Jung, S. H. Suh and J. S. Kim, *J. Nanosci. Nanotechnol.*, 2006, **6**, 3325–3328.

35 S. S. Garje, D. J. Eisler, J. S. Ritch, M. Afzaal, P. O'Brien and T. Chivers, *J. Am. Chem. Soc.*, 2006, **128**, 3120–3121.

36 R. K. Sharma, G. Kedarnath, V. K. Jain, A. Wadawale, M. Nalliath, C. G. S. Pillai and B. Vishwanadh, *Dalton Trans.*, 2010, **39**, 8779–8787.

37 R. Huang, S. L. Benjamin, C. Gurnani, Y. Wang, A. L. Hector, W. Levason, G. Reid and C. H. De Groot, *Sci. Rep.*, 2016, **6**, 275931–2759310.

38 F. S. Minaye Hashemi, B. R. Birchansky and S. F. Bent, *ACS Appl. Mater. Interfaces*, 2016, **8**, 33264–33272.

39 B. J. Choi, S. Choi, Y. C. Shin, K. M. Kim, C. S. Hwang, Y. J. Kim and Y. J. Son, *Chem. Mater.*, 2007, **19**, 4387–4389.

40 W. Levason and G. Reid, *J. Chem. Soc. Dalton Trans.*, 2001, 2953–2960.

41 R. Venkatasubramanian, E. Siivola, T. Colpitts and B. O'Quinn, *Nature*, 2001, **413**, 597–602.

42 X. Guo, X. Jia, K. Jie, H. Sun, Y. Zhang, B. Sun and H. Ma, *CrystEngComm*, 2013, **15**, 7236–7242.

43 C. Zhang, Z. Peng, Z. Li, L. Yu, K. A. Khor and Q. Xiong, *Nano Energy*, 2015, **15**, 688–696.

44 A. J. Barton, A. R. J. Genge, W. Levason and G. Reid, *J. Chem. Soc. Dalton Trans.*, 2000, **2000**, 859–865.

45 A. J. Barton, N. J. Hill, W. Levason and G. Reid, *J. Chem. Soc. Dalton Trans.*, 2001, 1621–1627.

46 E. Gaudin, S. Jobic, M. Evain, R. Brec and J. Rouxel, *Mater. Res. Bull.*, 1995, **30**, 549–561.

47 S. Nakajima, *J. Phys. Chem. Solids*, 1963, **24**, 479–485.

48 J. Zhang, Z. Peng, A. Soni, Y. Zhao, Y. Xiong, B. Peng, J. Wang, M. S. Dresselhaus and Q. Xiong, *Nano Lett.*, 2011, **11**, 2407–2414.

49 D. E. Newbury and N. W. M. Ritchie, *Scanning*, 2013, **35**, 141–168.

50 N. W. Tideswell, F. H. Kruse and J. D. McCullough, *Acta Cryst.*, 1957, **10**, 99–102.

51 J. Wang, Z. Deng and Y. Li, *Mater. Res. Bull.*, 2002, **37**, 495–502.

52 A. Bera, K. Pal, D. V. S. Muthu, S. Sen, P. Guptasarma, U. V. Waghmare and A. K. Sood, *Phys. Rev. Lett.*, 2013, **110**, 1–5.

53 Z. G. Ivanova, E. Cernoskova, V. S. Vassilev and S. V Boycheva, *Mater. Lett.*, 2003, **57**, 1025–1028.

54 B. Y. T. L. Anderson and H. B. Krause, *Acta Cryst.*, 1974, **B30**, 1307–1310.

55 G. C. Sosso, S. Caravati and M. Bernasconi, *J. Phys. Condens. Matter*, 2009, **21**, 0954101–0954106.

56 C. H. de Groot, C. Gurnani, A. L. Hector, R. Huang, M. Jura, W. Levason and G. Reid, *Chem. Mater.*, 2012, **24**, 4442–4449.

57 S. L. Benjamin, C. H. de Groot, C. Gurnani, A. L. Hector, R. Huang, K. Ignatyev, W. Levason, S. J. Pearce, F. Thomas and G. Reid, *Chem. Mater.*, 2013, **25**, 4719–4724.

58 A. N. Mansour, W. Wong-Ng, Q. Huang, W. Tang, A. Thompson and J. Sharp, *J. Appl. Phys.*, 2014, **116**, 0835131–08351314.

59 D. J. Gulliver, E. G. Hope, W. Levason, S. G. Murray, D. M. Potter, S. Sn, G. L. Marshall, R. A. East and L. Se, *J. Chem. Soc. Perkin Trans. 2*, 1984, **0**, 429–434.

60 E. G. Hope, T. Kemmitt and W. Levason, *Organometallics*, 1988, **7**, 78–83.

# Chapter 3: Precursors for the Deposition of Germanium Telluride

## 3.1 Introduction

GeTe, is an interesting material with a plethora of properties which sees it as a promising candidate for a number of applications.[1] It is valuable in the fields of thermoelectric,[2,3] ferroelectric[4–6] and spintronic materials,[7–9] as well as being an important phase change material useful for rewritable storage applications.[10–13] Commonly, GeTe is layered alternately with $Sb_2Te_3$[14,15] or the ternary $Ge_2Sb_2Te_5$[4,16] is used in these types of applications.

There are three phases of crystalline GeTe: α-GeTe, β-GeTe, γ-GeTe.[17] Two of these are shown in Figure 3-1. β-GeTe exists in a rocksalt structure (Fm3-m) and is found only above 630 K.[17,18] Interestingly, due to the lack of electrons needed to form saturated bonds with all six neighbours in this structure, β-GeTe exists in a resonant state,[19–22] to stabilise the compound, in which each unsaturated resonant p orbital binds each atom with two opposing neighbouring atoms.[23]

At lower temperature GeTe exists either in the rhombohedral, distorted rocksalt structure (α-GeTe, R3-m) or the orthorhombic structure (γ-GeTe), with the orthorhombic structure prevalent at Te > 51.2 %.[17] It is the Peierls distortion, otherwise known as the Jahn-Teller effect, that causes the distortion in the rocksalt structure to form α-GeTe.[24] The outcome is alternating short strong and long weak GeTe bonds aligned in the (1 1 1) plane causing the unit cell to become elongated in this direction.[19,25,26] This distortion induces a ferroelectric polarization due to the change in position of Ge atoms in relation to the Te atoms.[4,6,27,28]

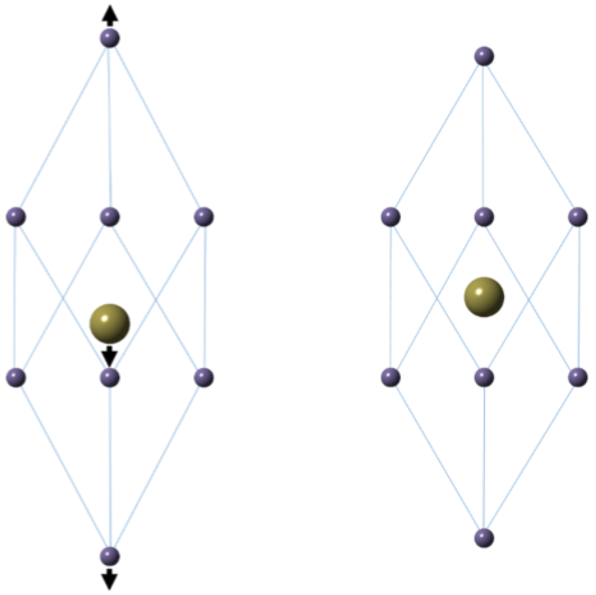

Figure 3-1: The crystal structures of and α-GeTe (left) β-GeTe (right).[29]

Germanium vacancies are intrinsic in GeTe.[30] Not only is this the reason for the observed p type conduction[31,32] and high carrier concentration of ~$10^{20}$ $cm^{-3}$,[33–35] but it also has an effect on its thermoelectric properties.[36,37] The Ge vacancies result in a low electrical resistivity of 1.4 and 5.2 μΩm at 300 and 720 K respectively and power factors of up to 42 $\mu Wcm^{-1}K^{-2}$ at 720 K have been reported for GeTe.[38]

GeTe is also an important phase change material.[11–13] To be useful, a phase change material must have significantly different electrical (or optical) properties between an amorphous and crystalline state. GeTe has a highly reflective and conductive crystalline state whilst its amorphous state is highly resistive and has low reflectivity.[19,29,39,40] Amorphous GeTe has been reported to have a band gap of 0.8 eV,[40] whilst 0.5 eV has been reported as an indirect band gap of α-GeTe.[41] Bahl *et al.* have also shown the resistivity shifts from $10^2$ Ωcm in the amorphous state to $4 \times 10^{-4}$ Ωcm when crystalline.[40] Finally, Bruns *et al.* have shown that GeTe is an extremely fast phase change material with switching speeds as low as 1 ns.[13]

GeTe has been deposited by a number of different methods. GeTe nanowires and single crystals have been grown by VLS growth.[42–44] Thin films of GeTe have been produced ubiquitously by sputtering[45–52] and MBE.[35,53,54] GeTe has also been deposited by thermal coevaporation,[55] whilst Gwon *et al.* have also deposited GeTe thin films using ALD with $\{(CH_3)_3Si\}_2Te$ as the tellurium source and $HGeCl_3$ or $Ge\{N[Si(CH_3)_3]_2\}_2$ as the germanium source.[56] GeTe nanocrystals have also been synthesised from $GeCl_2$.dioxane or $Ge\{N[Si(CH_3)_3]_2\}_2$ with TOP-Te (trioctyl phosphine telluride).[57]

CVD has also been used in the synthesis of GeTe films. Salicio *et al.* used Ge(NMe$_2$)$_4$ and Te($^i$Pr)$_2$ in toluene in a pulsed liquid injection method to produce tellurium rich GeTe films (Ge$_{0.79}$Te$_{1.00}$),[58] this method has also been used by Abrutis *et al*.[59] Ovshinsky *et al* used diisopropyl tellurium and isobutyl germane along with a N$_2$ carrier gas.[60] An interesting technique was employed by Kim *et al,* in which a film of germanium was deposited first from [Ge(allyl)$_4$] in the presence of catalytic [Sb($^i$Pr)$_3$], Te was then deposited from [Te($^t$Bu)$_2$] to react with the germanium film to produce GeTe.[61] An argon carrier gas was used.

With other Group 14 metal chalcogenides, such as tin chalcogenides, typical single source precursors for CVD have included coordination compounds composed of Sn(IV) halides and neutral chalcogenoether ligands such as [SnCl$_4${$^n$BuSe(CH$_2$)$_n$Se$^n$Bu}] (n= 2,3)[62] and [SnCl$_4$(SeEt$_2$)$_2$],[63] (see Chapter 4). However, the coordination chemistry of germanium (IV) is limited. GeCl$_4$ is an extremely weak Lewis acid and consequently there are no known complexes of Ge(IV) chloride with neutral chalcogenoether ligands. GeF$_4$ is a stronger Lewis acid than GeCl$_4$ and a small number of coordination complexes of Ge(IV) fluoride with neutral thioethers has been reported ([GeF$_4${MeS(CH$_2$)$_2$SMe}] and [GeF$_4${EtS(CH$_2$)$_2$SEt}]).[64] Whilst crystallographic data confirm the distorted octahedral structures, the complexes are unstable with weak (long) Ge-S bonds.[64] Selenoethers and telluroethers, however, are weaker Lewis bases and hence are expected to have a weaker interaction towards Ge(IV) and consequently, typical coordination compounds are not feasible as single source precursors for the chemical vapour deposition of GeTe thin films.

A small number of single source precursors for the deposition of GeTe crystals are reported in the literature, though these methods are not CVD based. Gupta *et al.* synthesised (R$_2$GeTe)$_3$ (R = Et, Bu) from the reaction of Li$_2$Te and R$_2$GeCl$_2$, and thermal decomposition of the precursor in trioctyl phosphine at 300 °C resulted in rhombohedral GeTe.[65] Kim *et al.* created a Ge=Te double bond in the synthesis of [Te=Ge(dmampS)$_2$], (dmampS = Me$_2$NCH$_2$(Me)CH$_2$CH$_3$SH) the hard nitrogen donors are able to stabilise the germanium by chelation. This precursor could be dissolved in hexadecane and thermally decomposed at 270 °C to produce tellurium rich rhombohedral Ge$_{40}$Te$_{57}$.[66] The precursors are shown in Figure 3-2 overleaf.

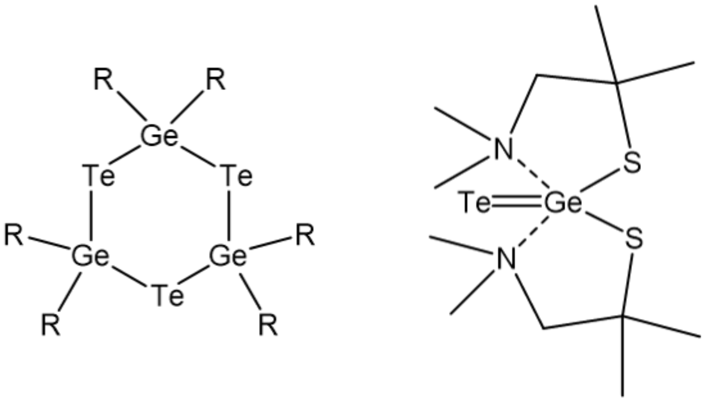

Figure 3-2: Single source precursors [$(R_2GeTe)_3$] (R= Et, Bu)[65] (left) and [Te=Ge$(dmampS)_2$][66] (right) that thermally decompose to give rhombohedral GeTe.

To the best of my knowledge, there is at least one example in the literature of a single source precursor for the deposition of GeTe thin films via CVD. Chen *et al.* used an insertion reaction to insert Te$^i$Pr into a germylene to synthesise [Ge{N($SiMe_2CH_2CH_2Me_2Si$)}$_2${$^i$Pr}{Te$^i$Pr}] as shown in Figure 3-3. In $NH_3$, Chen *et al.* claimed this precursor functioned as a single source precursor for the CVD of GeTe thin films between 280 and 400 °C evidenced by XRF data.[67] However, none of this evidence was provided.

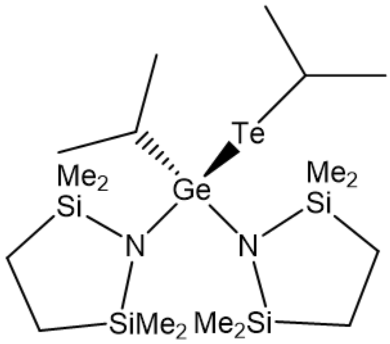

Figure 3-3: Single source CVD precursor [Ge{N($SiMe_2CH_2CH_2Me_2Si$)}$_2${$^i$Pr}{Te$^i$Pr}] for GeTe film growth .[67]

The aims of this chapter were to develop a single source precursor for the low pressure chemical vapour deposition of GeTe thin films and the subsequent characterisation of the composition and properties of the films.

## 3.2 Results and Discussion

### 3.2.1 Synthesis of [Ge(Te$^n$Bu)$_4$] by Method 1

Due to the extremely weak Lewis acidity of $GeCl_4$ and the complete absence of any telluroether complexes of germanium in the literature, coordination complexes are not suitable for use as single source precursors for germanium telluride thin films. However, successful single source precursors such as the antimony chalcogenolate compounds [$Me_xSb(E^nBu)_{3-x}$] (E = Se, Te) have previously been synthesised by the direct reaction of $^nBuELi$ with 1/(3-x) $Me_xSbCl_{3-x}$. For x = 0,1, these were shown to function as efficient single source precursors for the deposition of $Sb_2E_3$ thin films.[68] The first method attempted for preparation of an analogous germanium tellurolate compound is depicted in Scheme 3-1 below.

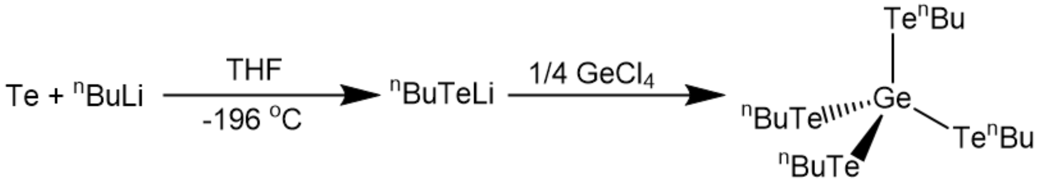

Scheme 3-1: Showing the attempted synthesis of [Ge(Te$^n$Bu)$_4$] (method 1)

The reaction mixture afforded was dark red and work up resulted in a viscous dark red oil. Characterisation by $^1H$ and $^{13}C\{^1H\}$ NMR spectroscopy indicates that the desired compound had been synthesised but small quantities of $^nBu_2Te$ and $^nBu_2Te_2$ were also present as evidenced by the $^{13}C\{^1H\}$ NMR signals at 2.54 and 4.67 ppm (see Table 3-1). Attempts to separate this mixture by placing under vacuum or by distillation were unsuccessful.

Subsequent attempts at the synthesis route, adjusting the reaction temperature, reaction times and $^nBuLi$: Te ratio, offered no improvement and often there were additional chlorinated species present. The reaction described above requires absolute stoichiometry. Addition of excess butyl lithium would result in $^nBuTeLi$ with additional $^nBuLi$ which could go on to react further with the resultant [Ge(Te$^n$Bu)$_4$] species. This would result in $^nBu_2Te$ being formed as well as additional chloro species as evidenced by the addition of signals in the NMR (a triplet at 3.76 ppm in the $^1H$ NMR and signals at 1.01, 42.69 and 43.61 in the $^{13}C\{^1H\}$ NMR). In contrast, too little $^nBuLi$ would result in an excess of Te which would result in the formation of by-products such as the $^{n}Bu_2Te$ and $^{n}Bu_2Te_2$ discussed previously.

### 3.2.2 Deposition and Characterisation of GeTe Films onto PVD $SiO_2$

Initial LPCVD experiments were completed using the precursor produced from method one (with small amounts of $^{n}Bu_2Te$ and $^{n}Bu_2Te_2$ present). A typical experiment used ~50 mg of precursor, a temperature of 723 K and PVD $SiO_2$ substrates. The tube was repositioned in the furnace, once the appropriate temperature had been reached, such that the precursor was at the edge of the hot zone. Partial evaporation of the precursor was observed with some black residue remaining. Deposition only occurred on the substrate closest to the precursor. The film was silver and very reflective, one edge (closest to the precursor) was a dull grey.

Grazing incidence XRD analysis revealed that the reflective film was GeTe and the dull grey section formed of a mixture of GeTe and crystalline tellurium. The XRD patterns shown in Figure 3-4 confirm that the material is crystalline and there are no other significant crystalline phases present (reflective film). The reflection marked with an asterisk is from the Si underlying the $SiO_2$ in the substrate and demonstrates that the film is very thin.

The XRD pattern shows a rhombohedral GeTe phase (α-GeTe) of space group R3mH. Refined lattice parameters (a = 4.145(2) Å, c = 10.620(8) Å) are consistent with those reported in the literature (a = 4.156(3) Å, c = 10.663(5) Å;[69] a = 4.164(2) Å, c = 10.69(4) Å).[70] Lattice parameters were calculated by optimisation of the fit in PDXL2.

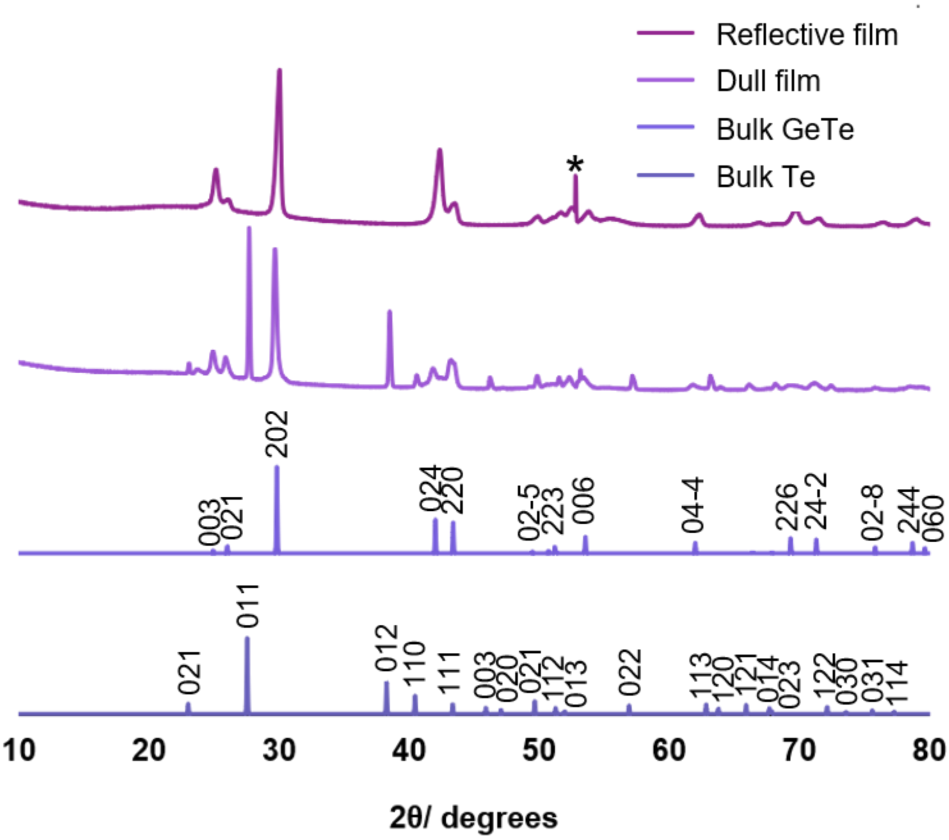

Figure 3-4: Grazing incidence XRD patterns from two regions (reflective and dull) of GeTe deposited from $[Ge(Te^nBu)_4]$ synthesised in 'method 1' at 723 K onto PVD $SiO_2$ and indexed bulk patterns of GeTe[71] and Te.[72] The peak due to the Si underlying the $SiO_2$ in the substrate is marked with an asterisk.

SEM analysis showed a regular array of crystallites. The film also appears to be very smooth, and therefore reflective. Crystallites appeared to be about 200 nm in diameter, (Figure 3-5). EDX analysis shows that the film is very thin (as discussed later) with the peaks from the substrate similar in intensity to those for Ge or Te. Quantification of multiple spectra across the film (one shown in Figure 3-5) resulted in a ratio of Ge to Te of 49:51. This shows a good stoichiometry of GeTe. It is worth noting that the error in the EDX, especially due to the large substrate to sample ratio in a thin film, is large. However, GeTe is often found in an imperfect stoichiometry due to intrinsic point defects (dominated by Ge vacanicies).[30,32]

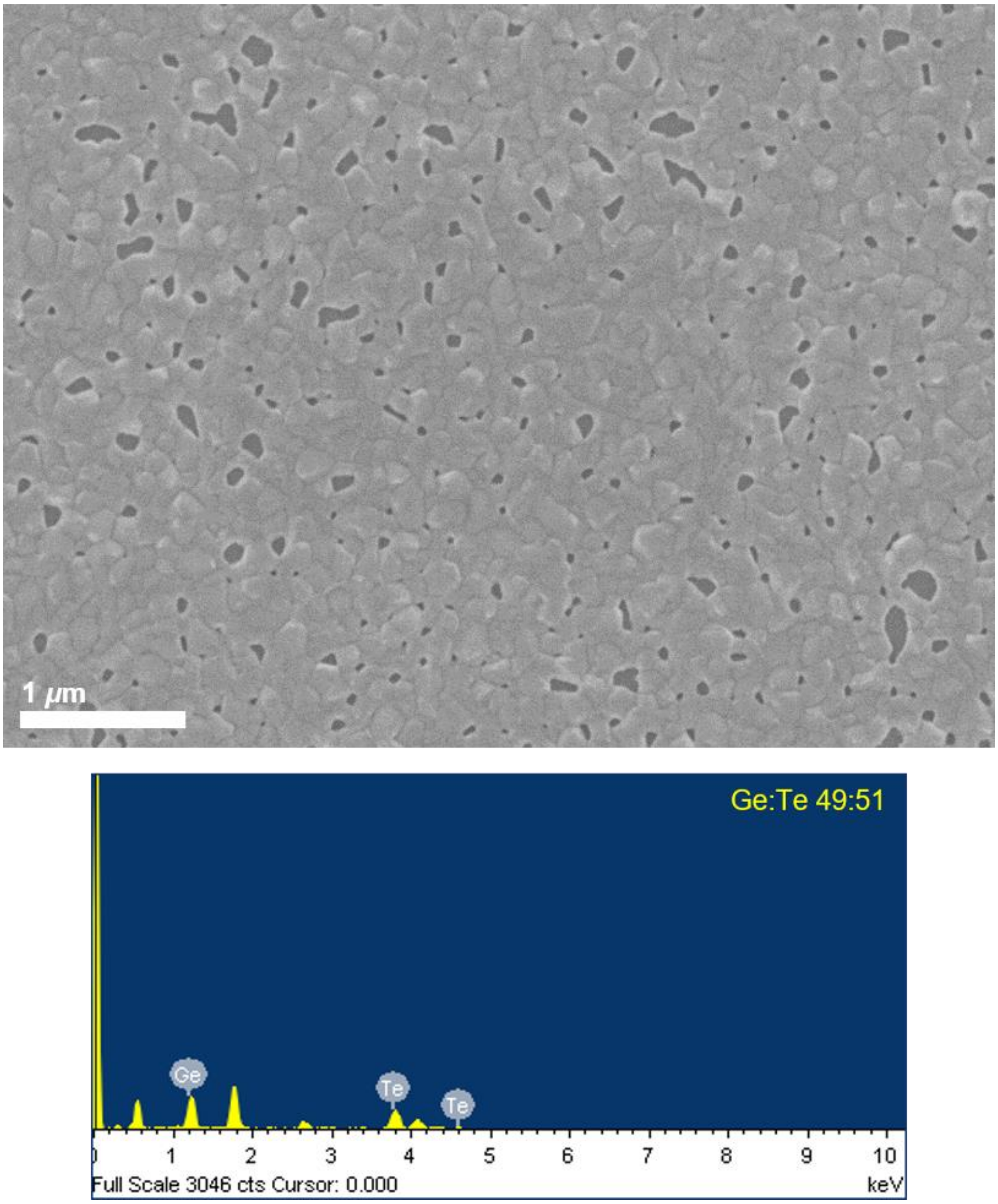

Figure 3-5: SEM image and EDX spectrum for GeTe deposited from [Ge(Te$^n$Bu)$_4$] synthesised in 'method 1' at 723 K onto PVD SiO$_2$. The peaks at 0.5 and 1.8 keV are due to oxygen and silicon from the substrate.

Cross sectional SEM shows that an extremely thin continuous film has been deposited. Figure 3-6 shows that the film deposited is less than 100 nm in thickness.

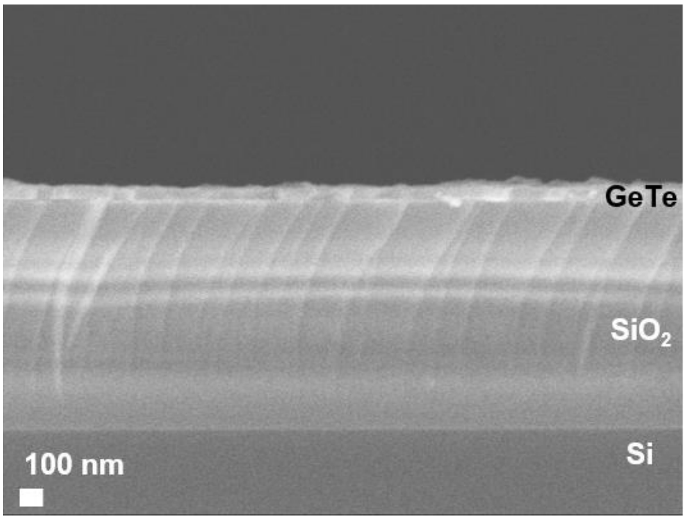

Figure 3-6 Cross sectional SEM image of GeTe deposited from $[Ge(Te^nBu)_4]$ synthesised in ‘method 1’ at 723 K onto PVD $SiO_2$.

The resistivity of the GeTe thin film grown from $[Ge(Te^nBu)_4]$ at 723 K was determined by van der Pauw measurements. The film shows a slightly higher resistivity of, $\rho = 3.2(1) \times 10^{-4}$ Ωcm, compared with other reported values ($\rho = 1.4 \times 10^{-4}$ Ωcm).[38] This is consistent with a small amount of excess Te being present ($\rho = 1.0 \times 10^{-3}$ Ωcm).[73] Thus, while the impure samples of $Ge(Te^nBu)_4$, formed via method 1 to deposit GeTe thin films, the presence of the impurities ($Te^nBu_2$ etc) also appear to give rise to elemental Te, therefore, an improved synthesis was required.

### 3.2.3 Synthesis of $[Ge(Te^nBu)_4]$ by Method 2

The tellurium contamination mentioned previously may be due to the impurities in the precursor and consequently a higher quality precursor is required. An alternative method has been used by Schlecht *et al*. who reacted activated germanium with $Ph_2E_2$ (E = Se, Te) to form $[Ge(EPh)_4]$.[74] Whilst the selenolate was produced in a good yield, the tellrurolate was afforded in a yield of just 26 %. Replicating this experiment for the tellurolate resulted in a mixture of $Ph_2Te_2$ and $[Ge(TePh)_4]$. The purity of the product could be increased by washing with ice cold diethyl ether, but this reduces the yield dramatically.

In an attempt to improve the purity of the desired precursor, the above method was adapted to use the $^n$butyl analogue, requiring the synthesis of $^nBu_2Te_2$ also. This was synthesized via the reaction of $^nBuTeLi$ with 1,2-dichloroethane. The resulting 1,2-dibutyl(telluro)ethane is unstable and decomposes into $^nBu_2Te_2$ and ethene which can be removed under low pressure. This synthesis route to [Ge(TeR)$_4$] is shown in Scheme 3-2 below.

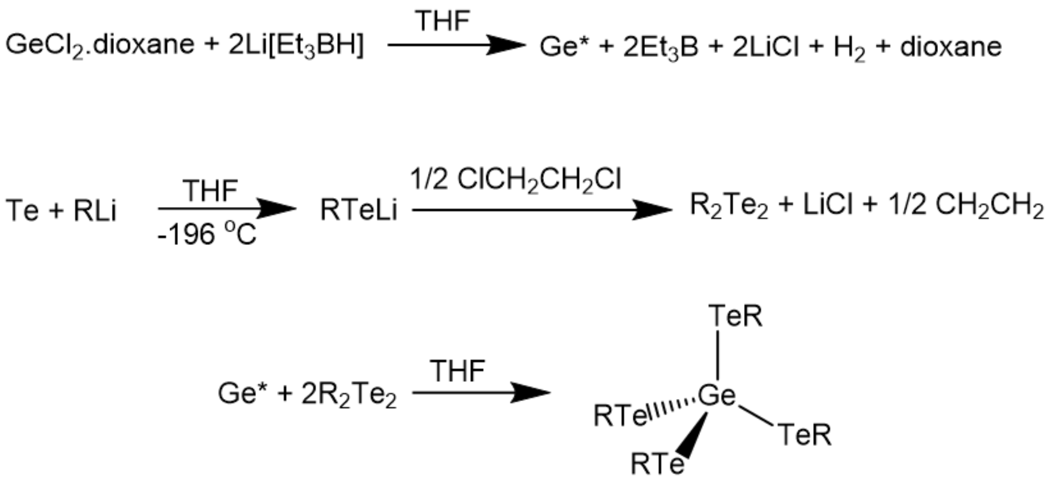

Scheme 3-2 Showing the synthesis route to [Ge(TeR)$_4$]. * represents that the Ge is activated.

Synthesis of $^{n}Bu_2Te_2$ resulted in a dark red oil. It was stored under nitrogen in the freezer to avoid decomposition. Characterisation by $^{1}H$ and $^{13}C\{^{1}H\}$ NMR spectroscopy showed a clean product.

[Ge(TePh)$_4$] [74] is a solid and purification was completed by washing with cold diethyl ether. However, as the $^{n}$butyl analogue, [Ge(Te$^{n}$Bu)$_4$], is an oil, separation by this method is not possible. $^{1}H$ NMR of the [Ge(TePh)$_4$], after one purification step, showed that there was a 60:40 molar ratio of [Ge(TePh)$_4$] to $Ph_2Te_2$. Consequently, in the synthesis of [Ge(Te$^{n}$Bu)$_4$] only half of stoichiometric amount of $^{n}Bu_2Te_2$ was added in an attempt to minimise impurities, resulting in the synthesis of a dark red oil. Microanalytical data was consistent with the proposed stoichiometry: Anal. Calcd. for $C_{16}H_{36}Te_4Ge$: C, 23.68 and H, 4.47 %. Found: C,24.32 and H, 4.77 %.

Characterisation by $^{1}H$ and $^{13}C\{^{1}H\}$ NMR spectroscopy showed that the desired product had been synthesised with NMR signals significantly different from other 'Te$^{n}$Bu' species as shown in Table 3-1 below. The $^{13}C\{^{1}H\}$ NMR shows only one 'butyl' species to be present (Figure 3-7).

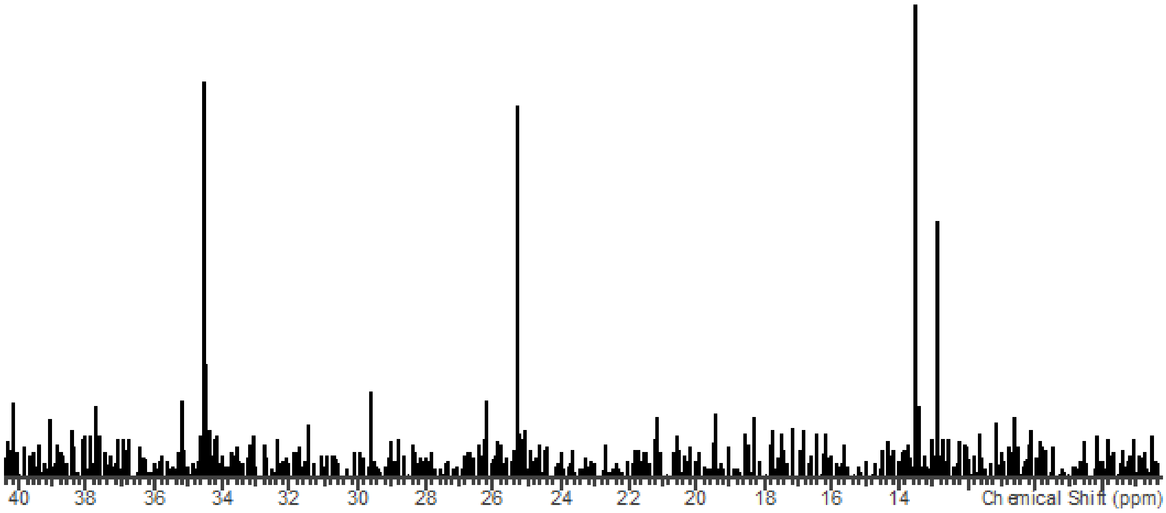

Figure 3-7: The $^{13}C\{^1H\}$ NMR spectrum of $[Ge(Te^nBu)_4]$, deposited via ‘method 2’, in $CDCl_3$ at room temperature.

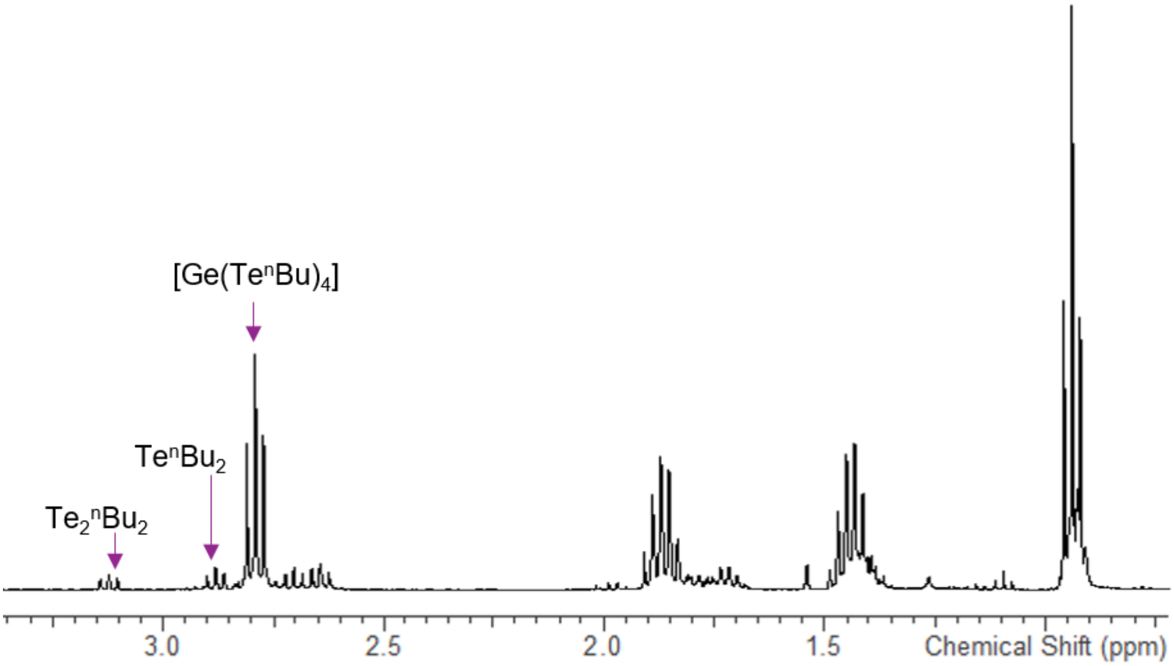

Figure 3-8: The $^1H$ NMR spectrum of $[Ge(Te^nBu)_4]$, deposited via ‘method 2’, in $CDCl_3$ at room temperature.

| Compound | $^{13}C\{^1H\}$: δ/ ppm | | | |
|---|---|---|---|---|
| $[Ge(Te^nBu)_4]$ | 12.90 | 13.53 | 25.29 | 34.53 |
| $Te^nBu_2$ | 2.24 | 13.33 | 25.03 | 34.32 |
| $Te_2{}^nBu_2$ | 4.22 | 13.32 | 24.56 | 35.72 |

Table 3-1: $^{13}C\{^1H\}$ NMR resonances for $[Ge(Te^nBu)_4]$ and other relevant '$Te^nBu$' species in $CDCl_3$ at room temperature.

However, it is important to note that there were a few minor $^n$butyl containing impurities evident in the $^1H$ NMR spectrum (Figure 3-8). This was negligible and as mentioned earlier, the microanalysis is consistent with the proposed formulation, $[Ge(TePh)_4]$.

This compound is not previously known but $^{125}Te\{^1H\}$ NMR spectroscopy revealed no signal. This is consistent with no $^{125}Te\{^1H\}$ NMR having been reported for these types of compounds in the literature.[74] Monitoring by NMR spectroscopy showed that the compound decomposed slowly over time, spitting out $^nBu_2Te_2$; it can be seen that there is a greater concentration of $^nBu_2Te_2$ in the $^1H$ NMR spectrum in Figure 3-9 compared to Figure 3-8. It is worth noting that this decomposition was enhanced in the presence of light. In the freezer, degradation of the compound was slow.

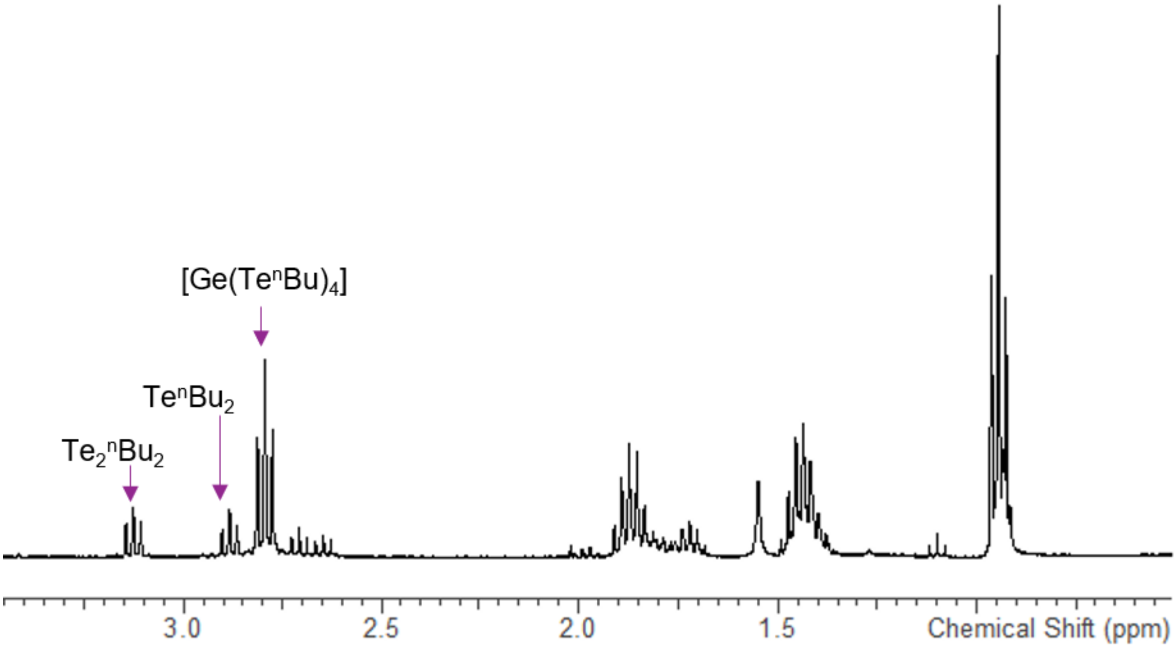

Figure 3-9: A $^1H$ NMR spectrum, one month after synthesis, of $[Ge(Te^nBu)_4]$, deposited via 'method 2', in $CDCl_3$ at room temperature.

IR spectroscopy showed bands at 238 and 251 cm$^{-1}$ tentatively assigned to the Ge-Te stretches. These are consistent with values reported in the literature for [Ge(TePh)$_4$] of 238 and 252 cm$^{-1}$.[74]

Thus, method 2 appears to be more successful than method 1 for the preparation of [Ge(Te$^n$Bu)$_4$]. However, assuming that the yield of Ge* (activated germanium) is not 100 % due to some germanium being lost in purification, it is impossible to know the exact yield of Ge* and consequently a small deficit of Te$_2$R$_2$ is required to ensure the ditelluride present in the final product is negligible. In the case described here, only 50 % of the stoichiometric Te$_2$R$_2$ was used.

### 3.2.4 Deposition and Characterisation of GeTe Thin Films

LPCVD experiments using the [Ge(Te$^n$Bu)$_4$] synthesized via method 2 used ~60 mg of precursor, a temperature of 723 K and a pressure of 0.02 mm Hg onto PVD SiO$_2$.Typically, the precursor was repositioned at the edge of the hot zone once the target temperature was reached and partial evaporation was observed with some black residue remaining. Good coverage of the substrates was observed with films on the substrates nearest the precursor a grey colour, and films that were deposited further into the hot zone, thin and reflective silver in colour.

Characterisation of the films by grazing incidence XRD showed that on the substrates nearest the precursor (1) just elemental tellurium was deposited, whereas on substrates 3 and 4, only GeTe was identified, with space group R3mH. The substrates with GeTe deposited showed no trace of crystalline tellurium (Figure 3-10). A peak due to the Si in the substrate was present in the GIXRD pattern indicating that the film was thin. The GIXRD pattern shows no evidence of preferred orientation. Lattice parameters of these films (a = 4.1565(10), c = 10.646(3) Å) match well with the literature (a = 4.156(3), c = 10.663(5);[69] a = 4.164(2), c = 10.69(4)).[70] Lattice parameters were calculated by optimisation of the fit in PDXL2.

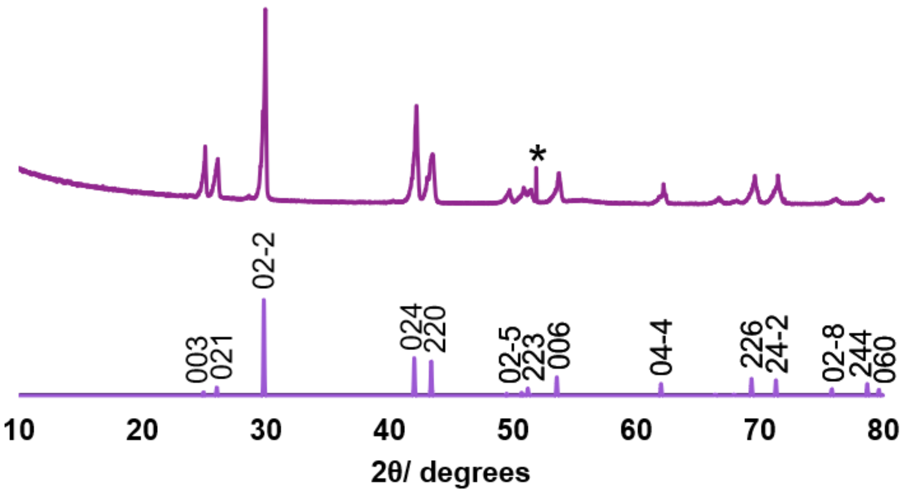

Figure 3-10: Grazing incidence XRD pattern of GeTe deposited from [Ge(Te$^n$Bu)$_4$] synthesised via 'method 2,' at 723 K and 0.02 mm Hg onto PVD $SiO_2$ and an indexed bulk pattern of GeTe.[71] The peak due to the Si underlying the $SiO_2$ in the substrate is marked with an asterisk.

SEM analysis (Figure 3-11) shows much larger crystallites than in the film deposited from the material from method 1 (micrometres in diameter), but the film appears to be discontinuous with the substrate visible. EDX analysis revealed both germanium and tellurium present with no indication of any residual chloride or carbon ($K_\alpha$ = 2.622 and 0.277 keV respectively), indicating a clean deposition of GeTe. Quantification of the germanium and tellurium peaks gave a ratio of 49:51 Ge:Te, the same as for the previous film.

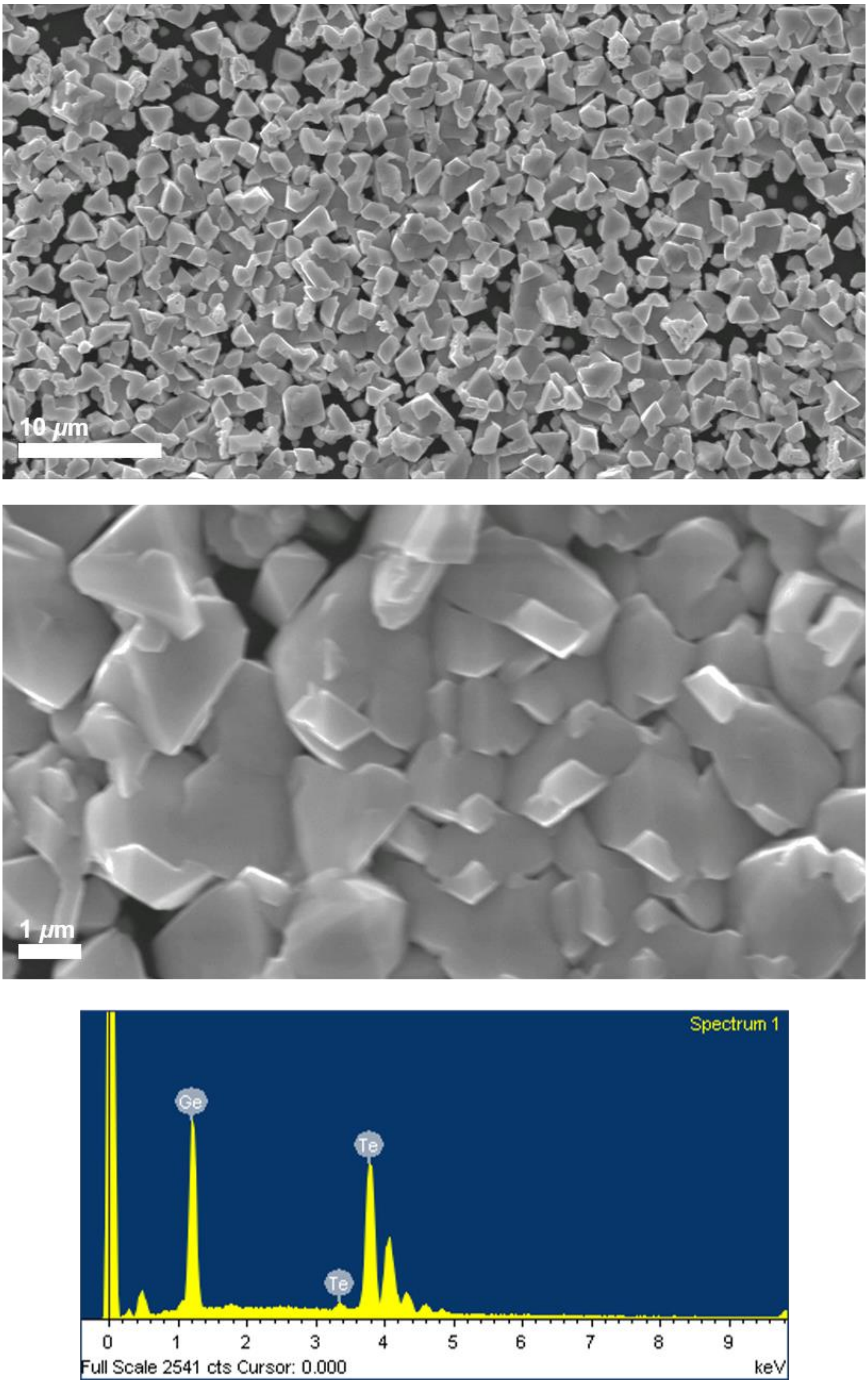

Figure 3-11: SEM images and an EDX spectrum of GeTe deposited from $[Ge(Te^{n}Bu)_4]$ synthesized from 'method 2' at 723 K onto PVD $SiO_2$.

Raman spectra from the films show peaks at 125 cm$^{-1}$ and ~142 cm$^{-1}$, consistent with those reported in the literature.[44,53,75] The peak at 125 cm$^{-1}$ can be assigned to the symmetric stretching vibrations of the Ge-Te bonds ($A_{1g}$) and the peak at 142 cm$^{-1}$ is due to Te-Te bonds.[75]

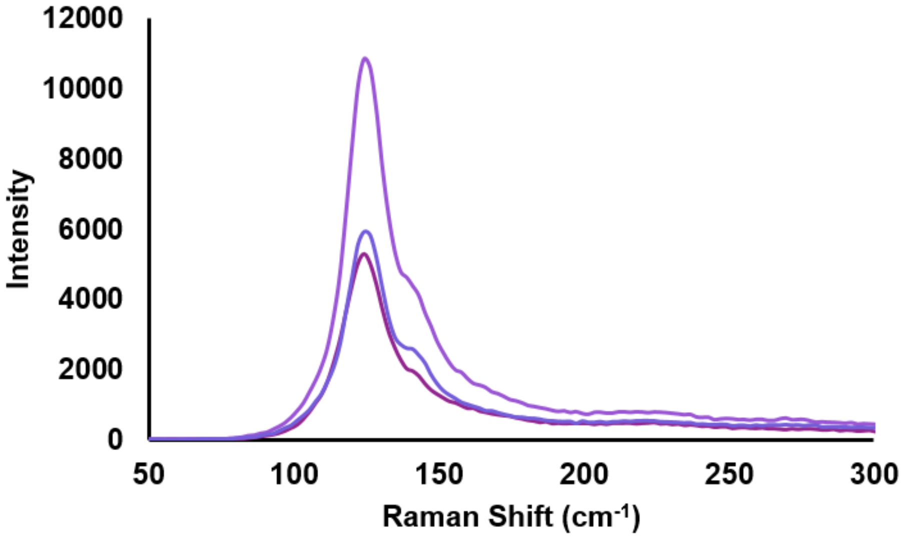

Figure 3-12: Raman spectra from three regions of a GeTe film deposited from [Ge(Te$^n$Bu)$_4$] (method 2) at 723 K onto PVD SiO$_2$.

Unfortunately, electrical measurements could not be obtained for these films due to the discontinuous form of the films.

## 3.3 Conclusions and Further Work

A new precursor, [$Ge(Te^nBu)_4$], has been synthesised, the synthesis route modified to produce a purer product, and the precursor evaluated as a single source precursor for the LP CVD of germanium telluride thin films. It has been demonstrated that crystalline germanium telluride (α-GeTe) thin films can be deposited from [$Ge(Te^nBu)_4$], as evidenced by grazing incidence XRD, SEM, EDX and Raman spectroscopy. However, it is important to note that the precursor decomposes slowly over time, and that some of the films were contaminated with crystalline tellurium. This is most likely due to the 4:1 ratio of tellurium to germanium in the precursor and the fact that the tellurium is not volatile enough to be removed under low pressure.

Modification of the structure and composition of the precursor, so that the ratio of germanium to tellurium is 1:1 (that desired for the film) would hopefully improve the deposition such that clean GeTe could be deposited reliably without the excess crystalline tellurium. Precursors such as [$R_3Ge(Te^nBu)$] (R = Me, Et, $^n$Bu) may be suitable.

Moving forward, selective depositions of GeTe may be possible, as well as combining a modified precursor with [$MeSb(Te^nBu_2)_2$] or [$SbCl_3(Te^nBu_2)_3$ to deposit the ternary material, GST ($Ge_2Sb_2Te_5$), which is a significant material due to its phase change properties. Alternatively, these precursors could be used to build up layers of GeTe and $Sb_2Te_3$ which have been used for interfacial memory and has been shown to have faster switching times than GST. These have been reported at 10 ns, and these superlattices have also shown increased write/erase lifetimes when used in data storage applications.[14,15]

## 3.4 Experimental

### 3.4.1 Synthesis and Characterisation of $[Ge(Te^{n}Bu)_4]$

All reactions were conducted using Schlenk, vacuum line and glove box techniques under a dry nitrogen atmosphere. The reagents were stored and manipulated using a glove box. Dichloromethane was dried by distillation over $CaH_2$. THF was dried by distillation over Na/ benzophenone ketyl. Reagents were acquired from Sigma-Aldrich and used as received unless otherwise stated.

**Attempted preparation of $[Ge(Te^{n}Bu)_4]$ 'method 1':**

Te powder (3.23 g, 25.0 mmol) was suspended in anhydrous THF (100 mL) and this was frozen in liquid nitrogen (- 196 °C). $^{n}$BuLi (1.6 M, 16.4 mL, 25.0 mmol) was added slowly. The solution was allowed to thaw and was stirred for 2 hours. A dark brown solution was formed. $GeCl_4$ (0.723 mL, 6.33 mmol) in anhydrous THF (10 mL) was added and the solution was allowed to stir for 16 hours. The solvent was removed *in vacuo* to leave a dark brown solid. This was extracted with anhydrous $CH_2Cl_2$ and filtered. The filtrate was a bright red solution. The solvent was removed *in vacuo* to leave a red viscous oil. It was stored in the freezer. $^{1}$H NMR ($CDCl_3$, 298 K) δ/ ppm $[Ge(Te^{n}Bu)_4]$: 0.93 (t, [3H], $CH_3$), 1.42 (m, [2H], $CH_2$), 1.86 (m, [2H], $CH_2$), 2.79 (m, [2H], $TeCH_2$), $^{n}Bu_2Te$: 0.93 (t, [3H], $CH_3$), 1.42 (m, [2H], $CH_2$), 1.86 (m, [2H], $CH_2$), 2.63 (m, [2H], $TeCH_2$), $^{n}Bu_2Te_2$: 0.93 (t, [3H], $CH_3$), 1.42 (m, [2H], $CH_2$), 1.86 (m, [2H], $CH_2$), 3.11 (m, [2H], $TeCH_2$) .$^{13}C\{^{1}H\}$ NMR ($CDCl_3$, 298 K) δ/ ppm $[Ge(Te^{n}Bu)_4]$: 13.33, 13.66, 25.69, 35.18, $^{n}Bu_2Te$: 2.54, 13.33, 25.12, 35.07, $^{n}Bu_2Te_2$: 4.67, 13.87, 25.86, 36.32 IR (neat thin film) v/cm$^{-1}$: 238, 251 cm$^{-1}$ (br) Ge-Te.

**$[Ge(TePh)_4]$:**

Synthesised according to the literature method.[74] $GeCl_2$ dioxane (232 mg, 1.0 mmol) was dissolved in anhydrous THF (50 mL).It was reduced with $Li(Et_3BH)$ (1 M, 2 mL). Once $H_2$ evolution had ceased, the solution was decanted, and the precipitated Ge washed with anhydrous THF (3 x 50 mL). It was then suspended in anhydrous THF (60 mL) and $Ph_2Te_2$ (818 mg, 2.0 mmol) was added. The reaction mixture was stirred at room temperature for 2 hrs to form a red solution. The THF was removed *in vacuo*. The remaining solid was dissolved in anhydrous diethyl ether (50 mL) and filtered. The filtrate was evacuated to dryness and washed with ice cold diethyl ether (3 x 5 mL) to afford a bright red solid. .$^{1}$H NMR ($CDCl_3$, 298 K) δ/ ppm $[Ge(TePh)_4]$: 7.19 (m, [8H]), 7.38 (m, [4H]), 7.60 (m, [8H],), $Ph_2Te_2$: 7.24 (m), 7.80 (m).

**$Te_2{}^nBu_2$:**

ground Te powder (6.40 g, 0.05 mol) was suspended in anhydrous THF (100 mL) and frozen at -196 °C in liquid nitrogen. $^nBuLi$ (1.6 M, 31.3 mL, 0.05 mol) was added slowly. It was allowed to thaw to form a dark red solution. It was cooled in ice and additional $^nBuLi$ was added dropwise until a pale-yellow solution was formed. It was again frozen in liquid nitrogen and 1,2- dichloroethane (2 mL, 0.025 mol) was added. It was allowed to thaw and stirred for a further hour to afford a red solution. The solvent was removed *in vacuo* and then it was extracted with anhydrous $CH_2Cl_2$ and washed with water. The solvent was removed *in vacuo* to leave a red oil (7.77 g, 0.032 mol, 64 %). $^1H$ NMR ($CDCl_3$, 298 K) δ/ ppm: 0.94 (t, [3H], C$H_3$), 1.40 (m, [2H], $CH_2$), 1.72 (m, [2H], $CH_2$), 3.12 (m, [2H], $TeCH_2$). $^{13}C\{^1H\}$ NMR ($CDCl_3$, 298 K) δ/ ppm: 4.22, 13.32, 24.56, 35.72. $^{125}Te\{^1H\}$ NMR ($CDCl_3$, 298 K) δ/ ppm: 112.9 ppm.

**$[Ge(Te^nBu)_4]$ method 2:**

$GeCl_2$.dioxane (464 mg, 2.00 mmol) was dissolved in anhydrous THF (100 mL) and it was reduced by addition of $Li(Et_3BH)$ (4.00 mL, 4.00 mmol). A yellow orange precipitate was formed. The THF was decanted and the activated Ge was washed with anhydrous THF (3 x 50 mL). It was then suspended in anhydrous THF (50 mL) and $^nBu_2Te_2$ (0.488 g, 2.00 mmol) in anhydrous THF (10 mL) was added and the solution left to stir under $N_2$ for 3 hours. The THF was removed *in vacuo*. The residue was extracted with anhydrous diethyl ether and filtered. The solvent was removed *in vacuo* to afford a dark red oil. $^1H$ NMR ($CDCl_3$, 298 K) δ/ ppm: 0.94 (t, [3H], C$H_3$), 1.43 (m, [2H], $CH_2$), 1.87 (m, [2H], $CH_2$), 2.79 (m, [2H], $TeCH_2$).$^{13}C\{^1H\}$ NMR ($CDCl_3$, 298 K) δ/ ppm: 12.90, 13.53, 25.29, 34.53. $^{125}Te\{^1H\}$ NMR ($CDCl_3$, 298 K, 90 K) δ/ ppm: no signal observed. IR (neat thin film) v/$cm^{-1}$: 238, 251 $cm^{-1}$ (br) Ge-Te. Anal. calcd for $GeTe_4C_{16}H_{36}$: C 23.68, H 4.47; found: C 24.32, H 4.77 %

### 3.4.2 LPCVD

Typical experiments involved loading the 50 - 100 mg of neat precursor into the end of a sealed silica tube followed by six $SiO_2$ substrates. The silica tube was then sealed with a tap and placed in a furnace and connected to a Schlenk line. The tube was positioned such that the precursor was 2 cm from the hot zone and the tube was evacuated to 0.02 mm Hg. The furnace was set to 450 °C, once the temperature was reached the tube was repositioned such that the precursor was 0 cm from the hot zone and remained at this position until the precursor had evaporated. Some grey residue was present in the bulb and silver/ grey deposition was present on the substrates closest to the precursor.

### 3.4.3 Substrate and Pre-treatment

See Appendix 1

### 3.4.4 Thin Film Characterisation

See Appendix 1

## 3.5 References

1 J. E. Boschker, R. Wang and R. Calarco, *CrystEngComm*, 2017, **19**, 5324–5335.

2 C. Wood, *Reports Prog. Phys.*, 1988, **51**, 459–539.

3 D. Wu, L. D. Zhao, S. Hao, Q. Jiang, F. Zheng, J. W. Doak, H. Wu, H. Chi, Y. Gelbstein, C. Uher, C. Wolverton, M. Kanatzidis and J. He, *J. Am. Chem. Soc.*, 2014, **136**, 11412–11419.

4 J. Arciniega, E. Prokhorov, F. Beltran and G. Trapaga, in *Crystallization - Science and Technology*, ed. M. R. B. Andreeta, InTech, Vienna, 2012, pp. 433–460.

5 M. J. Polking, M. G. Han, A. Yourdkhani, V. Petkov, C. F. Kisielowski, V. V. Volkov, Y. Zhu, G. Caruntu, A. Paul Alivisatos and R. Ramesh, *Nat. Mater.*, 2012, **11**, 700–709.

6 A. V. Kolobov, D. J. Kim, A. Giussani, P. Fons, J. Tominaga, R. Calarco and A. Gruverman, *APL Mater.*, 2014, **2**, 0661011–0661017.

7 D. Di Sante, P. Barone, R. Bertacco and S. Picozzi, *Adv. Mater.*, 2013, **25**, 509–513.

8 M. Liebmann, C. Rinaldi, D. Di Sante, J. Kellner, C. Pauly, R. N. Wang, J. E. Boschker, A. Giussani, S. Bertoli, M. Cantoni, L. Baldrati, M. Asa, I. Vobornik, G. Panaccione, D. Marchenko, J. Sánchez-Barriga, O. Rader, R. Calarco, S. Picozzi, R. Bertacco and M. Morgenstern, *Adv. Mater.*, 2016, **28**, 560–565.

9 H. J. Elmers, R. Wallauer, M. Liebmann, J. Kellner, M. Morgenstern, R. N. Wang, J. E. Boschker, R. Calarco, J. Sánchez-Barriga, O. Rader, D. Kutnyakhov, S. V. Chernov, K. Medjanik, C. Tusche, M. Ellguth, H. Volfova, S. Borek, J. Braun, J. Minár, H. Ebert and G. Schönhense, *Phys. Rev. B*, 2016, **94**, 1–5.

10 M. Wuttig and N. Yamada, *Nat. Mater.*, 2007, **6**, 824–832.

11 A. V. Kolobov, P. Fons, J. Tominaga, A. I. Frenkel, A. L. Ankuoinov, S. N. Yannopoulos, K. S. Andrikopoulos and T. Uruga, *Japanese J. Appl. Physics, Part 1 Regul. Pap. Short Notes Rev. Pap.*, 2005, **44**, 3345–3349.

12 S. Raoux, H. Y. Cheng, M. A. Caldwell and H. S. P. Wong, *Appl. Phys. Lett.*, 2009, **95**, 0719101–0719103.

13 G. Bruns, P. Merkelbach, C. Schlockermann, M. Salinga, M. Wuttig, T. D. Happ, J. B. Philipp and M. Kund, *Appl. Phys. Lett.*, 2009, **95**, 0431081–0431083.

14 T. C. Chong, L. P. Shi, R. Zhao, P. K. Tan, J. M. Li, H. K. Lee, X. S. Miao, A. Y. Du and C. H. Tung, *Appl. Phys. Lett.*, 2006, **88**, 3–6.

15 S. Cecchi, E. Zallo, J. Momand, R. Wang, B. J. Kooi, M. A. Verheijen and R. Calarco, *APL Mater.*, 2017, **5**, 0261071–0261076.

16 N. Yamada, E. Ohno, K. Nishiuchi, N. Akahira and M. Takao, *J. Appl. Phys.*, 1991, **69**, 2849–2856.

17 D. I. Bletskan, *J. Ovonic Res.*, 2005, **1**, 53–60.

18 K. M. Rabe and J. D. Joannopoulos, *Phys. Rev. B*, 1987, **36**, 6631.

19 K. Shportko, S. Kremers, M. Woda, D. Lencer, J. Robertson and M. Wuttig, *Nat. Mater.*, 2008, **7**, 653–658.

20 B. Huang and J. Robertson, *Phys. Rev. B - Condens. Matter Mater. Phys.*, 2010, **81**, 1–4.

21 A. V. Kolobov, P. Fons, J. Tominaga and M. Hase, *J. Phys. Chem. C*, 2014, **118**, 10248–10253.

22 G. Lucovsky and R. M. White, *Phys. Rev. B*, 1973, **8**, 660–667.

23 D. Lencer, M. Salinga and M. Wuttig, *Adv. Mater.*, 2011, **23**, 2030–2058.

24 J. P. Gaspard, A. Pellegatti, F. Marinelli and C. Bichara, *Philos. Mag. B Phys. Condens. Matter; Stat. Mech. Electron. Opt. Magn. Prop.*, 1998, **77**, 727–744.

25 T. Nonaka, G. Ohbayashi, Y. Toriumi, Y. Mori and H. Hashimoto, *Thin Solid Films*, 2000, **370**, 258–261.

26 V. L. Deringer, M. Lumeij and R. Dronskowski, *J. Phys. Chem. C*, 2012, **116**, 15801–15811.

27 F. Kadlec, C. Kadlec, P. Kužel and J. Petzelt, *Phys. Rev. B - Condens. Matter Mater. Phys.*, 2011, **84**, 1–8.

28 M. J. Polking, J. J. Urban, D. J. Milliron, H. Zheng, E. Chan, M. A. Caldwell, S. Raoux, C. F. Kisielowski, J. W. Ager, R. Ramesh and A. P. Alivisatos, *Nano Lett.*, 2011, **11**, 1147–1152.

29 S. Raoux, W. Wełnic and D. Ielmini, *Chem. Rev.*, 2010, **110**, 240–267.

30 A. V. Kolobov, J. Tominaga, P. Fons and T. Uruga, *Appl. Phys. Lett.*, 2003, **82**, 382–384.

31 J. E. Lewis, *Phys. Status Solidi Basic Res.*, 1969, **35**, 737–745.

32 A. H. Edwards, A. C. Pineda, P. A. Schultz, M. G. Martin, A. P. Thompson, H. P. Hjalmarson and C. J. Umrigar, *Phys. Rev. B - Condens. Matter Mater. Phys.*, 2006, **73**, 1–13.

33 T. Siegrist, P. Jost, H. Volker, M. Woda, P. Merkelbach, C. Schlockermann and M. Wuttig, *Nat. Mater.*, 2011, **10**, 202–208.

34 H. Przybylińska, G. Springholz, R. T. Lechner, M. Hassan, M. Wegscheider, W. Jantsch and G. Bauer, *Phys. Rev. Lett.*, 2014, **112**, 472021–372025.

35 R. Wang, J. E. Boschker, E. Bruyer, D. Di Sante, S. Picozzi, K. Perumal, A. Giussani, H. Riechert and R. Calarco, *J. Phys. Chem. C*, 2014, **118**, 29724–29730.

36 R. Shaltaf, X. Gonze, M. Cardona, R. K. Kremer and G. Siegle, *Phys. Rev. B*, 2009, **79**, 0752041–0752047.

37 D. Campi, D. Donadio, G. C. Sosso, J. Behler and M. Bernasconi, *J. Appl. Phys.*, 2015, **117**, 0153041–0153049.

38 E. M. Levin, M. F. Besser and R. Hanus, *J. Appl. Phys.*, 2013, **114**, 0837131–0837139.

39 W. Wełnic, S. Botti, L. Reining and M. Wuttig, *Phys. Rev. Lett.*, 2007, **98**, 1–4.

40 S.K.Bahl and K.L.Chopra, *J. Appl. Phys.*, 1970, **41**, 2196–2212.

41 R. Tsu, W. E. Howard and L. Esaki, *Solid State Commun.*, 1967, **5**, 167–171.

42 P. Nukala, C.-C. Lin, R. Composto and R. Agarwal, *Nat. Commun.*, 2016, **7**, 104821–104828.

43 P. Nukala, R. Agarwal, X. Qian, M. H. Jang, S. Dhara, K. Kumar, A. T. C. Johnson, J. Li and R. Agarwal, *Nano Lett.*, 2014, **14**, 2201–2209.

44 G. Kalra and S. Murugavel, *AIP Adv.*, 2015, **5**, 0471271–0471278.

45 G. Navarro, V. Sousa, A. Persico, N. Pashkov, A. Toffoli, J. C. Bastien, L. Perniola, S. Maitrejean, A. Roule, P. Zuliani, R. Annunziata and B. De Salvo, *Solid. State. Electron.*, 2013, **89**, 93–100.

46 A. H. Gwin and R. A. Coutu, *SPIE Proc.*, 2015, **9364**, 93640G1-93640G10.

47 L. Perniola, V. Sousa, A. Fantini, E. Arbaoui, A. Bastard, M. Armand, A. Fargeix, C. Jahan, J. F. Nodin, A. Persico, D. Blachier, A. Toffoli, S. Loubriat, E. Gourvest, G. B. Beneventi, H. Feldis, S. Maitrejean, S. Lhostis, A. Roule, O. Cueto, G. Reimbold, L. Poupinet, T. Billon, B. De Salvo, D. Bensahel, P. Mazoyer, R. Annunziata, P. Zuliani and F. Boulanger, *IEEE Electron Device Lett.*, 2010, **31**, 488–490.

48 J. W. Park, S. H. Baek, T. D. Kang, H. Lee, Y. S. Kang, T. Y. Lee, D. S. Suh, K. J. Kim, C. K. Kim, Y. H. Khang, J. L. F. Da Silva and S. H. Wei, *Appl. Phys. Lett.*, 2008, **93**, 3–6.

49 M. A. Hughes, Y. Fedorenko, B. Gholipour, J. Yao, T.-H. Lee, R. M. Gwilliam, K. P. Homewood, S. Hinder, D. W. Hewak, S. R. Elliott and R. J. Curry, *Nat. Commun.*, 2014, **5**, 53461–53469.

50 K. S. Andrikopoulos, S. N. Yannopoulos, G. A. Voyiatzis, A. V Kolobov, M. Ribes and J. Tominaga, *J. Phys. Condens. Matter*, 2006, **18**, 965–979.

51 K. S. Andrikopoulos, S. N. Yannopoulos, A. V. Kolobov, P. Fons and J. Tominaga, *J. Phys. Chem. Solids*, 2007, **68**, 1074–1078.

52 C. Longeaud, J. Luckas, D. Krebs, R. Carius, J. Klomfass and M. Wuttig, *J. Appl. Phys.*, 2012, **112**, 1137141–1137148.

53 V. Bragaglia, K. Holldack, J. E. Boschker, F. Arciprete, E. Zallo, T. Flissikowski and R. Calarco, *Sci. Rep.*, 2016, **6**, 285601–285607.

54 A. Giussani, K. Perumal, M. Hanke, P. Rodenbach, H. Riechert and R. Calarco, *Phys. Status Solidi Basic Res.*, 2012, **249**, 1939–1944.

55 J.-W. Park, M. Song, S. Yoon, H. Lim, D. S. Jeong, B. Cheong and H. Lee, *Phys. Status Solidi*, 2013, **210**, 267–275.

56 T. Gwon, T. Eom, S. Yoo, H. K. Lee, D. Y. Cho, M. S. Kim, I. Buchanan, M. Xiao, S. Ivanov and C. S. Hwang, *Chem. Mater.*, 2016, **28**, 7158–7166.

57 M. J. Polking, H. Zheng, R. Ramesh and A. P. Alivisatos, *J. Am. Chem. Soc.*, 2011, **133**, 2044–2047.

58 O. Salicio, C. Wiemer, M. Fanciulli, W. Gawelda, J. Siegel, C. N. Afonso, V. Plausinaitiene and A. Abrutis, *J. Appl. Phys.*, 2009, **105**, 0335201–0335206.

59 A. Abrutis, V. Plausinaitiene, M. Skapas, C. Wiemer, W. Gawelda, J. Siegel and S. Rushworth, *J. Cryst. Growth*, 2009, **311**, 362–367.

60 S. . Ovshinsky and S. Kamepalli, *US Pat., 083 481, 2006*.

61 R.-Y. Kim, H.-G. Kim and S.-G. Yoon, *J. Electrochem. Soc.*, 2008, **155**, D137.

62 C. H. de Groot, C. Gurnani, A. L. Hector, R. Huang, M. Jura, W. Levason and G. Reid, *Chem. Mater.*, 2012, **24**, 4442–4449.

63 S. D. Reid, A. L. Hector, W. Levason, G. Reid, B. J. Waller and M. Webster, *Dalton Trans.*, 2007, **4**, 4769–4777.

64 M. F. Davis, W. Levason, G. Reid, M. Webster and W. Zhang, *Dalton Trans.*, 2008, **4334**, 533–538.

65 G. Gupta, T.-M. Jeong, C. G. Kim and J. Kim, *Mater. Lett.*, 2015, **156**, 121–124.

66 H. S. Kim, E. A. Jung, S. H. Han, J. H. Han, B. K. Park, C. G. Kim and T. M. Chung, *Inorg. Chem.*, 2017, **56**, 4084–4092.

67 T. Chen, W. Hunks, P. S. Chen, G. T. Stauf, T. M. Cameron, C. Xu, A. G. DiPasquale and A. L. Rheingold, *Eur. J. Inorg. Chem.*, 2009, **2009**, 2047–2049.

68 S. L. Benjamin, C. H. de Groot, A. L. Hector, R. Huang, E. Koukharenko, W. Levason and G. Reid, *J. Mater. Chem. C*, 2015, **3**, 423–430.

69 P. Bauer Pereira, I. Sergueev, S. Gorsse, J. Dadda, E. Müller and R. P. Hermann, *Phys. Status Solidi Basic Res.*, 2013, **250**, 1300–1307.

70 T. Chattopadhyay, J. X. Boucherle and H. G. VonSchnering, *J. Phys. C Solid State Phys.*, 1987, **20**, 1431–1440.

71 S. G. Parker, J. E. Pinnell and L. N. Swink, *J. Mater. Chem.*, 1974, **9**, 1829–1832.

72 A. J. Bradley, *Philos. Mag. Ser. 6*, 1924, **48**, 477–496.

73 S. Lin, W. Li, Z. Chen, J. Shen, B. Ge and Y. Pei, *Nat. Commun.*, 2016, **7**, 1–6.

74 S. Schlecht and K. Friese, *Eur. J. Inorg. Chem.*, 2003, **2003**, 1411–1415.

75 D. Sarkar, G. Sanjeev and M. G. Mahesha, *Appl. Phys. A Mater. Sci. Process.*, 2015, **119**, 49–54.

# Chapter 4: Precursors for the Deposition of Tin Chalcogenides

## 4.1 Introduction

Tin chalcogenides ($SnE_x$) (E = S, Se) (x = 1, 2) are semiconducting materials that are widely becoming acknowledged as important materials for a variety of electronic applications; specifically optoelectronics,[1–5] thermoelectric[6,7] and phase change devices.[8,9] $SnS_2$ shows potential for use in photodetectors, with its high external quantum efficiency of 3.2 x $10^5$%;[1] high performance sodium storage, with a high reversible capacity reported of 576 mA h $g^{-1}$;[10] and phototransistors with a high on/off ratio reported of $>10^6$.[2] SnS, on the other hand, has a very low thermal conductivity ~ 0.29 W ($mK^{-1}$) and ZT value of 0.41[7] which are properties of particular interest for thermoelectric devices. Remarkably, ZT values of up to 2.6 have been reported for single crystals of SnSe.[6] Thermoelectric devices are important as sustainable energy sources. In the increasingly technological world, phase change materials are of interest for data storage applications. Fast recrystallisation times are key and $SnSe_2$, with a recrystallisation time of 20 ns,[9] is a promising material in this field.

SnS[11] and SnSe[12] crystallise in an orthorhombic phase, whereas $SnS_2$[13] and $SnSe_2$[14] are typically found with the $PbI_2$ structure. Interestingly, $SnS_2$ exhibits polytypism and over seventy forms are known in which the c parameter of the unit cell varies.[15] The mixed valence compound $Sn_2S_3$ is also known. [16]

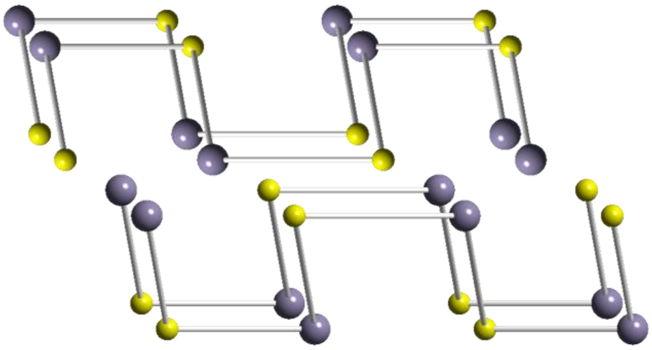

Figure 4-1: An illustration of the crystal structure of orthorhombic SnS.

Tin chalcogenide thin films can be produced by a variety of methods. Dip deposition has been used to synthesise SnS and $SnS_2$,[17] and thermal evaporation has been used to deposit SnS.[18] SnS has also been deposited from a variety of tin and sulfur sources using chemical bath deposition techniques.[19–23] For example, Ristov *et al.* used solutions of $SnCl_2$ and either $Na_2S$ or $(NH_4)_2S$[19] whilst Tanusevski *et al.* used $NH_4F$, $SnCl_2.H_2O$, $NH_4OH$ and $Na_2S_2O_3$.[22] $SnS_2$ has been deposited from elemental tin and sulfur via chemical vapour transport.[24] Other methods of deposition of tin sulfide thin films include melt growth,[25] spray pyrolysis[26] and atomic layer deposition.[27]

Using atmospheric pressure chemical vapour deposition and a dual source precursor approach, $SnCl_4$ with either $H_2S$ or $Et_2Se$ can produce $SnS_2$ or SnS,[28,29] and $SnSe_2$ or SnSe,[30] respectively, depending on the conditions employed. A single source approach, in which the metal and chalcogen are incorporated into one molecular compound, can lead to easier to handle precursors (since coordinatively saturated), potentially easier control of stoichiometry and, in some cases, the ability to deposit the binary material selectively onto specific regions of a substrate on the micro[31] or nano-scale.[32] While this substrate selectivity is rather atypical of CVD, it can be highly advantageous for certain applications. The degree of selectivity has been shown to be very strong for $SnSe_2$.[33]

In the literature, SnS and $SnS_2$ have been produced from the tin(IV) thiolate complex $[Sn(SCH_2CH_2S)]$ using aerosol assisted CVD in the presence of $H_2S$ gas,[34] or using alkyl tin dithiocarbamates[35] and SnS nanosheets by liquid exfoliation.[36] Previous single source approaches to tin sulfide and selenide thin films at the University of Southampton have used the thio- and selno-ether complexes, $[SnCl_4\{o\text{-}C_6H_4(CH_2EMe)_2\}]$ (E = S, Se)[37] to produce $SnS_2$ and small amounts of SnS and SnSe; $[SnCl_4(SeEt_2)_2]$[37] and $[SnCl_4\{^nBuSe(CH_2)_xSe^nBu\}]$ (x = 2,3)[33] to form $SnSe_2$. Within the chalcogenoether and chalcogenolate based precursors, terminal butyl substituents have been shown to be well suited for the growth of high quality binary chalcogenide thin films. This is attributed to their clean, low energy β-hydride elimination pathway.

Distorted octahedral tin(IV) halide complexes with a range of neutral thio-, seleno- and telluro-ether ligands have been reported previously, with the chloro complexes proving rather less hydrolytically sensitive than either those of the heavier halide analogues or indeed $SnCl_4$ itself.[38–40] Furthermore, LPCVD studies using the selenoether complexes, $[SnCl_4(SeEt_2)_2]$[37] (Figure 4-2) and $[SnCl_4\{^nBuSe(CH_2)_3Se^nBu\}]$,[33] have been shown to produce polycrystalline $SnSe_2$ thin films.

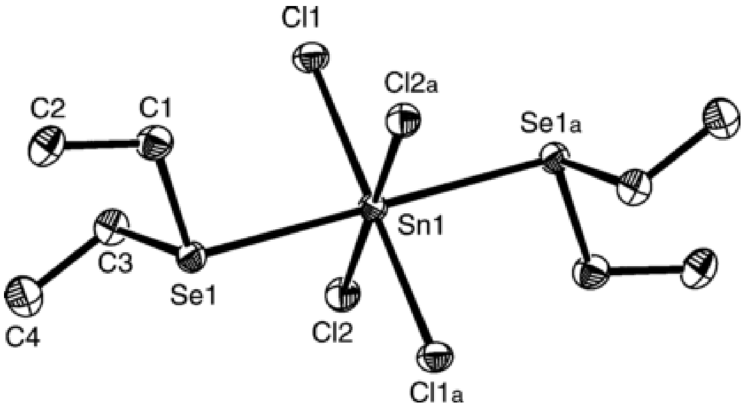

Figure 4-2: The crystal structure of trans-[$SnCl_4(Et_2Se)_2$].[37] (Reproduced from reference 37 with permission from the RSC).

LPCVD of [$SnCl_4\{o\text{-}C_6H_4(CH_2SeMe)_2\}$] at 873 K resulted in SnSe,[37] and, despite the S–C bonds in thioethers being stronger than Se–C bonds,[41] [$SnCl_4\{o\text{-}C_6H_4(CH_2SMe)_2\}$] has been shown to be suitable as a single source precursor for the deposition of tin sulfide thin films, forming $SnS_2$ at 923 K (furnace temperature), with some SnS forming further into the hot zone.[37] However, deposition of the monochalcogenides, SnE (E = S, Se), led to rather poor, non-continuous substrate coverage in all cases, and with $SnS_2$ typically deposited on the same substrate.[37] This may occur because the temperature required for the sublimation of the [$SnCl_4\{o\text{-}C_6H_4(CH_2SMe)_2\}$] precursor is very close to that of the temperature switch between the deposition of $SnS_2$ and SnS.

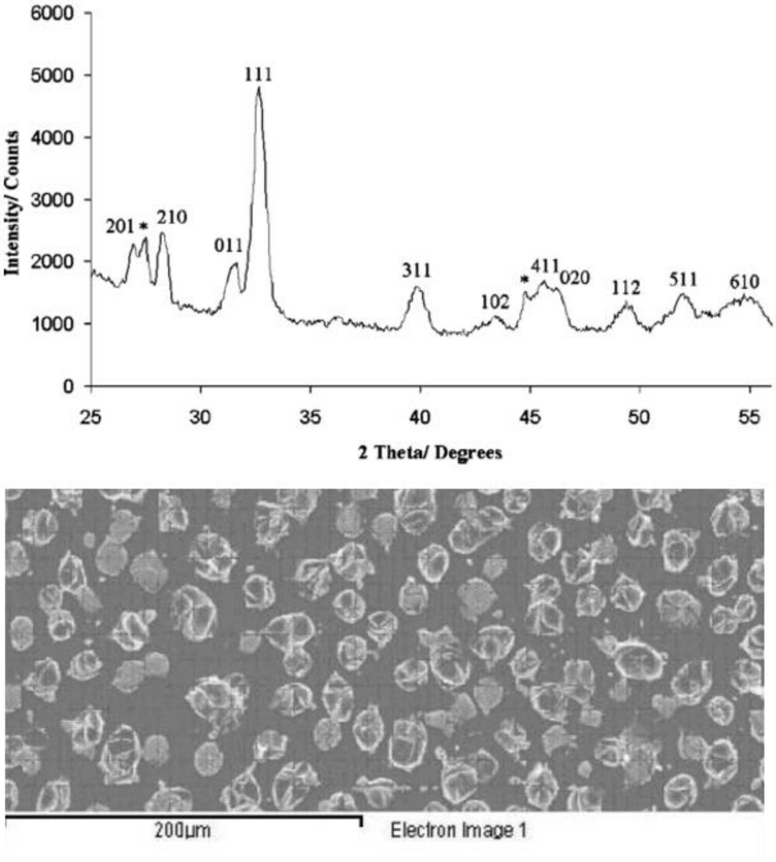

Figure 4-3: GIXRD (top) and SEM image (bottom) of SnS deposited from [$SnCl_4${o-$C_6H_4(CH_2SMe)_2$}].[37] (Reproduced from reference 37 with permission from the RSC).

By modifying the precursor to be more volatile, as well as incorporating $^n$Bu substituents in place of Me groups (the former have been shown to lead to cleaner growth of metal chalcogenides in other work)[33], it was proposed that the temperature difference between sublimation of precursor and deposition of the metal chalcogenide would be increased and better film quality achieved. Additionally, precursors containing the monodentate $E^nBu_2$ (E = S, Se) ligands would be more convenient for use by other workers than bidentate ligands. Finally, it was anticipated that these precursors may facilitate growth of both $SnE_2$ and SnE depending upon the deposition conditions used (with any excess $^nBu_2E$ being distilled off readily under the low-pressure CVD conditions employed or acting as a source of chalcogen to maintain stoichiometry).

The aims of this chapter were to synthesise novel tin(IV) thioether and selenoether precursors for the LPCVD of tin chalcogenide thin films and to attempt to tailor the CVD experiments with the aim to deposit thin films of tin monochalcogenides in preference to tin dichalcogenides.

## 4.2 Results and Discussion

### 4.2.1 Synthesis and Characterisation of [SnCl$_4${$^n$BuE(CH$_2$)$_3$E$^n$Bu}] and [SnCl$_4$(E$^n$Bu$_2$)$_2$] (E = S, Se)

The novel complexes, [SnCl$_4$($^n$Bu$_2$E)$_2$] (E = S, Se) and [SnCl$_4${$^n$BuS(CH$_2$)$_3$S$^n$Bu}] were synthesised in good yield by the direct reaction of SnCl$_4$ and the appropriate ligand in anhydrous hexane at room temperature (Scheme 4-1). The complexes were readily isolated as white or off white powdered solids by filtration. They are somewhat hydrolytically sensitive and therefore were stored and handled in a dry N$_2$-purged glove-box. They have been characterised by $^1$H, $^{13}$C{$^1$H} and variable temperature $^{77}$Se{$^1$H} and $^{119}$Sn NMR spectroscopy, IR spectroscopy, and by microanalysis, as appropriate. The IR and microanalytical data were fully consistent with the formulations, while solution phase NMR data for [SnCl$_4$($^n$Bu$_2$E)$_2$] reveal similar chemical shift ranges and dynamic behaviour in solution, fully consistent with that of *cis* and *trans* distorted octahedral complexes.

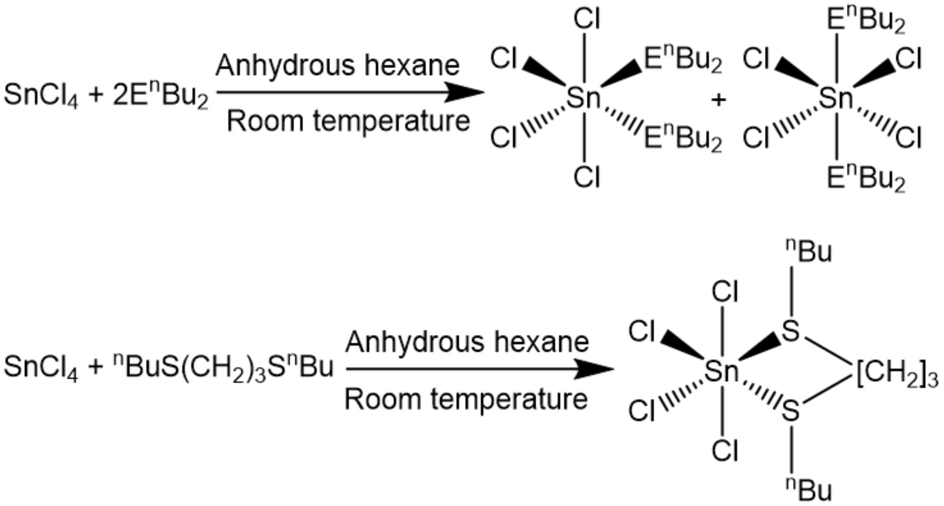

Scheme 4-1: The reactions of SnCl$_4$ with thioether and selenoether ligands. (E = S, Se)

As with the previously reported tin(IV) halide complexes with dithioether ligands,[38–40] the low temperature $^{119}$Sn NMR spectrum from [SnCl$_4${$^n$BuS(CH$_2$)$_3$S$^n$Bu}] shows two singlets representing the meso and DL diastereoisomers. Meso and DL diasteroisomers were also present for the Sn(IV) complexes with monodentate chalcogenoether ligands. In the low temperature NMR spectra for [$SnCl_4(Se^nBu_2)_2$] (Figure 4-4), coupling between the $^{119}Sn$ and $^{77}Se$ nuclei can be observed. The couplings were observed as 530 Hz (minor) and 478 Hz (major).

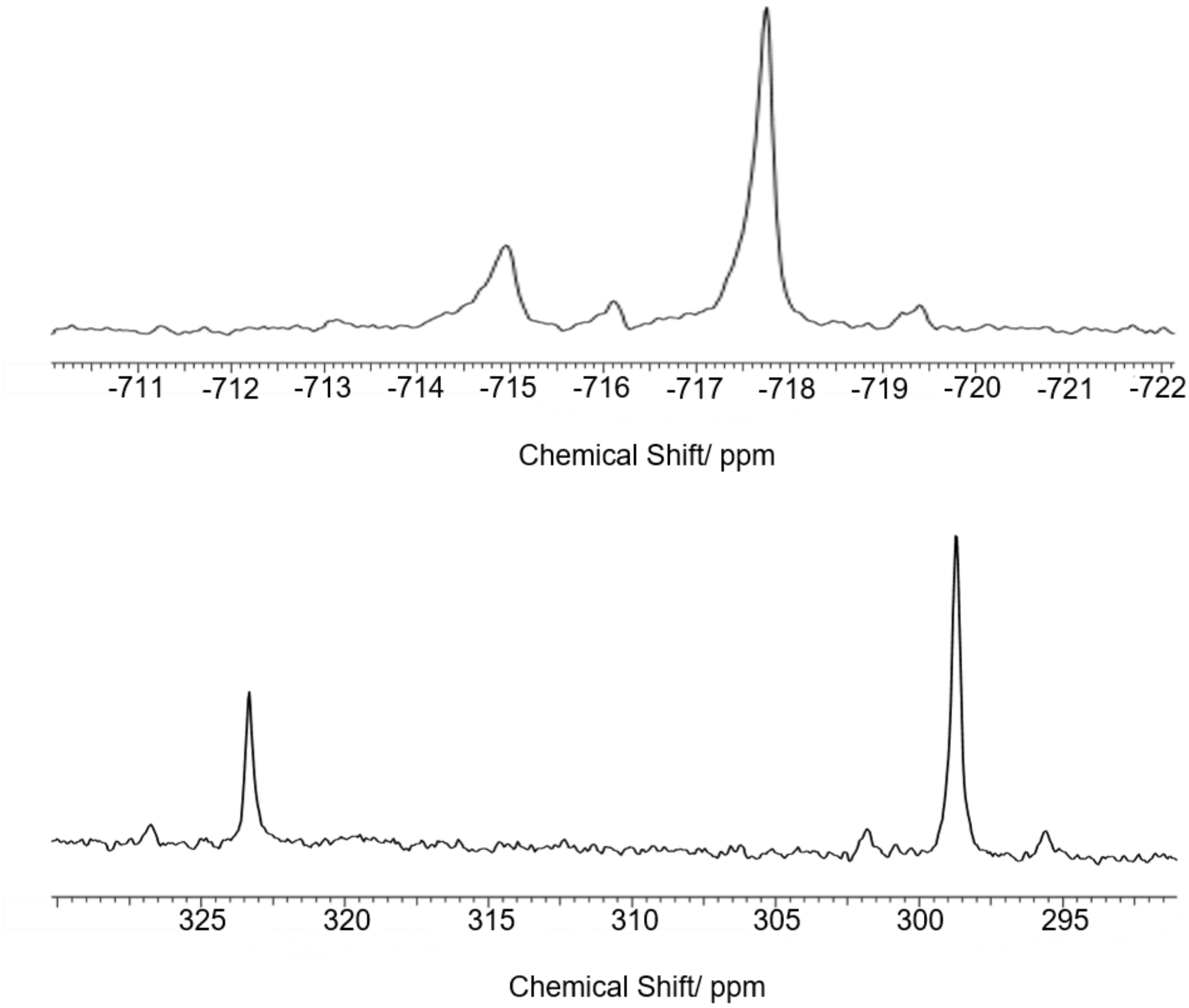

Figure 4-4: Low temperature $^{119}Sn$ NMR spectrum of [$SnCl_4(Se^nBu_2)_2$] ($CH_2Cl_2$, −90 ˚C) (top) and low temperature $^{77}Se\{^1H\}$ NMR spectrum of [$SnCl_4(Se^nBu_2)_2$] ($CH_2Cl_2$, −90 ˚C) (bottom). $^{119}Sn$ satellites are also shown.

Characterisation of these new precursors by IR spectroscopy shows broad Sn-Cl bands at 324 $cm^{-1}$ for [$SnCl_4\{^nBuS(CH_2)_3S^nBu\}$], 300, 318 and 330 $cm^{-1}$ for [$SnCl_4(S^nBu_2)_2$] and 292, 302 and 324 $cm^{-1}$ for [$SnCl_4(Se^nBu_2)_2$]. These values are consistent with those reported in the literature for Sn-Cl bands, with 236, 264 and 319 $cm^{-1}$, and 311 $cm^{-1}$ reported for [$SnCl_4\{^nBuSe(CH_2)_nSe^nBu\}$] (n = 2,3) respectively.[33]

Thermogravimetric analysis (TGA) of all of the precursors under an argon atmosphere showed clean and complete sublimation of $[SnCl_4\{^nBuS(CH_2)_3S^nBu\}]$, $[SnCl_4(^nBu_2S)_2]$ and $[SnCl_4(^nBu_2Se)_2]$ at 468 K, 411 K and 477 K, respectively as shown in Figure 4-5 below.

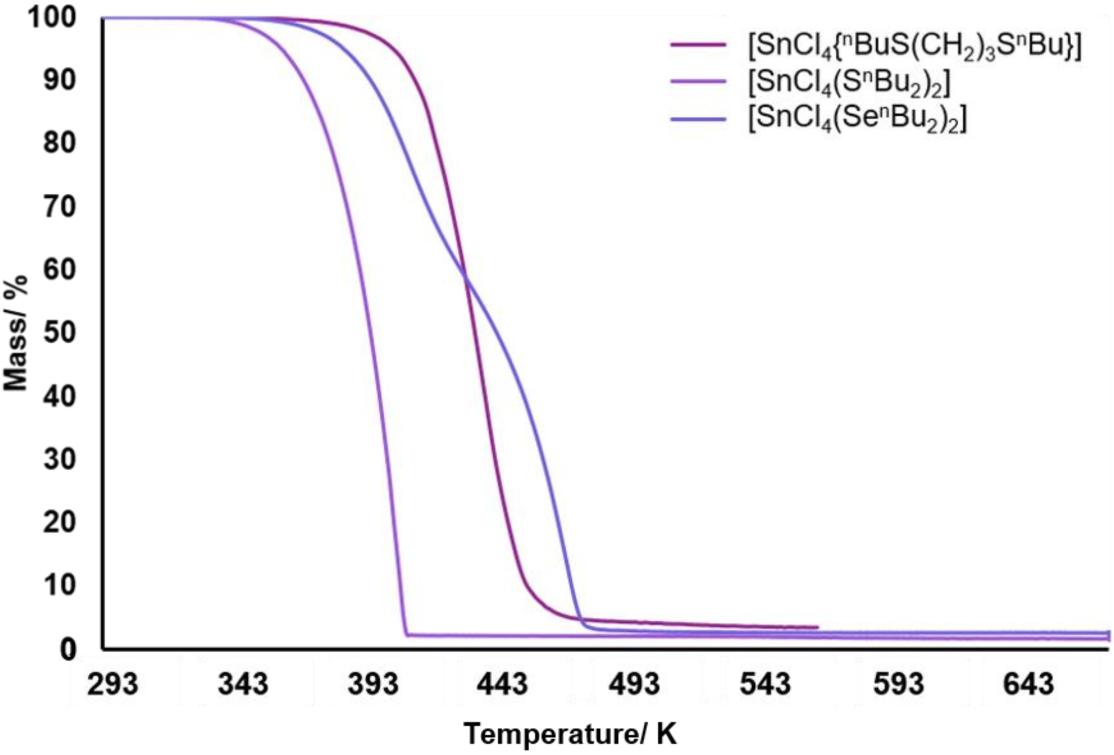

Figure 4-5: The TGA profiles of $[SnCl_4\{^nBuS(CH_2)_3S^nBu\}]$, $[SnCl_4(S^nBu_2)_2]$ and $[SnCl_4(Se^nBu_2)_2]$ under a 40 SCCM argon atmosphere with a ramp rate of 5 Kmin$^{-1}$.

### 4.2.2 Deposition and Characterisation of $SnS_2$ Thin Films

LPCVD experiments using the precursors $[SnCl_4\{^nBuS(CH_2)_3S^nBu\}]$ and $[SnCl_4(S^nBu_2)_2]$ at 559 and 645 K (0.02 mmHg), respectively, resulted in the deposition of $SnS_2$ in both cases, without the need for an additional chalcogen source. Film deposition tended to occur mostly at the edge of the heated zone nearest to the precursor, typically leading to *ca.* 50% coverage of the substrate.

SEM images of the thin films (Figure 4-6) revealed hexagonal platelets formed from both precursors, with higher uniformity and larger crystallites observed in the deposit formed from $[SnCl_4\{^nBuS(CH_2)_3S^nBu\}]$. In the deposition from $[SnCl_4(S^nBu_2)_2]$, larger truncated crystallites are also observed. EDX analysis revealed composition of 36% Sn and 64% S and 34% Sn, 66% S for the films deposited from [$SnCl_4\{^nBuS(CH_2)_3S^nBu\}$] (at T = 559 K) and [$SnCl_4(S^nBu_2)_2$] (at T = 645 K), respectively, consistent within experimental error of $SnS_2$, with no residual Cl observed.

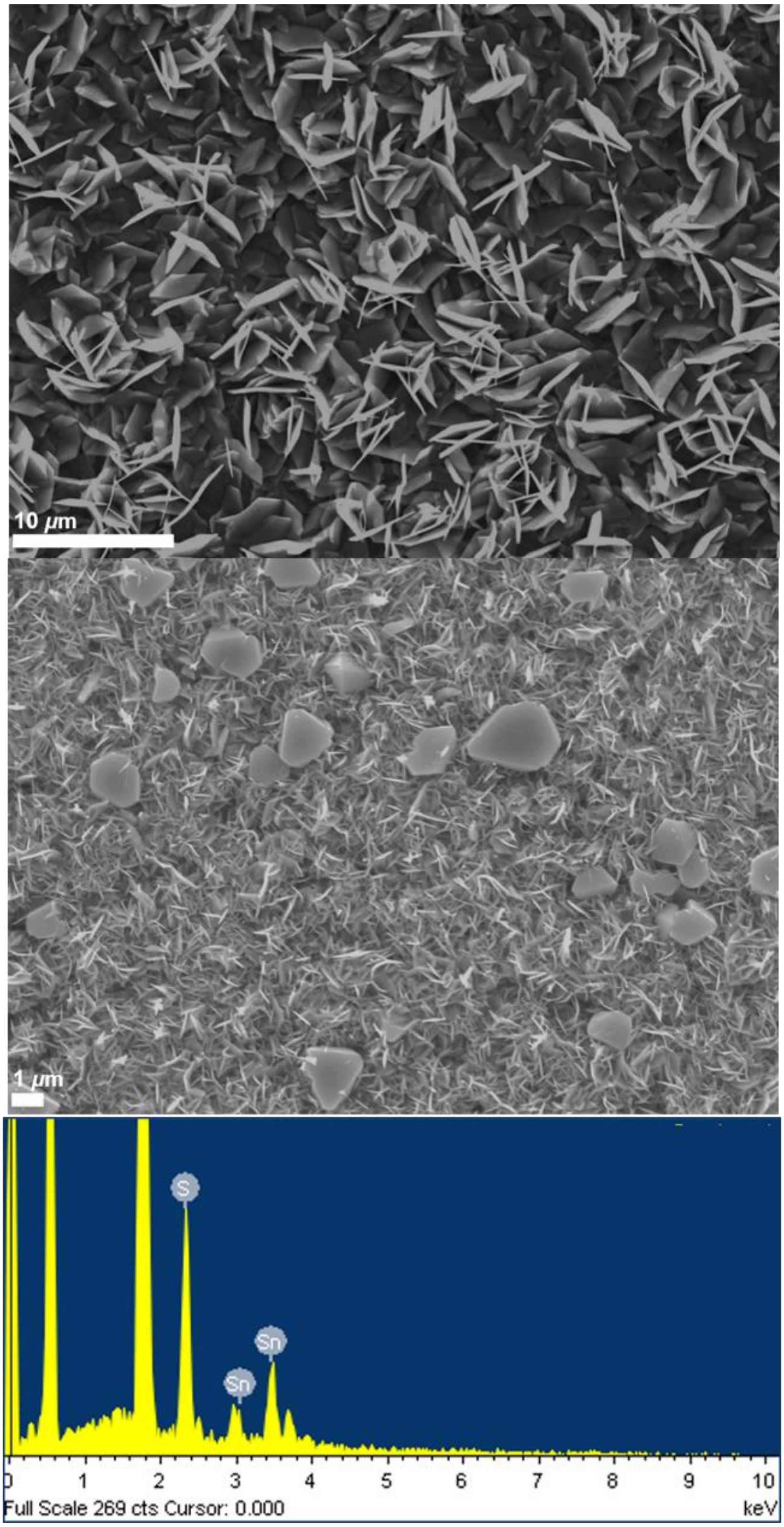

Figure 4-6: SEM images of $SnS_2$ films deposited from $[SnCl_4\{^nBuS(CH_2)_3S^nBu_2\}]$ (top) at 559 K and $[SnCl_4(S^nBu_2)_2]$ (middle) at 645 K and a typical EDX spectrum of the film deposited from $[SnCl_4\{^nBuS(CH_2)_3\,S^nBu\}]$ at 559 K. The dominating peaks at ~0.5 kEV and 1.7 keV are due to O and Si respectively from the substrate.

Grazing incidence XRD patterns also show that crystalline $SnS_2$ was formed in both cases and are consistent with the space group $P\bar{3}m1$ (2H-$SnS_2$). In the deposition from $[SnCl_4(S^nBu_2)_2]$, a second phase of $SnS_2$, in space group P63mc, was also present (4H-$SnS_2$) and SEM analysis shows larger truncated crystallites. The refined lattice parameters for the films deposited from $[SnCl_4\{^nBuS(CH_2)_3S^nBu\}]$ (a = 3.664(3), c = 5.935(8) Å) also match well with literature values of Berndtite-2H $SnS_2$ (*a* = 3.62–3.70, *c* = 5.66–5.90 Å).[13,28,42] Lattice parameters for the film deposited from $\{SnCl_4(S^nBu_2)_2]$ (a = 3.642(3), c = 5.930(9) Å) and (a =3.643(7), c = 11.84(4) Å) match well with those of Berndtite-2H (*a* = 3.62-3.70, *c* = 5.66-5.90 Å)[13,28,42] and Berndtite-4H (*a* = 3.64, *c* = 11.80 Å) $SnS_2$,[43] respectively. Lattice parameters were calculated by optimisation of the fit in PDXL2.

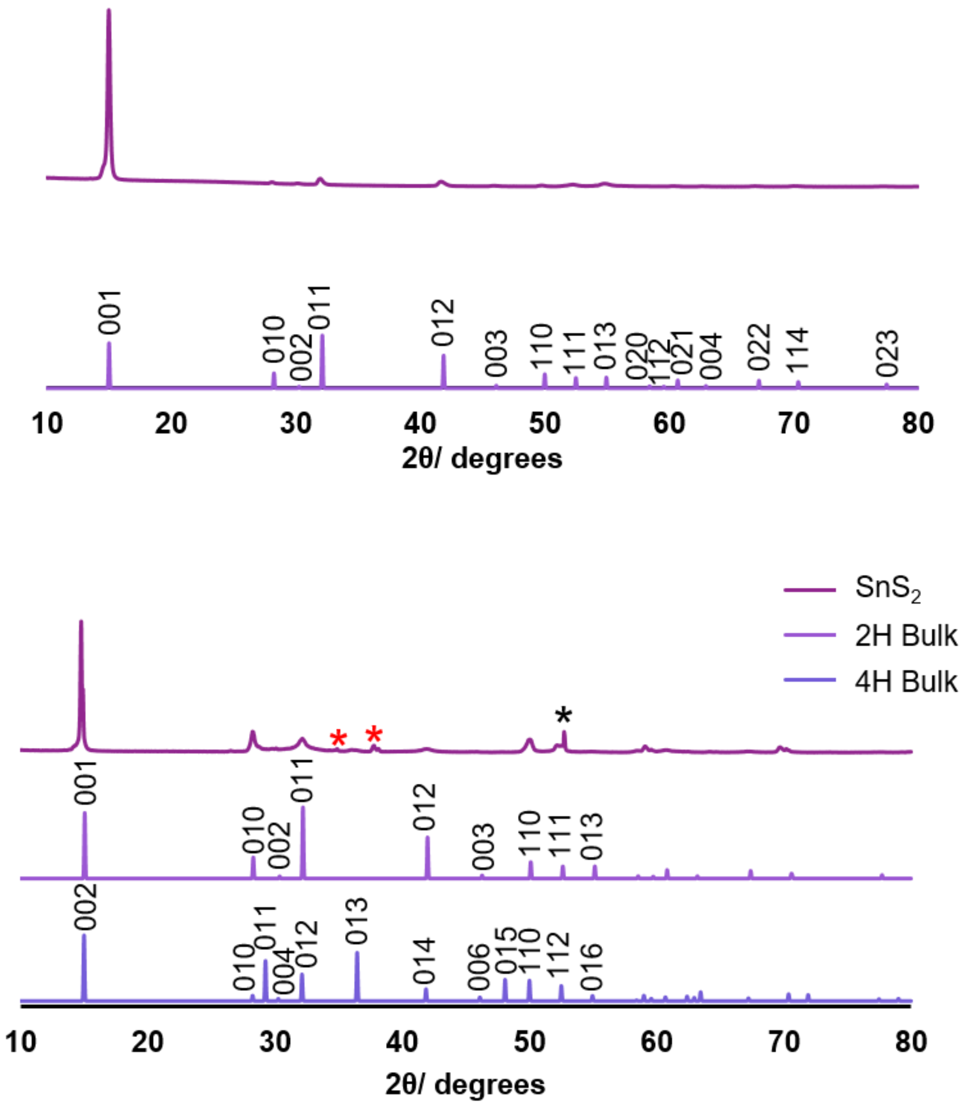

Figure 4-7: Grazing incidence XRD patterns from the $SnS_2$ film deposited from $[SnCl_4\{^nBuS(CH_2)_3S^nBu\}]$, with stick pattern from the literature data for bulk 2H-$SnS_2$[13] (top) and from $SnS_2$ film deposited from $[SnCl_4(^nBu_2S)_2]$ and stick patterns for bulk 2H-$SnS_2$[13] and 4H-$SnS_2$.[43] The reflections marked with a red asterisk are from the TiN layer underlying the top $SiO_2$ on the substrate, whilst the reflection marked with a black asterisk is from the Si (bottom).

The (0 0 1) reflection is very intense in both samples, which is typical for thin films of these crystal types and indicates significant preferred orientation. Pole figure measurements were also acquired for the key reflections in the film grown from $[SnCl_4\{^nBuS(CH_2)_3S^nBu\}]$ in order to further investigate the preferred orientation further (Figure 4-8). The pole figure for the (0 0 1) reflection reveals a sharp spot in the projection and a narrow peak in the integral at α = 90 °. This is consistent with strong orientation of the *c* axis perpendicular to the substrate and the crystallites lying parallel. The SEM images show the edges of crystallites which suggests the c-axis in the film plane, so the pole figure shows the bulk of the underlying material is lying flat. For the (0 1 1) reflection, a ring is observed at α = 28 °. The expected value for this reflection with crystallites in the (0 0 1) orientation is calculated as α = 28.1 ° (tan α = *a*cos30/*c*).

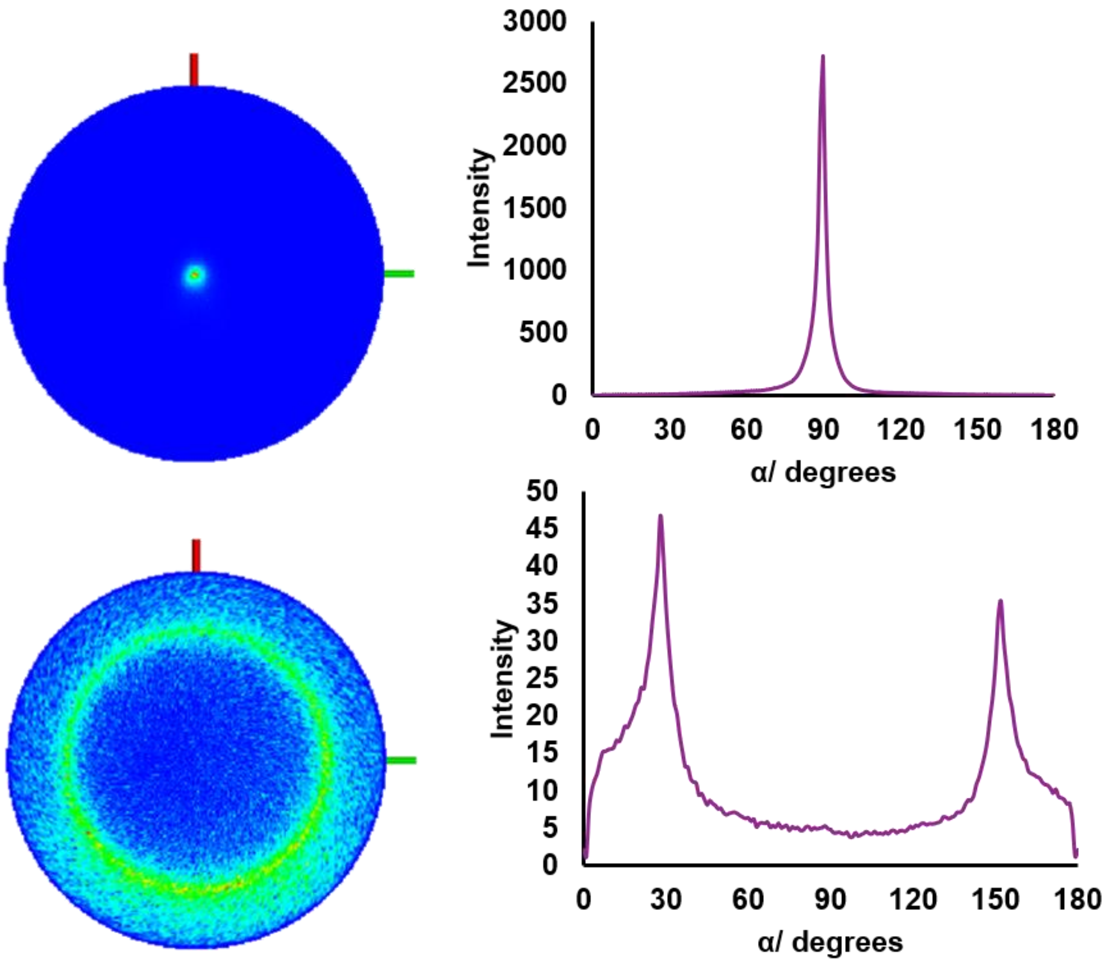

Figure 4-8: 3D Pole figure projections with α integral of the $SnS_2$ thin film deposited from $[SnCl_4\{{}^nBuS(CH_2)_3S{}^nBu\}]$ at 559 K, showing the (0 0 1) plane (top) and (0 1 1) plane (bottom) where α is the tilt angle from the sample surface normal direction.

The Pole figure showing that the film is highly orientated with the (0 0 1) lattice vector perpendicular to the surface is in contrast to the SEM image which shows the crystallites standing up. This suggests that the majority of the film lies flat beneath the surface crystallites which are orientated with the lattice vectors parallel to the surface.

Raman spectra (Figure 4-9) recorded for the thin films deposited from [$SnCl_4${$^nBuS(CH_2)_3S^nBu$}] showed an intense peak at ~ 320 cm$^{-1}$ and a small broad feature at ~ 200 cm$^{-1}$. This is consistent with values reported in the literature of 313 cm$^{-1}$ and 205 cm$^{-1}$, representing the $A_{1g}$ and $E_g$ modes for 2H-$SnS_2$.[44,45] It is noted that an additional peak positioned at ~190 cm$^{-1}$ was also detected in some regions (asterisk in Figure 4-9). This could be attributed to the $E_2$ peak of the 4H-$SnS_2$ phase, although this phase is not evident in the XRD data. The broad feature at ~200 cm$^{-1}$, present in the Raman spectrum of the film deposited from [$SnCl_4(S^nBu_2)_2$] is attributed to the overlapping peaks (200-214 cm$^{-1}$) associated with the 4H$SnS_2$ and 2H-$SnS_2$ phases.[45]

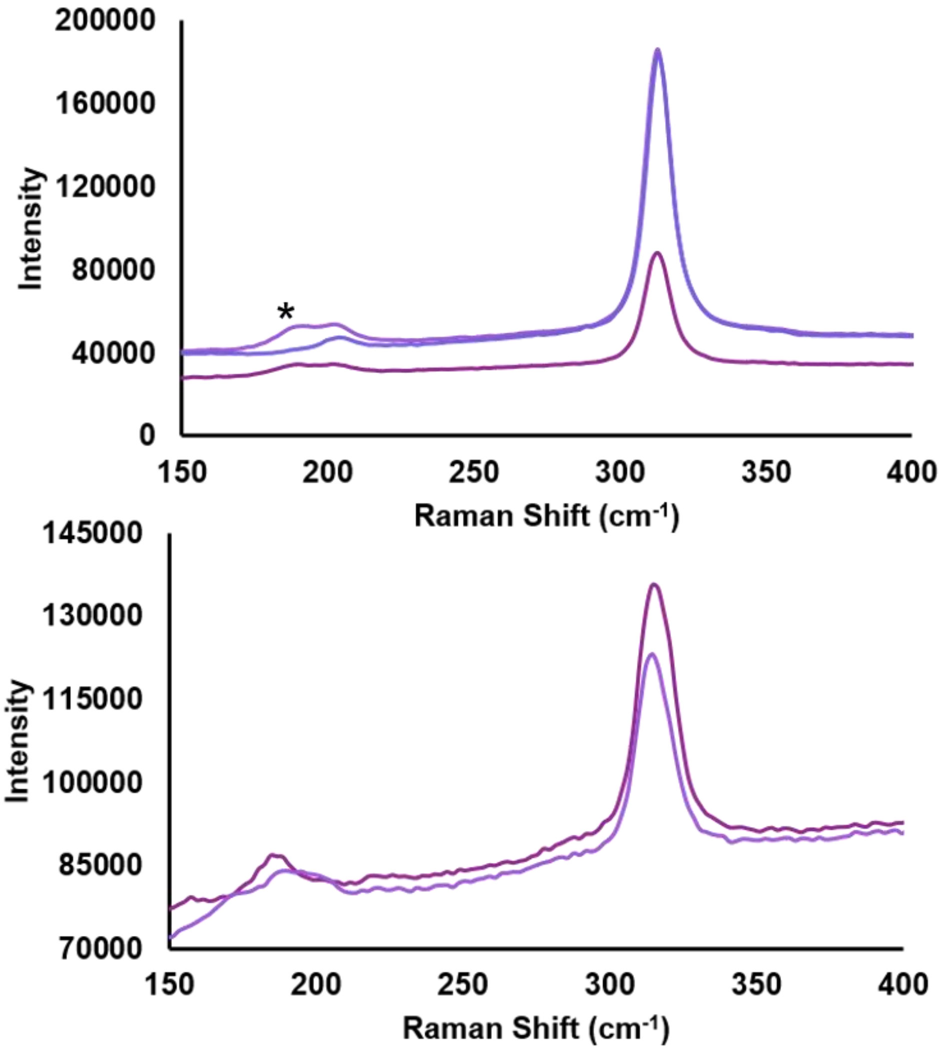

Figure 4-9: Raman spectra of the $SnS_2$ films deposited from $[SnCl_4\{^nBuS(CH_2)_3S^nBu\}]$ at 559 K (top) and $[SnCl_4(S^nBu_2)_2]$ at 645 K (bottom).

The resistivity of the $SnS_2$ thin film grown from $[SnCl_4\{^nBuS(CH_2)_3S^nBu\}]$ at 559 K was determined by van der Pauw measurements. The film shows a low resistivity, $\rho = 2.9(9)$ Ω·cm, compared with other reported values.[46,47] This could be attributed to the deviation from precise 1:2 stoichiometry. Similar behaviour was also reported by Kourtakis *et al*. in which a low n-type resistivity of $\rho = 4.5(5)$ Ω·cm was observed due to a deficit of sulfur in the $SnS_2$ film. In that case annealing in a sulfur atmosphere led to the film resistivity increasing to $2\text{x}10^5$ Ω·cm, demonstrating that non-stoichiometry was predominantly responsible for the low $SnS_2$ resistivity.[48]

### 4.2.3 Attempted Deposition and Characterisation of SnS Thin Films

Depositions were also carried out at an increased temperature in an effort to promote the formation of SnS over $SnS_2$. Using the hotter furnace temperature, LPCVD of $[SnCl_4\{^nBuS(CH_2)_3S^nBu\}]$ still gave $SnS_2$ mainly (at the region nearer the precursor where the temperature isn't significantly increased), but there was also evidence of some SnS formation in a hotter region of the furnace (831 K). The morphology of the SnS film appears similar to that of $SnS_2$ (Figure 4-10), but EDX analysis show a 49%:51% Sn:S stoichiometry, within experimental error of that expected for SnS (no Cl was observed).

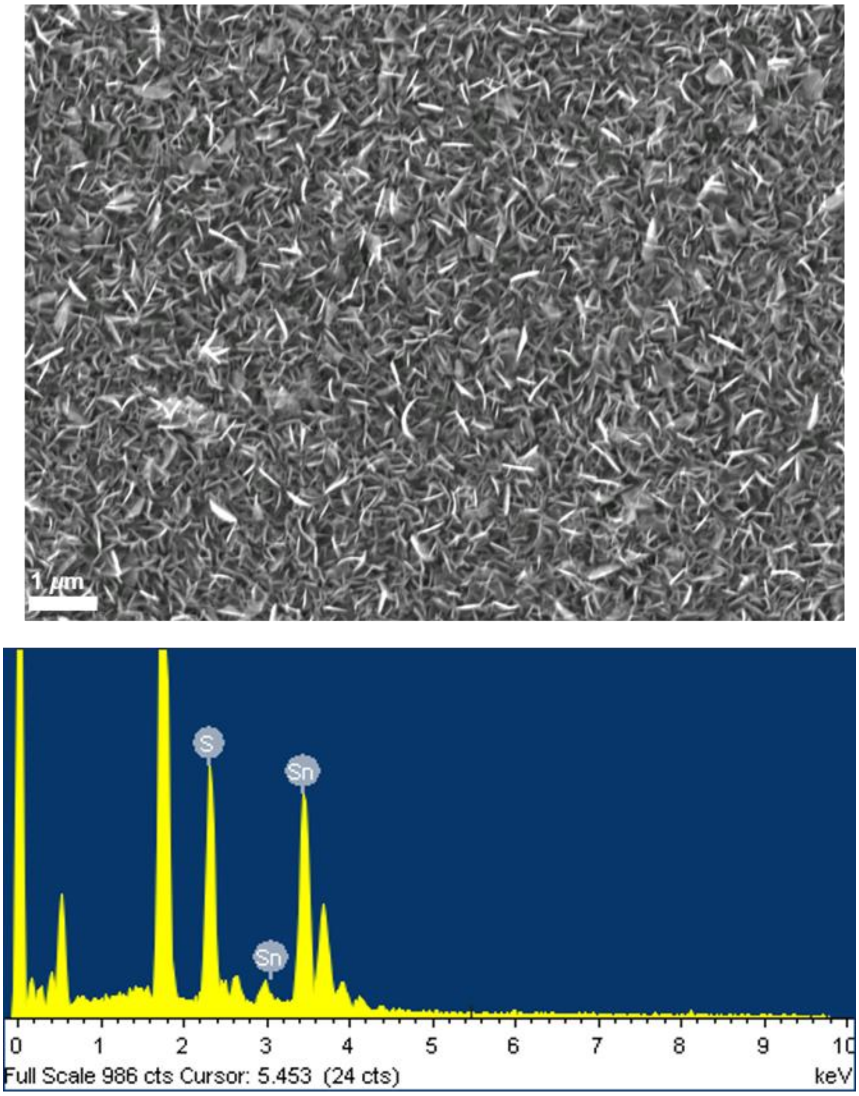

Figure 4-10: SEM image (top) and an EDX spectrum (bottom) of a thin film of SnS deposited from $[SnCl_4\{^nBuS(CH_2)_3S^nBu\}]$ at 831 K. The peaks at ~0.5 kEV and 1.7 keV are due to O and Si respectively from the substrate.

The orthorhombic SnS phase is further confirmed by grazing incidence XRD analysis (Figure 4-11) and the refined lattice parameters (a = 11.19(16), b = 3.98(3), c = 4.24(3) Å) match well with the literature values (a = 11.20, b = 3.99, c = 4.30).[29] These were calculated by the optimisation of the fit in PDXL2.

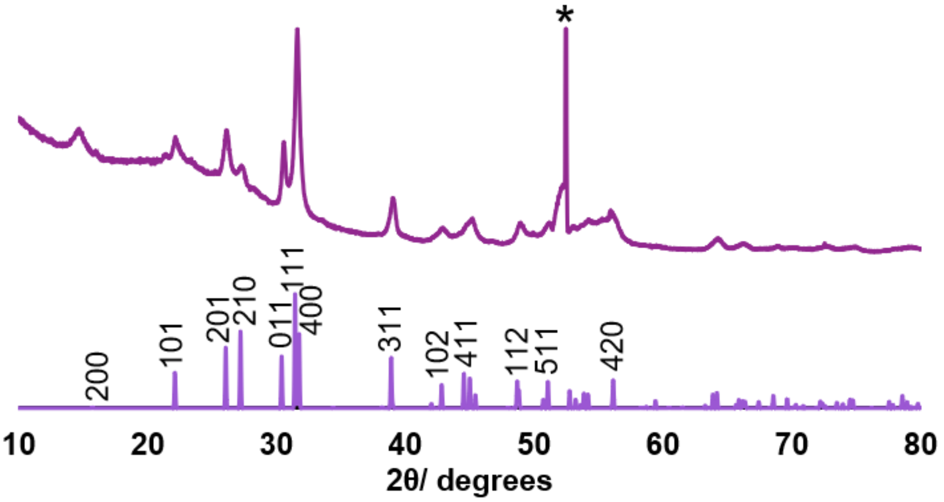

Figure 4-11: Grazing incidence XRD pattern of a thin film of SnS deposited from [$SnCl_4\{^nBuS(CH_2)_3S^nBu\}$] in a hotter region of the furnace (831 K) and an indexed bulk pattern of SnS.[11] The peak due to the Si in the substrate is marked with an asterisk.

The Raman spectrum (Figure 4-12) of the film also clearly shows SnS with peaks at 220, 190 and 165 cm$^{-1}$. The 165 cm$^{-1}$ peak represents the $B_{3g}$ mode, whilst the 190 cm$^{-1}$ and 220 cm$^{-1}$ peaks are associated with the $A_g$ modes and the 290 cm$^{-1}$ peak is ascribed to the $B_{2g}$ mode.[3]

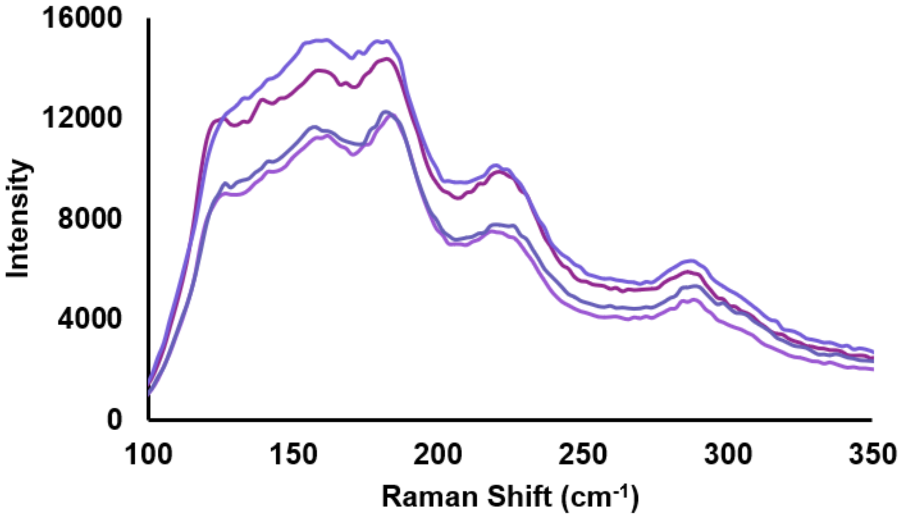

Figure 4-12: Raman spectra of different regions of a thin film of SnS deposited from [$SnCl_4\{^nBuS(CH_2)_3S^nBu\}$] in a hotter region of the furnace (831 K).

The SnS film deposited in this work exhibits a resistivity of 266(3) Ω·cm, which is comparable to SnS films deposited via other techniques.[49,50]

In contrast, whilst $SnS_2$ films were obtained at 645 K using [$SnCl_4(S^nBu_2)_2$] (containing the monodentate ligand), LPCVD experiments at higher temperature where deposition occurred at 743 K showed mainly $Sn_2S_3$, evidenced by EDX analysis. SEM images show that the crystallites of $Sn_2S_3$ form clusters of small florets. However, there was also significant Cl incorporation evident from EDX analysis and the Sn:S ratio varies across the film, consistent with inhomogeneity. In the film obtained at 668 K, several morphologies can be observed by SEM analysis and the XRD pattern obtained from this film showed a mixture of SnS, $SnS_2$ and $Sn_2S_3$ (Figure 4-13). Therefore, it was concluded that the precursor was not suitable for the deposition of phase pure SnS.

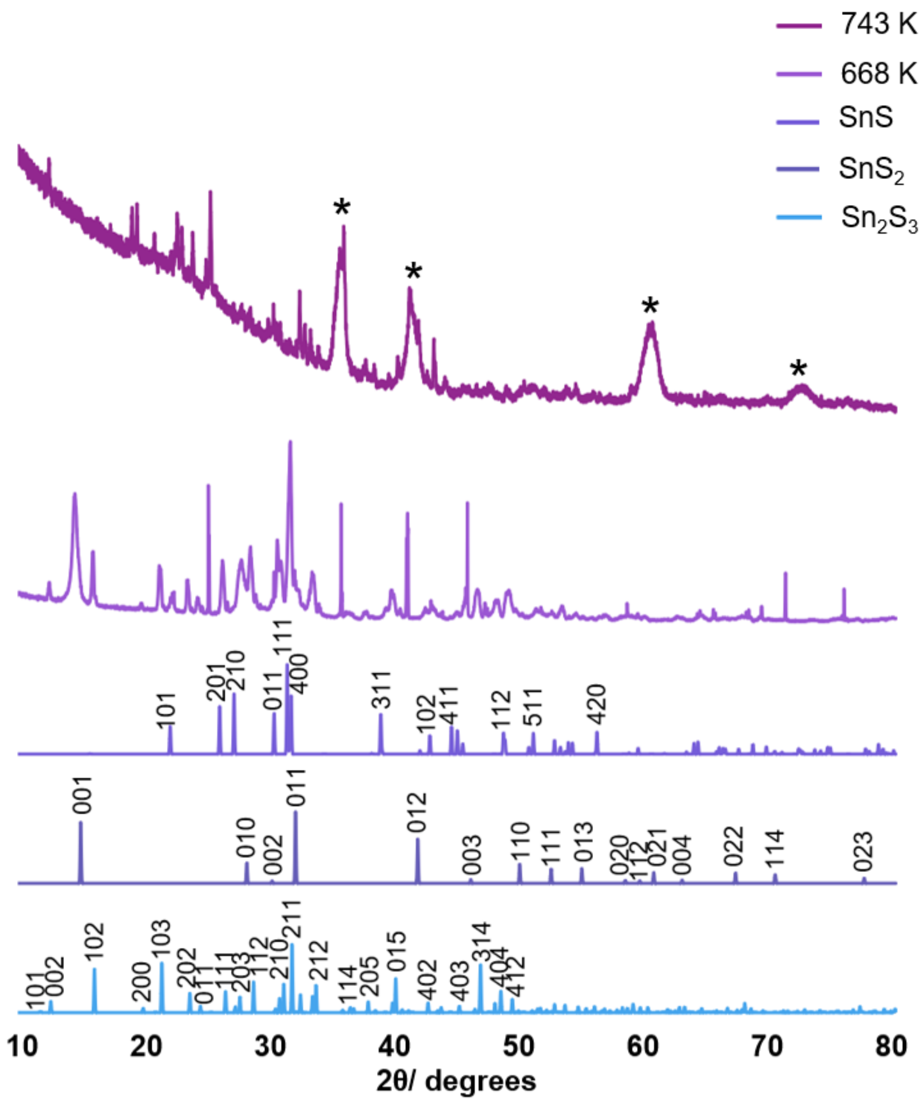

Figure 4-13: Grazing incidence XRD patterns for thin films deposited from $[SnCl_4(S^nBu_2)_2]$ at 743 and 668 K, respectively, and indexed patterns of bulk SnS,[11] $SnS_2$[13] and $Sn_2S_3$.[16]

### 4.2.4 Deposition and Characterisation of $SnSe_2$ Thin Films

LPCVD experiments were also conducted using the tin(IV) chloride selenoether complex, $[SnCl_4(Se^nBu_2)_2]$. At 598 K and 743 K, a reflective silver and a black film were obtained, respectively. These were single phase $SnSe_2$ as identified by XRD. SEM images (Figure 4-15) showed regular hexagonal platelets, typical of this space group, constituting the film deposited at 598 K. A thinner region of this film, however, showed a more disordered morphology, and it was apparent that the platelets initially lie parallel to the substrate, before more material grows upon its surface. At an elevated temperature, the crystallites appear to be a lot smaller and rougher, though still ordered. EDX analysis showed a 34:66 and 35:65 Sn:Se stoichiometry for the films deposited at 598 and 743 K respectively. There is no evidence for incorporation of Cl into the films.

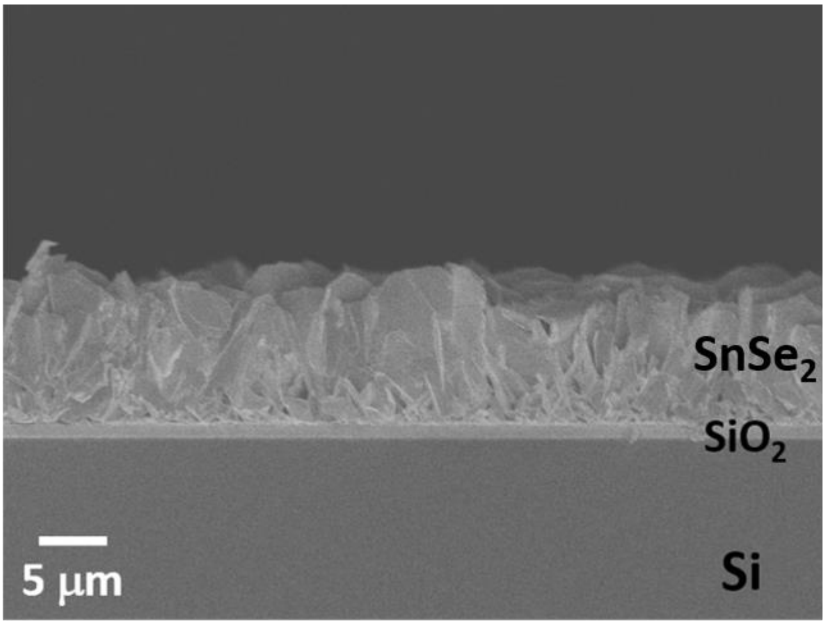

Figure 4-14: The Cross section of the $SnSe_2$ film deposited at 598 K from $[SnCl_4(Se^nBu_2)_2]$

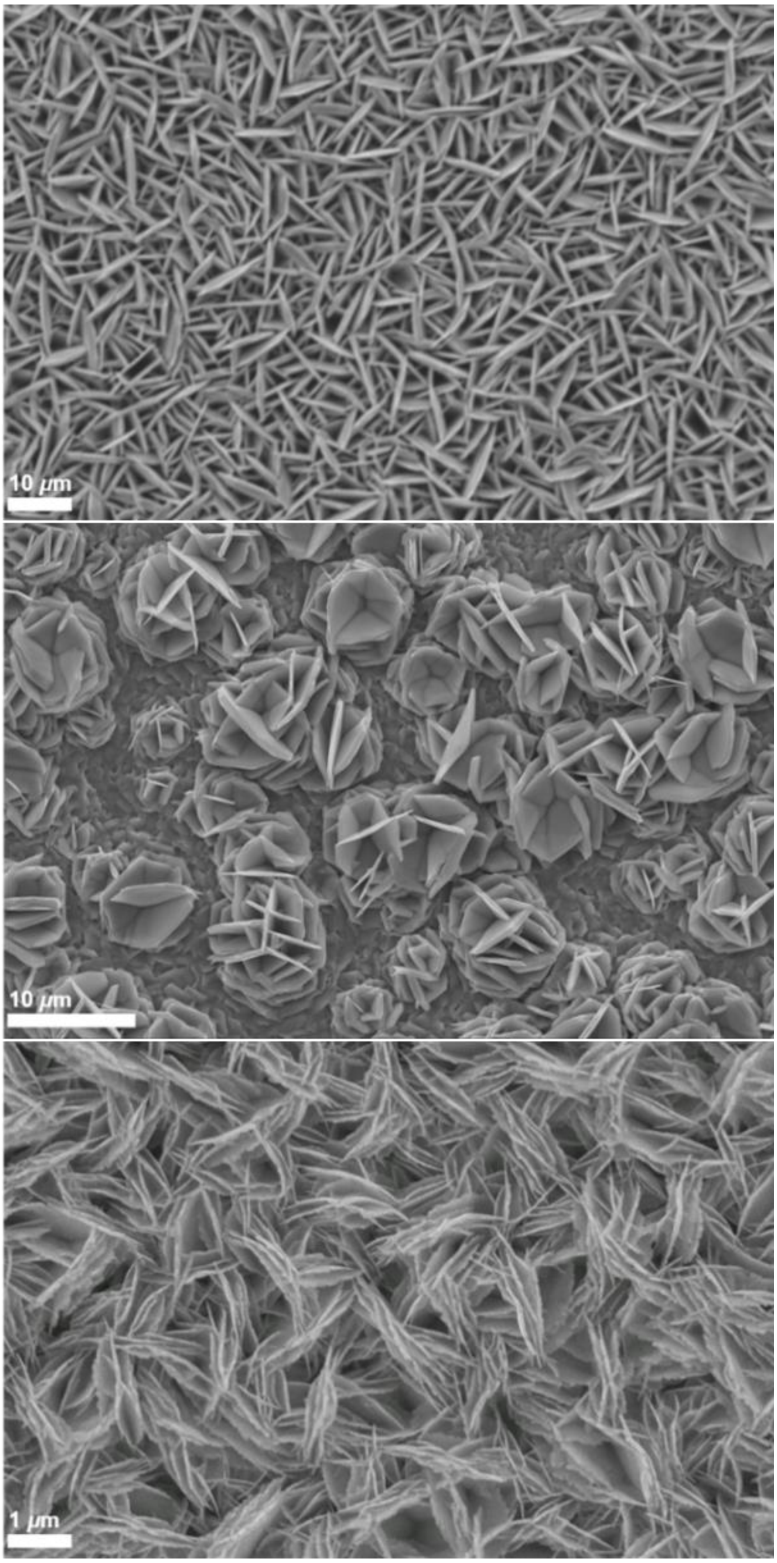

Figure 4-15: SEM images of $SnSe_2$ deposited from $[SnCl_4(Se^nBu_2)_2]$, showing a thick (top) and thin (middle) region of a film deposited at 598 K and a film deposited at 743 K (bottom).

XRD analysis shows that the $SnSe_2$ crystallises in space group of $P\bar{3}m1$ in all cases. The decrease in intensity of the (0 1 1) reflection relative to the (0 0 1) reflection (Figure 4-16), suggests that the film deposited at 743 K is thinner (and hence more strongly (0 0 1) oriented) than that deposited at 598 K. This is borne out by cross-sectional SEM imaging and further supported by the appearance of reflections belonging to the substrate. Lattice parameters determined for the films deposited at 598 K (a = 3.8051(17), c = 6.187(4) Å) and 743 K (a = 3.826(11), c = 6.101(12) Å) are consistent with those reported from films deposited from the previously reported [$SnCl_4\{^nBuSe(CH_2)_nSe^nBu\}$] (n = 2, 3) (a = 3.81-3.83 and c = 6.14-6.16 Å).[33] Lattice parameters were calculated by the optimisation of the fit in PDXL2.

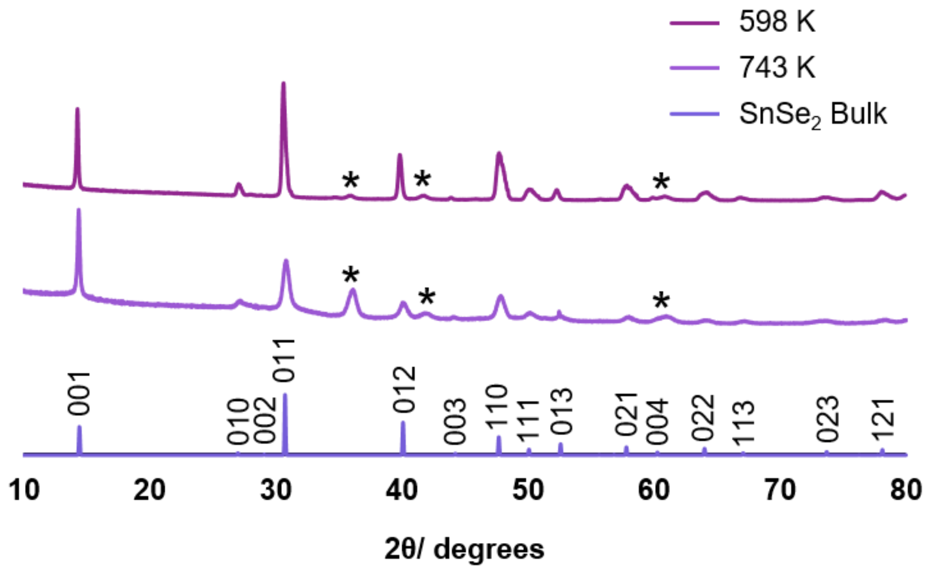

Figure 4-16: Grazing incidence XRD of $SnSe_2$ deposited from [$SnCl_4(Se^nBu_2)_2$] at 598 K and 743 K and an indexed bulk pattern of $SnSe_2$.[14] The reflections marked with an asterisk are due to TiN underlying the $SiO_2$ substrate.

Raman spectra (Figure 4-17) show an intense peak at 185 cm$^{-1}$ and a weaker feature at 115 cm$^{-1}$. These can be assigned to the $A_{1g}$ and $E_g$ modes of $SnSe_2$, respectively.[44]

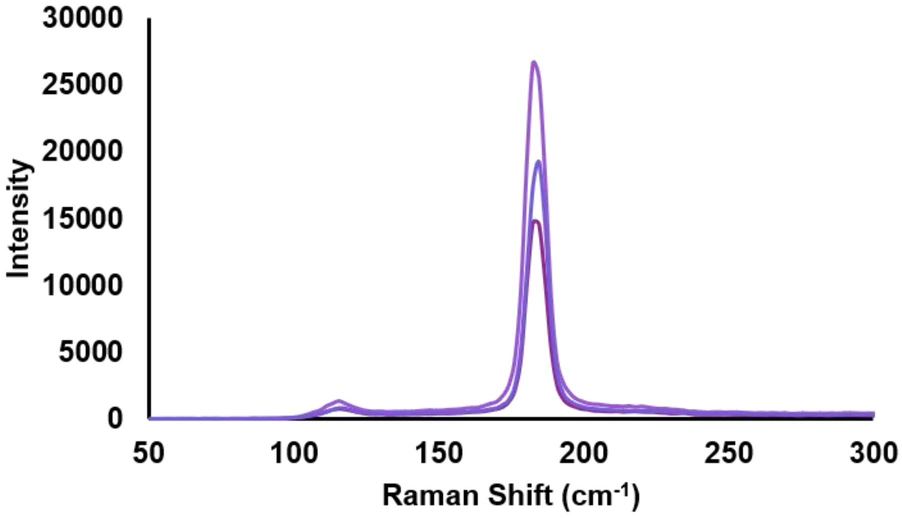

Figure 4-17: Raman spectra from different areas of a thin film of $SnSe_2$ deposited from $[SnCl_4(Se^nBu_2)_2]$ at 598 K.

A resistivity of 4.4(3) mΩ·cm was obtained from this $SnSe_2$ film. The value is lower than for the $SnSe_2$ films deposited via spin-coating and annealing (~30 mΩ·cm),[9] molecular beam epitaxy (22 mΩ·cm)[8] and CVD (210 mΩ·cm).[33]

### 4.2.5 Deposition and Characterisation of SnSe Thin Films

Further LPCVD studies to investigate film growth at higher temperatures using precursor $[SnCl_4\{^nBuSe(CH_2)_3Se^nBu\}]$, containing the bidentate diselenoether ligand,[33] were also undertaken.

Similarly to the high temperature depositions using $[SnCl_4\{^nBuS(CH_2)_3S^nBu\}]$ described above, these showed that increasing the furnace temperature still resulted in significant $SnSe_2$ film growth at the edge of the hot zone as before. However, where the precursor travelled further into the hotter region of the furnace, crystalline SnSe was observed. In contrast, there was no evidence for SnSe deposition using $[SnCl_4(Se^nBu_2)_2]$

The SEM images (Figure 4-18) of the SnSe deposited reveal a non-continuous, orthorhombic structure. EDX analysis of the film showed a 53:47 Sn:Se (with no Cl evident).

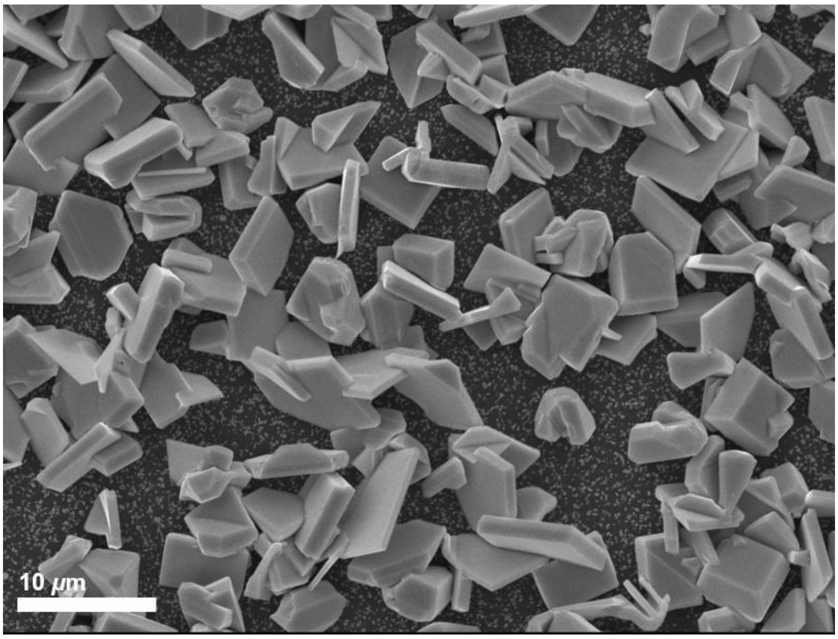

Figure 4-18: SEM image of SnSe deposited from $[\mathrm{SnCl_4\{^nBuSe(CH_2)_3Se^nBu\}}]$ at 861 K.

GIXRD patterns (Figure 4-19) show the material to be orthorhombic SnSe. The refined lattice parameters (a = 11.459(17), c = 4.166(8) Å) match well with the literature values (a = 11.48-11.53, b = 4.06-4.09, c = 4.25-4.28).[30] These were calculated by optimisation of the fit in PDXL2.

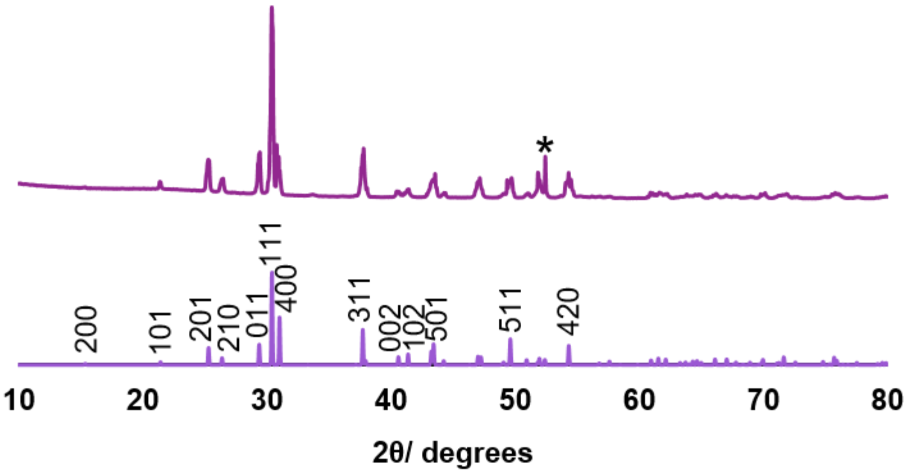

Figure 4-19: Grazing incidence XRD pattern of a SnSe film deposited from $[\mathrm{SnCl_4\{^nBuSe(CH_2)_3Se^nBu\}}]$ at 861 K and an indexed bulk pattern of SnSe.[12] the asterisk marks the Si in the substrate.

The Raman spectrum (Figure 4-20) shows peaks at 150, 135 and 115 cm$^{-1}$, consistent with SnSe. The weak band at 185 cm$^{-1}$ suggests a small $SnSe_2$ component is present, although this is not evident in the XRD data. The peak at 115 cm$^{-1}$ can be assigned to the $B_{3g}$ mode, 135 cm$^{-1}$ the $A_{2g}$ mode and 150 cm$^{-1}$ the $A_{3g}$ mode.[51] The discontinuous SnSe film coverage precluded electrical measurements.

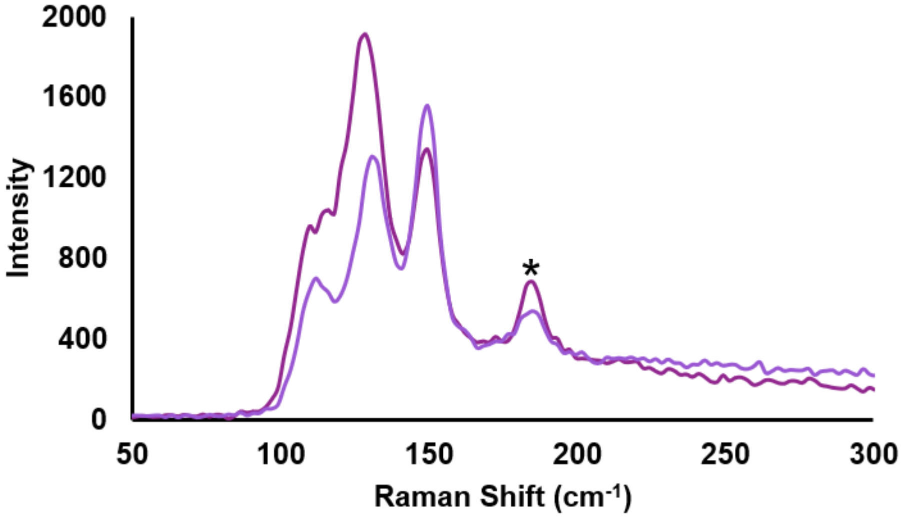

Figure 4-20: Raman spectra of different areas of a thin film of SnSe deposited from $[SnCl_4\{^nBuSe(CH_2)_3Se^nBu\}]$ at 861 K. The peak marked with an asterisk is due to $SnSe_2$.

## 4.3 Conclusion and Further Work

Several new molecular tin(IV) chloride complexes with monodentate and bidentate thio- and selenoether ligands bearing n-butyl terminal substituents have been prepared and evaluated as single source precursors for the LPCVD of both tin dichalcogenide (Sn(IV)) and tin monochalcogenide (Sn(II)) thin films. All four complexes have been shown to be suitable as precursors for the deposition of crystalline $SnE_2$ thin films, the identities of which were established by grazing incidence XRD, SEM, EDX, Raman spectroscopy, and, where a single phase was obtained, van der Pauw resisitivity measurements. Using higher deposition temperatures, precursors $[SnCl_4\{^nBuSe(CH_2)_3Se^nBu\}]$ and $[SnCl\{^nBuS(CH_2)_3Sn^nBu\}]$ have also been shown to form tin monochalcogenide thin films, which were characterised similarly. In contrast, higher temperature LPCVD experiments using the monothioether complex, $[SnCl_4(S^nBu_2)_2]$, produces multiple phases ($SnS_2$, $Sn_2S_3$, SnS).

The resistivities measured for the $SnS_2$ and SnS films are comparable to those reported for similar films produced from other deposition processes, whilst that for $SnSe_2$ is at the lower end of the values reported.

In order to further facilitate the deposition of the tin monochalcogenide thin films, a more optimised CVD set up is required with a greater control over the temperature so that the gradient of temperature over the hot zone is reduced. Furthermore, altering the composition of the precursors so that the ratio of metal to chalcogen is 1:1 may also improve the deposition. Some example compositions of potential precursors for SnE thin films include $[R_3SnER']$ or $[SnCl_4\{Me_2N(CH_2)_3ER\}]$ (R, R' = Et, $^nBu$; E = S, Se).

$SnS_xSe_{1-x}$[52] and $Sn(S_xSe_{1-x})_2$[53] compounds are known which means that properties such as band gap can be tuned. Consequently, by using both a Sn(IV) selenoether precursor together with a Sn(IV) thioether precursor such as $[SnCl_4\{^nBuSe(CH_2)_3Se^nBu\}]$ and $[SnCl_4\{^nBuS(CH_2)_3S^nBu\}]$, these ternary solid solutions could be deposited.

## 4.4 Experimental

### 4.4.1 Synthesis and Characterisation of Tin Chalcogenide Precursors

All reactions were conducted using Schlenk, vacuum line and glove box techniques under a dry nitrogen atmosphere. The reagents were stored and manipulated using a glove box. Hexane was dried by distillation over a sodium wire. $SnCl_4$, $^nBuLi$ (1.6 mol dm$^{-3}$ in diethyl ether) and $^nBu_2S$ were obtained from Sigma-Aldrich. $^nBu_2S$ was dried over sieves, $SnCl_4$ and $^nBuLi$ were used as received. $^nBu_2Se$,[54] $^nBuSe(CH_2)_3Se^nBu$[33] and $[SnCl_4\{^nBuSe(CH_2)_3Se^nBu\}]$[33] were prepared according to the literature methods. Preparation of $^nBuSe(CH_2)_3Se^nBu$ is also described in Section 6.2.1. IR spectra were recorded as Nujol mulls between CsI plates using a Perkin-Elmer Spectrum 100 instrument. $^1H$ and $^{13}C\{^1H\}$ NMR spectra were recorded from solutions in $CDCl_3$ or $CD_2Cl_2$ on a Bruker AV400 spectrometer, $^{77}Se\{^1H\}$ and $^{119}Sn$ NMR spectra on a Bruker AV400-II spectrometer and referenced to external neat $SeMe_2$ and $SnMe_4$ respectively. A small amount of $[Cr(acac)_3]$ was added as a relaxation agent to the samples for $^{119}Sn$ NMR measurements. Microanalytical results were obtained from Medac Ltd.

***$^nBuS(CH_2)_3S^nBu$*:**

Obtained by dissolving $HS(CH_2)_3SH$ (6.05 g, 56 mmol) in anhydrous EtOH (60 mL) with addition of elemental sodium (2.8 g, 112 mmol) cut into small pieces. After dissolution of the sodium, the reaction mixture was refluxed for 1 h, cooled to ambient temperature and $^nBuBr$ (15.34 g, 12.03 mL, 112 mmol) was added slowly. The reaction mixture was then refluxed for 1 h, forming a white solid. After cooling, saturated aqueous NaCl and $NaHCO_3$ solutions were added. After filtering, the product was extracted from the aqueous filtrate with $Et_2O$ (4 x 50 mL), dried overnight ($Na_2SO_4$) and, after removal of the drying agent, the solvent was removed *in vacuo*, leaving a colourless oil. Yield: 6.0 g, 48 %. $^1H$ NMR ($CDCl_3$, 298 K) $\delta$/ppm: 0.92 (t, [6H], $CH_3$), 1.41 (m, [4H], $-CH_2CH_3$), 1.57 (m, [4H], $-SCH_2CH_2CH_2CH_3$), 1.86 (m, [2H], $-SCH_2CH_2CH_2S-$), 2.52 (t, [4H], $SCH_2-$), 2.62 (t, [4H], $SCH_2-$). $^{13}C\{^1H\}$ NMR ($CDCl_3$, 298K) $\delta$/ppm 13.65 ($CH_3$), 21.98, 29.43, 30.96, 31.74, 31.81 (all $CH_2$).

This ligand was synthesised by other members of the research group.

***[SnCl$_4${$^n$BuS(CH$_2$)$_3$S$^n$Bu}]*:**

A solution of $^n$BuS(CH$_2$)$_3$S$^n$Bu (0.24 g, 1.09 mmol) in anhydrous hexane (5 mL) was added slowly to a solution of SnCl$_4$ (0,15 mL, 1.25 mmol) in anhydrous hexane (10 mL) under constant stirring at room temperature and under a dinitrogen atmosphere. A white solid immediately precipitated out of solution. It was collected by filtration after 20 minutes and dried *in vacuo* to afford a white solid. Yield: 0.46 g, 88 %. Anal. Calcd for $C_{11}H_{24}Cl_4S_2Sn$: C 27.5, H 5.0. Found: C 26.9, H 5.3 %. $^1$H NMR (CDCl$_3$, 298 K) $\delta$/ppm: 0.98 (t, [6H], C*H*$_3$), 1.49 (m, [4H], C*H*$_2$CH$_3$), 1.76 (m, [4H], CH$_2$), 2.39 (m, [2H], -SCH$_2$C*H*$_2$CH$_2$S-), 3.17 (m, [4H], SC*H*$_2$), 3.32 (m, [4H], SC*H*$_2$). $^{13}$C{$^1$H} NMR (CDCl$_3$) $\delta$/ppm: 13.50 (*C*H$_3$), 21.87 (*C*H$_2$), 24.02 (*C*H$_2$), 29.40 (*C*H$_2$), 34.19 (*C*H$_2$), 36.74 (*C*H$_2$). $^{119}$Sn NMR (CH$_2$Cl$_2$/ CD$_2$Cl$_2$, 298 K): –575 (br); (200 K) $\delta$/ppm: –567, –585. IR (Nujol) $\nu$/cm$^{-1}$: 324 (s br) Sn−Cl.

***[SnCl$_4$($^n$Bu$_2$S)$_2$]*:**

A solution of $^n$Bu$_2$S (0.944 g, 6.45 mmol) in anhydrous hexane (5 mL) was added slowly to a solution of SnCl$_4$ (0.840 g, 3.22 mmol) in anhydrous hexane (10 mL) under constant stirring at room temperature to afford a colourless solution. It was stirred for 20 minutes. It was concentrated *in vacuo*, yielding a white precipitate. The solution was decanted and the precipitate washed with anhydrous hexane and dried *in vacuo*. Yield: 1.57 g, 86 %. Anal. Calcd for $C_{16}H_{36}Cl_4S_2Sn$: C 34.8, H 6.6. Found: C 34.7, H 6.8 %. $^1$H NMR (CDCl$_3$) $\delta$/ppm: 0.97 (t, [3H], C*H*$_3$), 1.49 (m, [2H], SCH$_2$CH$_2$C*H*$_2$CH$_3$), 1.76 (br, [2H], SCH$_2$C*H*$_2$CH$_2$CH$_3$), 3.00 (vbr, [2H], SC*H*$_2$-). $^{13}$C{$^1$H} NMR (CDCl$_3$) $\delta$/ppm: 13.56 (*C*H$_3$), 21.89 (*C*H$_2$), 30.47 (*C*H$_2$), 43.22 (S*C*H$_2$). $^{119}$Sn NMR (CH$_2$Cl$_2$/ CD$_2$Cl$_2$, 298 K) $\delta$/ppm: –594 (br), –603 (br); (223 K) $\delta$/ ppm: −581 (s), –589 (s). IR (Nujol) $\nu$/cm$^{-1}$: 330 (sh), 318 (s), 300 (sh) Sn−Cl.

***[SnCl$_4$($^n$Bu$_2$Se)$_2$]*:**

A solution of $^n$Bu$_2$Se (1.25 g, 6.45 mmol) in anhydrous hexane (5 mL) was added slowly to a solution of SnCl$_4$ (0.840 g, 3.22 mmol) in anhydrous hexane (10 mL) under constant stirring at room temperature to afford a pale-yellow solution. It was stirred for 20 minutes. It was concentrated *in vacuo,* yielding a pale orange precipitate. The solution was decanted, and the precipitate washed with anhydrous hexane and dried *in vacuo*. Yield: 0.924 g, 52 %. Anal. Calcd for $C_{16}H_{36}Cl_4Se_2Sn$: C 29.71, H 5.61. Found: C 29.41, H 5.61%. $^1$H NMR (CDCl$_3$) $\delta$/ppm: 0.98 (t, [3H], C*H*$_3$), 1.50 (m, [2H], SeCH$_2$CH$_2$C*H*$_2$CH$_3$), 1.86 (br, [2H], SeCH$_2$C*H*$_2$-), 3.10 (br, [2H], SeC*H*$_2$-). $^{13}$C{$^1$H} NMR (CDCl$_3$) $\delta$/ppm: 13.48 (*C*H$_3$), 22.83 (*C*H$_2$), 30.42 (*C*H$_2$), 35.64 (Se*C*H$_2$). $^{119}$Sn NMR (CD$_2$Cl$_2$, 298 K) $\delta$/ppm: –717 (br, s); (183 K) $\delta$/ppm: −719 ($^1J_{SnSe}$ = 530 Hz, minor), –718 ($^1J_{SnSe}$ = 478 Hz, major). $^{77}$Se{$^1$H} NMR ($CD_2Cl_2$, 298 K) $\delta$/ppm: 284 (br), 297 (br); (183 K) $\delta$/ppm: 299 ($^1J_{SnSe}$ = 530 Hz), 323 ($^1J_{SnSe}$ = 478 Hz). IR (Nujol) $v$/cm$^{-1}$: 324 (s), 302 (sh), 292 (s) Sn−Cl.

### 4.4.2 LPCVD

In a typical LPCVD experiment the reagent (70–80 mg) and PVD $SiO_2$ substrates were loaded into a closed end silica tube in a glove box (precursor in bulb at closed end and followed by four substrate tiles (each 20 x 8 x 1 mm) positioned adjacently along the tube). The tube was placed horizontally in the furnace such that the precursor was outside of the heated zone. The tube was evacuated to 0.02 mm Hg. The furnace was then heated to the desired temperature and the temperature was allowed to stabilise. The tube was then repositioned, if necessary, to move the precursor closer to the heated zone to a point where sublimation could be observed. At this point the position of the tube was maintained until the deposition was complete (i.e. the precursor was completely sublimed). This typically took 1-3 hours. Once complete, the tube was allowed to cool to room temperature and transferred to the glove box where the substrates were removed and stored under $N_2$ before characterisation.

The LPCVD experiments produced black or silver films. Precursors [$SnCl_4${$^nBuSe(CH_2)_3Se^nBu$}] and [$SnCl_4(Se^nBu_2)_2$] typically gave $SnSe_2$ at all temperatures up to 1023 K. Precursor [$SnCl_4${$^nBuS(CH_2)_3S^nBu$}] gave $SnS_2$ at all temperatures and [$SnCl_4(S^nBu_2)_2$] gave $SnS_2$ at low temperatures and $Sn_2S_3$ at higher temperatures. These results were confirmed to be reproducible. It was noted that on the occasions when precursors [$SnCl_4${$^nBuSe(CH_2)_3Se^nBu$}] and [$SnCl_4${$^nBuS(CH_2)_3S^nBu$}] travelled further into the heated zone, SnSe and SnS films, respectively, were obtained.

### 4.4.3 Substrates

See Appendix 1.

### 4.4.4 Thin Film Characterisation

See Appendix 1.

## 4.5 References

1 Y. Fu, G. Gou, X. Wang, Y. Chen, Q. Wan, J. Sun, S. Xiao, H. Huang, J. Yang and G. Dai, *Appl. Phys. A*, 2017, **123**, 2991–2998.

2 Y. Huang, H.-X. Deng, K. Xu, Z.-X. Wang, Q.-S. Wang, F.-M. Wang, F. Wang, X.-Y. Zhan, S.-S. Li, J.-W. Luo and J. He, *Nanoscale*, 2015, **7**, 14093–14099.

3 I. Y. Ahmet, M. S. Hill, A. L. Johnson and L. M. Peter, *Chem. Mater.*, 2015, **27**, 7680–7688.

4 F. K. Butt, M. Mirza, C. Cao, F. Idrees, M. Tahir, M. Safdar, Z. Ali, M. Tanveer and I. Aslam, *CrystEngComm*, 2014, **16**, 3470–3473.

5 M. S. Mahdi, K. Ibrahim, A. Hmood, N. M. Ahmed, F. I. Mustafa and S. A. Azzez, *Mater. Lett.*, 2017, **200**, 10–13.

6 L.-D. Zhao, S.-H. Lo, Y. Zhang, H. Sun, G. Tan, C. Uher, C. Wolverton, V. P. Dravid and M. G. Kanatzidis, *Nature*, 2014, **508**, 373–377.

7 C. Wang, Y. Chen, J. Jiang, R. Zhang, Y. Niu, T. Zhou, J. Xia, H. Tian, J. Hu and P. Yang, *RSC Adv.*, 2017, **7**, 16795–16800.

8 K.-M. Chung, D. Wamwangi, M. Woda, M. Wuttig and W. Bensch, *J. Appl. Phys.*, 2008, **103**, 0835231–0835237.

9 R. Y. Wang, M. A. Caldwell, R. G. D. Jeyasingh, S. Aloni, R. M. Shelby, H. S. P. Wong and D. J. Milliron, *J. Appl. Phys.*, 2011, **109**, 1135061–1135066.

10 P. Zhou, X. Wang, W. Guan, D. Zhang, L. Fang and Y. Jiang, *ACS Appl. Mater. Interfaces*, 2017, **9**, 6979–6987.

11 W. Hofmann, *Zeitschrift. Krist.*, 1935, **92**, 161–173.

12 K. Adouby, C. Perez-Vicente and J. C. Jumas, *Zeitschrift fur Krist.*, 1998, **213**, 343–349.

13 R. M. Hazen and L. W. Finger, *Am. Mineral.*, 1978, **63**, 293–296.

14 G. Busch, C. Froehlich and F. Hullinger, *Helv. Phys. Acta*, 1961, **34**, 359–368.

15 T. Jiang and G. A. Ozin, *J. Mater. Chem.*, 1998, **8**, 1099–1108.

16 R. Kniep, D. Mootz, U. Severin and H. Wunderlich, *Acta Crystallogr. Sect. B*, 1932, **38**, 2022–2023.

17 S. C. Ray, M. K. Karanjai and D. DasGupta, *Thin Solid Films*, 1999, **350**, 72–78.

18 A. Abou Shama and H. M. Zeyada, *Opt. Mater. (Amst).*, 2003, **24**, 555–561.

19 M. Ristov, G. Sinadinovski, I. Grozdanov and M. Mitreski, *Thin Solid Films*, 1989, **173**, 53–58.

20 P. K. Nair, M. T. S. Nair and J. Campos, *J. Electrochem. Soc.*, 1993, **140**, 539–541.

21 R. D. Engelken, H. E. McCloud, C. Lee, M. Slayton and H. Ghoreishi, *J. Electrochem. Soc.*, 1987, **134**, 2696–2707.

22 A. Tanusevski, *Semicond. Sci. Technol.*, 2003, **18**, 501–505.

23 C. Gao and H. Shen, *Thin Solid Films*, 2012, **520**, 3523–3527.

24 S. K. Arora, D. H. Patel and M. K. Agarwal, *J. Cryst. Growth*, 1993, **131**, 268–270.

25 E. Schonherr and W. Stetter, *J. Cryst. Growth*, 1975, **30**, 96–98.

26 M. Calixto-Rodriguez, H. Martinez, A. Sanchez-Juarez, J. Campos-Alvarez, A. Tiburcio-Silver and M. E. Calixto, *Thin Solid Films*, 2009, **517**, 2497–2499.

27 P. Sinsermsuksakul, J. Heo, W. Noh, A. S. Hock and R. G. Gordon, *Adv. Energy Mater.*, 2011, **1**, 1116–1125.

28 L. S. Price, I. P. Parkin, T. G. Hibbert and K. C. Molloy, *Chem. Vap. Depos.*, 1998, **4**, 222–225.

29 L. S. Price, I. P. Parkin, A. M. E. Hardy, R. J. H. Clark, T. G. Hibbert and K. C. Molloy, *Chem. Mater.*, 1999, **11**, 1792–1799.

30 N. D. Boscher, C. J. Carmalt, R. G. Palgrave and I. P. Parkin, *Thin Solid Films*, 2008, **516**, 4750–4757.

31 S. L. Benjamin, C. H. de Groot, A. L. Hector, R. Huang, E. Koukharenko, W. Levason and G. Reid, *J. Mater. Chem. C*, 2015, **3**, 423–430.

32 R. Huang, S. L. Benjamin, C. Gurnani, Y. Wang, A. L. Hector, W. Levason, G. Reid and C. H. De Groot, *Sci. Rep.*, 2016, **6**, 275931–2759310.

33 C. H. de Groot, C. Gurnani, A. L. Hector, R. Huang, M. Jura, W. Levason and G. Reid, *Chem. Mater.*, 2012, **24**, 4442–4449.

34 I. P. Parkin, L. S. Price, T. G. Hibbert and K. C. Molloy, *J. Mater. Chem.*, 2001, **11**, 1486–1490.

35 K. Ramasamy, V. L. Kuznetsov, K. Gopal, M. A. Malik, J. Raftery, P. P. Edwards and P. O'Brien, *Chem. Mater.*, 2013, **25**, 266–276.

36 J. R. Brent, D. J. Lewis, T. Lorenz, E. A. Lewis, N. Savjani, S. J. Haigh, G. Seifert, B. Derby and P. O'Brien, *J. Am. Chem. Soc.*, 2015, **137**, 12689–12696.

37 S. D. Reid, A. L. Hector, W. Levason, G. Reid, B. J. Waller and M. Webster, *Dalton Trans.*, 2007, **4**, 4769–4777.

38 S. E. Dann, A. R. J. Genge, W. Levason and G. Reid, *J. Chem. Soc. Dalton Trans.*, 1996, 4471–4478.

39 S. E. Dann, A. R. J. Genge, W. Levason and G. Reid, *J. Chem. Soc. Dalton Trans.*, 1997, **0**, 2207–2214.

40 A. R. J. Genge, W. Levason and G. Reid, *J. Chem. Soc., Dalton Trans*, 1997, 4549–4553.

41 S. Patai and Z. Rappoport, in *The Chemistry of Organic Selenium and Tellurium Compounds Vol 1*, Wiley, NY.

42 Y. Kumagai, L. A. Burton, A. Walsh and F. Oba, *Phys. Rev. Appl.*, 2016, **6**, 1–14.

43 J. R. Guenter and H. R. Oswald, *Naturwissenschaften*, 1968, **55**, 177–177.

44 D. Walsh, S. Jandl and J. Y. Harbec, *J.Phys.C Solid St. Phys*, 1980, **13**, 125–127.

45 A. J. Smith, P. E. Meek and W. Y. Liang, *J. Phys. Chem. C*, 1977, **10**, 1321–1333.

46 A. Voznyi, V. Kosyak, A. Opanasyuk, N. Tirkusova, L. Grase, A. Medvids and G. Mezinskis, *Mater. Chem. Phys.*, 2016, **173**, 52–61.

47 L. Amalraj, C. Sanjeeviraja and M. Jayachandran, *J. Cryst. Growth*, 2002, **234**, 683–689.

48 K. Kourtakis, J. Di Carlo, R. Kershaw, K. Dwight and A. Wold, *J. Solid State Chem.*, 1988, **76**, 186–191.

49 K. T. Ramakrishna Reddy, P. Purandhara Reddy, P. K. Datta and R. W. Miles, *Thin Solid Films*, 2002, **403–404**, 116–119.

50 T. Gotoh, *Phys. Status Solidi*, 2016, **213**, 1869–1872.

51 S. Luo, X. Qi, H. Yao, X. Ren, Q. Chen and J. Zhong, *J. Phys. Chem. C*, 2017, **121**, 4674–4679.

52 H. Wei, Y. Su, S. Chen, Y. Lin, Z. Yang, X. Chen and Y. Zhang, *J. Mater. Chem.*, 2011, **21**, 12605–12608.

53 P. Perumal, R. K. Ulaganathan, R. Sankar, Y. M. Liao, T. M. Sun, M. W. Chu, F. C. Chou, Y. T. Chen, M. H. Shih and Y. F. Chen, *Adv. Funct. Mater.*, 2016, **26**, 3630–3638.

54 D. J. Gulliver, E. G. Hope, W. Levason, S. G. Murray, D. M. Potter, G. L. Marshall, *J. Chem. Soc. Perkin Trans. 2*, 1984, **0**, 429–434.

# Chapter 5: Deposition of Metal Chalcogenide Nanowires from Single Source Precursors

## 5.1 Introduction

Metal chalcogenides have many properties of interest and were discussed previously in Chapters 2 and 4. Tin chalcogenides ($SnE_x$) (E = S, Se) (x = 1, 2) are semiconducting materials that are widely becoming acknowledged as important materials for a wide variety of electronic applications; specifically optoelectronics,[1–5] thermoelectric[6,7] and phase change devices.[8,9] Phase change materials are of interest for data storage applications and $SnSe_2$ with a fast recrystallisation time of 20 ns[9] is a promising material in this field. $Sb_2Se_3$ has a high absorption coefficient (> $10^5$ $cm^{-1}$)[10] and a dielectric constant of 29-18 within a 2 KHz to 2 MHz frequency range.[11] Such properties make it an ideal candidate for use in photovoltaics.[12,13] $Bi_2Se_3$ as a topological insulator, is a candidate for spintronic devices.[14]

Whilst the rest of the work in this thesis focuses on 2D materials, this chapter looks at nanowires (1D nanostructures). Reducing the dimensionality of the metal chalcogenide gives rise to the possibility of more interesting or enhanced properties. Reducing the dimensionality will lead to the increase of band gap and the metal chalcogenide's surface to volume ratio will be greatly increased. Nanowires also exhibit anisotropy, meaning that properties are dependent on direction.[4] This control of direction is of use for a number of applications such as energy harvesting or field effect transistors.[15]

Nanowires are also of major interest for phase change applications. Decreasing the dimensionality reduces the power consumption making them more cost effective.[16] Furthermore, the high surface area to volume ratio results in higher density storage[16] and better data retention.[17]

Nanowires can be deposited by a variety of methods. Sn nanowires have been produced by electrodeposition and these sulfurized to $SnS_2$ (400 nm by 3-5 µm).[18] Solution phase synthesis has been used to deposit SnSe (20.8 nm by tens of µm) nanowires from $Sn[N(SiMe_3)_2]_2$ and trioctyl phosphine selenide (TOP-Se) in oleyamine.[19] Surfactant assisted methods have been utilised for the deposition on SnS (120 nm by ~10 µm) by exposure of tin foil to $H_2S$ gas.[20]

Deposition of nanowires by CVD is common. $Bi_2Se_3$ nanowires (90 nm by tens of µm have been grown from $Bi_2Se_3$ crystals at 973 K using a $H_2$ carrier gas[21] whilst SnSe nanowires have been grown from SnSe powder at ~ 843 K under 50 SCCM Ar.[22] More commonly, a vapour-liquid-solid technique (VLS) is employed in which gold is incorporated into the substrate in order to catalyse the CVD process. Examples of this include GeTe and $Sb_2Te_3$ nanowires deposited at 723 K onto AuNPs (gold nanoparticles) on Si substrates from GeTe and $Sb_2Te_3$ powders respectively to produce nanowires of 50-200 nm diameter and up to tens of µm long.[23] $Sb_2Te_3$ nanowires (~100 nm by 20 µm) have also been synthesised from individual Sb and Te targets.[24]

Interestingly, the use of $SnS_2$ powder at 1073 K and an argon flow rate of 250 SCCM resulted in the deposition of SnS nanowires (70-80 nm by tens of µm) on the gold coated Si substrate.[25] SnS nanowires (12-15 nm by several µm), however, have also been produced using the same method through the use of sulfur rich SnS powder and a gold catalyst at 873-973 K.[26] The higher temperature in the first case is most likely required in order to remove the excess volatile sulfur. SnSe nanowires, meanwhile, have been deposited from from SnSe and Se powder at 823 K to produce wires of 30-40 nm by tens of µm, via a VLS mechanism as shown below in Figure 5-1.[4]

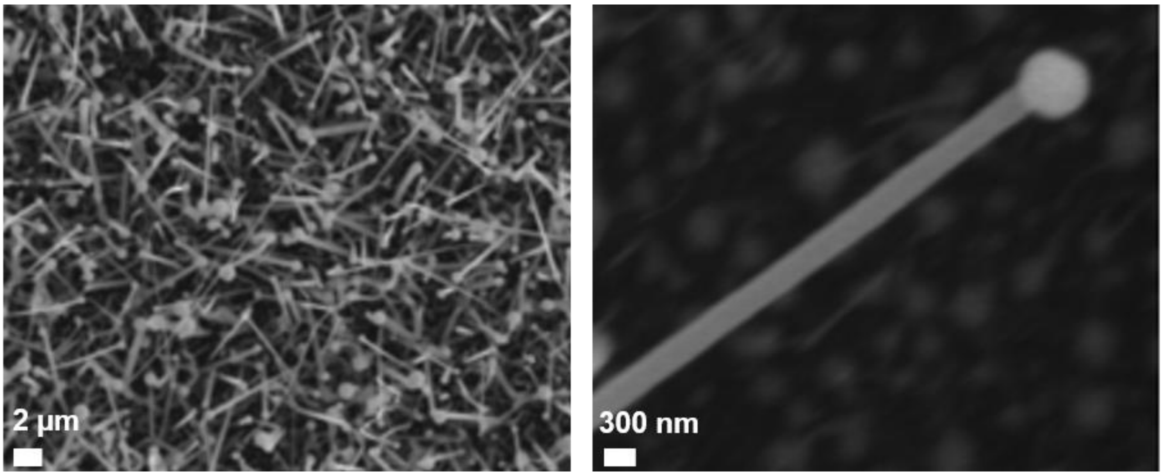

Figure 5-1: High resolution SEM images of SnSe nanowires (left) and an individual nanowire with Au seed (right) deposited via VLS growth from SnSe and Se powders.[4] (Reproduced from reference 4 with permission from the RSC).

Molecular precursors for VLS deposited metal chalcogenides have also been reported in the literature. Yang and co-workers utilized a pulsed VLS method using $Sb(NMe_2)_3$ as the antimony source and $Et_2Se_2$ or $H_2S$ as the chalcogen source at 623 K, again, AuNPs were incorporated into the substrate, in order to deposit $Sb_2E_3$ (E = S, Se) nanowires (40-200 nm by tens of µm).[27] $[Ge\{N(CH_3)_2\}_4]$ and $Te(C_3H_7)_2$ were used to deposit GeTe nanowires (50-70 nm by 0.8-1 µm) at 653-693 K.[28] The depositions discussed here relied upon SEM, TEM and PXRD in order to characterise the nanowires.

Single source precursors, however, remain relatively rare for the deposition of nanowires via VLS and chemical vapour deposition techniques. One example in the literature is the use of $Bi[Se_2P(O^iPr)_2]_3$ to synthesize $BiPO_4$ nanowires (40-60 nm by 1 µm) and $Bi_2Se_3$ nanoplates, though in this case the nanowires are not a metal chalcogenide.[29]

Other mechanisms of nanowire growth include via Ostwald ripening or chemical transformations.[30,31] For example Se nanowires have been grown from Se nano crystallites,[30] whilst $Ag_2Te$ nanowires have been transformed into CdTe, ZnTe and PbTe by cation exchange and CdTe converted into $PtTe_2$ by a thermodynamically favourable reaction.[31]

The aims of this chapter are to use single source precursors, developed in the previous chapters (2 and 4), and optimised CVD set ups and conditions in order to deposit nanowires instead of thin films as well as characterisation of the resulting nanowires. As can be seen from the literature review above, an excess of chalcogen is typically required and often the monochalcogenide is produced. By using a single source precursor with the desired stoichiometry of metal to chalcogen, metal dichalcogenide nanowires should be able to be produced.

Au films or nanoparticles will be incorporated into the substrate as vapour liquid solid growth has been demonstrated to be an efficient method for the deposition of nanowires. The aim is to deposit long nanowires of 10s of µm in length and to have diameters on the nm scale. Nanowires will be characterised by SEM, EDX, XRD and TEM. Electrical properties may also be characterised.

## 5.2 Results and Discussion

### 5.2.1 LPCVD of $SnSe_2$ Nanowires

The precursor, $[SnCl_4\{^nBuSe(CH_2)_3Se^nBu\}]$, was synthesised as per the synthesis described in Chapter 4. The precursor, sealed in a glass tube, under $N_2$ was posted to UCC. In UCC, CVD set ups used included LICVD and LPCVD.

Initial experiments involved loading roughly 20-30 mg of the precursor, $[SnCl_4\{^nBuSe(CH_2)_3Se^nBu\}]$, and substrates (AuNps on Si) into silica boats. These were loaded into a silica tube and placed in a furnace with an argon gas flow (45 bubbles per min) and the furnace heated to 873 K. The set up used is illustrated in Figure 5-2. Initial experiments resulted in the formation of tin dioxide. SEM and TEM images of these nanowires, 50 nm in diameter and µm in length, are shown in Figure 5-3. Tetragonal $SnO_2$ was identified from the diffraction pattern. As it is single crystalline, this suggests that the nanowires grew as $SnO_2$ as opposed to oxidation of $SnSe_2$ nanowires. Consequently, subsequent experiments were completed with an oxygen filter in place. These experiments resulted in minor grey/silver deposition onto the substrates.

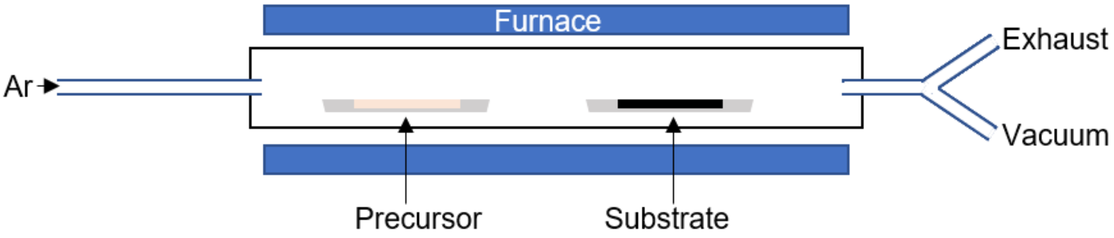

Figure 5-2: LPCVD set up used for the deposition of nanowires.

SEM and EDX analysis in Figure 5-4 reveal that there are some $SnSe_2$ nanowires forming but these are in a very low yield. The nanowires formed appear to be less than 1 µm in length and about 100 nm in diameter and there appears to be some other morphologies present. The wires produced appear to be uniform.

EDX analysis show that individual wires have been grown from a gold nanoparticle seed and EDX spectra in this end of the nanowires show large gold contents whereas analysis of the wire reveals a stoichiometry of $SnSe_{1.8}$. This suggests that the wires grown are slightly selenium deficient.

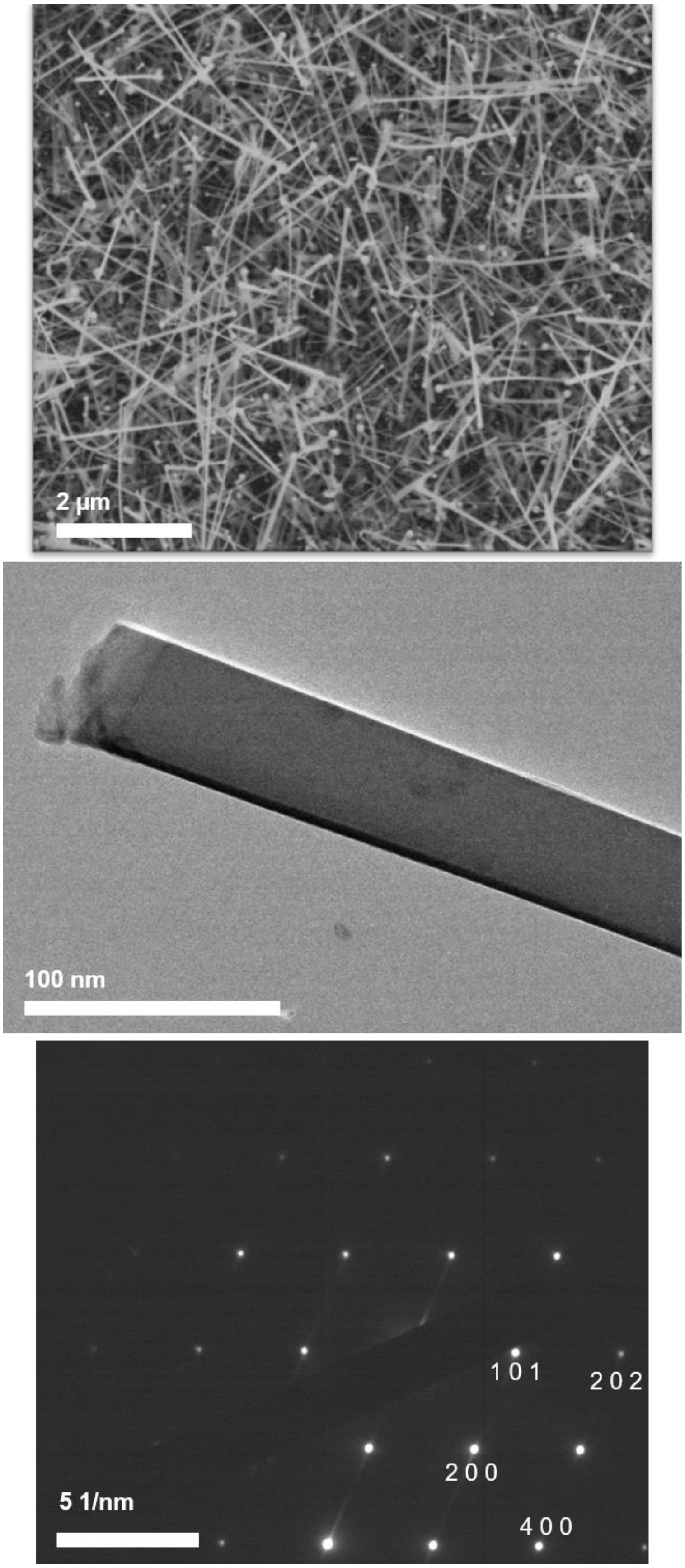

Figure 5-3: SEM (top) and TEM image (middle) of $SnO_2$ deposited from $[SnCl_4\{^nBuSe(CH_2)_3Se^nBu]$ and selected area diffraction pattern (bottom) showing $SnO_2$ reflections.

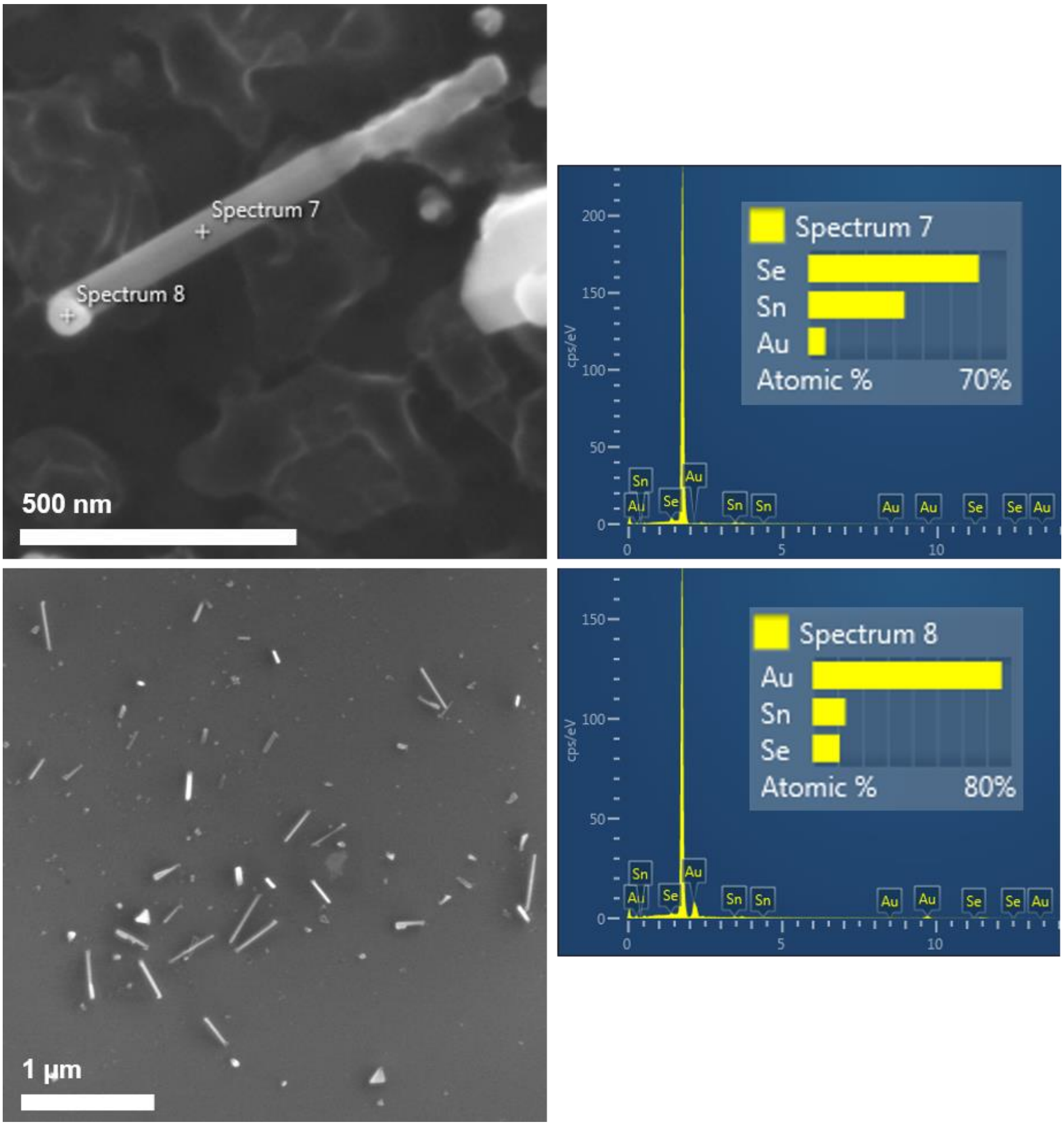

Figure 5-4: SEM of bulk (top) and an individual nanowire (middle) and EDX spectra of two sections of the nanowire deposited from $[SnCl_4\{^nBuSe(CH_2)_3Se^nBu\}]$ onto AuNPs on Si at 873 K via LPCVD.

### 5.2.2 LICVD of $SnSe_2$ Nanowires

Using a liquid injection CVD method, illustrated in Figure 5-5, instead may lead to a better yield and morphology of the nanowires by better controlling the rate at which the precursor, $[SnCl_4\{^nBuSe(CH_2)_3Se^nBu\}]$, meets the substrate in the hot zone. In the initial experiment, the precursor (~50 mg) was dissolved in anhydrous toluene (~20 mL) and injected into a steel cell containing the substrate (AuNP on Si). The steel cell was in a furnace at a temperature of 873 K. Once complete, the furnace was allowed to cool to room temperature. This resulted in silver/ grey deposition on the substrate.

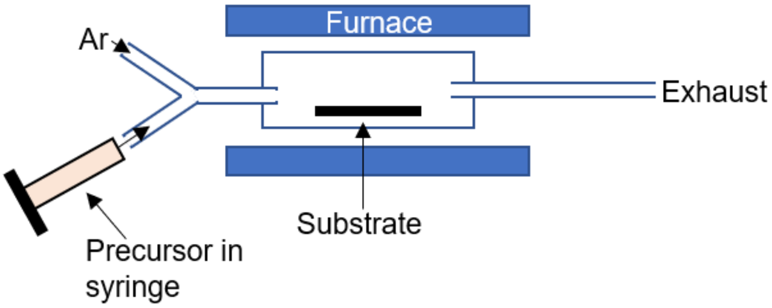

Figure 5-5: Illustration of the set up used for LICVD experiments.

SEM imaging shows good coverage of nanowires on the substrate as evidenced in Figure 5-6. A network of nanowires is present. This shows that this method produces a much higher density of nanowires in comparison with the previous method.

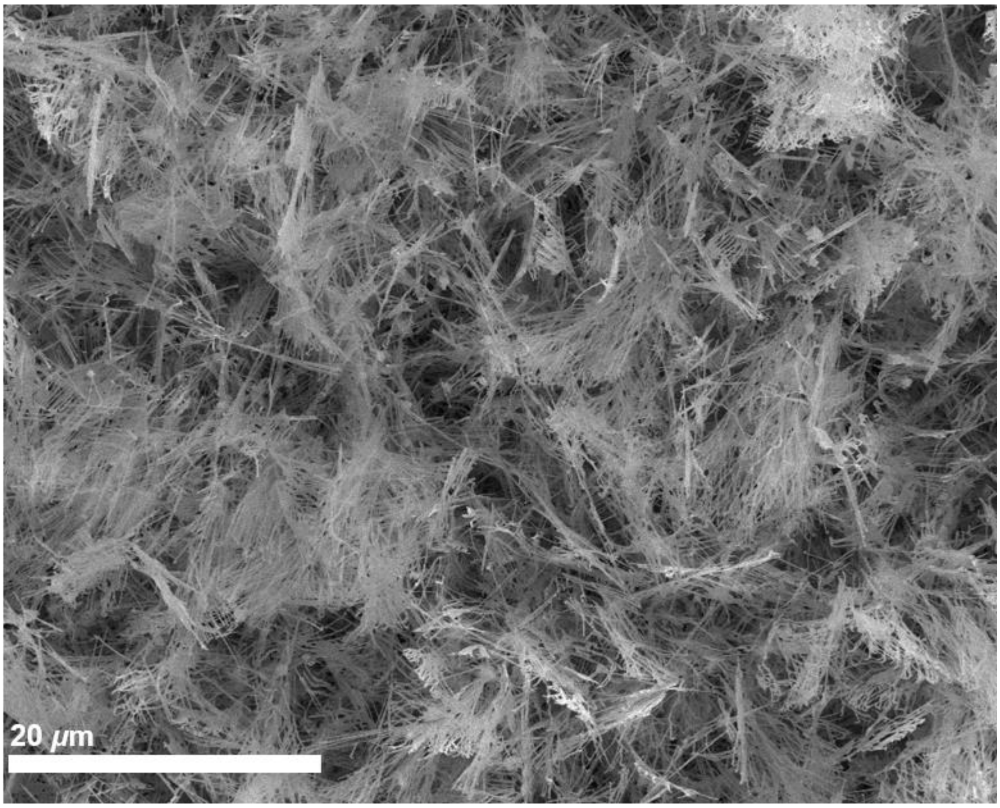

Figure 5-6: SEM image of $SnSe_2$ nanowires deposited from $[SnCl_4\{^nBuSe(CH_2)_3Se^nBu\}]$ in anhydrous toluene at 873 K onto a AuNPs on Si substrate via LICVD into a steel cell.

However, both PXRD and Raman measurements reveal there to be $SnSe_2$ and SnSe present. Analysing the PXRD, shown in Figure 5-7, it can be seen that the (0 0 1), (0 1 1) and (1 1 0) reflections of $SnSe_2$ are clearly present at 15.3, 31.0 and 47.3 °. The main reflections of SnSe, (0 1 1), (1 1 1) and (3 1 1), are observed at 29.2, 30.2 and 37.7 ° respectively. A number of smaller reflections from SnSe are indexed in Figure 5-7.

Looking at the Raman spectrum in Figure 5-8, the sharp peak at ~ 180 $cm^{-1}$ can be attributed to the $A_{1g}$ band of $SnSe_2$,[32] whilst the features at 105, 130 and 150 $cm^{-1}$ can be attributed to the $B_{3g}$, $A_{2g}$ and $A_{3g}$ modes of SnSe.[33] This is comparable to 115, 135 and 150 $cm^{-1}$ seen for SnSe in Chapter 4. This, along with the PXRD, is consistent with a mixture of $SnSe_2$ and SnSe being formed.

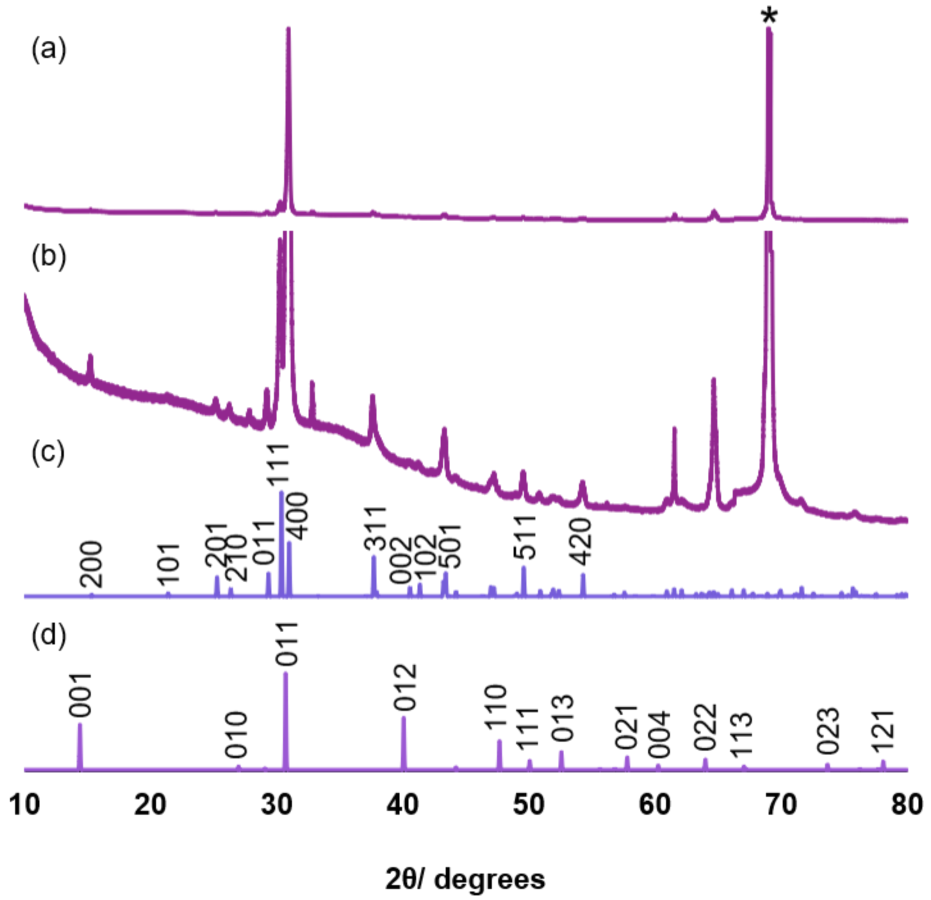

Figure 5-7: Powder XRD spectrum of the bulk $SnSe_2$ nanowires and SnSe film deposited from $[SnCl_4\{^nBuSe(CH_2)_3Se^nBu\}]$ in anhydrous toluene at 873 K onto a AuNPs on Si substrate via LICVD into a steel cell (a) and with the baseline expanded (b) and indexed patterns of bulk SnSe (c)[34] and bulk $SnSe_2$ (d).[35] The reflection marked with an asterisk is due to the Si (400) Substrate.

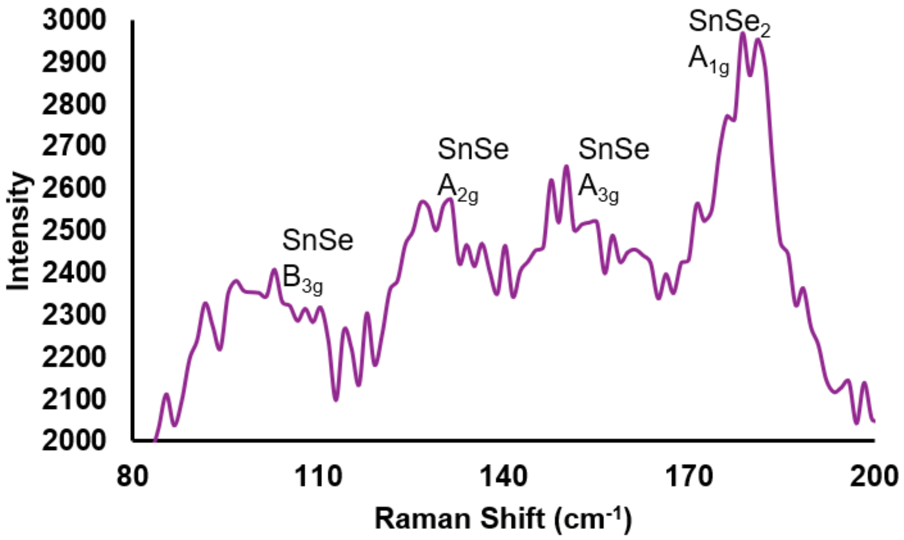

Figure 5-8: Raman spectrum of the bulk sample deposited from $[SnCl_4\{^nBuSe(CH_2)_3Se^nBu\}]$ in anhydrous toluene at 873 K onto a AuNPs on Si substrate via LICVD into a steel cell.

Nevertheless, the nanowires were removed via sonication and dropped onto a TEM grid for further analysis. TEM showed that nanowires produced were over 5 µm in length and about 135 nm in diameter as seen in Figure 5-9. In the diffraction pattern obtained, the (0 0 1) and (1 0 0) reflections of hexagonal $SnSe_2$ could be identified.

Furthermore, analysis by both EDX and Raman spectroscopy was consistent with the nanowires being $SnSe_2$. EDX analysis showed a composition of $SnSe_{2.1}$. Also, little gold was detected via EDX in these nanowires, this may be due to the Au seed becoming detached during the sonication process. Raman analysis (Figure 5-11) of the individual nanowires show the $A_{1g}$ mode of $SnSe_2$ at 180 $cm^{-1}$ which is comparable to 180 $cm^{-1}$ seen for $SnSe_2$ in Chapter 4 and in the literature.[32] Analysis of the remainder of the bulk post sonication reveals a large quantity of SnSe. Therefore, this suggests that an SnSe film forms closer to the hot substrate surface. This is consistent with what was seen in Chapter 4 with SnSe formed at higher temperatures in comparison to $SnSe_2$ from the same precursor. EDX analysis of the thin film remaining on the substrate post sonication reveals a stoichiometry of $SnSe_{1.1}$.

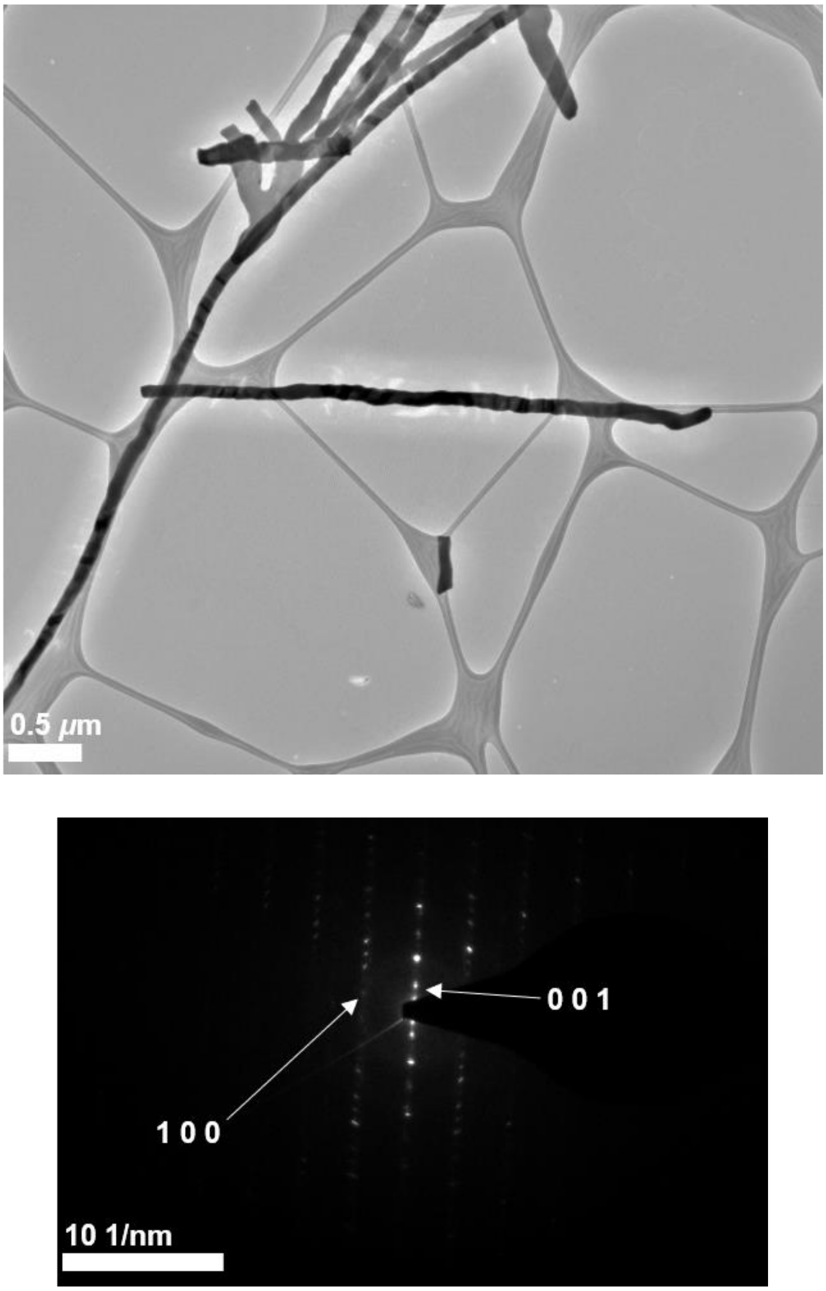

Figure 5-9: TEM image (top) and diffraction pattern (bottom) of $SnSe_2$ nanowires sonicated from bulk sample deposited from $[SnCl_4\{^nBuSe(CH_2)_3Se^nBu\}]$ in anhydrous toluene at 873 K onto a AuNPs on Si substrate via LICVD in a steel cell.

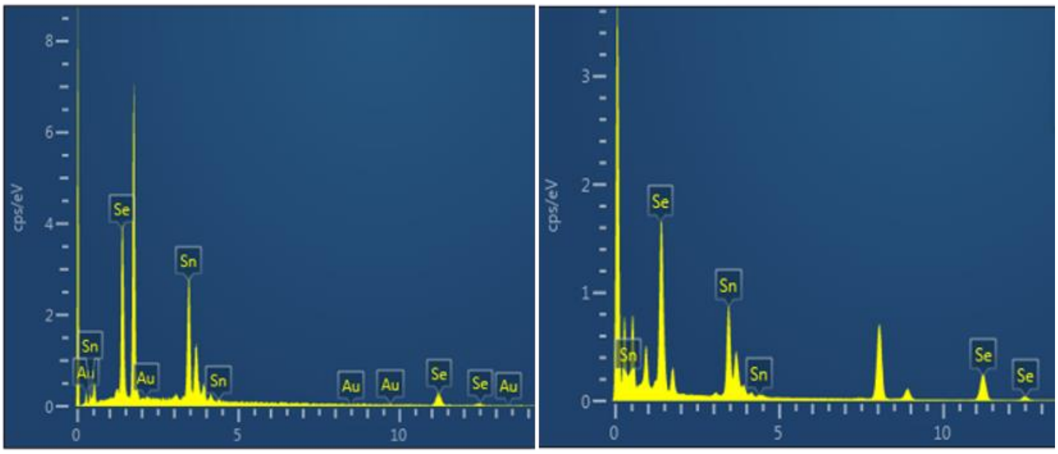

Figure 5-10: EDX spectrum of remainder of bulk sample after sonication (left) and an $SnSe_2$ nanowire sonicated from bulk sample (right) deposited from $[SnCl_4\{^nBuSe(CH_2)_3Se^nBu\}]$ in anhydrous toluene at 873 K onto a AuNPs on Si substrate via LICVD into a steel cell.

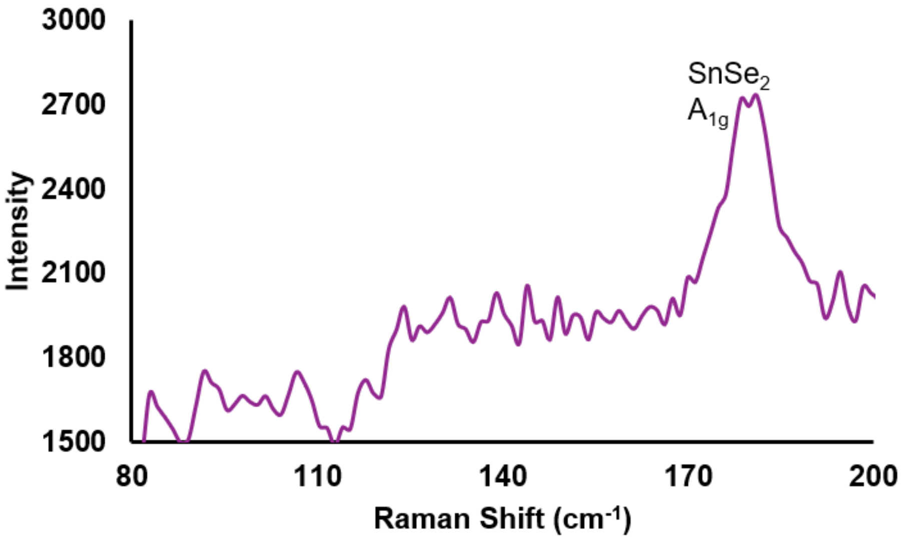

Figure 5-11: Raman spectrum of an $SnSe_2$ nanowire sonicated from the bulk sample deposited from $[SnCl_4\{^nBuSe(CH_2)_3Se^nBu\}]$ in anhydrous toluene at 873 K onto a AuNPs on Si substrate via LICVD into a steel cell.

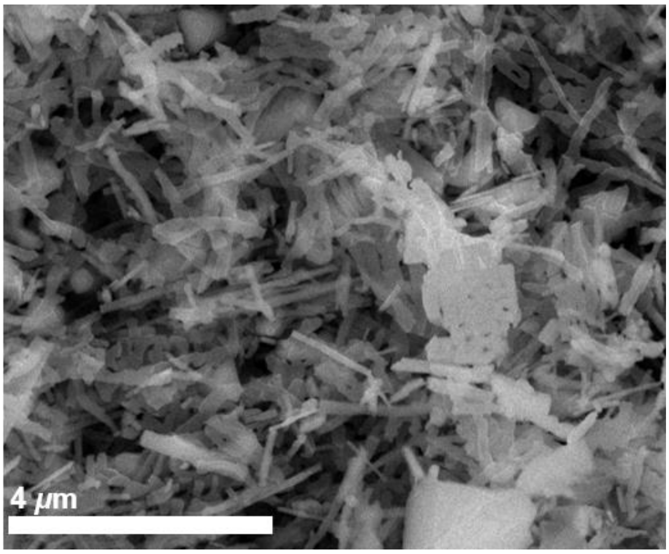

Figure 5-12: SEM image of thin film produced, post sonication, deposited from $[SnCl_4\{^nBuSe(CH_2)_3Se^nBu\}]$ in anhydrous toluene at 873 K onto a AuNPs on Si substrate via LICVD into a steel cell.

Further experiments resulted in iron contamination of the tin selenide nanowires. This was most likely due to the cell not being sufficiently cleaned and residual precursor decomposing into $SnO_2$ and HCl, leading to the corrosion of the steel cell. To eliminate this problem, the set up was changed in order to replace the steel cell with a quartz tube. A range of experiments was conducted, using this equipment, varying precursor concentration, argon flow rate and temperature. The substrate type was also varied and AuNPs on Si wafers or a 3 nm Au film on a Si wafer were used.

At 773 K, platelets of $SnSe_2$ typically formed with no evidence of nanowire formation. In contrast, the best temperature for nanowire formation appeared to be 823 to 873 K. At 823 K it can be seen from the SEM images, in Figure 5-14, that varying either the precursor concentration or the argon flow rate had a similar effect on the density of the nanowires produced. This is most clearly observed in the similar morphologies deposited from 7.5 mg/ mL with a 2 SCCM gas flow and 3.8 mg/ mL with a 4 SCCM gas flow. In both cases, a similar quantity of precursor is being injected at a similar rate leading to the deposition of a network of nanowires.

The optimum conditions at 823 K appear to be using 7.5 mg/ mL at 1 SCCM where regular straight nanowires, tens of µm in length, can be observed. Below this rate of precursor injection (3.8 mg/ mL at 0.65 SCCM), a very poor yield of nanowires is produced, instead 2D thin film dominates. Equally, an increased rate of precursor injection (7.5 mg/ mL at 4 SCCM) also results in the deposition of more 2D thin film growth. Interestingly, at 823 K, 7.5 mg/ mL and 2 SCCM nanoribbons have been deposited. These are of importance for applications such as solid state supercapacitors where tubular or layered structures can encourage the diffusion of ions resulting in increased power density.[36]

As the role of the gold catalyst is to direct nanowire growth, a too slow a rate of precursor injection may result in a slower rate of saturation of the Au liquid droplet and lead to a more typical CVD growth mechanism rather than VLS. Conversely, a too fast a rate of precursor injection may result in the formation of platelets due to the favoured in plane bonding overriding the VLS method, which directs nanowire growth, because of excess precursor.

At 1 SCCM, deposition at 823 K led to a composition of $SnSe_{1.82}$ by EDX analysis, indicating that the nanowires deposited are slightly selenium deficient. Depositions undertaken using an argon flow rate of 2 SCCM and a precursor concentration of 7.5 mg/ mL at a range of temperatures showed variation in the elemental composition of the nanowires produced as can be observed in Table 5-1 below. The deposition at 873 K produces nanowires of the composition closest to $SnSe_2$.

PXRD analysis of the sample at 1 SCCM and 823 K (Figure 5-13) indicates that SnSe (31.0 °,(4 0 0)) is also present alongside the $SnSe_2$ (50.2 °,(1 1 1)) nanowires. That being said, the pattern is extremely weak due to the low sample to substrate ratio present.

| Temperature/ K | Composition |
|---|---|
| 823 | $SnSe_{1.78}$ |
| 873 | $SnSe_{1.94}$ |
| 923 | $SnSe_{2.16}$ |

Table 5-1: Showing the change in composition of the nanowires with deposition temperature using a constant precursor concentration (7.5 mg/ mL) and flow rate (2 SCCM).

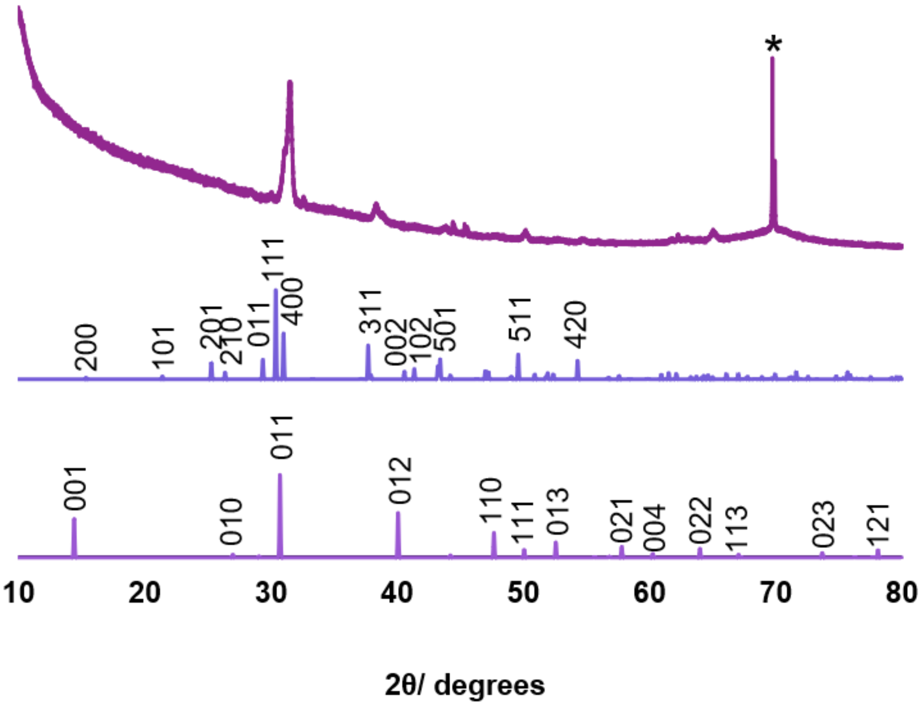

Figure 5-13:Powder XRD pattern of $SnSe_2$ deposited from $[SnCl_4\{^nBuSe(CH_2)_3Se^nBu\}]$ at 823 K and 1 SCCM on an Au film on $SiO_2/Si$ and indexed bulk patterns of SnSe (middle)[34] and $SnSe_2$ (bottom).[35]

Observing the morphology of the $SnSe_2$ deposited at 873 K and from 7.5 mg/ mL with change in argon flow rate in Figure 5-15, it can be seen that by increasing the flow rate and hence the rate of precursor injection, the density of nanowires produced is increased. It is worth noting that a larger precursor injection rate is needed at this temperature in comparison with depositions at 823 K in order to synthesize the same density of nanowires. At a flow rate of 1 SCCM very few nanowires are deposited, and it is mostly a non-continuous thin film. At 2 SCCM, there are more nanowires, and these have diameters of 300-600 nm, there are also some nanorods present. At a flow rate of 4 SCCM, the density of nanowires (10 µm by ~100 nm) is still relatively low.

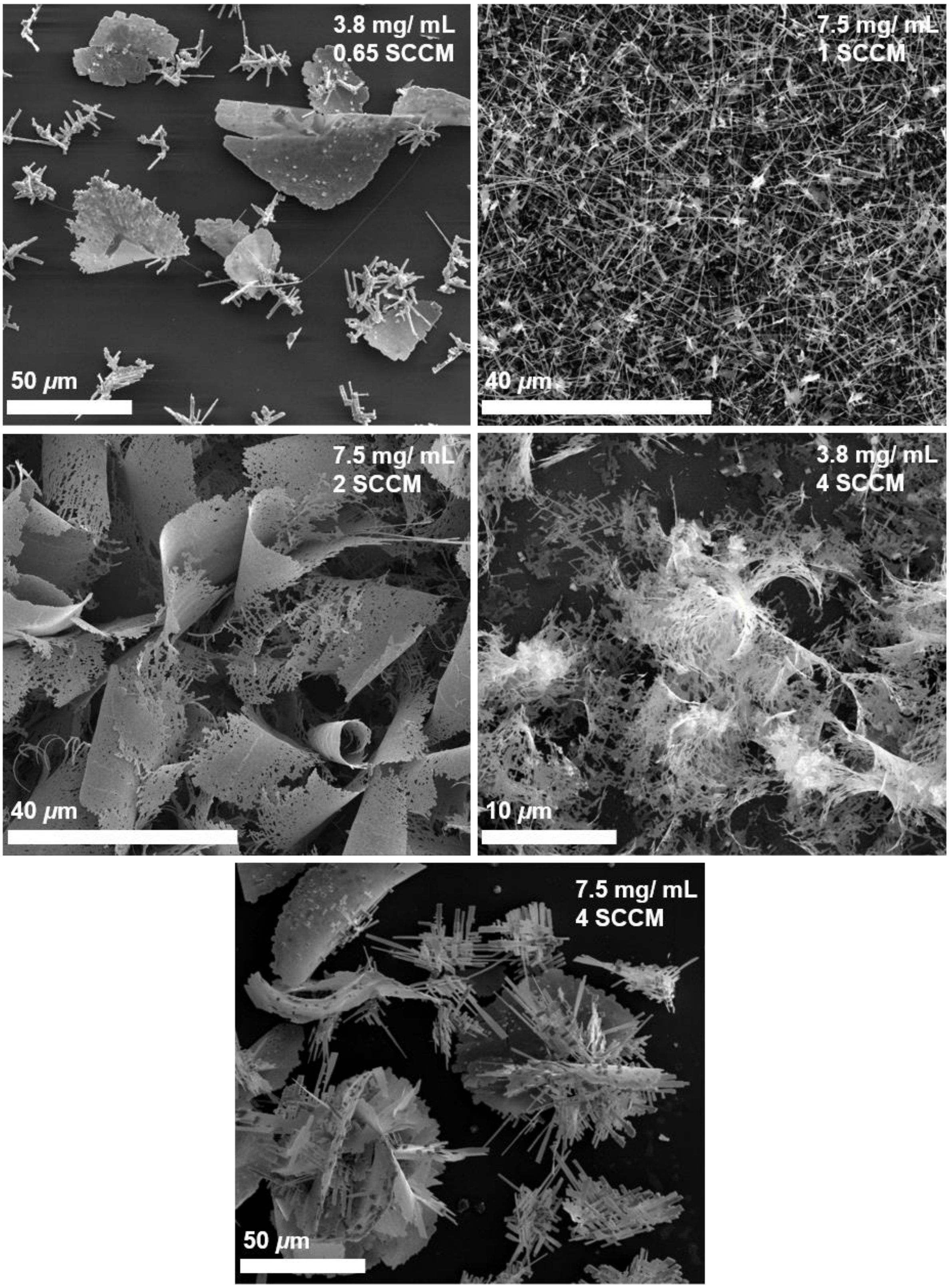

Figure 5-14: SEM images of $SnSe_2$ deposited via LICVD from $[SnCl_4\{^nBuSe(CH_2)_3Se^nBu\}]$ in anhydrous toluene at 823 K with a range of concentrations and argon flow rates used. The substrates used were a 3 nm Au film on $SiO_2$/Si except for 7.5 mg/ mL and 4 SCCM (bottom) in which a AuNPs on Si substrate was used.

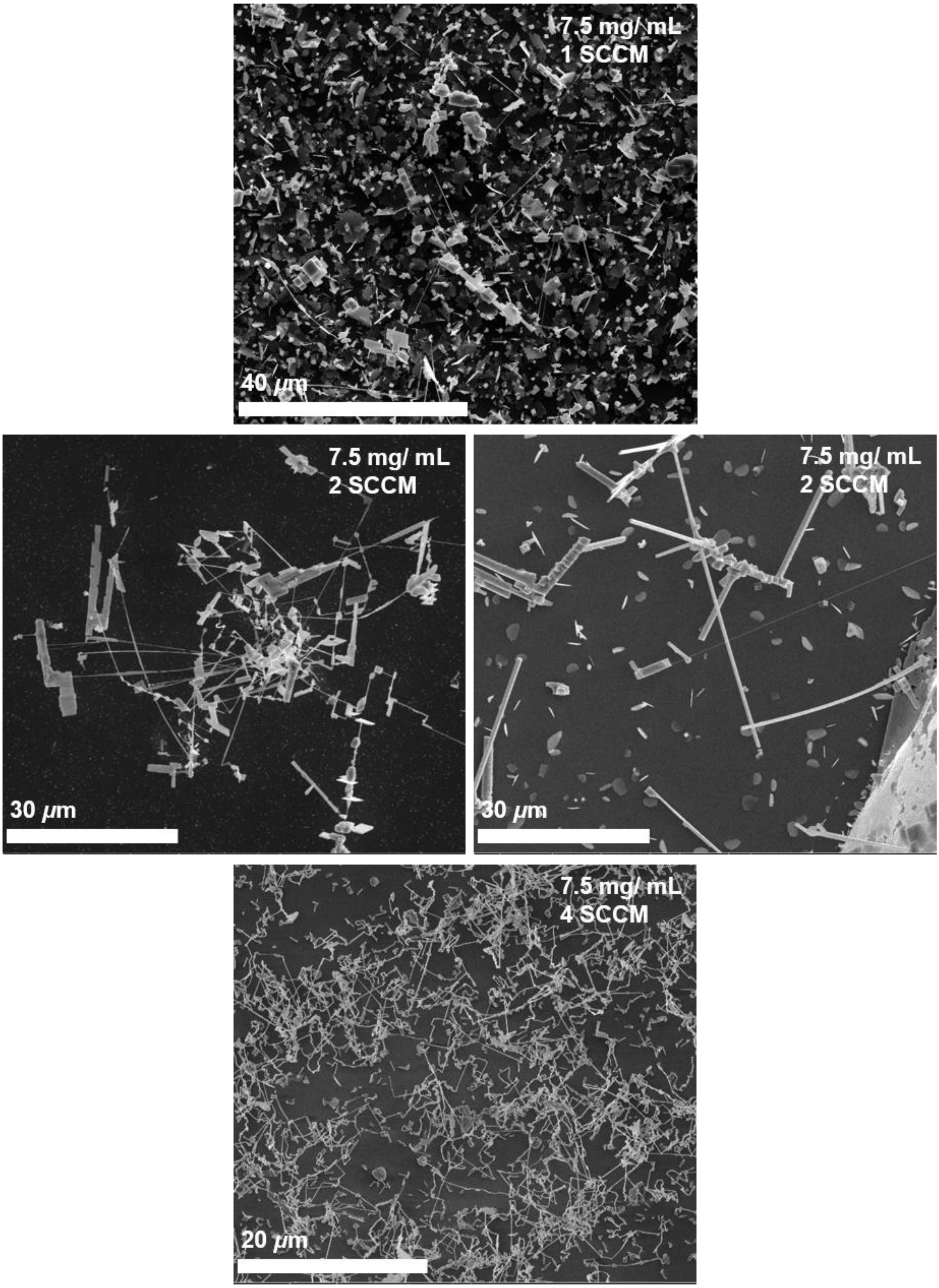

Figure 5-15: SEM images of $SnSe_2$ deposited via LICVD $[SnCl_4\{^nBuSe(CH_2)_3Se^nBu\}]$ in anhydrous toluene at 873 K and precursor concentration of 7.5 mg/ mL and a range of argon flow rates used. The substrates used were a 3 nm Au film on $SiO_2$/Si.

The nanowires deposited from a 7.5 mg/ mL solution at 873 K under an argon gas flow of 4 SCCM, have a very small (5 nm) oxide layer present in comparison to the wires deposited in the steel cell. This means the nanowires are of better quality for photoresponse devices.

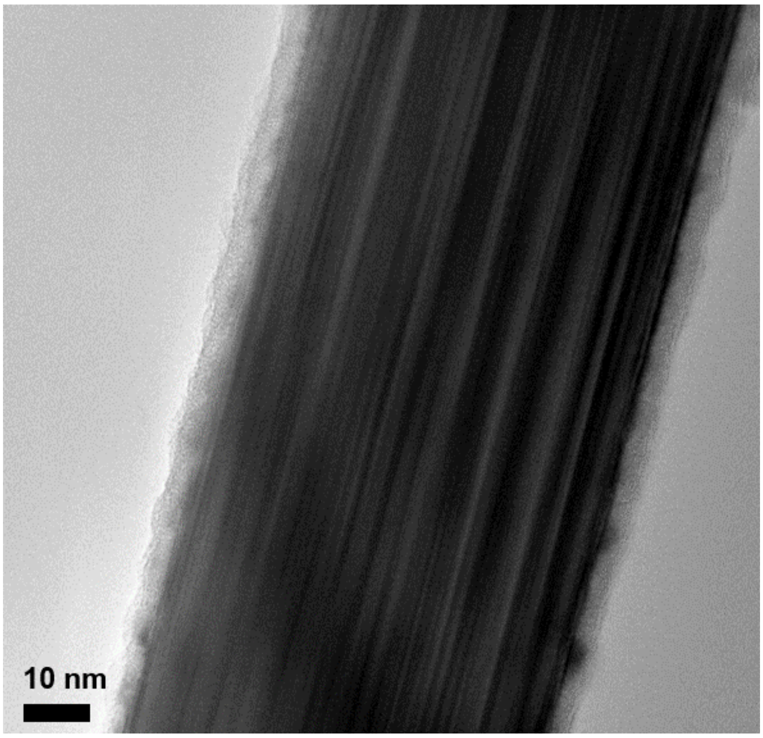

Figure 5-16: TEM image of an individual $SnSe_2$ nanowire showing a 5nm oxide layer on a nanowire of diameter 60 nm.

### 5.2.3 Preliminary Results for LPCVD/LICVD of $Bi_2Se_3$ and $Sb_2Se_3$ Nanowires

As well as using a precursor previously used for the LPCVD of $SnSe_2$, precursors for the LPCVD of other metal chalcogenides have also been tested in preliminary experiments. This was with the aim of depositing metal chalcogenide nanowires from single source precursors. $[BiCl_3(Se^nBu_2)_3]$ has been tested under the LPCVD set up mentioned previously. ~50 mg of precursor at 823 K led to silver grey deposition on the AuNPs on Si substrate under LPCVD conditions. SEM images revealed that there was a poor yield of nanowires in comparison to other morphologies. In Figure 5-17 below, an individual nanowire can be seen with an AuNP seed.

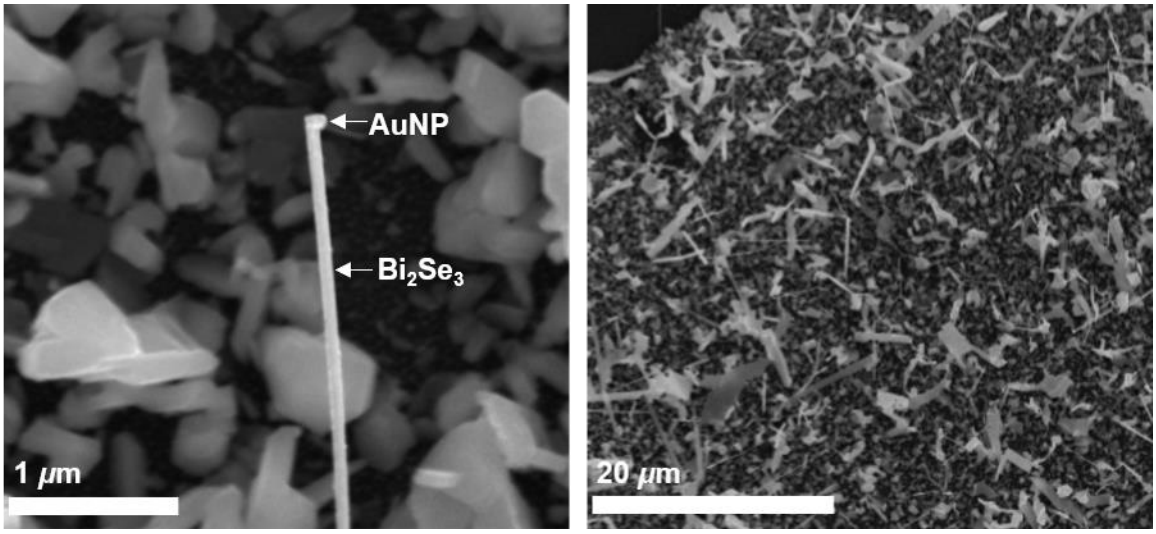

Figure 5-17: SEM images of $Bi_2Se_3$ deposited from $[BiCl_3(Se^nBu_2)_3]$ via LPCVD with an argon carrier gas onto AuNPs on Si at 823 K.showing a few nanowires amongst a thin film.

EDX analysis (Figure 5-18) of individual nanowires revealed a stoichiometry of $Bi_2Se_{3.2}$ indicating that the nanowires are selenium rich but due to the large substrate to sample ratio large errors will be present. It is worth noting that there is also some gold incorporation. A Raman spectrum of the sample is consistent with $Bi_2Se_3$ with features at ~ 130 and 170 $cm^{-1}$ which can be assigned to the $E^2_g$ and $A^2_{1g}$ modes.[37]

TEM imaging reveals an individual nanowire of ~ 3 µm in length and 100 nm in diameter. Rhombohedral $Bi_2Se_3$ was identified.

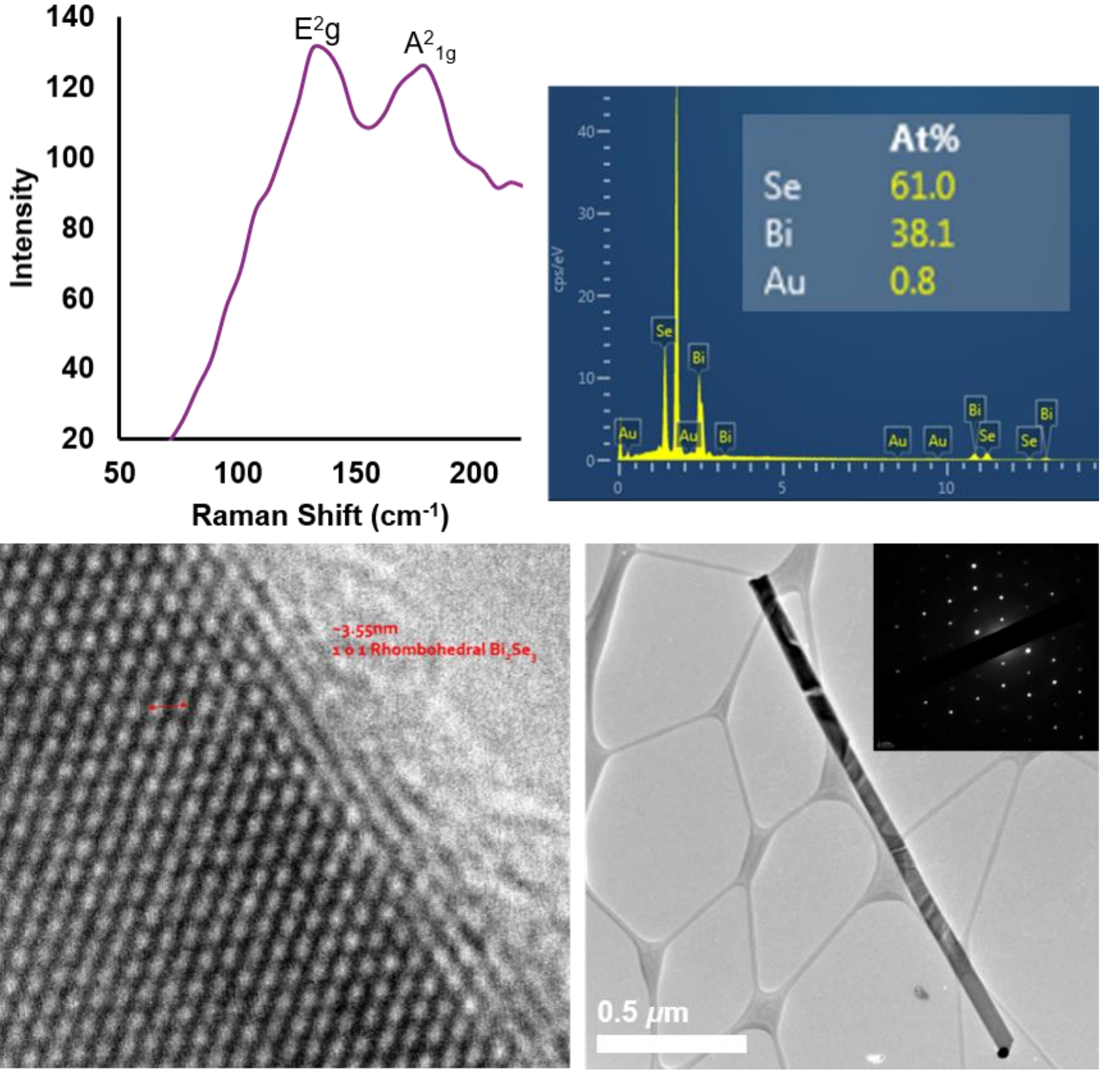

Figure 5-18: Raman spectrum (top left), EDX spectrum (top right) and TEM (bottom) of an individual nanowire deposited from [$BiCl_3(Se^nBu_2)_3$] via LPCVD with an argon carrier gas onto AuNPs on Si.

The analogous [$SbCl_3(Se^nBu_2)_3$] precursor was also tested using the LICVD method. This was completed at 773 K using the steel cell set up, approximately 50 mg of precursor was used and led to silver grey deposition on the AuNPs on Si substrate. SEM images in Figure 5-19 show nanowires (tens of µm by 65 nm in diameter) have been produced across the substrate. However, there are also other morphologies present. The coverage appears to be sparse.

A PXRD pattern, shown in Figure 5-20, is consistent with $Sb_2Se_3$. The PXRD pattern is quite weak due to the small nanowire to substrate ratio present but some of the more intense reflections are present.

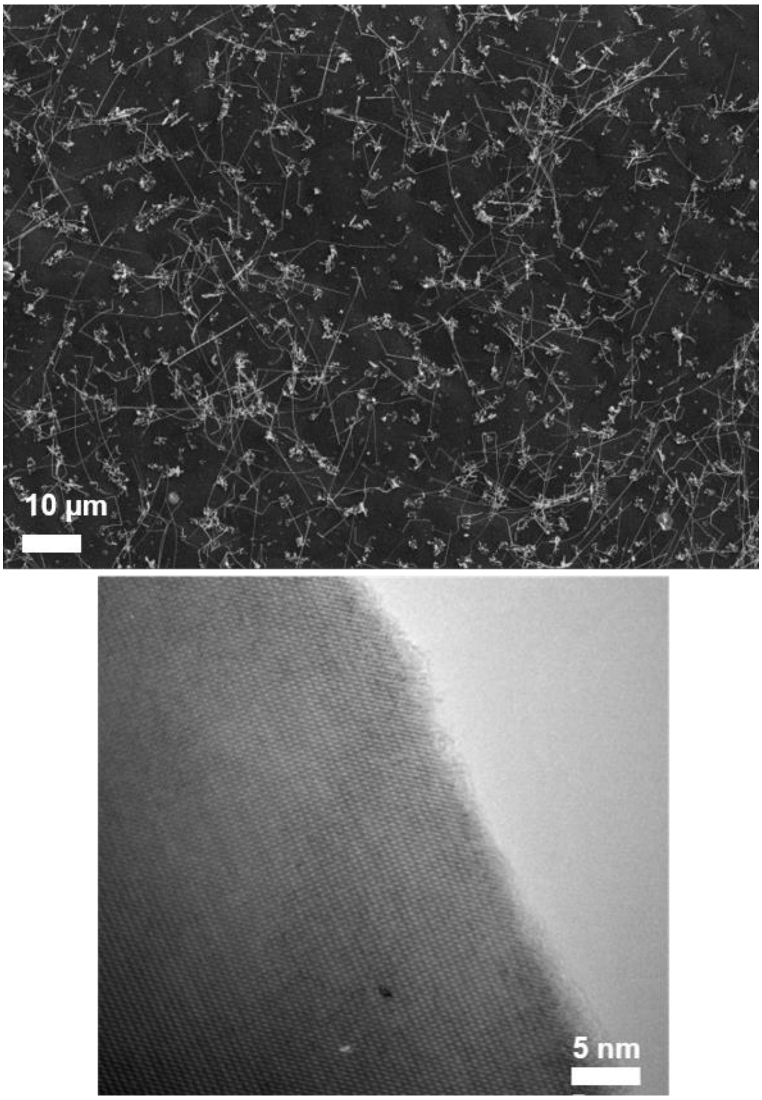

Figure 5-19: SEM (top) and TEM (bottom) images of $Sb_2Se_3$ deposited from 50 mg [$SbCl_3(Se^nBu_2)_3$] via LICVD onto a AuNPs on Si substrate at 773 K under an Ar gas flow at 1 SCCM.

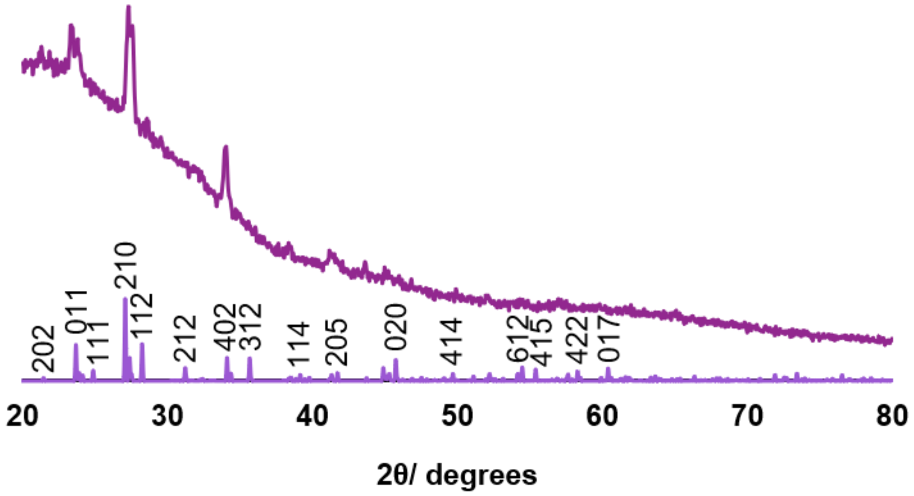

Figure 5-20: Powder XRD pattern of $Sb_2Se_3$ nanowires deposited [$SbCl_3(Se^nBu_2)_3$] at 773 K via LICVD onto a AuNPs on Si substrate and an indexed bulk pattern of $Sb_2Se_3$.[38]

## 5.3 Conclusions and Further Work

In conclusion, it has been demonstrated that $[SnCl_4\{^nBuSe(CH_2)_3Se^nBu\}]$ acts as a suitable single source precursor for the deposition of $SnSe_2$ nanowires via LICVD. It is catalysed by the gold in the substrate in a vapour liquid solid/ CVD technique.

Preliminary investigations showed that $[BiCl_3(Se^nBu_2)_3]$ and $[SbCl_3(Se^nBu_2)_3]$ have potential to be used in the same way to deposit $M_2Se_3$ (M = Bi, Sb) nanowires. Optimisation of conditions should result in a good yield of high purity nanowires.

The work in this chapter has demonstrated the versatility of single source precursors. It shows that those suitable for the LPCVD of thin films are also often suitable for the deposition of nanowires via LICVD methods. The experiments showed that density and morphology of nanowires could be controlled by the precursor concentration and argon flow rate. The precursors used in this piece of work are soluble in an appropriate solvent, toluene. This is a necessity for this method. Also, this suggests that the precursors can be used for other deposition techniques such as AACVD. This leads to the possibility of exploring the suitability of other single source precursors, discussed in this thesis, for the deposition of metal chalcogenide nanowires.

The conditions of these CVD techniques could be optimised in order to deposit high density, uniform nanowires. Furthermore, the electrical properties and phase change behaviour of the deposited nanowires could be tested to determine suitability for a range of applications.

## 5.4 Experimental

### 5.4.1 Synthesis and Characterisation of Precursors

Precursors were synthesized as described in Chapters 2 and 4.

### 5.4.2 LPCVD

In a clean dry glove box, both the precursor and substrates were loaded into silica boats and these were placed in a silica tube sealed with taps at either end. This was removed from the glove box and placed in a furnace. The tap closest to the precursor was attached to an argon gas line and the other to a vacuum line. The set up was flushed with $N_2$ and the furnace allowed to heat up and stabilise before the start of each experiment.

### 5.4.3 LICVD

In a typical experiment the precursor was dissolved in anhydrous toluene in a clean dry glove box and stirred for ~ 30 minutes. The solution was loaded into a syringe and removed from the glove box and connected to a syringe pump which was used to inject the precursor solution at a given rate into the quartz tube/ steel cell containing the substrate. The quartz tube/steel cell were flushed with $N_2$ before each experiment and were placed in a furnace and the furnace allowed to heat up and stabilise before the start of each experiment.

### 5.4.4 Substrates and Pre-treatment

Si substrates were cleaned in water and the IPA and dried with nitrogen by Fionan and I.

The Au nanopaticles were synthesised according to the literature method[39] by Fionan at University College Cork. They were dispersed in toluene and spin-cast, using a Specialty Coating Systems 6800, onto the Si substrates by Fionan and I.

Au Film on Si: Si substrates were coated with a 3 nm Au film in a Temescal e-beam evaporator by Dr. Subhajit Biswas at UCC.

### 5.4.5 Nanowire Characterisation

Powder XRD was undertaken on a Philips X'pert Pro MPD with a Panalytical Empyrean Cu X-ray tube with a Philips X'celerator detector.

SEM images were obtained from a FEI Helios Nanolab 600i, and EDX data was acquired from the attached Oxford X-Max 80 EDX detector.

TEM was obtained from a 200kV JEOL 2100.

Raman spectroscopy was collected with a Renishaw InVia Raman spectrometer equipped with a 2400 lines/mm grating using a 514 nm 30 mW Argon Ion laser, spectra were collected using a RenCam CCD camera. The beam was focused onto the samples using either a 20×/50× objective lens.

## 5.5 References

1 Y. Fu, G. Gou, X. Wang, Y. Chen, Q. Wan, J. Sun, S. Xiao, H. Huang, J. Yang and G. Dai, *Appl. Phys. A*, 2017, **123**, 2991–2998.

2 Y. Huang, H.-X. Deng, K. Xu, Z.-X. Wang, Q.-S. Wang, F.-M. Wang, F. Wang, X.-Y. Zhan, S.-S. Li, J.-W. Luo and J. He, *Nanoscale*, 2015, **7**, 14093–14099.

3 I. Y. Ahmet, M. S. Hill, A. L. Johnson and L. M. Peter, *Chem. Mater.*, 2015, **27**, 7680–7688.

4 F. K. Butt, M. Mirza, C. Cao, F. Idrees, M. Tahir, M. Safdar, Z. Ali, M. Tanveer and I. Aslam, *CrystEngComm*, 2014, **16**, 3470–3473.

5 M. S. Mahdi, K. Ibrahim, A. Hmood, N. M. Ahmed, F. I. Mustafa and S. A. Azzez, *Mater. Lett.*, 2017, **200**, 10–13.

6 L.-D. Zhao, S.-H. Lo, Y. Zhang, H. Sun, G. Tan, C. Uher, C. Wolverton, V. P. Dravid and M. G. Kanatzidis, *Nature*, 2014, **508**, 373–377.

7 C. Wang, Y. Chen, J. Jiang, R. Zhang, Y. Niu, T. Zhou, J. Xia, H. Tian, J. Hu and P. Yang, *RSC Adv.*, 2017, **7**, 16795–16800.

8 K.-M. Chung, D. Wamwangi, M. Woda, M. Wuttig and W. Bensch, *J. Appl. Phys.*, 2008, **103**, 0835231–0835237.

9 R. Y. Wang, M. A. Caldwell, R. G. D. Jeyasingh, S. Aloni, R. M. Shelby, H. S. P. Wong and D. J. Milliron, *J. Appl. Phys.*, 2011, **109**, 1135061–1135066.

10 Y. Zhou, M. Leng, Z. Xia, J. Zhong, H. Song, X. Liu, B. Yang, J. Zhang, J. Chen, K. Zhou, J. Han, Y. Cheng and J. Tang, *Adv. Energy Mater.*, 2014, **4**, 13018461–13018468.

11 C. Chen, D. C. Bobela, Y. Yang, S. Lu, K. Zeng, C. Ge, B. Yang, L. Gao, Y. Zhao, M. C. Beard and J. Tang, *Front. Optoelectron.*, 2017, **10**, 18–30.

12 Y. C. Choi, T. N. Mandal, W. S. Yang, Y. H. Lee, S. H. Im, J. H. Noh and S. Il Seok, *Angew. Chem. Int. Ed.*, 2014, **53**, 1329–1333.

13 X. Liu, J. Chen, M. Luo, M. Leng, Z. Xia, Y. Zhou, S. Qin, D. J. Xue, L. Lv, H. Huang, D. Niu and J. Tang, *ACS Appl. Mater. Interfaces*, 2014, **6**, 10687–10695.

14 V. Gunasekaran, G. H. Park, M. Suemitsu and H. Fukidome, *Mater. Sci. Semicond. Process.*, 2017, **68**, 128–132.

15 K. Thorkelsson, P. Bai and T. Xu, *Nano Today*, 2015, **10**, 48–66.

16 Q. Zheng, Y. Wang and J. Zhu, *J. Phys. D. Appl. Phys.*, 2017, **50**, 2430021–243000213.

17 P. Nukala and R. Agarwal, *RSC Smart Mater.*, 2015, **2015**, 111–166.

18 Y. T. Lin, J. Bin Shi, Y. C. Chen, C. J. Chen and P. F. Wu, *Nanoscale Res. Lett.*, 2009, **4**, 694–698.

19 S. Liu, X. Guo, M. Li, W. H. Zhang, X. Liu and C. Li, *Angew. Chemie - Int. Ed.*, 2011, **50**, 12050–12053.

20 S. K. Panda, A. Datta, A. Dev, S. Gorai and S. Chaudhuri, *Cryst. Growth Des.*, 2006, **6**, 2177–2181.

21 J. T. Mlack, A. Rahman, G. L. Johns, K. J. T. Livi, N. Marković, J. T. Mlack, A. Rahman, G. L. Johns, K. J. T. Livi and N. Markovic, *Appl. Phys. Lett.*, 2013, **102**, 1931081–1931085.

22 J. Liu, J. Jian, Z. Yu, Z. Zhang, B. Cao and B. Du, *Cryst. Growth Des.*, 2017, **17**, 6163–6168.

23 S. Meister, H. Peng, K. McIlwrath, K. Jarausch, X. F. Zhang and Y. Cui, *Nano Lett.*, 2006, **6**, 1514–1517.

24 J. S. Lee, S. Brittman, D. Yu and H. Park, *J. Am. Chem. Soc.*, 2008, **130**, 46252–6258.

25 S. R. Suryawanshi, S. S. Warule, S. S. Patil, K. R. Patil and M. A. More, *ACS Appl. Mater. Interfaces*, 2014, **6**, 2018–2025.

26 D. Mudusu, K. R. Nandanapalli, S. R. Dugasani, J. W. Kang, S. H. Park and C. W. Tu, *RSC Adv.*, 2017, **7**, 41452–41459.

27 R. Bin Yang, J. Bachmann, E. Pippel, A. Berger, J. Woltersdorf, U. Gösele and K. Nielsch, *Adv. Mater.*, 2009, **21**, 3170–3174.

28 M. Longo, C. Wiemer, O. Salicio, M. Fanciulli, L. Lazzarini and E. Rotunno, *J. Cryst. Growth*, 2011, **315**, 152–156.

29 Y. F. Lin, H. W. Chang, S. Y. Lu and C. W. Liu, *J. Phys. Chem. C*, 2007, **111**, 18538–18544.

30 U. Jeong, P. H. C. Camargo, Y. H. Lee and Y. Xia, *J. Mater. Chem.*, 2006, **16**, 3893.

31 G. D. Moon, S. Ko, Y. Xia and U. Jeong, *ACS Nano*, 2010, **4**, 2307–2319.

32 D. Walsh, S. Jandl and J. Y. Harbec, *J.Phys.C Solid St. Phys*, 1980, **13**, 125–127.

33 S. Luo, X. Qi, H. Yao, X. Ren, Q. Chen and J. Zhong, *J. Phys. Chem. C*, 2017, **121**, 4674–4679.

34 K. Adouby, C. Perez-Vicente and J. C. Jumas, *Zeitschrift fur Krist.*, 1998, **213**, 343–349.

35 G. Busch, C. Froehlich and F. Hullinger, *Helv. Phys. Acta*, 1961, **34**, 359–368.

36 C. Zhang, H. Yin, M. Han, Z. Dai, H. Pang, Y. Zheng, Y. Q. Lan, J. Bao and J. Zhu, *ACS Nano*, 2014, **8**, 3761–3770.

37 J. Zhang, Z. Peng, A. Soni, Y. Zhao, Y. Xiong, B. Peng, J. Wang, M. S. Dresselhaus and Q. Xiong, *Nano Lett.*, 2011, **11**, 2407–2414.

38 N. W. Tideswell, F. H. Kruse and J. D. McCullough, *Acta Cryst.*, 1957, **10**, 99–102.

39 S. T. He, S. S. Xie, J. N. Yao, H. J. Gao and S. J. Pang, *Appl. Phys. Lett.*, 2002, **81**, 150–152.

# Chapter 6: Precursors for the Deposition of Titanium Chalcogenides

## 6.1 Introduction

$TiSe_2$ is a layered metal chalcogenide with a structure similar to $CdI_2$.[1] Its structure is the 1T polytype, with one layer per repeat unit, tetragonal symmetry and octahedral coordination around the titanium atoms. It is known to show semi metallic or semiconducting behaviour,[2] as well as exhibiting superconductivity and charge density waves.[2,3]

Both dual source and single source precursor approaches to the deposition of thin films have been demonstrated. Previous work at the University of Southampton has shown depositions from a range of single source precursors under LPCVD conditions. These include $[TiCl_4(ER_2)_2]$ (E = S or Se) (R = Et or $^n$Bu) and $[TiCl_4\{o\text{-}C_6H_4(CH_2EMe)_2\}]$.[4,5] Furthermore, $[TiCl_4(Se^nBu)_2]$ has been used successfully to demonstrate substrate selectivity with $TiSe_2$ showing an affinity for TiN over $SiO_2$.[4] It has been suggested that high conductivity and hydrophobicity of TiN is the reason for this.[6] Despite these SSPs being successful in deposition of metal dichalcogenide films, they are very readily hydrolysed. It is hoped that the use of chelated ligands will produce a much more stable complex.

In a dual source approach to CVD of titanium dichalcogenide films, $TiCl_4$ is often used as a precursor. Carmalt et *al*. have shown the deposition of $TiS_2$ films from $TiCl_4$ with $HS(CH_2)_2SH$, $HSC(CH_3)_3$ or $S(Si(CH_3)_3)_2$ using APCVD. Despite, deposition occurring from as low as 548 K, the films produced were only crystalline when deposited at temperatures of 773 K or higher.[7] An earlier dual source approach used simply $H_2S$ and $TiCl_4$ to deposit $TiS_2$ via PECVD.[8] Selenide and telluride analogues of this reagent are unsuitable for CVD and are also extremely toxic.

Single source precursors have also been used successfully in the deposition of $TiS_2$. The coordination complex $[Ti(SBu^t)_4]$ was used to produce amorphous films of TiS via LPCVD at temperatures of 403 – 473 K.[9] However, the same precursor has since been used to produce $TiS_2$ films also via LPCVD at 383 – 623 K and the use of molybdenum analogues has also been successful.[10] Interestingly, it has been observed that $[TiCl_4(SMe_2)_2]$ and $[(TiCl_4)_2(CH_3SSCH_3)]$ deposit $TiS_2$ at temperatures of 673 – 873 K.[11] Usually, complexes containing methyl groups do not make good precursors due to the lack of a clean elimination pathway leading to carbon contamination.

$TiSe_2$ has also been deposited from a variety of different precursors. APCVD using $TiCl_4$ with $Se^tBu_2$ or $SeEt_2$ has produced matt navy blue and purple titanium chalcogenide films respectively. It was observed that at 823 K stoichiometry was 1:2 Ti: Se, however, an increase in temperature to 873 K led to a 1:1.5 stoichiometry obtained.[12] Furthermore, $TiCl_4$ and $Se^tBu_2$ have also been used alongside $NbCl_5$ to produce composite films.[13] $[TiCl_4(SeMe_2)_2]$ has been synthesised, as a decomposition product, and shown to be a poor precursor for CVD whilst $[TiCl_4(SeEt_2)_2]$ can be used to produce 'rose bronze' $TiSe_2$ films at 773 – 873 K.[14]

Previous work, on chemical vapour deposition, has resulted in the deposition of air and moisture stable $TiS_2$ and $TiSe_2$ films from single source precursors such as $[TiCl_4\{o\text{-}C_6H_4(CH_2EMe)_2\}]$ (E= S or Se).[5] Zirconium and tin analogues of these compounds were also made with the tin analogues successful in the deposition of analogous $ME_2$ films under specific temperatures with SnS produced at higher temperatures for the sulfide analogues.[5] Furthermore, the use of $[TiCl_4(Se^nBu_2)_2]$ and TiN/ $SiO_2$ patterned substrates has demonstrated the selectivity of deposition of $TiSe_2$ on TiN as opposed to $SiO_2$.[4] It has also been demonstrated that $[SnCl_4\{^nBuSe(CH_2)_nSe^nBu\}]$ (n = 2 or 3), as a precursor for $SnSe_2$, shows high substrate selectivity.[15] Furthermore, an extremely high degree of positional and orientational control over the growth of $Bi_2Te_3$ has been demonstrated using low pressure chemical vapour deposition.[16] Achieving this control in the deposition of other key materials would be a significant progression.

Other Ti(IV) complexes synthesised include $[TiCl_4\{MeE(CH_2)_nEMe\}]$, $[TiCl_4\{PhE(CH_2)_2EPh\}]$ and $[TiCl\{o\text{-}C_6H_4(EMe)_2\}]$ (E = S or Se) (n = 2 or 3).[17] However, these have not been tested as single source precursors and are not typical of single source precursors for LPCVD due to the inclusion of methyl groups or having high molecular weights. Despite much work being carried out on the deposition of titanium sulfides and selenides, the deposition of $TiTe_2$ has proved far more challenging with no single source precursors for $TiTe_2$ reported in the literature, to the best of my knowledge. Furthermore, tellurium carbon bonds are far more unstable than their selenide analogues which often results in decomposition. However, crystals of $TiTe_2$ have been grown via iodine vapour transport techniques.[18]

Two chalcogenoether ligands that have been utilised to good effect in this field are $^nBuSe(CH_2)_nSe^nBu$ (n = 2 or 3). The vanadium (IV) complex, $[VCl_4\{^nBuSe(CH_2)_2Se^nBu\}]$, proved insufficiently soluble,[19] but the tin (IV) complexes $[SnCl_4\{^nBuSe(CH_2)_nSe^nBu\}]$ (n = 2 or 3) (Figure 6-1) have been shown to deposit $SnSe_2$ films, which has also been selectively deposited onto lithographically patterned substrates.[15]

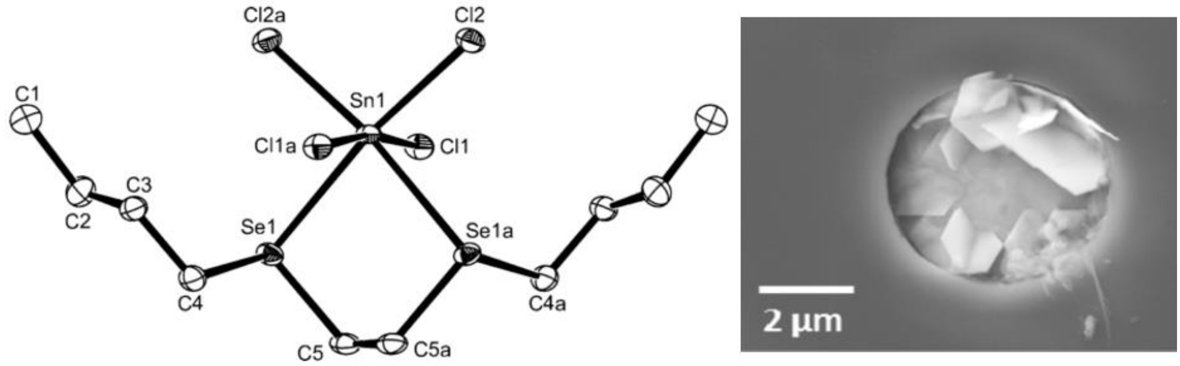

Figure 6-1: The crystal structure of [$SnCl_4\{^nBuSe(CH_2)_2Se^nBu\}$] and $SnSe_2$ crystals deposited in a 5 µm TiN well on a TiN/$SiO_2$ substrate.[15] (Reproduced from reference 15 with permission from ACS).

Regarding Ti (IV) halide complexes with tellurium containing species, there are none to be found in the literature. Electronegativities and E-H, E-C and E-E bond energies are displayed in Table 6-1. Tellurium is less electronegative than selenium or sulfur and forms comparatively weaker bonds to metal chlorides. This results in telluroether ligands being far more labile than their selenoether and thioether counterparts.[20] Furthermore, the weak Te-C bond results in ligands which undergo easy dealkylation and are also thermally and photolytically sensitive, as well as readily oxidising in air. This means that the structure of new telluroether ligands must be carefully designed.

| Chalcogen | S | Se | Te |
|---|---|---|---|
| Pauling Electronegativity | 2.6 | 2.6 | 2.1 |
| E-H Bond Energy/ kJmol$^{-1}$ | 366 | 276 | 238 |
| E-C Bond Energy/ kJmol$^{-1}$ | 272 | 234 | 200 |
| E-E Bond Energy/ kJmol$^{-1}$ | 266 | 192 | 149 |

Table 6-1: The electronegativities and bond energies for the chalcogens.[21]

Recently there has been a breakthrough in this field with the first examples of metal telluride films deposited from telluroether metal complexes. [$GaCl_3(Te^nBu_2)$] and [$\{GaCl_3\}_2\{^nBuTe(CH_2)_3Te^nBu\}$] have been used to deposit crystalline $Ga_2Te_3$ via an LPCVD technique.[22] This has been followed in the synthesis of [$BiCl_3(Te^nBu_2)$] for the deposition of crystalline $Bi_2Te_3$ thin films.[16] Extremely high selectivity of this material was observed with $Bi_2Te_3$ deposited in 100 nm TiN wells on a TiN/$SiO_2$ substrate and it was found that the orientation of the crystals could be controlled by control of the dimension of the TiN wells.[16]

Hybrid ligands with mixed donors may provide a solution to the soft donor character of the chalcogenoethers and in particular telluroethers and allow coordination to hard metal chloride acceptors There are many examples of hybrid ligands in the literature. These include both tellurides and selenides such as *o*-$C_6H_4$(EMe)(Y) (E = Se, Te; Y = $NMe_2$, $PMe_2$, $AsMe_2$, $SbMe_2$).[23,24] Hybrid ligands have also been used in complexes for catalytic applications due to the electronic differences of the donors, these were $[PdX_2\{RE(CH_2)_3NMe_2\}]$ (X = Cl, OAc; R = Ph, Mes, *o*-tol; E = Se, Te).[25]

The aim of this chapter is to develop novel single source precursors for the deposition of titanium dichalcogenide thin films. The synthesis and use of $[TiCl_4\{^nBuSe(CH_2)_nSe^nBu\}]$ (n = 2 or 3) will be attempted in order to establish whether the use of a bidentate ligand increases hydrolytic stability compared to the use of $[TiCl_4(Se^nBu_2)_2]$.[4] LPCVD conditions will be varied in order to optimise conditions to establish whether the deposition of ultrathin smooth films can be obtained.

In an attempt to develop $TiCl_4$ chalcogenoether precursors with increased stability and in particular to facilitate the deposition of $TiTe_2$ thin films, a synthesis route to novel single source precursors including hybrid, mixed donor ligands will be attempted. These will include: $[TiCl_4\{RE(CH_2)_3NMe_2\}]$ (E = Se: R = Me, Et, $^n$Bu; E = Te: R = Ph). Although the use of a phenyl group may result in a decrease in volatility due to increased molecular weight, it is hypothesised that, in this mixed donor ligand, there will be an increase in the Te-C bond stability and that the hard nitrogen donor will help tether the ligand to the titanium atom. Although the M:E ratio in the precursor is 1:1, it has been demonstrated that single source precursors such as $[NbCl_5(E^nBu_2)]$[26] (E = S, Se) have deposited crystalline $ME_2$ films in the past. These novel ligands will be included in a Ti(IV) system, in the aim to deposit $TiSe_2$ and $TiTe_2$ crystalline films.

## 6.2 Results and Discussion

### 6.2.1 Synthesis and Characterisation of Bidentate Selenoether Ligands

$^n$BuSe(CH$_2$)$_3$Se$^n$Bu was produced as a yellow oil in a moderate yield of 58 % according to the literature method.[15] Selenium powder was frozen in THF and reacted with 1 equivalent of $^n$BuLi. It was thawed and stirred at room temperature for 2 hours. The resulting pale yellow/ orange solution was reacted with slightly less than half a molar equivalent of 1,3-dichloropropane and refluxed for 1 hour. It was quenched with water and extracted with diethyl ether to obtain a yellow oil. $^1$H and $^{13}$C{$^1$H} NMR data were consistent with the proposed structure. The C$_2$ backboned compound can be made in the same way.[15] This reaction is depicted in Scheme 6-1 below.

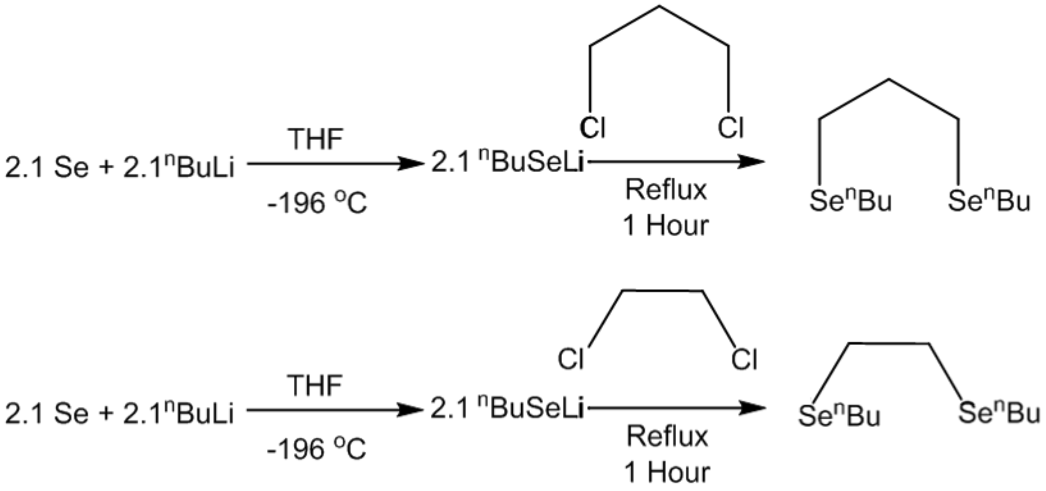

Scheme 6-1: The synthesis of bidentate selenoether ligands.

### 6.2.2 Synthesis and Characterisation of [TiCl$_4${$^n$BuSe(CH$_2$)$_n$Se$^n$Bu}] (n = 2, 3)

The reactions of TiCl$_4$ with $^n$BuSe(CH$_2$)$_2$Se$^n$Bu (made in the same way as above, using 1,2- dichloroethane instead of 1,3- dichloropropane, by other research group members) and $^n$BuSe(CH$_2$)$_3$Se$^n$Bu in a 1:1 stoichiometry are illustrated in Scheme 6-2 below.

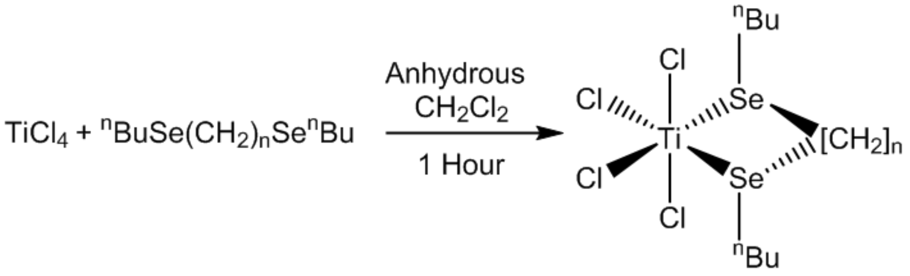

Scheme 6-2: The reaction of $TiCl_4$ with bidentate selenoethers (n= 2,3).

The six coordinate titanium complexes $[TiCl_4\{^nBuSe(CH_2)_2Se^nBu\}]$ and $[TiCl_4\{^nBuSe(CH_2)_3Se^nBu\}]$ were synthesised and isolated in good yields as a red, viscous oil and a soft red solid, respectively, by direct reaction of $TiCl_4$ and bidentate selenoether ligand in anhydrous $CH_2Cl_2$. In both reactions the immediate colour change from colourless to red indicated the instantaneous coordination of the selenoether ligand to the titanium metal centre as a red/ orange colour is characteristic of titanium chloro selenoether complexes as indicated by the literature.[4,17] Samples were manipulated in an $N_2$ purged, dry glove box.

Previous work at the University of Southampton has demonstrated the synthesis of a similar complexes: $[SnCl_4\{^nBuSe(CH_2)_nSe^nBu\}]$ (n =2 or 3).[15] This was shown to be in a distorted octahedral coordination. Characterisation of the new complexes by IR spectroscopy, $^1H$, $^{13}C\{^1H\}$ and $^{77}Se\{^1H\}$ NMR spectroscopy and microanalysis show the data to be in good agreement with the proposed structures and composition, and consistent with a distorted cis-octahedral coordination environment.

The proton NMR spectra show a high frequency coordination shift for the protons in close proximity to the selenium donor atoms. This shows the deshielding of these protons due to the coordination of the ligand to the metal centre. A shift is seen from 2.62 – 3.13 ppm and from 2.62-3.18 ppm for the $CH_2$-Se protons in the $C_2$ and $C_3$ linked complexes respectively. The $^{77}Se\{^1H\}$ NMR spectroscopy shows that a small amount of excess ligand is still present in the solution.

| Proton | $^{n}$BuSe(CH$_2$)$_3$Se$^{n}$Bu/ ppm | [TiCl$_4${$^{n}$BuSe(CH$_2$)$_3$Se$^{n}$Bu}]/ ppm |
|---|---|---|
| C**H**$_3$ [6H] | 0.93 | 0.96 |
| C**H**$_2$CH$_3$ [4H] | 1.41 | 1.47 |
| C**H**$_2$CH$_2$CH$_3$ [4H] | 1.65 | 1.78 |
| CH$_2$C**H**$_2$CH$_2$ [2H] | 2.00 | 2.39 |
| SeC**H**$_2$ [4H] | 2.58 | 3.10 |
| C**H**$_2$Se [4H] | 2.65 | 3.18 |

Table 6-2: $^1$H NMR data of $^{n}$BuSe(CH$_2$)$_3$Se$^{n}$Bu and [TiCl$_4${$^{n}$BuSe(CH$_2$)$_3$Se$^{n}$Bu}] in CDCl$_3$ at 298 K.

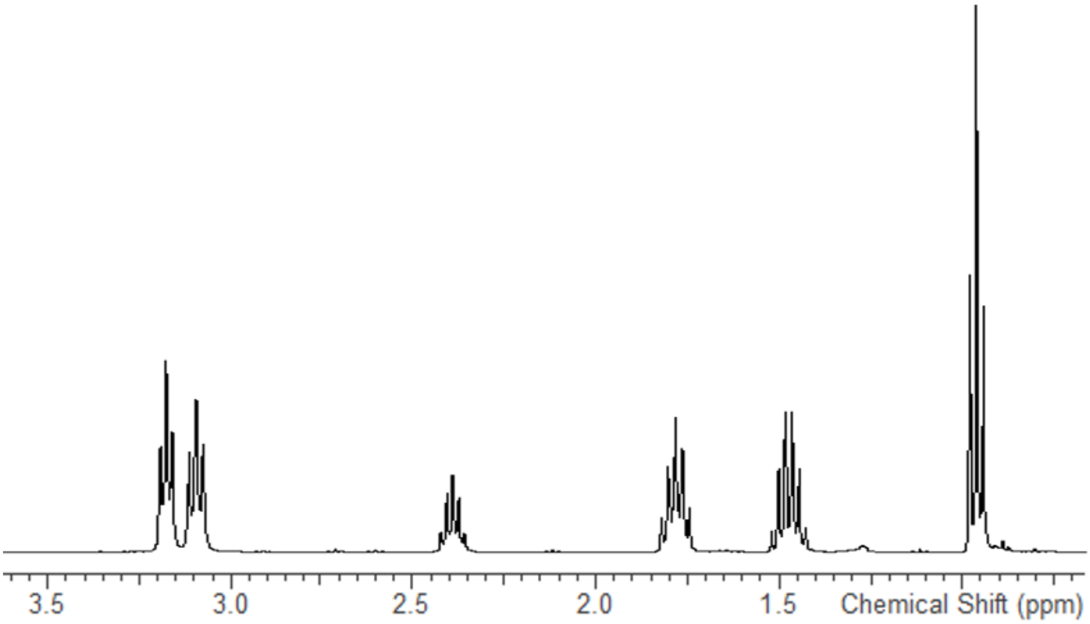

Figure 6-2: $^1$H NMR spectrum of [TiCl$_4${$^{n}$BuSe(CH$_2$)$_3$Se$^{n}$Bu}] in CDCl$_3$ at 298 K.

The IR spectrum, of the C$_2$ linked complex is illustrated in Figure 6-3, showing a broad peak at 379 cm$^{-1}$ with a shoulder at ca. 402 cm$^{-1}$, corresponding to the Ti-Cl stretching mode bonds. Group theory predicts four Ti-Cl IR active stretches for a cis octahedral environment ($C_{2v}$) as discussed in Chapter 1. This is further evidenced by complexes documented in the literature. For example [TiCl$_4${MeSe(CH$_2$)$_2$SeMe}] and [TiCl$_4${MeSe(CH$_2$)$_3$SeMe}] give Ti-Cl stretches at 414, 402, 393, 380 cm$^{-1}$ and 396, 384, 378, 373 cm$^{-1}$in their respective IR spectra.[17] However, complexes including butyl groups seem to give much broader bands. [TiCl$_4$(Se$^{n}$Bu$_2$)$_2$] gives a broad Ti-Cl stretch at 395 cm$^{-1}$ with two shoulders at 354 and 430 cm$^{-1}$.[4] Furthermore, group theory predicts only 1 IR active Ti-Cl stretch for a trans-octahedral environment ($D_{4h}$). Therefore, the IR spectra are consistent with the proposed structures.

Microanalytical data was consistent with the proposed stoichiometry. [$TiCl_4$\{$^n$BuSe($CH_2$)$_2$Se$^n$Bu\}]: Anal. Calcd for $C_{10}H_{22}Cl_4Se_2Ti$: C, 24.52; H, 4.53. Found: C, 24.24; H, 4.94 %. [$TiCl_4$\{$^n$BuSe($CH_2$)$_3$Se$^n$Bu\}]: Anal. Calcd for $C_{11}H_{24}Cl_4Se_2Ti$: C, 26.22; H, 4.80. Found: C, 26.82; H, 5.59 %.

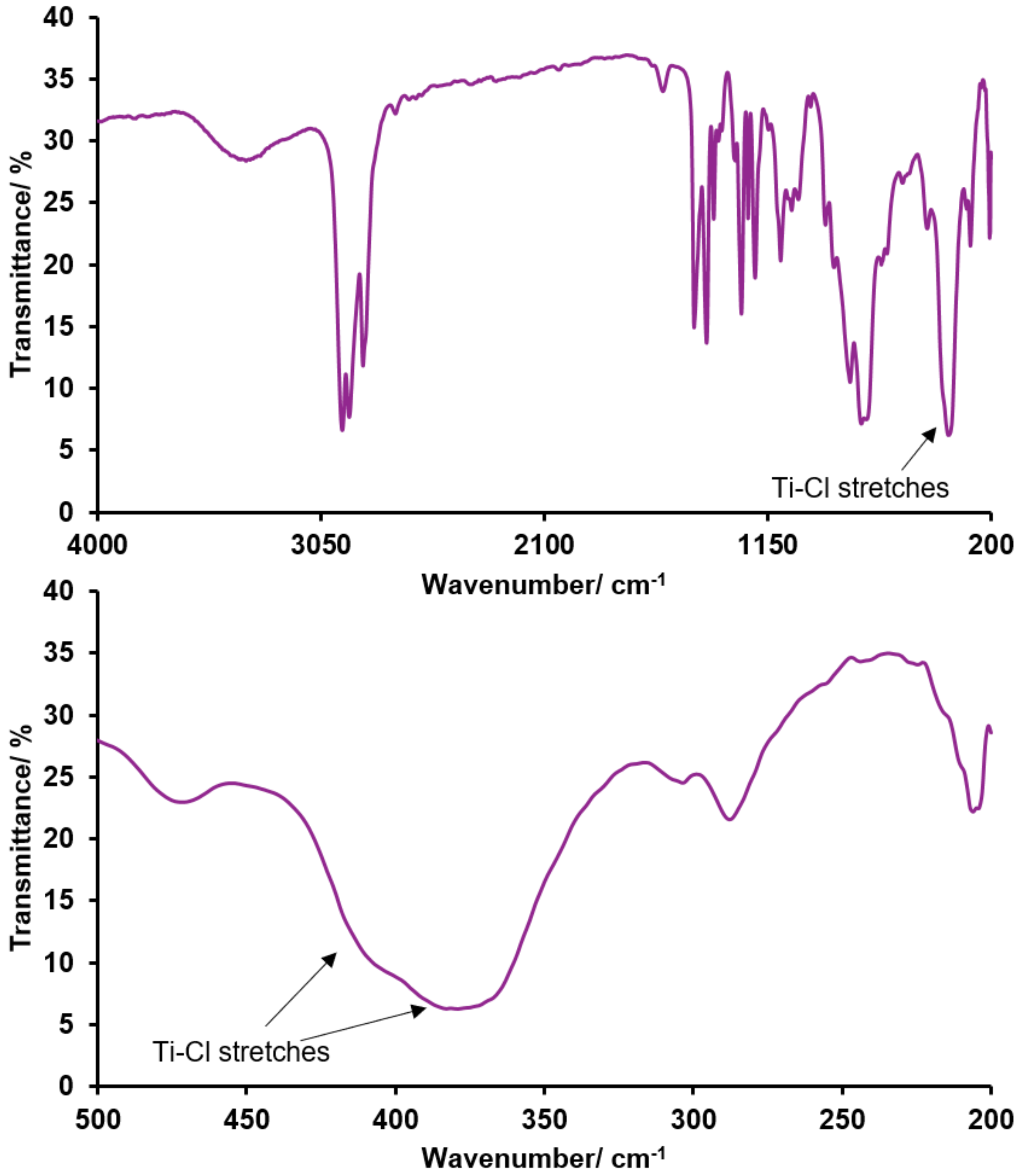

Figure 6-3: IR spectrum of [$TiCl_4$\{$^n$Bu($CH_2$)$_2$Se$^n$Bu\}] as a neat thin film between CsI Plates and an expanded section of the fingerprint region to observe the Ti-Cl stretching vibrations.

### 6.2.3 Deposition of $TiSe_2$ Thin Films

LP CVD experiments using precursors [$TiCl_4\{^nBuS(CH_2)_nS^nBu\}$] (n=2,3) at 873 K (0.02 mmHg) resulted in the deposition of $TiSe_2$ in both cases, without the need for an additional chalcogen source. Matt black film deposition tended to occur on the first 2-3 substrates nearest to the precursor, typically leading to *ca.* 70-100% coverage of the fused $SiO_2$ substrate.

The GIXRD measurements on these films, depicted in Figure 6-4 below, show it to be crystalline hexagonal $TiSe_2$; the diffraction pattern shows reflections matching that of hexagonal $TiSe_2$ of point group $P\bar{3}m1$. Although the GIXRD pattern shows that there are no crystalline impurities present in the film, there is a small amorphous peak present at ~ 21 °. This is due to the underlying silica substrate, indicating that the GIXRD is sampling through both the film and substrate. The stick diagram shows the diffraction pattern for bulk $TiSe_2$ with each vertical line represents an allowed reflection.[27]

Both precursors, [$TiCl_4\{^nBuSe(CH_2)_2Se^nBu\}$] and [$TiC_4l\{^nBuSe(CH_2)_3Se^nBu\}$], give $TiSe_2$ with very similar diffraction patterns indicating that the addition of an extra carbon atom into the backbone of the bidentate ligand has little effect on the ability of the complex as a single source precursor for LPCVD.

Refinement of these patterns revealed lattice parameters of a = 3.520(6) Å, c = 6.011(18) Å and a= 3.525(9) Å, c = 5.928(19) Å for [$TiCl_4\{^nBuSe(CH_2)_nSe^nBu\}$] (n = 2,3) respectively, These are values very close to that from bulk $TiSe_2$ (space group $P\bar{3}m1$, a= 3.540(1) Å and c = 6.008(3) Å).[27] Lattice parameters were calculated by optimisation of the fit in PDXL2.

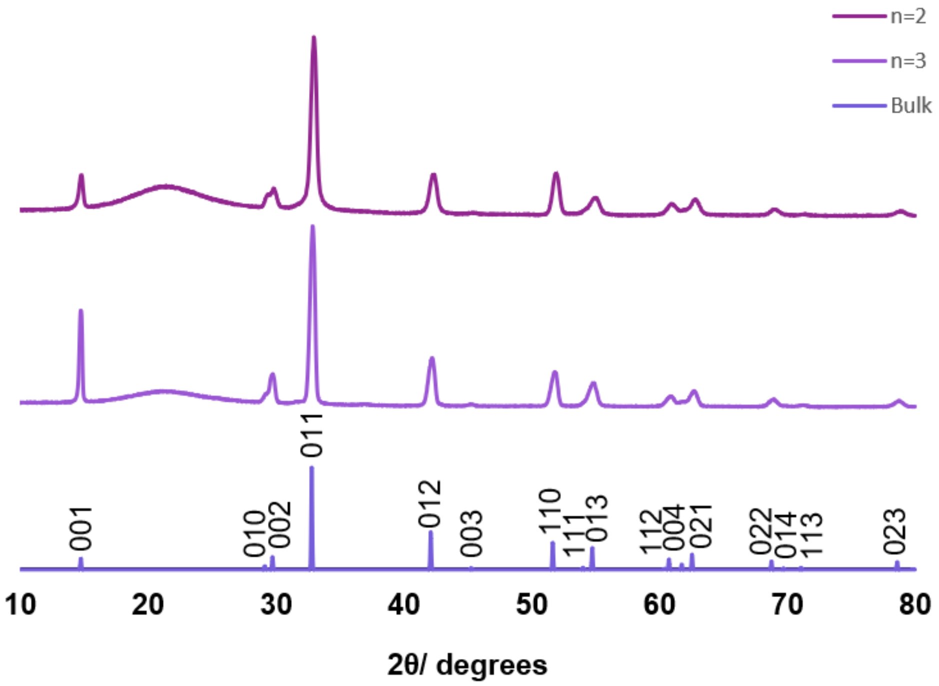

Figure 6-4: Grazing incidence XRD patterns obtained from TiSe$_2$ thin films deposited in fused silica at 873 K at 0.02 mm Hg by LPCVD from 75 mg of [TiCl$_4${$^n$BuSe(CH$_2$)$_n$Se$^n$Bu}] (n=2, 3) and a bulk indexed pattern of TiSe$_2$.[27] The feature at ~ 21 ° is due to the underlying SiO$_2$ substrate.

EDX analysis, (Figure 6-5) below, of the deposited TiSe$_2$ film, showed an almost perfect ratio of 1:2 of titanium to selenium giving a stoichiometry of TiSe$_2$. This suggests that the reagent used is suitable as a single source precursor and that high-quality films are attainable with this precursor. Negligible amounts of Cl and C were detected.

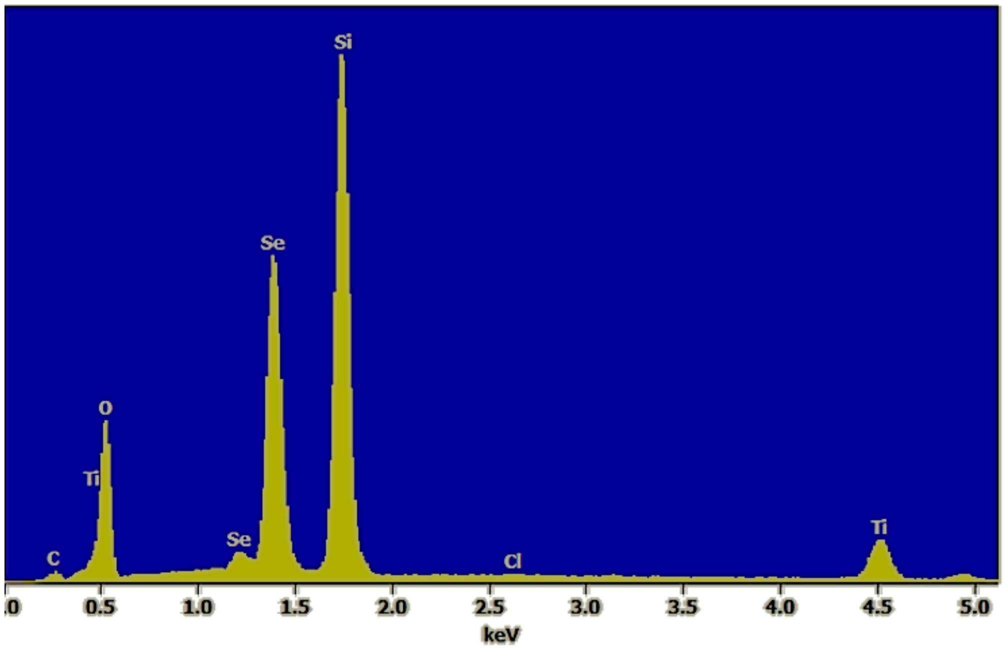

Figure 6-5: Energy dispersive X-ray spectrum of a thin film of $TiSe_2$ deposited from [$TiCl_4\{^nBuSe(CH_2)_2Se^nBu\}$] at 773 K and 0.02 mm Hg. The large features at 1.7 and 0.5 keV are due to the $SiO_2$ substrate.

| Element Line | Weight/ % | Atom/ % |
|---|---|---|
| Cl K | 0.3 | 0.5 |
| Ti K | 22.9 | 32.7 |
| Se L | 76.9 | 66.8 |

Table 6-3: Quantitative analysis of the EDX spectra above, showing the weight percentage and atom percentage of each atom species present in the thin film.

After the initial experiments had been undertaken, a number of studies were completed investigating the effect of temperature, quantity of reagent used and the stability of the films under ambient conditions.

To test the stability of the $TiSe_2$ films produced, GIXRD patterns of the film of $TiSe_2$ deposited on silica were recorded after storing for 3 months. During this time, the samples were stored in air and Figure 6-6 shows that the film has not been degraded over this time, and there are no $TiO_2$ reflections present in the diffraction pattern. As a result, we can conclude that the films remain stable for long periods (months) when stored under ambient conditions. This is an improvement on that reported in the literature such as [$TiCl_4(SeEt_2)_2$] which produced $TiSe_2$ films which oxidised within a week.[14]

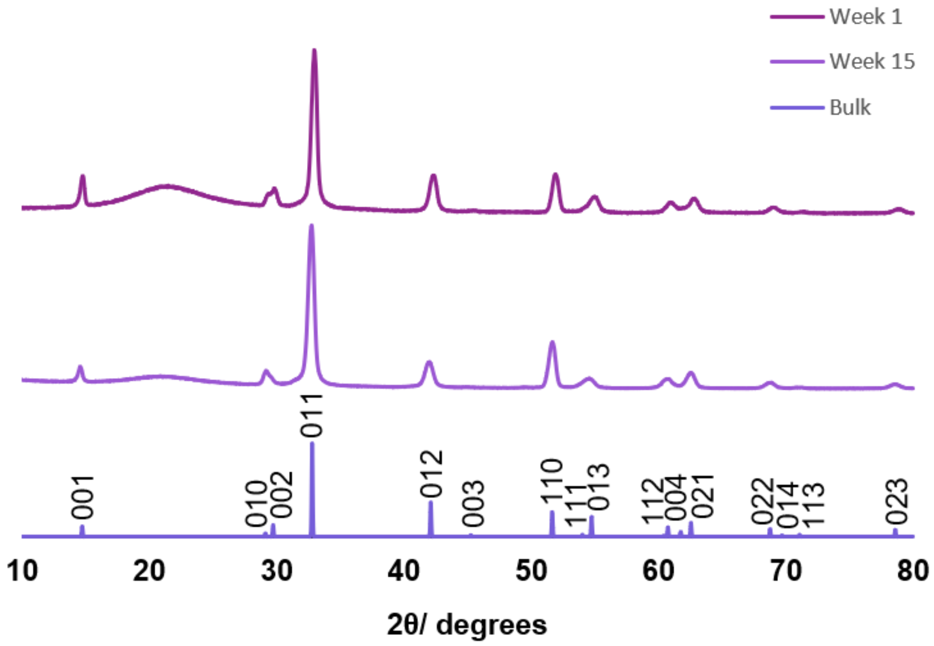

Figure 6-6: Grazing incidence XRD patterns obtained from $TiSe_2$ thin films, on silica at 873 K by LPCVD from 75 mg of [$TiCl_4\{^nBuSe(CH_2)_2Se^nBu\}$], 3 months apart which match well to the allowed reflections for bulk $TiSe_2$.[27] The feature at ~ 21 ° is due to the underlying $SiO_2$ substrate.

In order to attempt to deposit ultra-thin smooth films of $TiSe_2$, investigations varying temperature and reagent quantity were conducted. In these experiments, a far lower quantity (5-10 mg) of precursor than was used for the initial experiments was used. In each, the effects on film composition and morphology were assessed. LPCVD of $TiSe_2$ using 5 or 10 mg of [$TiCl_4\{^nBuSe(CH_2)_nSe^nBu\}$] (n = 2) were completed with the furnace temperature set to a range of temperatures between 723 and 823 K, leading to complete evaporation of the precursor compound and deposition of black/blue/purple films onto the $SiO_2$ substrate. Despite deposition occurring, it was apparent that some of the precursor had merely been distilled along the silica tube, despite the fact than a much smaller quantity of reagent was used per experiment.

XRD measurements of the $TiSe_2$ films produced over varying temperature, depicted in Figure 6-7, show them to be crystalline hexagonal $TiSe_2$ in all cases. However, there appears to be a slight impurity in the film deposited at 823 K at ~25 °, this can be assigned to the (1 0 1) reflection of $TiO_2$. Furthermore, the amorphous peaks in these films are a lot higher in intensity compared to the films deposited from 75 mg of reagent. This is because these films, deposited from 10 mg of precursor, are expected to be much thinner and hence there is a larger substrate: film ratio. The film deposited at 823 K appears to be thicker than those deposited at lower temperatures with the XRD pattern showing far more intense reflections. This suggests that, at a higher temperature, less of the precursor is distilled along the silica tube and more deposited on the hot substrate. This indicates an increased rate of surface reactions at higher temperatures.

XRD measurements on the film deposited using 5 mg at 773 K shows it to be crystalline hexagonal $TiSe_2$, point group $P\bar{3}m1$. There are no crystalline impurities visible in this film (by XRD) and the intensity of the reflections are relatively similar to those in the film deposited from 10 mg of reagent at 773 K.

Comparing the films grown from 75 mg of reagent at 873 K and from 10 mg of reagent at 823 K (Figure 6-8), a great difference can be seen between the relative intensity of reflections within a sample. For example, in the thicker film, the reflection at 32.77 ° is far more intense relative to the peak at 14.73 °. The same is apparent for the peaks at 51.60 ° and 53.96 °. In the film deposited from 5 mg of reagent however, these relative intensities are reversed. The reflections at 14.73 ° and 32.77 ° represent the (0 0 1) and (0 1 1) reflections, consequently, an increase in the (0 0 1) reflection relative to the (0 1 1) reflection suggests that the thinner film has more crystallites with their c-axis perpendicular to the substrate surface.

Previous research has shown that preferred orientation is strongly influenced by the dimensions of the substrate.[16] However, this is clearly not the case here as the substrate used is not patterned and is on the mm scale. The same preferred orientation is also seen in the deposition of thick and thin films of $SnSe_2$ showing that films initially grow in the 001 direction and then crystallites grow up.[15] Furthermore, it has been shown that the mechanism of nucleation is predominantly by the diffusion of adatoms across the surface of the substrate.[6] Consequently, by limiting the precursor quantity there is a lower concentration of adatoms and the film grows along parallel to the surface. By increasing the precursor quantity and thus increasing the adatom concentration there is greater chance of the crystallites growing up and perpendicular to the substrate.

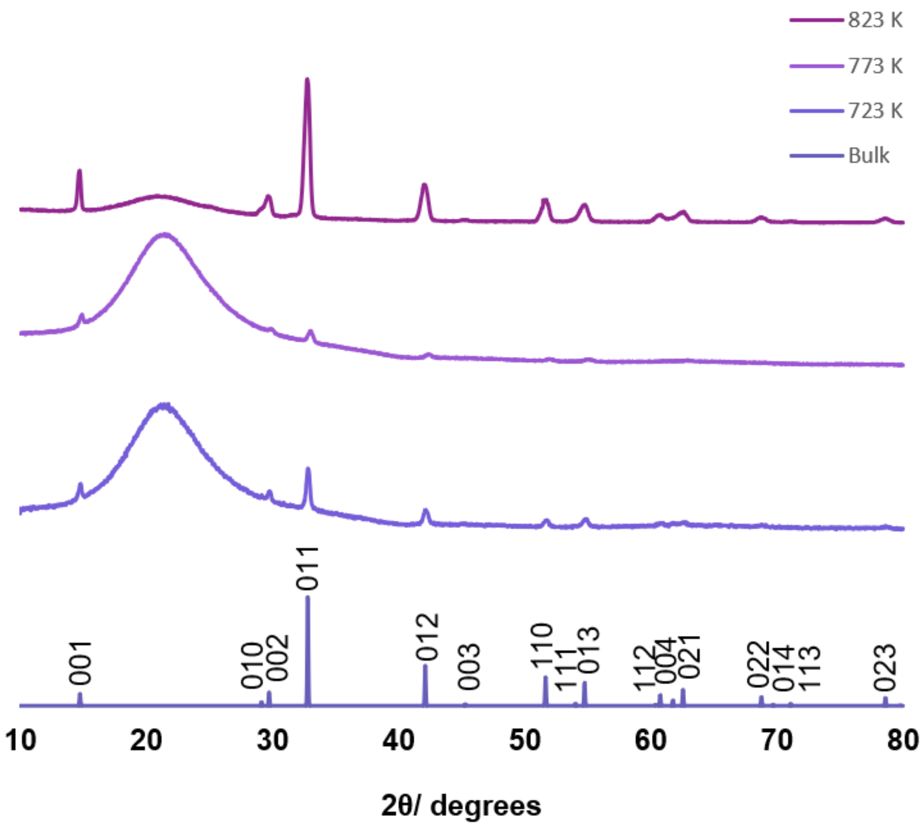

Figure 6-7: Grazing incidence XRD patterns obtained from $TiSe_2$ thin films, on silica at 723, 773 and 823 K by LPCVD from 10 mg of $[TiCl_4\{^nBuSe(CH_2)_2Se^nBu\}]$, which match well to the allowed reflections of bulk $TiSe_2$.[27] The broad feature at ~ 21 ° is due to the underlying $SiO_2$ substrate.

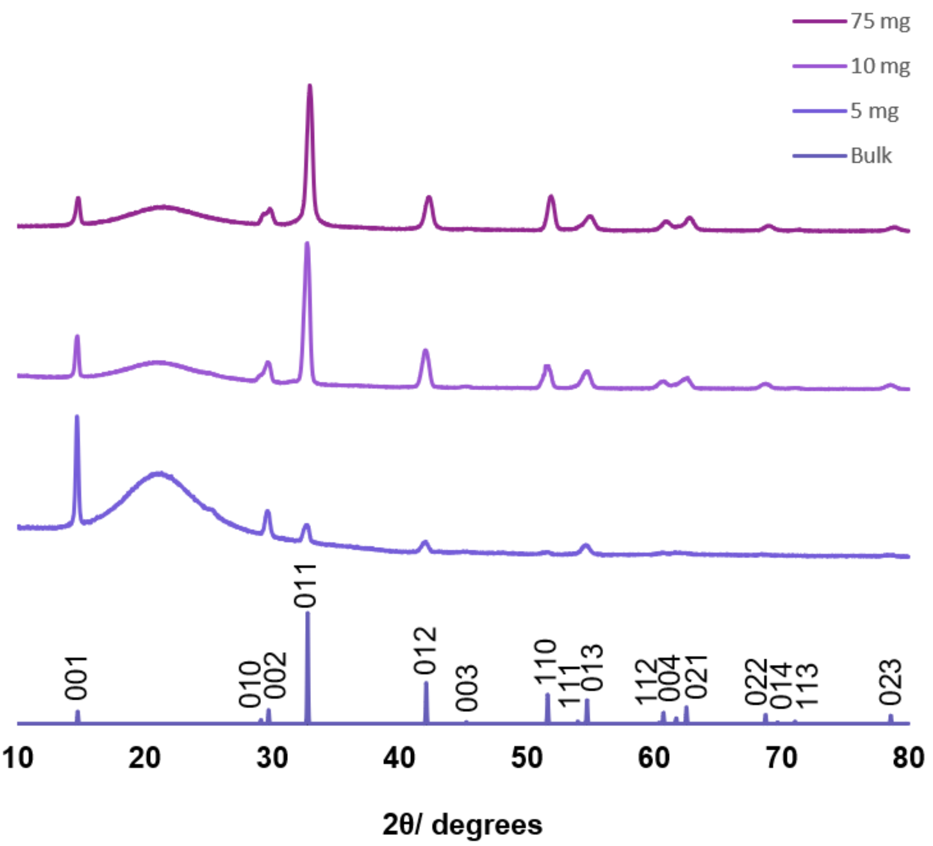

Figure 6-8: The effect of precursor quantity on the XRD patterns obtained from $TiSe_2$ thin films, on silica by LPCVD from 5 and 10 mg at 773 K and 75 mg at 873 K of $[TiCl_4\{^nBuSe(CH_2)_2Se^nBu\}]$, all match well to the allowed reflections for bulk $TiSe_2$.[27] The broad feature at ~ 21 ° is due to the underlying $SiO_2$ substrate.

The lattice parameters, obtained after refinement of the XRD patterns of the $TiSe_2$ films are documented in Table 6-4 below. These are very close to that from bulk $TiSe_2$ (space group $P\bar{3}m1$, a= 3.540(1) Å and c = 6.008(3) Å).[27] There is no significant variations in the lattice parameters of all the films.

| Deposition Conditions | a, b / Å | c / Å |
|---|---|---|
| 75 mg at 873 K | 3.525(9) | 5.928(19) |
| 10 mg at 823 K | 3.526(8) | 6.03(3) |
| 10 mg at 773 K | 3.481(12) | 6.00(5) |
| 10 mg at 723 K | 3.533(3) | 5.993(5) |
| 5 mg at 773 K | 3.49(2) | 6.07(15) |

Table 6-4: Lattice parameters obtained after refinement of XRD patterns obtained from a range of depositions of thin films of $TiSe_2$ from $[TiCl_4\{^nBuSe(CH_2)_2Se^nBu\}]$. Lattice parameters were refined by optimisation of the fit in PDXL2.

As well as characterising the films with GIXRD measurements, the films were imaged by scanning electron microscopy (SEM) and tapping mode atomic force microscopy (AFM) to analyse the morphology of the films. The AFM was also utilised to acquire measurements of the roughness of the surface of the film. AFM images are displayed in Figure 6-9, and accompanying roughness measurements are displayed in Table 6-5. SEM images of the thickest film, 75 mg at 873 K, and the thinnest film, 5 mg at 773 K are shown in Figure 6-10.

The AFM images show that the films are not particularly smooth. The roughest film was that produced at 823 K, using 10 mg of precursor, and shows large hexagonal features whilst the smoothest was the one produced at the lowest temperature used, 723 K. Despite it appearing that the majority of crystallites align perpendicular with the surface of the substrate in the thickest film, it is one of the smoother films deposited. SEM images are consistent with the AFM images shown. Neither SEM nor AFM show continuous films for the thinner films deposited.

Although the GIXRD patterns suggest that the thinner films may have more crystallites lying flat relative to the surface of the substrate, the AFM and SEM show that these crystallites tend to stack on top of one another to form columns, rather than side by side to form a continuous film.

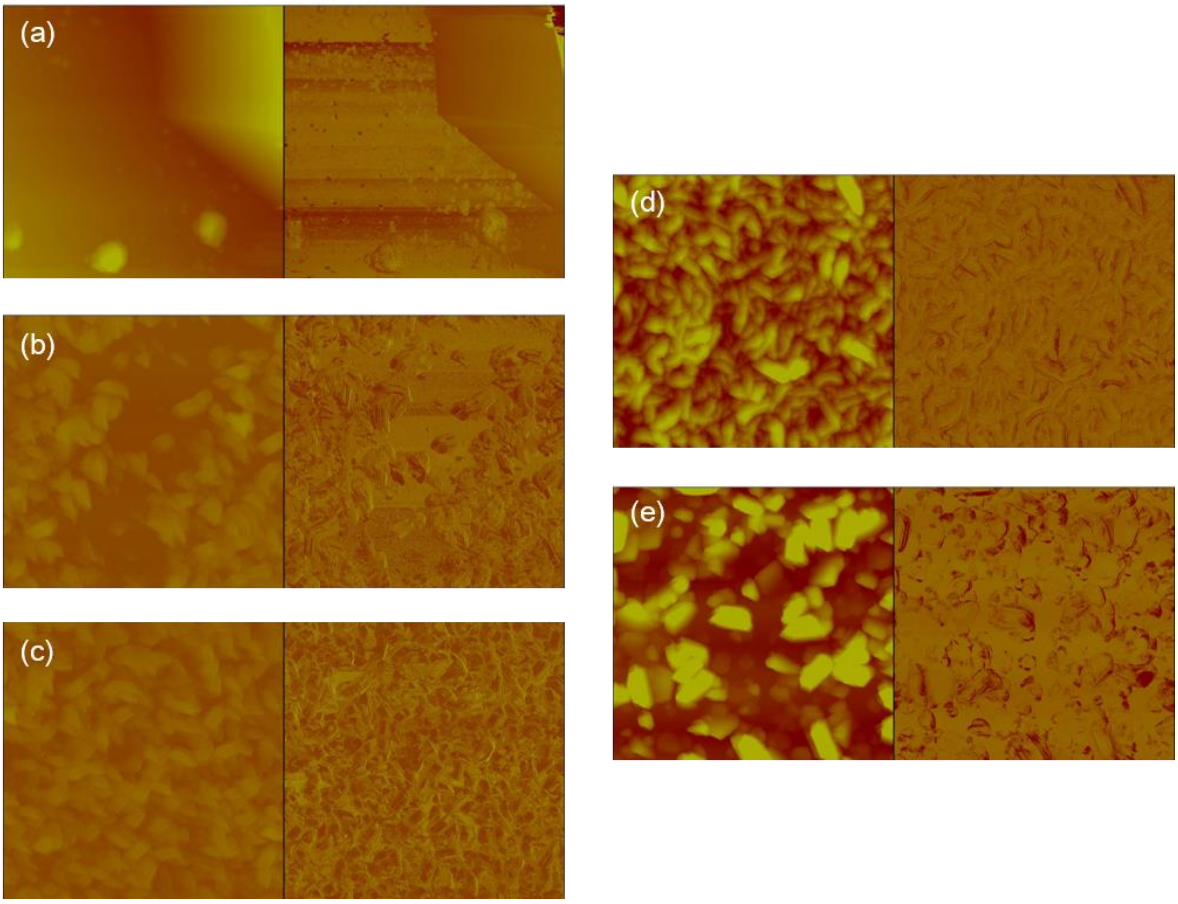

Figure 6-9: AFM image of 25 µm square sections of $TiSe_2$ films deposited from $[TiCl_4\{^nBuSe(CH_2)_2Se^nBu\}]$, height right and phase left of a) 10 mg at 823 K, b) 10 mg at 773 K, c) 10 mg at 723 K, d) 75 mg at 873 K and e) 5 mg at 773 K.

| Deposition Conditions | Roughness/ nm |
|---|---|
| 10 mg at 823 K | 303 |
| 10 mg at 773 K | 228 |
| 10 mg at 723 K | 202 |
| 75 mg at 873 K | 212 |
| 5 mg at 773 K | 244 |

Table 6-5: Average roughness of the surface of the $TiSe_2$ films deposited from $[TiCl_4\{^nBuSe(CH_2)_2Se^nBu\}]$ at a range of deposition temperatures.

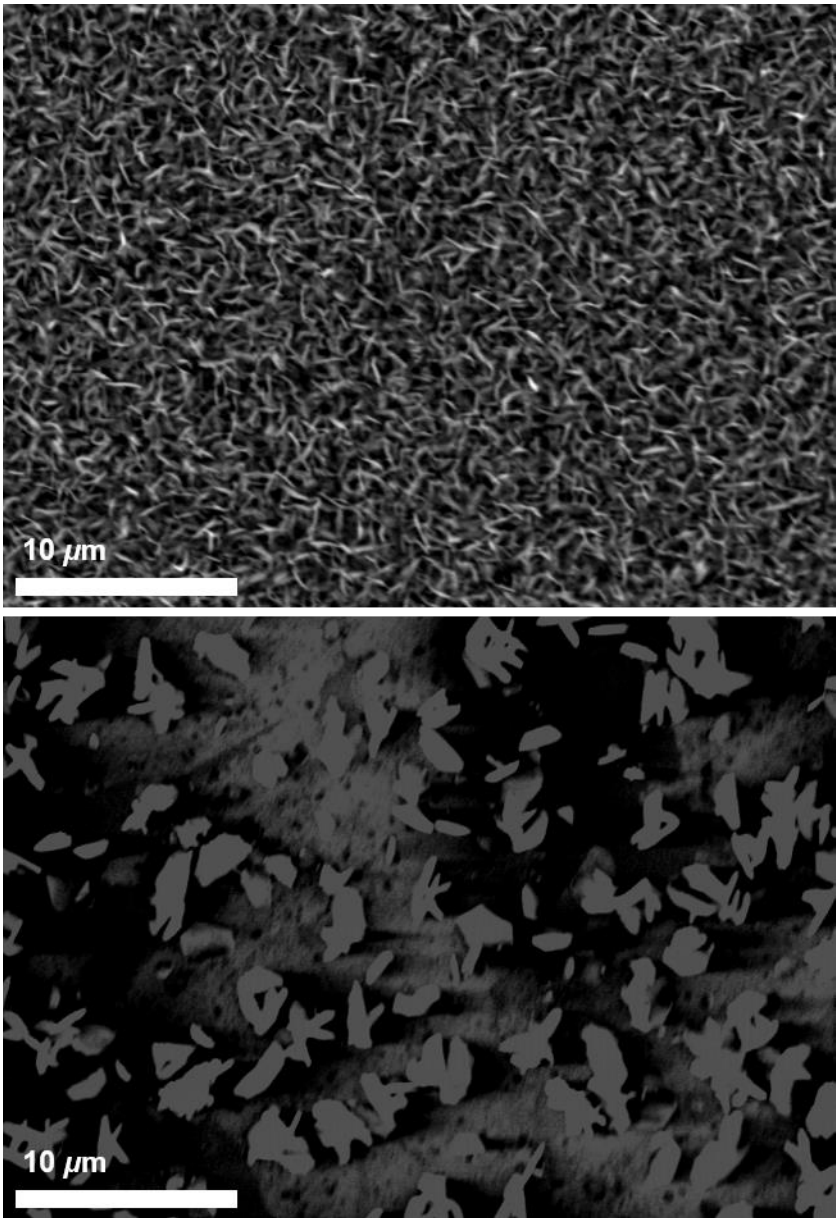

Figure 6-10: SEM images of $TiSe_2$ deposited from 75 mg of [$TiCl_4\{{}^nBuSe(CH_2)_3Se^nBu\}$] at 873 K (top) and 5 mg at 773 K (bottom).

Depositions on fused (non-crystalline) $SiO_2$ seems to produce very rough films and previous work has shown the affinity of $TiSe_2$ for TiN or PVD $SiO_2$ over fused $SiO_2$. Consequently, a range of substrates will be investigated to analyse whether the orientation of the crystals are affected. The aim is to produce an ultrathin continuous film with the crystallites lying flat to the surface of the substrate.

As well as investigating temperature and reagent quantity, effect of type of substrate was also studied. Depositions were carried out in the same way as previously, using the [$TiCl_4\{{}^nBuSe(CH_2)_3Se^nBu\}$] precursor, with deposition onto PVD $SiO_2$ and PVD TiN substrates. These are substrates are formed of crystalline material that has been deposited onto a silicon wafer. In each experiment, the PVD substrate was placed in a region where the highest deposition typically occurred in previous reactions. Depositions were performed at 873 K and at 0.1 mm Hg. XRD and EDX measurements were obtained. The films deposited were non-continuous with widely dispersed crystallites. Analysis of the deposition onto PVD TiN is documented below.

The SEM image of the film deposited onto TiN (Figure 6-11) shows that the film is not continuous but there are crystallites scattered on the surface. Individual hexagonal crystallites and rosette structures can be observed.

Analysis by grazing incidence X-ray diffraction shows that the film deposited on the PVD TiN substrate (Figure 6-12) is crystalline hexagonal $TiSe_2$. Evidence of a $TiO_2$ phase (anatase) is also present but this may be due to surface oxidation of the TiN substrate. The allowed reflections of each respective phase are indicated by the stick diagrams below the grazing incidence diffraction pattern of the deposited thin film in the figure below.

The EDX spectrum of the film is also shown in Figure 6-13. Negligible amounts of Cl, C and O can be observed. Due to the technique probing micrometres into a sample, the use of TiN as a substrate prevents calculation of a Ti:Se ratio.

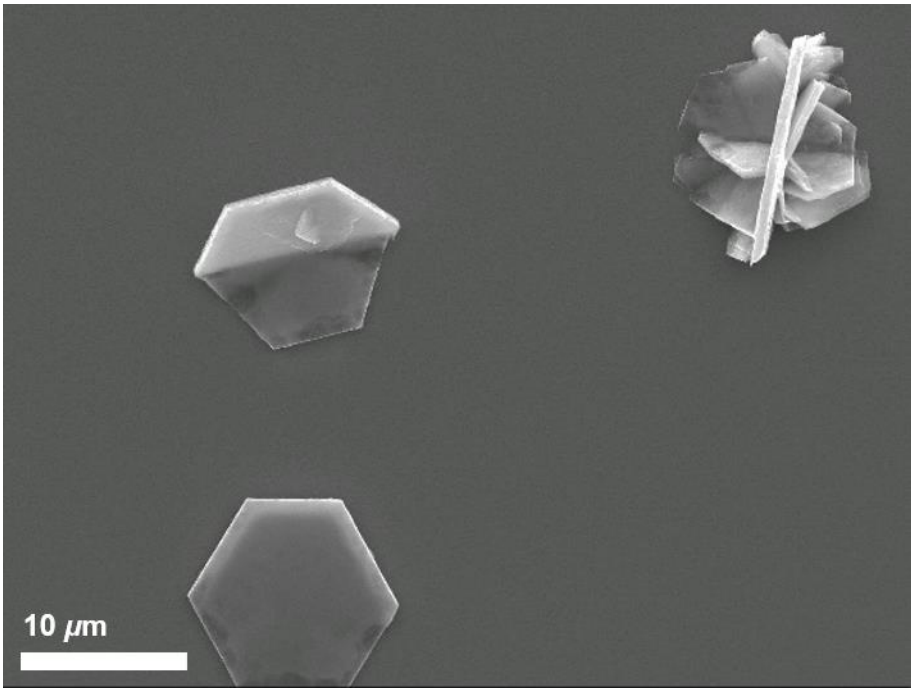

Figure 6-11: SEM image of crystallites of $TiSe_2$ deposited from 10 mg $[TiCl_4\{^nBuSe(CH_2)_3Se^nBu\}]$ onto TiN at 873 K.

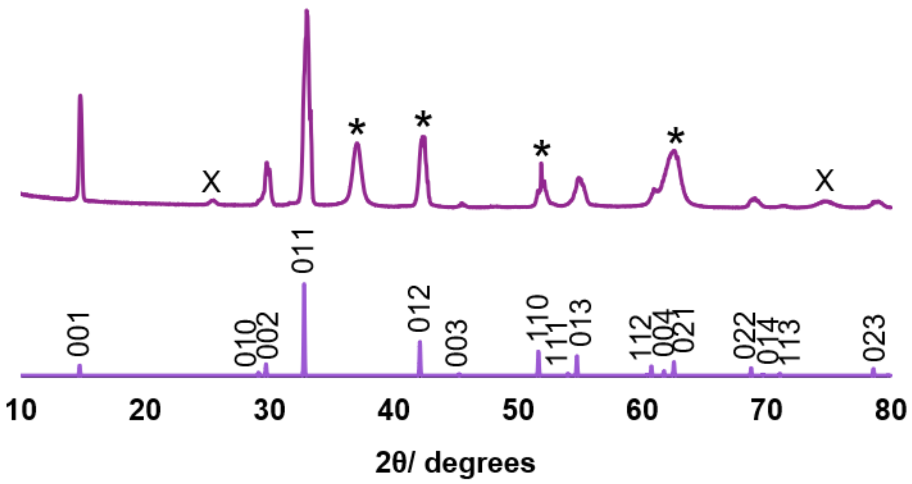

Figure 6-12: Grazing incidence XRD pattern of $TiSe_2$ deposited from 10 mg $[\mathrm{TiCl_4\{^nBuSe(CH_2)_3Se^nBu\}}]$ onto TiN at 873 K and an indexed pattern of bulk $TiSe_2$.[27] The reflections due to the TiN substrate and Si underlying the substrate are marked with an asterisk. Impurities ($TiO_2$) are marked with an X.

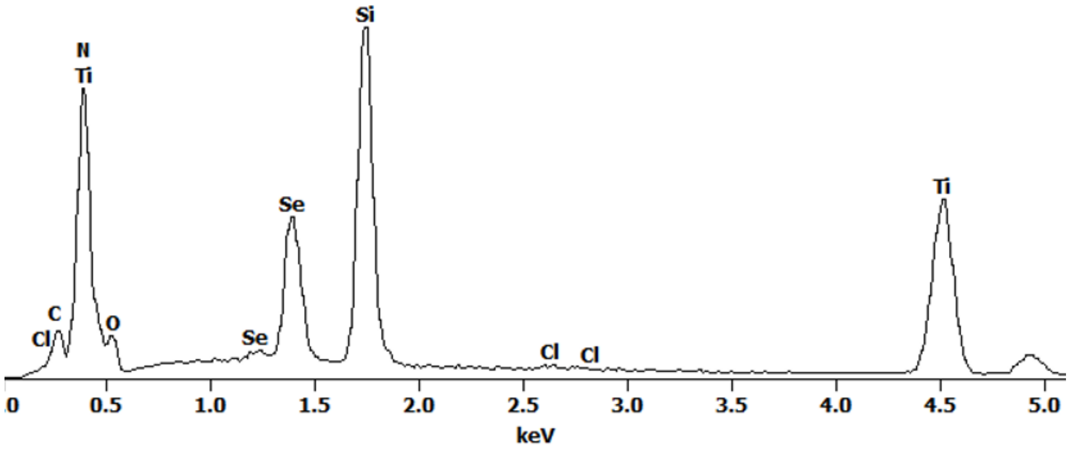

Figure 6-13: EDX spectrum of $TiSe_2$ deposited from 10 mg $[\mathrm{TiCl_4\{^nBuSe(CH_2)_3Se^nBu\}}]$ onto TiN at 873 K. Signals from Si at ~ 1.7 keV are due to the Si underlying the TiN substrate. Both the film and substrate contribute to Ti signals at 0.4 and 4.5.

### 6.2.4 Synthesis and Characterisation of Hybrid N/Te and N/Se Donor Ligands

$TiCl_4$ is a hard Lewis acid, whilst chalcogen ligands are soft Lewis bases. This results in a weak coordination complex. A hybrid, mixed donor ligand may be a solution to increase the stability of theses complexes, particularly in the case of telluride ligands.

$MeSe(CH_2)_3NMe_2$ was produced as a yellow oil in a very poor yield of 10 % by a simple nucleophilic substitution reaction as depicted in Scheme 6-3. Once 3-dimethylamino-1-propyl chloride hydrochloride had been reacted with NaOH to form 3-dimethylamino-1-propyl chloride. 3-dimethylamino-1-propyl chloride was reacted with NaSeMe in a 1:1 ratio in anhydrous MeOH for 15 hours. The reaction remained at room temperature and under an inert atmosphere throughout. $^1H$ and $^{13}C\{^1H\}$ NMR data for the associated compound was consistent with the proposed structure. A large singlet was present at 2.26 ppm corresponding to the $NMe_2$ and the signals at 2.00 and 2.39 ppm had selenium satellites (8 Hz) and correspond to SeMe and $CH_2Se$. The salt, produced by addition of excess MeI was characterised by microanalysis which suggested the reaction had proceeded with a 1:1 ratio to form $[Me_2Se(CH_2)_3NMe_2]^+[I]^-$ or $[MeSe(CH_2)_3NMe_3]^+[I]^-$ with 25.32 % C expected and 25.00 % found, 5.46 % H expected and 5.58 % found.

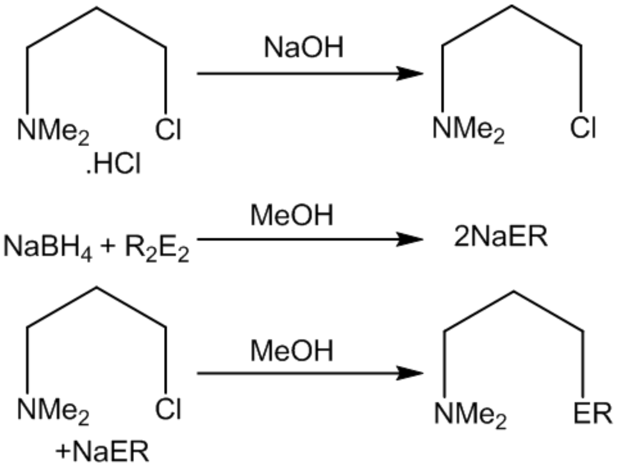

Scheme 6-3: The method used to produce the hybrid ligands synthesised. This synthesis was adapted from a method found in the literature.[25]

3-dimethylamino-1-propyl chloride was found to be extremely volatile and consequently on synthesis and after the separation from the aqueous phase it was readily lost upon removal of the solvent *in vacuo*. After a slight adaptation to the neutralisation step of the general method (no organic solvent used to separate material from the aqueous phase,

$EtSe(CH_2)_3NMe_2$ was synthesized as a yellow oil in a moderate yield of 42 % by a nucleophilic substitution reaction of 3-dimethylamino-1-propyl chloride and NaSeEt in a 1:1 ratio. The reagents were stirred in anhydrous MeOH for 15 hours at room temperature and under an inert atmosphere. Again, the NMR data were consistent with the proposed structure with the $NMe_2$ singlet at 2.23 ppm and $CH_2Se$ overlapping multiplets at 2.39 ppm. However, in all cases there was ~ 25% $Et_2Se_2$ present in the final mixture evidenced by signals at 1.47 ppm (Me) and 2.92 ppm ($SeCH_2$). Attempts to purify the ligand via krugelrohr distillations have so far been unsuccessful as the product and starting material appear to have very similar volatilities. Despite this, the $^{77}Se\{^1H\}$ NMR spectrum is clean showing a singlet at 195 ppm.

The red oil $PhTe(CH_2)_3NMe_2$, was produced in a moderate yield of 46 % in a similar method to the preparations of the selenoethers described previously. The NMR data was consistent with the proposed structure. Its salt, $[Ph(Me)Te(CH_2)_3NMe_3]^{2+}[I]^{2-}$, produced by addition of excess MeI was characterised by microanalysis. The results suggested that the reaction had proceeded in a 1:2 ratio of telluroether: MeI to form $[Ph(Me)Te(CH_2)_3NMe_3]^{2+}[I]^{2-}$ with 27.15 % C expected and 26.45 % found and 4.03 % H expected and 4.06 % found. NMR data are consistent with this, showing a signal for $Te^+Me$, and an increase in integral from 6 to 9H for the $NMe_x$ signal in the proton NMR spectrum. NMR data relevant to the hybrid ligands are presented in Table 6-6 below. The $NMe_x$ signal, in both proton and carbon NMR spectra show a significant high frequency shift from $PhTe(CH_2)_3NMe_2$ to $[Ph(Me)Te(CH_2)_3NMe_3]^{2+}[I]^{2-}$. The chemical shift in the $^{125}Te\{^1H\}$ NMR spectrum of 609 ppm is typical of telluronium salts with values of 565 and 606 ppm reported in the literature for $[PhTeMe_2I]$[28] and $[Te(Ph)(Me)CH_2RCH_2OH]$[29] respectively. The telluroether is not a novel compound and the NMR data are in agreement with that from the literature.[25]

| 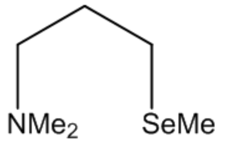 | 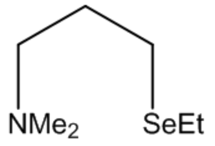 | 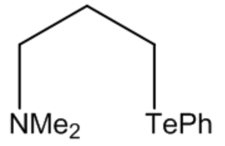 | 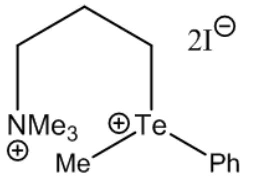 |
|---|---|---|---|
| **$^1$H NMR ($CDCl_3$, 295 K): δ/ ppm** | | | **$(CD_3)_3SO$: δ/ ppm** |
| 1.85 (m, 2H, $-CH_2-$)<br>2.00 (s, 3H, SeMe)<br>2.26 (s, 6H, $NMe_2$)<br>2.39 (t, 2H, $SeCH_2$)<br>2.58 (t, 2N, $NCH_2$) | 1.42 (t, 3H, Me)<br>1.83 (m, 2H, $-CH_2$)<br>2.23 (s, 6H, $NMe_2$)<br>2.35 (t, 2H, $NCH_2$)<br>2.39 (m, 4H, $SeCH_2$ x2) | 2.05 (m, 2H, $-CH_2-$)<br>2.25 (s, 6H, $NMe_2$)<br>2.40 (t, 2H, $NCH_2$)<br>3.00 (m, 2H, $TeCH_2$)<br>7.25 (m, 3H, Ph)<br>775 (m, 2H, Ph) | 2.15 (m, 3H, $Te^+Me$)<br>2.47 (m, 2H, $-CH_2-$)<br>2.85 (t, 2H, $N^+CH_2$)<br>3.01 (s, 9H, $N^+Me_3$)<br>3.34 (m, 2H, $Te^+CH_2$)<br>7.54 (m, 3H, Ph)<br>7.87 (m, 2H, Ph) |
| **$^{13}C\{^1H\}$ NMR ($CDCl_3$, 295K): δ/ ppm** | | | **$(CD_3)_3SO$: δ/ ppm** |
| 4.40 (s, SeMe)<br>23.3 (s, $SeCH_2$)<br>28.4 (s, $-CH_2-$)<br>45.7 (s, $NMe_2$)<br>59.8 (s, $NCH_2$) | 15.8 (s, $SeCH_2Me$)<br>17.3 ($CH_2Me$)<br>21.1 (s, $SeCH_2$)<br>28.7 (s, $-CH_2-$)<br>45.5 (s, $NMe_2$)<br>59.7 (s, $NCH_2$) | 6.22 (s, $TeCH_2$)<br>29.1 (s, $-CH_2-$)<br>45.5 (s, $NMe_2$)<br>61.1 (s, $NCH_2$)<br>114 (s, 1-C, Ph)<br>127 (s, 4-C, Ph)<br>129 (s, 3,5-C, Ph)<br>138 (s, 2,6-C, Ph) | 9.19 (s, $Te^+CH_2$)<br>19.2 (s, $Te^+Me$)<br>24.1 (s, $-CH_2-$)<br>52.4 (s, $N^+Me_3$)<br>65.2 (s, $N^+CH_2$)<br>123 (s, 1-C, Ph)<br>130 (s, 4-C, Ph)<br>131 (s, 3,5-C, Ph)<br>134 (s, 2,6-C, Ph) |
| **$^{77}Se\{^1H\}/^{125}Te\{^1H\}$ NMR ($CH_2Cl_2/CD_2Cl_2$); δ/ ppm** | | | **$(CH_3)_3SO/(CD_3)_3SO$: δ/ ppm** |
| - | 195 | 472 | 609 |

Table 6-6: NMR spectroscopy data for the synthesised hybrid ligands.

Se-Se bonds (192 $kJmol^{-1}$)[21] are stronger than Te-Te bonds (149 $kJmol^{-1}$)[21] and this may be why there is a problem in the cleaving of the Se-Se bond in diethyl diselenide. In the case of the selenoether ligands, the methyl substituted analogue is the only one in which a pure synthesis is achievable as $Me_2Se_2$ has a sufficiently lower volatility than the desired product and can be easily removed under low pressure.

### 6.2.5 Synthesis and Characterisation of $TiCl_4$ Complexes with Hybrid Donor Ligands

The red powder produced in the attempted synthesis of [$TiCl_4${ $MeSe(CH_2)_3NMe_2$}], by the reaction of $TiCl_4$ with $MeSe(CH_2)_3NMe_2$ in a 1:1 molar ratio in anhydrous $CH_2Cl_2$ and at room temperature, was poorly soluble. This resulted in an extremely weak $^1$H NMR spectrum. Crystals were obtained by adding $CH_2Cl_2$ solutions of the two reagents together slowly without stirring and allowing them to diffuse into each other. These were analysed by single crystal X-ray diffraction and were characterised to be the zwitterionic $[Ti^{-}Cl_5\{MeSe(CH_2)_3N^{+}HMe_2\}]$ as shown in Figure 6-14.

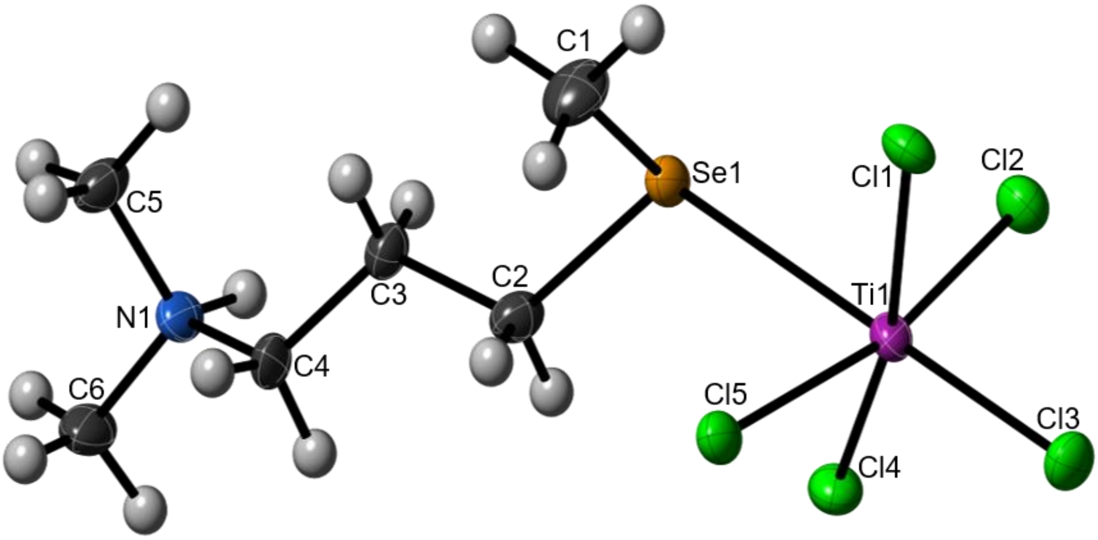

Figure 6-14: View of the crystal structure of the zwitterionic $[Ti^{-}Cl_5\{MeSe(CH_2)_3N^{+}HMe_2\}]$ complex with atom numbering scheme. Ellipsoids are shown at the 50 % probability level.

| | | | |
|---|---|---|---|
| Ti(1)-Cl(1) | 2.351(3) | Cl(1)-Ti(1)-Cl(2) | 87.82(9) |
| Ti(1)-Cl(2) | 2.303(3) | Cl(1)-Ti(1)-Cl(3) | 94.22(9) |
| Ti(1)-Cl(3) | 2.257(3) | Cl(1)-Ti(1)-Cl(4) | 167.0(1) |
| Ti(1)-Cl(4) | 2.297(3) | Cl(1)-Ti(1)-Cl(5) | 89.01(9) |
| Ti(1)-Cl(5) | 2.325(3) | Cl(2)-Ti(1)-Cl(3) | 98.2(1) |
| Ti(1)-Se(1) | 2.775(2) | Cl(4)-Ti(1)-Cl(3) | 98.8(1) |
| N(1)-C(4) | 1.48(1) | Cl(1)-Ti(1)-Se(1) | 83.55(7) |
| N(1)-C(5) | 1.48(1) | Cl(2)-Ti(1)-Se(1) | 83.60(7) |
| N(1)-C(6) | 1.46(1) | Cl(3)-Ti(1)-Se(1) | 177.06(9) |
| Se(1)-C(1) | 1.947(8) | Cl(4)-Ti(1)-Se(1) | 83.50(8) |
| Se(1)-C(2) | 1.947(8) | Cl(5)-Ti(1)-Se(1) | 84.11(7) |

Table 6-7: Selected bond distances (Å) and angles (°) for $[\mathrm{Ti^{-}Cl_5\{MeSe(CH_2)_3N^{+}HMe_2\}}]$.

The crystal structure shows that the ligand is coordinated through only one of the donor atoms. Surprisingly this is through the soft selenium atom rather than the hard nitrogen donor and the nitrogen in the $NMe_2$ group is pronated. Furthermore, the additional H and Cl is likely due to some minor hydrolysis of the $TiCl_4$. The bond lengths reported are close to those reported in the literature for compounds containing aTi-Se bond.[5,30] The Ti-Se bond, at 277 Å, is slightly longer that those reported in $[\mathrm{Cp_2Ti(SeMe)_2}]$ (2.53 Å) and $[\mathrm{Cp_2Ti(Se^tBu)_2}]$ (2.54 Å).[30]

The attempted synthesis of $[\mathrm{TiCl_4\{PhTe(CH_2)_3NMe_2\}}]$, involved reaction of $TiCl_4$ with $\mathrm{PhTe(CH_2)_3NMe_2}$ in a 1:1 molar ratio in anhydrous DCM and at room temperature, resulted in the production of a light brown powder. It appears to be insoluble in both DCM and chloroform hence obtaining an NMR has proved challenging. The IR spectrum shows typical Ti-Cl stretches (404 $cm^{-1}$ (vs), 380 $cm^{-1}$ (sh) and 357 $cm^{-1}$ (sh)) consistent with $TiCl_4$ complexes and are in the same region as those for $[\mathrm{TiCl_4\{^nBuSe(CH_2)_2Se^nBu\}}]$. However, microanalysis was not consistent with the proposed stoichiometry. Anal. Calcd for $C_{11}H_{17}Cl_4NTeTi$: C, 27.49; H, 3.57, N, 2.91. Found: C, 18.12; H, 3.22, N, 1.63 %. It is more consistent with $[\mathrm{(TiCl_5)_2PhTe(CH_2)_3NMe_2}]^{2-}\,2H^+$. Anal. Calcd for $C_{11}H_{19}Cl_{10}NTeTi_2$: C, 17.8; H, 2.58, N, 1.88. The attempted synthesis was unsuccessful.

In the attempted synthesis of [$TiCl_4${ $EtSe(CH_2)_3NMe_2$}], produced in the same way as above, a dark red solid was afforded. This colour is characteristic of Ti(IV) selenoether complexes. The solid appears to be insoluble in both dichloromethane and chloroform, hence NMR of this compound has not been acquired. The red solid afforded is very tar like in consistency, this may be due to the impurity in the ligand. Again, this synthesis is regarded as unsuccessful.

### 6.2.6 Attempted LPCVD experiments using Complexes with Hybrid Donor Ligands

Depositions were attempted using the [$TiCl_5${$MeSe(CH_2)_3N(H)Me_3$}] precursor and were completed using ~ 75 mg of precursors at a temperature of 873 K. In all attempts, very little material was deposited on the substrate and a large amount of black residue was present in the bulb. XRD analysis picked up no reflections, indicating that no crystalline material was deposited.

## 6.3 Conclusions and Further Work

In conclusion, several titanium chloride complexes with chalcogenoether ligands were synthesised.

The distorted octahedral selenoether complexes, [$TiCl_4(^nBuSe(CH_2)_nSe^nBu\}$] (n=2,3), were shown to be efficient single source precursors for thin films of $TiSe_2$. Variation of conditions showed that in thinner films, more crystallites lay parallel to the surface, however, these films were not continuous. Films were stable in ambient conditions for a number of months.

The mixed donor ligands $MeSe(CH_2)_3NMe_2$ and $PhTe(CH_2)_3NMe_2$ were successfully synthesised, as confirmed by $^1H$ and $^{13}C\{^1H\}$ NMR spectroscopy. $EtSe(CH_2)_3NMe_2$ could not be isolated from $Et_2Se_2$. [$Ti^-Cl_5\{MeSe(CH_2)_3N^+HMe_2\}$] was synthesized from $TiCl_4$ and $MeSe(CH_2)_3NMe_{2.}$ This complex was not suitable as a single source precursor for the LPCVD of $TiSe_2$ thin films.

In order to facilitate the deposition of titanium telluride thin films, a different precursor design could be used. Analogous hybrid ligands could be synthesised such as $^nBuTe(CH_2)_3NMe_2$.

## 6.4 Experimental

### 6.4.1 Synthesis and Characterisation of Ligands

All reactions were conducted using Schlenk, vacuum line and glove box techniques under a dry nitrogen atmosphere. The reagents were stored and manipulated using a glove box. Hexane was dried by distillation over a sodium wire. Dichloromethane was dried by distillation over $CaH_2$. Reagents were acquired from Sigma-Aldrich and used as received unless otherwise stated. $TiCl_4$ was distilled before use.

**$^nBuSe(CH_2)_3Se^nBu$**:

Selenium powder (5.0 g, 63 mmol) in dry THF (140 mL) was frozen in a liquid nitrogen bath. $^nBuLi$ (40 mL of a 1.6 M solution in hexane, 63 mmol) was added and the mixture was allowed to thaw and then stirred at room temperature for 2 hours to give a pale orange (almost colourless) solution. 1,3-dichloropropane (3.57 g, 30 mmol) was added dropwise to the solution which was then refluxed for 1 hour. The solution was hydrolysed with water (100 mL saturated with NaCl) and extracted with diethyl ether, dried over $MgSO_4$, filtered and the solvent removed *in vacuo* to leave a yellow oil. Yield: 58%. $^1H$ NMR ($CDCl_3$) δ: 0.93 (t, [6H], $CH_3$), 1.41 (m, [4H], $CH_2$), 1.65 (m, [4H], $CH_2$), 2.00 (m, [2H], $CH_2$), 2.58 (m, [4H], $CH_2Se$, $^1J_{SeC}$ = 60 Hz), 2.65 (m, [4H], $SeCH_2$, $^1J_{SeC}$ = 60 Hz). $^{13}C\{^1H\}$ ($CDCl_3$, 295 K): δ = 13.48, 22.89, 23.45, 23.64, 31.15, 32.60. $^{77}Se\{^1H\}$ NMR ($CH_2Cl_2$) δ: 158. A value of 156 ppm can be found in the literature.[15]

**$^nBuSe(CH_2)_2Se^nBu$**:

Prepared in the same way as above by other members of the group. The spectroscopic data match those in the literature.[15]

**$MeSe(CH_2)_3NMe_2$**:

$Me_2NCH_2CH_2CH_2Cl.HCl$ (1.58 g, 10 mmol) was neutralised with NaOH (0.4 g in 10 mL $H_20$). $Me_2NCH_2CH_2CH_2Cl$ was extracted with $CH_2Cl_2$ (40 mL) and the solvent was removed *in vacuo*. $NaBH_4$ (0.38 g, 10 mmol) was stirred with $Me_2Se_2$ (0.94 g, 5 mmol) in MeOH (60mL) under nitrogen at room temperature for ~ 1 hour. $Me_2NCH_2CH_2CH_2Cl$ in MeOH (20 mL) was added and the solution stirred for a further 15 hours. The solvent was removed *in vacuo*. The mixture was quenched with water and the organic product was extracted with $CH_2Cl_2$ (250 mL). The solvent was removed in vacuo to leave a yellow oil (200 mg, 10 %). $^1H$ NMR ($CDCl_3$) δ: 1.85 (m, [2H], $-CH_2-$), 2.01 (s, [3H], SeMe, $^1J_{SeC}$ = 8

Hz), 2.26 (s, [6H] $NMe_2$), 2.39 (t, [2H], $SeCH_2$, $^1J_{SeC}$ = 8 Hz), 2.58 (t, [2H], $NCH_2$). $^{13}C\{^1H\}$ NMR ($CDCl_3$) δ: 4.4 (s, SeMe), 23.3 (s, $SeCH_2$), 28.4 (s, $-CH_2-$), 45.7 (s, $NMe_2$), 59.8 (s, $NCH_2$).

**$MeSe(CH_2)_3NMe_2$ MeI salt**:

Excess MeI (5 mL) was reacted with $MeSe(CH_2)_3NMe_2$ and residual MeI removed *in vacuo* to afford a yellow solid. Anal. Calcd for $C_7H_{18}NSeI$: C, 25.32; H, 5.46; N, 4.22. Found: C, 25.00; H, 5.58; N, 4.11 %.

**$EtSe(CH_2)_3NMe_2$**:

$Me_2NCH_2CH_2CH_2Cl.HCl$ (3.43 g, 21.7 mmol) was neutralised with NaOH (0.87 g in 6 mL $H_20$). $Me_2NCH_2CH_2CH_2Cl$ was extracted using a separating funnel. $NaBH_4$ (0.76 g, 20 mmol) was stirred with $Et_2Se_2$ (2.18 g, 10 mmol) in MeOH (60mL) under nitrogen at room temperature for ~ 1 hour. $Me_2NCH_2CH_2CH_2Cl$ in MeOH (20 mL) was added and the solution stirred for a further 15 hours. The solvent was removed *in vacuo*. The mixture was quenched with water and the organic product was extracted with $CH_2Cl_2$ (5 x 50 mL). The solvent was removed *in vacuo* to leave a yellow oil (930 mg, 42 %). $^1H$ NMR ($CDCl_3$) δ: 1.41 (t, [3H], Me), 1.83 (m, [2H], $-CH_2-$), 2.23 (s, [6H] $NMe_2$), 2.35 (t, [2H], $NCH_2$), 2.39 (m, [4H], $SeCH_2$ x 2, $^1J_{SeC}$ = 16 Hz),. $^{13}C\{^1H\}$ NMR ($CDCl_3$) δ: 15.8 (s, $SeCH_2\underline{Me}$), 17.3 (s, $\underline{C}H_2Me$), 21.1 (s, $Se\underline{C}H_2$), 28.7 (s, $CH_2\underline{C}H_2CH_2$), 45.5 (s, $NMe_2$), 59.7 (s, $NCH_2$). $^{77}Se\{^1H\}$ ($CH_2Cl_2/CD_2Cl_2$) δ: 195.

**$PhTe(CH_2)_3NMe_2$**:

$Me_2NCH_2CH_2CH_2Cl.HCl$ (3.43 g, 21.7 mmol) was neutralised with NaOH (0.87 g in 6 mL $H_2O$). $Me_2NCH_2CH_2CH_2Cl$ was extracted. $NaBH_4$ (0.76 g, 20 mmol) was stirred with $Ph_2Te_2$ (2.91 g, 10 mmol) in MeOH (60mL) under nitrogen at room temperature for ~ 1 hour. $Me_2NCH_2CH_2CH_2Cl$ in MeOH (20 mL) was added and the solution stirred for a further 15 hours. The solvent was removed *in vacuo*. The mixture was quenched with water and the organic product was extracted under $N_2$ with $CH_2Cl_2$ (3 x 50 mL). The solvent was removed *in vacuo* to leave a red oil (2.70 g, 46 %) . $^1H$ NMR ($CDCl_3$) δ: 2.05 (m, [2H], $-CH_2-$), 2.25 (s, [6H] $NMe_2$), 2.40 (t, [2H], $NCH_2$), 3.00 (m, [2H], $TeCH_2$, $^1J_{TeC}$ = 16 Hz), 7.25 (m, [3H], Ph), 7.75 (m, [2H], Ph). $^{13}C\{^1H\}$ NMR ($CDCl_3$) δ: 6.22 (s, $TeCH_2$), 29.1 (s, $CH_2\underline{C}H_2CH_2$), 45.5 (s, $NMe_2$), 61.1 (s, $NCH_2$), 114 (s, 1-C, Ph), 127 (s, 4-C, Ph), 129 (s, 3,5-C, Ph), 138 (s, 2,6-C, Ph). $^{125}Te\{^1H\}$ NMR ($CH_2Cl_2/CD_2Cl_2$) δ: 472.

**$PhTe^+(Me)(CH_2)_3N^+Me_3$ $2I^-$ salt**:

Excess MeI was reacted with $PhTe(CH_2)_3NMe_2$ and residual MeI removed *in vacuo* to afford a yellow solid. $^1$H NMR ($(CD_3)_2SO$) δ: 2.15 (m, [3H], $Te^+Me$), 2.47 (m, [2H], $-CH_2-$), 2.85 (m, [2H], $N^+CH_2$), 3.01 (s, [9H], $N^+Me_3$), 3.34 (m, [2H], $Te^+CH_2$), 7.54 (m, [3H], Ph), 7.87 (m, [2H], Ph). $^{13}C\{^1H\}$ NMR ($(CD_3)_2SO$) δ: 9.19 (s, $Te^+CH_2$), 19.2 (s, $Te^+Me$), 24.1 (s, $-CH_2-$), 52.4 (s, $N^+Me_3$), 65.2 (s, $N^+CH_2$), 123 (s, 1-C, Ph), 130 (s, 4-C, Ph), 131 (s, 3,5-C, Ph), 134 (s, 2,6-C, Ph). $^{125}Te\{^1H\}$ NMR ($(CH_3)_2SO/(CD_3)_2SO$) δ: 609. Anal. Calcd for $C_{13}H_{23}I_2NTe$: C, 27.15; H, 4.03; N, 2.44. Found: C, 26.45; H, 4.06; N, 2.20 %.

### 6.4.2 Synthesis and Characterisation of $[TiCl_4\{^nBuSe(CH_2)_nSe^nBu\}]$ (n = 2,3)

**$[TiCl_4\{^nBuSe(CH_2)_2Se^nBu\}]$**:

$^nBuSe(CH_2)_2Se^nBu$ (0.277 g, 0.91 mmol) was dissolved in anhydrous hexane (20 mL) and a solution of $TiCl_4$ (0.10 mL, 0.91 mmol) was added. A red solution was formed immediately and further stirred for 1 hour at room temperature. The volatile components were removed *in vacuo* to give a soft red solid. IR: ν/cm$^{-1}$ = 379 (s), 410 (sh) Ti−Cl. $^1$H NMR ($CDCl_3$, 295K): δ = 0.90 (m) [3H] Me, 1.42 (m) [2H] $CH_2$, 1.75 (m) [2H] $CH_2$, 3.13 (m) [4H] $CH_2Se$. $^{13}C\{^1H\}$ ($CDCl_3$, 295 K): δ = 13.50, 22.94, 30.29, 32.33, 34.88. $^{77}Se\{^1H\}$ NMR ($CH_2Cl_2/CD_2Cl_2$, 183 K): δ = 380, 374. Anal. Calcd for $C_{10}H_{22}Cl_4Se_2Ti$: C, 24.52; H, 4.53. Found: C, 24.24; H, 4.94 %.

**$[TiCl_4\{^nBuSe(CH_2)_3Se^nBu\}]$**:

$^nBuSe(CH_2)_3Se$ $^nBu$ (0.286 g, 0.91 mmol) was dissolved in anhydrous hexane (20 mL) and a solution of $TiCl_4$ (0.10 mL, 0.91 mmol) was added. A red solution was formed immediately and further stirred for 1 hour at room temperature. A dark red oil was precipitated, and the solvent was decanted, and the volatile components were removed *in vacuo* to give a dark red extremely viscous oil. IR (neat thin film): ν/cm$^{-1}$ = 350 (sh), 391 (s), 456 (sh) Ti−Cl. $^1$H NMR ($CDCl_3$, 295K): δ = 0.96 (t) [3H] Me, 1.47 (m) [2H] $CH_2$, 1.78 (m) [2H] $CH_2$, 2.39 (quintet) [2H] $CH_2$, 3.10 (m) [2H] $CH_2Se$, 3.18 (m) [2H] $CH_2Se$ . $^{13}C\{^1H\}$ NMR ($CDCl_3$, 295 K): δ = 12.52, 21.91, 23.68, 29.69, 29.73, 33.89. $^{77}Se\{^1H\}$ NMR ($CH_2Cl_2/CD_2Cl_2$, 183 K): δ = 262. Anal. Calcd for $C_{11}H_{24}Cl_4Se_2Ti$: C, 26.22; H, 4.80. Found: C, 26.82; H, 5.59 %.

### 6.4.3 Synthesis and Characterisation of Hybrid Ligand Ti Complexes

**[$TiCl_5${ $MeSe(CH_2)_3NHMe_2$}]**:

$TiCl_4$ (0.11 mL, 1 mmol) was dissolved in anhydrous DCM (15 mL) and solution of $MeSe(CH_2)_3NMe_2$ (0.20 g, 1 mmol) in anhydrous DCM (5 mL) was added. A red precipitate was formed immediately, and the solution was further stirred for 1 hour at room temperature. The volatile components were reduced *in vacuo* and then the red solid was filtered off. $^1H$ NMR ($CDCl_3$) δ: 2.05 (m, [3H], SeMe), 2.27 (m, [2H], $-CH_2-$), 2.64 (m, [2H], $SeCH_2$), 2.82 (s, [6H] $NMe_2$), 3.13 (t, [2H], $NCH_2$). Anal. Calcd for $C_6H_{16}NSeTiCl_5$: C, 17.7; H, 3.97; N, 3.45 %. Found: C, 16.0; H, 3.98; N, 2.74 %. Crystals were obtained by adding solutions of the two reagents together slowly without stirring and allowing them to diffuse into each other.

**Attempted synthesis of [$TiCl_4${ $EtSe(CH_2)_3NMe_2$}]:**

$TiCl_4$ (0.15 mL, 1.44 mmol) was dissolved in anhydrous $CH_2Cl_2$ (15 mL) and $EtSe(CH_2)_3NMe_2$ (0.28 g, 1.44 mmol) was added. A red solution was formed immediately and further stirred for 1 hour at room temperature. The volatile components were removed *in vacuo* to give a soft dark red solid.

**Attempted synthesis of [$TiCl_4${$PhTe(CH_2)_3NMe_2$}]:**

$PhTe(CH_2)_3NMe_2$ (0.24 g, 0.70 mmol) was dissolved in anhydrous $CH_2Cl_2$ (10 mL) and a solution of $TiCl_4$ (excess) in $CH_2Cl_2$ (10 mL) was added. A brown solution was formed immediately and further stirred for 1.5 hours at room temperature. The volatile components were removed *in vacuo* to give a pale brown powder. It was stored under $N_2$ in a fridge. IR: 404 $cm^{-1}$, with shoulders at 380 and 351 $cm^{-1}$.

### 6.4.4 LPCVD

In a typical experiment, ca. 75, 10 or 5 mg of the reagent and 8 substrates (~2 × 5 × 20 mm) were loaded into a closed-end silica tube in a glove box. The substrates were sonicated in acetone before being dried in the oven overnight prior to experiments. The substrates were positioned adjacently through the heated zone. The tube was put in the furnace with the precursor positioned (ca. 2 cm) away from the edge of the heated zone. The tube was evacuated to 0.1 mmHg, and the furnace was set to the desired temperature. After ca. 20 min the tube position was adjusted to move the precursor further toward the hot zone (ca. 1 cm away from edge of the heated zone) until the oil gradually began to evaporate. At this point the sample position was maintained until the entire precursor had evaporated, leaving behind no residue. The tube was then cooled to room temperature and transferred to the glove box where the tiles were removed and stored for further characterisation. LPCVD using $[TiCl_4\{^nBuSe(CH_2)_nSe^nBu\}]$ (n = 2,3) was executed using temperatures between of 723 and 873 K and resulted in deposition of purple/blue/black films mainly concentrated on substrate 2 of 8. LPCVD using $[TiCl_4(S^nBu_2)_2]$ was executed using temperatures of 923 K and resulted in deposition of black films.

### 6.4.5 Substrate and Pre-treatment

Fused $SiO_2$ substrates were sonicated in acetone and dried in an oven overnight before use.

PVD $SiO_2$ substrates were fabricated by sputtering a high purity Si (99.99 %) target onto a silicon wafer using a medium frequency plasma assisted magnetron sputtering (Leybold Optics HELIOS Pro XL). This was done with a direct current power of 3000 W in an $O_2$/Ar atmosphere and at room temperature and a rotation speed of substrate at 180 rpm to achieve a uniform deposition. The surface was then etched via reactive ion etching. These were obtained from the ECS, University of Southampton.

TiN substrates were obtained from Si- Mat. TiN was applied to a Si wafer via PVD, the substrate then underwent PECVD of slow deposition of oxide onto TiN. The oxide was etched off using HF.

### 6.4.6 Thin Film Characterisation

Grazing incidence XRD - See Appendix 1.

AFM images were collected via tapping mode AFM on a Bruker Veeco Dimension 3100 and roughness measurements were acquired.

SEM images and EDX measurements were collected on a Philips XL30 ESEM with an UltraDry EDX spectrometer attachment. An accelerating voltage of 10 kV was used.

| Compound | $[TiCl_5\{ MeSe(CH_2)_3NHMe_2\}]$: |
|---|---|
| Formula | $C_6H_{16}Cl_5NSeTi$ |
| M | 406.31 |
| Crystal system | Monoclinic |
| Space group | $P\ 2_1/n$ |
| a[Å] | 7.1767(6) |
| b[Å] | 25.1904(17) |
| c[Å] | 8.0992(7) |
| α[deg] | 90 |
| β[deg] | 97.103(9) |
| γ[deg] | 90 |
| U[Å$^2$] | 1453.0(2) |
| Z | 4 |
| μ(Mo Kα) [mm$^{-1}$] | 3.980 |
| Total reflns | 7323 |
| Unique reflns | 2848 |
| $R_{int}$ | 0.090 |
| No. of parameters, restraints | 130,0 |
| $R_1$[b] $[I_o > 2\sigma(I_o)]$ | 0.069 |
| $R_1$[all data] | 0.135 |
| $wR_2$[b]$[I_o > 2\sigma(I_o)]$ | 0.114 |
| $wR_2$[all data] | 0.136 |

Table 6-8: Crystal data and structure refinement details[a]

[a] Common items: Temperature: 100 K; Wavelength (Mo Kα) = 0.71073 Å, θ(max) = 26.0 °.

[b] $R_1 = \Sigma|| F_o| - |F_c||/\Sigma|F_o|$.   $wR_2 = [\Sigma w(F_o^2 - F_c^2)^2/\Sigma wF_o^4]^{1/2}$

## 6.5 References

1 M. Chhowalla, H. S. Shin, G. Eda, L.-J. Li, K. P. Loh and H. Zhang, *Nat. Chem.*, 2013, **5**, 263–275.

2 J. Rasch, T. Stemmler, B. Müller, L. Dudy and R. Manzke, *Phys. Rev. Lett.*, 2008, **101**, 76021–76024.

3 E. Morosan, H. W. Zandbergen, B. S. Dennis, J. W. G. Bos, Y. Onose, T. Klimczuk, A. P. Ramirez, N. P. Ong and R. J. Cava, *Nat. Phys.*, 2006, **2**, 544–550.

4 S. L. Benjamin, C. H. de Groot, C. Gurnani, A. L. Hector, R. Huang, K. Ignatyev, W. Levason, S. J. Pearce, F. Thomas and G. Reid, *Chem. Mater.*, 2013, **25**, 4719–4724.

5 S. D. Reid, A. L. Hector, W. Levason, G. Reid, B. J. Waller and M. Webster, *Dalton Trans.*, 2007, **4**, 4769–4777.

6 R. Huang, S. L. Benjamin, C. Gurnani, Y. Wang, A. L. Hector, W. Levason, G. Reid and C. H. De Groot, *Sci. Rep.*, 2016, **6**, 275931–2759310.

7 C. J. Carmalt, I. P. Parkin and E. S. Peters, *Polyhedron*, 2003, **22**, 1263–1269.

8 S. Kikkawa, *Ceram. Int.*, 1997, **23**, 7–11.

9 M. Bochmann, I. Hawkins and L. M. Wilson, *J. Chem. Soc. Chem. Commun.*, 1988, **1578**, 344–345.

10 J. Cheon, J. E. Gozum and G. S. Girolami, *Chem. Mater.*, 1997, **4756**, 1847–1853.

11 T. Su. Lewkebandara, P. J. Mckarns, B. S. Haggerty, G. P. A. Yap, A. L. Rheingold and C. H. Winter, *Polyhedron*, 1998, **5387**, 1–9.

12 N. D. Boscher, C. J. Carmalt and I. P. Parkin, *Chem. Vap. Depos.*, 2006, **12**, 54–58.

13 N. D. Boscher, C. J. Carmalt and I. P. Parkin, *Appl. Surf. Sci.*, 2010, **256**, 3178–3182.

14 P. J. McKarns, T. S. Lewkebandara, G. P. A. Yap, L. M. Liable-Sands, A. L. Rheingold and C. H. Winter, *Inorg. Chem.*, 1998, **37**, 418–424.

15 C. H. de Groot, C. Gurnani, A. L. Hector, R. Huang, M. Jura, W. Levason and G. Reid, *Chem. Mater.*, 2012, **24**, 4442–4449.

16 S. L. Benjamin, C. H. de Groot, C. Gurnani, A. L. Hector, R. Huang, E. Koukharenko, W. Levason and G. Reid, *J. Mater. Chem. A*, 2014, **2**, 4865–4869.

17 W. Levason, B. Patel, G. Reid, V.-A. Tolhurst and M. Webster, *J. Chem. Soc. Dalton Trans.*, 2000, **4**, 3001–3006.

18 H. P. B. Rimmington and A. A. Balchin, *J. Cryst. Growth*, 1974, **15**, 51–56.

19 A. L. Hector, M. Jura, W. Levason, S. D. Reid and G. Reid, *New J. Chem.*, 2009, **33**, 641–645.

20 T. Chivers and R. S. Laitinen, *Chem. Soc. Rev.*, 2015, **44**, 1725–1739.

21 C. E. Housecroft and A. G. Sharpe, *Inorganic Chemistry*, Pearson Education Ltd., Essex, 2005.

22 K. George, C. H. de Groot, C. Gurnani, A. L. Hector, R. Huang, M. Jura, W. Levason and G. Reid, *Chem. Mater.*, 2013, **25**, 1829–1836.

23 E. G. Hope, T. Kermmitt and W. Levason, *J. Chem. Soc. Perkin Trans. 2*, 1987, **0**, 487–490.

24 T. Kemmitt and W. Levason, *Organometallics*, 1989, **8**, 1303–1308.

25 D. K. Paluru, S. Dey, A. Wadawale, D. K. Maity, N. Bhuvanesh and V. K. Jain, *Eur. J. Inorg. Chem.*, 2015, **2015**, 397–407.

26 S. L. Benjamin, Y.-P. Chang, C. Gurnani, A. L. Hector, M. Huggon, W. Levason and G. Reid, *Dalton Trans.*, 2014, **43**, 16640–16648.

27 C. Riekel, *J. Solid State Chem.*, 1976, **17**, 389–392.

28 N. J. Hill, W. Levason, G. Reid and A. J. Ward, *J. Organomet. Chem.*, 2002, **642**, 186–190.

29 S. Saito, J. Zhang, K. Tanida, S. Takahasgi and T. Koizumi, *Tetrahedron*, 1999, **55**, 2545–2552.

30 A. L. Hector, W. Levason, G. Reid, S. D. Reid and M. Webster, *Chem. Mater.*, 2008, **20**, 5100–5106.

# Chapter 7: Conclusions and Outlook

The aims of this work were to develop a range of single source precursors for the chemical vapour deposition of various metal chalcogenide thin films and nanowires and to optimise the conditions for deposition.

It was demonstrated that $[SbCl_3(Se^nBu_2)_3]$, $[SbCl_3(Te^nBu_2)_3]$ and $[BiCl_3(Se^nBu_2)_3]$, together with the previously reported $[BiCl_3(Te^nBu_2)_3]$, are efficient single source precursors for the deposition $Sb_2Se_3$, $Sb_2Te_3$ and $Bi_2Se_3$ respectively. NMR spectroscopy revealed that the complexes are extensively dissociated in solution and the ligands were easily removed under low pressure. Flash evaporation was required to avoid the removal of the ligand and subsequent tellurium contamination.

Combining the precursors $[SbCl_3(Te^nBu_2)_3]$ and $[BiCl_3(Te^nBu_2)_3]$ for LPCVD enabled the deposition of a ternary $(Sb_xBi_{1-x})_2Te_3$ phase. The ternary film composition was shown to be dependent on temperature. This is a p-type phase and, for thermoelectric applications, complements the n-type $[Bi_2(Te_xSe_{1-x})_3]$ ternary phase that has been deposited previously.[1] The CVD set up used in this work results in a temperature gradient and so there is a gradient in the ratio of Bi:Sb. Looking forward, a more uniform temperature profile to allow the deposition of a single ternary composition. Furthermore, both $Sb_2Te_3$, from $[SbCl_3(Te^nBu_2)_3]$, and $Bi_2Te_3$ , from $[BiCl_3(Te^nBu_2)_3]$,[2] have shown high levels of selectivity for TiN over $SiO_2$. The ability to achieve selective deposition of these ternary phases would be particularly interesting to create n-type and p-type elements for device fabrication.

Due to the extremely low Lewis acidity of $GeCl_4$, which results in no interaction with soft chalcogenoether ligands,[3] the research around precursor development for GeTe focussed upon a germanium tellurolate. Two synthesis routes to $[Ge(Te^nBu)_4]$ have been reported, the second of which was a reaction between activated germanium and dibutyl ditelluride and led to a lower level of impurity. GeTe has been deposited from this precursor at 723 K via LPCVD. Typically, no chloride was detected by EDX, but some films deposited also contained crystalline tellurium.

In order to consistently deposit low impurity GeTe thin films, modification of the precursor so that it contains germanium and tellurium in a stoichiometric ratio may be preferable. The compounds $R_3GeCl$ (R = Me, Et) are commercially available from Sigma-Aldrich and it may be possible to react these with $^nBuTeLi$ to obtain $[R_3GeTe^nBu]$. Alternatively, hard nitrogen-based ligands have been shown to bind to $GeCl_4$ and $GeCl_2$, for example

$[GeCl_4\{Me_2N(CH_2)_2NMe_2\}]$[4] and $[GeCl_2\{Me_2N(CH_2)_2NMe_2\}]$.[5] Consequently, a hybrid ligand approach may be suitable such as $Me_2N(CH_2)_3Te^nBu$, where the hard nitrogen donor can anchor the chalcogen to the germanium. Furthermore, combining a suitable precursor for GeTe, with $[SbCl_3(Te^nBu_2)_3]$ could enable the deposition of GST, or even layered $GeTe/Sb_2Te_3$.

A number of precursors for the LPCVD of $SnE_2$ (E = S, Se) have been described. It has been established that $[SnCl_4\{^nBuS(CH_2)_3S^nBu\}]$ and $[SnCl_4(E^nBu_2)_2]$ (E = S, Se) are effective single source precursors for the deposition of tin dichalcogenide thin films. Whilst the tin dichalcogenides were easy to deposit from these precursors via LPCVD, the tin monochalcogenides proved more challenging as a much higher temperature was required. However, SnS and SnSe were deposited from $[SnCl_4\{^nBuS(CH_2)_3S^nBu\}]$ and $[SnCl_4\{^nBuSe(CH_2)_3Se^nBu\}]$ at 831 K and 861 K respectively.

Due to the limitations of the setup used, it was difficult to reach the temperatures required to facilitate the deposition of tin monochalcogenides. Further work towards these materials is on-going in the group in order to optimise the conditions for deposition.

The work in this thesis has also demonstrated the versatility of the single source precursors developed over the course of the project. In particular, it shows that those suitable for the LPCVD of thin films are also often suitable for the deposition of metal chalcogenide nanowires via LICVD methods. In this context, $[SnCl_4\{^nBuSe(CH_2)_3Se^nBu\}]$ has been used to deposit $SnSe_2$ nanowires. To the best of my knowledge, there are no examples of $SnSe_2$ nanowires in the literature and this highlights one of the advantages of using a single source precursor over other reported methods which often require excess chalcogen. For example, SnSe has been deposited from SnSe and Se powder at 823 K.[6]

In preliminary experiments, other single source precursors, $[MCl_3(Se^nBu_2)_3]$ (M = Sb, Bi), were also used to deposit nanowires. The density of these $Sb_2Se_3$ and $Bi_2Se_3$ nanowires was low and optimisation of the CVD conditions will be required to increase the nanowire yield. The experiments depositing $SnSe_2$ nanowires showed that the density and morphology of nanowires could be controlled by the precursor concentration and argon flow rate. The precursors were dissolved in anhydrous toluene in this method and this means that they could also be suitable for use in other deposition methods where a solvent is required, such as AACVD.

$TiSe_2$ thin films have been deposited from the coordination complexes, $[TiCl_4\{^nBuSe(CH_2)_nSe^nBu\}]$ (n = 2,3) at 873 K. Films showed no residual chloride by EDX analysis and GIXRD revealed that the thinner films had more crystallites with their c axis perpendicular to the substrate. Films were stable for a period of months. Due to the $TiCl_4$ being a hard acceptor and the chalcogen a soft donor, a number of hybrid ligands, $MeSe(CH_2)_3NMe_2$ and $PhTe(CH_2)_3NMe_2$, were synthesised incorporating a hard amine function, with a view to anchoring the ligand on the $TiCl_4$. Interestingly, when $MeSe(CH_2)_2NMe_2$ was reacted with $TiCl_4$, the zwitterioninc complex, $[TiCl_5^-\{MeSe(CH_2)_3N^+HMe_2\}]$, was formed and the ligand was coordinated through the soft selenium donor atom as evidenced by single crystal X-ray diffraction.

Whilst the hybrid ligand route to tether soft chalcogenoethers to the hard nitrogen centre was unsuccessful, a route that could be explored is the synthesis of a tellurolate precursor such as $[Ti(Te^nBu)_4]$. In the literature there are examples of titanium thiolate precursors such as $[Ti(S^nBu)_4]$ used for thermal decomposition to deposit TiS.[7] Furthermore, there are examples of titanium tellurolate compounds in the literature such as $[Ti\{TeSi(SiMe_3)_3\}_4]$.[8]

Overall a range of novel single source precursors for a plethora of both binary and ternary metal chalcogenides have been synthesised and characterised by microanalysis, IR spectroscopy, $^1H$, $^{13}C\{^1H\}$ and where applicable $^{77}Se\{^1H\}$, $^{125}Te\{^1H\}$ and $^{119}Sn$ NMR spectroscopy. Thin films and nanowires have been characterised by XRD, SEM, EDX and Raman spectroscopy. Electrical measurements are consistent with those found in the literature.

## References

1 S. L. Benjamin, C. H. Kees de Groot, C. Gurnani, S. L. Hawken, A. L. Hector, R. Huang, M. Jura, W. Levason, E. Reid, G. Reid, S. Richards and G. B. G. Stenning, *Under Rev.*

2 S. L. Benjamin, C. H. de Groot, C. Gurnani, A. L. Hector, R. Huang, E. Koukharenko, W. Levason and G. Reid, *J. Mater. Chem. A*, 2014, **2**, 4865–4869.

3 M. F. Davis, W. Levason, G. Reid, M. Webster and W. Zhang, *Dalton Trans.*, 2008, **4334**, 533–538.

4 F. Cheng, M. F. Davis, A. L. Hector, W. Levason, G. Reid, M. Webster and W. Zhang, *Eur. J. Inorg. Chem.*, 2007, **2007**, 4897–4905.

5 F. Cheng, J. M. Dyke, F. Ferrante, A. L. Hector, W. Levason, G. Reid, M. Webster and W. Zhang, *Dalton Trans.*, 2010, **39**, 847–856.

6 F. K. Butt, M. Mirza, C. Cao, F. Idrees, M. Tahir, M. Safdar, Z. Ali, M. Tanveer and I. Aslam, *CrystEngComm*, 2014, **16**, 3470–3473.

7 M. Bochmann, I. Hawkins and L. M. Wilson, *J. Chem. Soc. Chem. Commun.*, 1988, **1578**, 344–345.

8 C. P. Gerlach, V. Christou and J. Arnold, *Inorg. Chem.*, 1996, **35**, 2758–2766.

# Appendix 1 – General Experimental Techniques

The following experimental techniques were used unless otherwise stated.

## Ligand and Precursor Characterisation

IR spectra were recorded as Nujol mulls or neat thin films between CsI plates using a Perkin-Elmer Spectrum 100 instrument over the range 4000-200 cm$^{-1}$.

$^{1}$H and $^{13}$C{$^{1}$H} NMR spectra were recorded from solutions in $CDCl_3$ or $CD_2Cl_2$ on a Bruker AV400 spectrometer, $^{77}$Se{$^{1}$H} and $^{125}$Te{$^{1}$H} NMR spectra were recorded from solutions in $CH_2Cl_2/CD_2Cl_2$ on a Bruker AV400-II spectrometer at 76.3 and 126.2 MHz and referenced to external neat $SeMe_2$ and $TeMe_2$, respectively.

Microanalytical results (combustion analysis) were obtained from Medac Ltd.

## PVD Substrates

PVD $SiO_2$ films with thickness of 1 μm were deposited by the medium frequency magnetron sputtering method using a pure Si (99.99% purity) target with a DC power of 2000 W in an $O_2$/Ar atmosphere. The $O_2$ and Ar flow rates were maintained at 20 and 40 SCCM respectively. With the same drive speed of 180 rpm, the deposition rate was 0.3 nm s$^{-1}$.

## Thin Film Characterisation

Grazing incidence and in plane X-ray diffraction (XRD) patterns and pole figure measurements were collected in grazing incidence mode on a Rigaku SmartLab system, using CuKα X-rays, a 2θ scan range of 10–80° and an ω-offset of 0.7 or 1°.

The grazing incidence and in plane XRD patterns were matched to literature patterns to determine the crystalline phase.[1]

Lattice parameters were calculated by optimisation of the fit of grazing incidence or in plane XRD patterns in PDXL2.[2]

Scanning electron microscopy (SEM) images and energy dispersive X-ray (EDX) measurements were obtained using a JEOL JSM 6500 F Field Emission Scanning Electron Microscope with an Oxford INCA x-sight 7418 EDX probe. An accelerating voltage of 10 or 15 kV was used, and samples were calibrated against standards. High resolution cross sectional SEM were obtained using a field emission SEM (Jeol JSM 7500F) at an accelerating voltage of 5 kV.

Raman scattering spectra of the deposited films were measured at room temperature on a Renishaw InVia Micro Raman Spectrometer using a helium–neon laser with a wave-length of 632.8 nm. The incident laser power was adjusted to 0.1mWfor all samples.

Hall and Van der Pauw measurements were performed at room temperature on a Nanometrics HL5500PC at 300 K. For each measurement, four copper probes with diameter of ca.1mm were carefully placed on the sample corners. Extra care was taken to ensure linear contact was obtained between each probe and the sample before each measurement.

### Temperature Profiling

This was used to determine the exact temperature where deposition occurred when the phase deposited was extremely sensitive to temperature. The furnace, insulated with glass wool at either end, was set to a specific temperature and allowed to heat up and stabilise. A temperature probe, positioned in the centre of the furnace, was used to measure the temperature in increments of 1 cm, it was left in each position until the temperature was stable.

## References

1 ICSD Inorg. Cryst. Struct. Database Fachinformationszentrum Karlsruhe (FIZ), accessed via EPSRC funded Natl. Database Serv. hosted by R. Soc. Chem.

2 S. Grazulis, D. Chateigner, R. T. Downs, A. F. T. Yokochi, M. Quirós, L. Lutterotti, E. Manakova, J. Butkus, P. Moeck and A. Le Bail, J. Appl. Crystallogr., 2009, 42, 726– 729